

AD-A265 407

2. REPORT DATE  
19923. REPORT TYPE AND DATES COVERED  
DISSERTATION

## 4. TITLE AND SUBTITLE

Observing and Modelling F-Region Ionospheric Dynamics  
Using the [OII] 7320A Emission

## 5. FUNDING NUMBERS

## 6. AUTHOR(S)

Stephen Scott Carr, Captain

## 7. PERFORMING ORGANIZATION NAME(S) AND ADDRESS(ES)

AFIT Student Attending: University of Michigan

8. PERFORMING ORGANIZATION  
REPORT NUMBER

AFIT/CI/CIA-92-031D

## 9. SPONSORING/MONITORING AGENCY NAME(S) AND ADDRESS(ES)

AFIT/CI  
Wright-Patterson AFB OH 45433-658310. SPONSORING/MONITORING  
AGENCY REPORT NUMBER

## 11. SUPPLEMENTARY NOTES

DTIC  
ELECTE  
JUN 7 1993  
S c D

## 12a. DISTRIBUTION/AVAILABILITY STATEMENT

Approved for Public Release IAW 190-1  
Distribution Unlimited  
MICHAEL M. BRICKER, SMSgt, USAF  
Chief Administration

## 12b. DISTRIBUTION CODE

## 13. ABSTRACT (Maximum 200 words)

93-12597



3308

## 14. SUBJECT TERMS

15. NUMBER OF PAGES  
295

## 16. PRICE CODE

17. SECURITY CLASSIFICATION  
OF REPORT18. SECURITY CLASSIFICATION  
OF THIS PAGE19. SECURITY CLASSIFICATION  
OF ABSTRACT

## 20. LIMITATION OF ABSTRACT

## ACKNOWLEDGEMENTS

I would like to thank all of you taxpayers for spending your monies so wisely.

I also need to thank the United States Air Force for sending me on my third academic tour. I shall repay this generosity by teaching the youth of our military at the USAFA. Major Smith, AFIT/CIRF, deserves a lot of credit for keeping the paperwork to a minimum, thereby allowing me to concentrate fully on academia.

I want to thank my committee, whose guidance kept me focussed and enabled me to get through this program in three years. Drs Brake, Killeen, Kuhn, Niciejewski and Yee formed a very diverse committee - their recommendations made this dissertation much more complete. I offer special thanks to Dr Niciejewski; north of the Arctic Circle, he introduced me to the rest of my life!

During my PhD Odyssey, many students, faculty/staff and family members guided me through these academic straits. Special thanks go to the following people: Gerry Schmitt, who taught me everything I know about computers - nine times out of 10, I can now successfully identify one; Qian Wu, who introduced me to Tom Clancy novels and scientific reasoning, and showed me how to decipher other people's FORTRAN code; Wei Deng, who pointed out two important facts to me - (1) absolutely *anything* can be proven mathematically and (2) *never* modify someone else's code; Young-in Won, who taught me to always have a song in my

heart, but 'Queen' on the tape-player; Rob Raskin, who persuaded me to take a job in Colorado instead of Washington D.C. (now *that* was tough!); Alan Burns, who correctly (I think) answered five questions per day for 687 straight days (ranging from "why is the perpendicular component of the ion temperature always greater than the parallel one above 180km in the polar F2-Region?" to "what really caused the Boer War?"); Ned Snell, who taught me that one person alone *can* keep the peanut butter industry profitable if one eats a PB&J sandwich everyday for three years; Claudia Alexander, who showed me that Stanford's football team is its marching band; Brian Johnson, who proved to me that as one's age increases, so does one's coffee consumption; John Daniel, who taught me that pet bunnies are great hand warmers, that weight-lifting is detrimental to one's tennis game, and that even 5'8" people can hang on basketball rims; Ed (I always microwave my jalapenos first) Hume, who taught me that after four weeks of making corrections, it's time to stop; Michael Minock, who taught me that some people can finish in five hours what it takes others one week to finish; Jeff Thayer, who taught me (unsuccessfully) how to dress GQish; Dick Cannata, who taught me that *anything* sounds good compared to Jimmy Buffet songs; Bruno Nardi, who taught me how to dream, smell the roses and swill ouzo; Steve Thomas, who frequently gave me the necessary attitude adjustment; Joan Lavalley, who proved to me that people who own yippee dogs can be normal; Nelly de Maldonado, who took care of every administrative need; Angelo Nuzzo, who made me come back for my PhD (Sunny and I know where you live, pal!); Chris Froehlich, who called me once a month for three years from somewhere overseas just to remind me what it was like to have a life; and my entire family, for offering the encouragement I needed to get through this three year hiatus from life.

I would also like to thank the management of the Powerhouse Gym and my friends who train there - without that vent for my academic frustrations, I may have turned into an engineer! I know each of you will read this dissertation between squats.

And finally, I would like to thank my wife Anette, whose love and patience made this easy (relatively speaking, of course).

And now, with Ann Arbor in the rearview mirror and the future straight ahead, fare thee well.

Accession For	
NTIS CRA&I	<input checked="" type="checkbox"/>
DTIC TAB	<input type="checkbox"/>
Unannounced	<input checked="" type="checkbox"/>
Justification	
By	
Distribution/	
Availability Codes	
Dist	Avail and/or Special
A-1	



## ABSTRACT

### OBSERVING AND MODELLING F-REGION IONOSPHERIC DYNAMICS USING THE [OII] 7320Å EMISSION

by  
Stephen Scott Carr

Chair: Timothy L. Killeen

Limb-scan observations of Doppler line profiles from the [OII]  $\lambda 7320\text{\AA}$  emission at F-Region altitudes, made with the Fabry-Perot interferometer (FPI) on the Dynamics Explorer-2 (DE-2) spacecraft, have been analyzed to provide measurements of the meridional component of the ion convection velocity along the instrument line-of-sight. The DE-2 results presented here demonstrate the first spaceborne use of the remote-sensing Doppler technique for measurements of ionospheric convection. The FPI meridional ion drift measurements have been compared with nearly simultaneous *in situ* ion drift measurements from the Retarding Potential Analyzer (RPA) on DE 2. Once allowance is made for the temporal lag between the *in situ* and remote measurements, the results from the two techniques are found to be in good agreement, within specified experimental errors, giving confidence in the FPI measurements.

The spaceborne interferometric technique has future utility for 2-dimensional imaging of polar ionospheric convection. Results from a simulated space-based observing platform, based on the DE-2 technique and an extension of a 7320Å aeronomical model, are presented to demonstrate that a large fraction of the entire polar ionospheric convection pattern can be monitored from space during ~16-minute polar passes of a suitably-

instrumented satellite. In the simulation, the polar-orbiting satellite's FPI system views the 7320Å emission at various tangent point altitudes at  $\pm 45^\circ$  and  $\pm 135^\circ$  to the satellite velocity vector. By adjusting the horizon scan angle, several swaths of vectors at different horizontal spacing from the satellite can be recovered.

Doppler line profiles from the [OII]  $\lambda 7320\text{\AA}$  emission at F-Region altitudes, made with the FPI at Søndre Strømfjord, Greenland, have been analyzed to provide ion drift vectors and temperatures. These measurements demonstrate a unique ground-based use of the remote sensing technique from within the auroral zone since they are compared to simultaneous incoherent scatter radar (ISR) measurements. Results from the two techniques are in reasonable agreement, within specified instrumental errors, giving confidence in ground-based FPI measurements of the high-latitude ionospheric convection pattern and temperature field.

## ABSTRACT

### OBSERVING AND MODELLING F-REGION IONOSPHERIC DYNAMICS USING THE [OII] 7320Å EMISSION

by  
Stephen Scott Carr

Chair: Timothy L. Killeen

Limb-scan observations of Doppler line profiles from the [OII]  $\lambda 7320\text{\AA}$  emission at F-Region altitudes, made with the Fabry-Perot interferometer (FPI) on the Dynamics Explorer-2 (DE-2) spacecraft, have been analyzed to provide measurements of the meridional component of the ion convection velocity along the instrument line-of-sight. The DE-2 results presented here demonstrate the first spaceborne use of the remote-sensing Doppler technique for measurements of ionospheric convection. The FPI meridional ion drift measurements have been compared with nearly simultaneous *in situ* ion drift measurements from the Retarding Potential Analyzer (RPA) on DE 2. Once allowance is made for the temporal lag between the *in situ* and remote measurements, the results from the two techniques are found to be in good agreement, within specified experimental errors, giving confidence in the FPI measurements.

The spaceborne interferometric technique has future utility for 2-dimensional imaging of polar ionospheric convection. Results from a simulated space-based observing platform, based on the DE-2 technique and an extension of a 7320Å aeronomical model, are presented to demonstrate that a large fraction of the entire polar ionospheric convection pattern can be monitored from space during ~16-minute polar passes of a suitably-

instrumented satellite. In the simulation, the polar-orbiting satellite's FPI system views the  $7320\text{\AA}$  emission at various tangent point altitudes at  $\pm 45^\circ$  and  $\pm 135^\circ$  to the satellite velocity vector. By adjusting the horizon scan angle, several swaths of vectors at different horizontal spacing from the satellite can be recovered.

Doppler line profiles from the  $[\text{OII}]\lambda 7320\text{\AA}$  emission at F-Region altitudes, made with the FPI at Søndre Strømfjord, Greenland, have been analyzed to provide ion drift vectors and temperatures. These measurements demonstrate a unique ground-based use of the remote sensing technique from within the auroral zone since they are compared to simultaneous incoherent scatter radar (ISR) measurements. Results from the two techniques are in reasonable agreement, within specified instrumental errors, giving confidence in ground-based FPI measurements of the high-latitude ionospheric convection pattern and temperature field.

**OBSERVING AND MODELLING F-REGION IONOSPHERIC DYNAMICS  
USING THE [OII] 7320Å EMISSION**

by

Stephen Scott Carr

A dissertation submitted in partial fulfillment  
of the requirements for the degree of  
Doctor of Philosophy  
(Atmospheric Sciences)  
in The University of Michigan  
1992

**Doctoral Committee:**

Professor Timothy L. Killeen, Chair  
Associate Professor Mary L. Brake  
Professor William R. Kuhn  
Assistant Research Scientist Rick Niciejewski  
Associate Research Scientist Jeng-Hwa Yee

© Stephen Scott Carr 1992  
All Rights Reserved

It is always in season for old men to learn.  
-Agamemnon

To my parents...  
You taught me everything I ever needed to know.



## PREFACE

Limb-scan observations of Doppler line profiles from the [OII]  $\lambda 7320\text{\AA}$  emission at F-Region altitudes, made with the Fabry-Perot interferometer (FPI) on the Dynamics Explorer-2 (DE-2) spacecraft, have been analyzed to provide measurements of the meridional component of the ion convection velocity along the instrument line-of-sight. The DE-2 results presented here demonstrate the first spaceborne use of the remote-sensing Doppler technique for measurements of ionospheric convection. The FPI meridional ion drift measurements have been compared with nearly simultaneous *in-situ* ion drift measurements from the Retarding Potential Analyzer (RPA) on DE 2. Once allowance is made for the temporal lag between the *in-situ* and remote measurements, the results from the two techniques are found to be in good agreement, within specified experimental errors, giving confidence in the FPI measurements.

The spaceborne interferometric technique has future utility for 2-dimensional imaging of polar ionospheric convection. Results from a simulated space-based observing platform, based on the DE-2 technique and an extension of a  $7320\text{\AA}$  aeronomical model, are presented to demonstrate that a large fraction of the entire polar ionospheric convection pattern can

be monitored from space during ~16-minute polar passes of a suitably-instrumented satellite. In the simulation, the polar-orbiting satellite's FPI system views the 7320Å emission at various tangent point altitudes at  $\pm 45^\circ$  and  $\pm 135^\circ$  to the satellite velocity vector. By adjusting the horizon scan angle, several swaths of vectors at different horizontal spacing from the satellite can be recovered.

Doppler line profiles from the [OII]  $\lambda 7320\text{\AA}$  emission at F-Region altitudes, made with the FPI at Søndre Strømfjord, Greenland, have been analyzed to provide ion drift vectors and temperatures. These measurements demonstrate a unique ground-based use of the remote sensing technique from within the auroral zone since they are compared to simultaneous incoherent scatter radar (ISR) measurements. Results from the two techniques are in reasonable agreement, within specified instrumental errors, giving confidence in ground-based FPI measurements of the high-latitude ionospheric convection pattern and temperature field.

## TABLE OF CONTENTS

<b>ACKNOWLEDGEMENTS .....</b>	<b>iii</b>
<b>PREFACE .....</b>	<b>vi</b>
<b>TABLE OF CONTENTS .....</b>	<b>viii</b>
<b>LIST OF FIGURES .....</b>	<b>xii</b>
<b>LIST OF TABLES .....</b>	<b>xxviii</b>
<b>LIST OF APPENDICES .....</b>	<b>xxix</b>
<b>CHAPTER</b>	
<b>1. INTRODUCTION.....</b>	<b>1</b>
1.1 DISSERTATION OBJECTIVE .....	1
1.2 INTRODUCTION AND ORGANIZATION.....	1
1.3 SOLAR MORPHOLOGY.....	6
1.4 THE SOLAR WIND AND INTERPLANETARY MAGNETIC FIELD.....	7
1.5 THE AURORA .....	13
1.6 INTRODUCTION TO THE IONOSPHERE.....	16
1.7 INTRODUCTION TO THE THERMOSPHERE .....	19
1.8 TRANSPORT EQUATIONS OF THE IONOSPHERE AND THERMOSPHERE .....	21
1.9 ELECTRIC FIELDS IN THE UPPER ATMOSPHERE.....	29
1.10 AIRGLOW.....	34
1.11 THE IONOSPHERIC [OII] 7320-7330Å AIRGLOW EMISSION .....	35
1.11.1 Sources of O <sup>+</sup> ( <sup>2</sup> P) Ions .....	37

1.11.2 Sinks of $O^+(2P)$ Ions.....	40
1.11.3 Number Densities and Emission Rates.....	43
1.11.4 Other Previous Studies.....	45
1.11.5 Viewing Conditions .....	48
<b>2. RESEARCH TOOLS.....</b>	<b>52</b>
2.1 THE FABRY-PEROT INTERFEROMETER (FPI).....	52
2.1.1 Mathematical Description.....	53
2.1.2 Recovery of Line of Sight Drifts, Temperatures and Brightnesses from the Spectrogram.....	62
2.1.3 DE-2 FPI.....	67
2.1.4 Søndre Strømfjord FPI.....	75
2.2 SØNDRE STRØMFJORD INCOHERENT SCATTER RADAR.....	79
2.3 THE DE-2 RETARDING POTENTIAL ANALYZER (RPA).....	82
2.4 MODELS USED IN THE $[OII]$ 7320Å VOLUME EMISSION RATE MODEL.....	85
2.4a The Vector Spherical Harmonics (VSH) Model .....	86
2.4b Solar Flux Model (SSFLUX) .....	86
2.4c Mass Spectrometer and Incoherent Scatter Model (MSIS).....	92
2.4d International Reference Ionosphere Model (IRI) .....	94
2.4e Photoelectron Model .....	96
<b>3. THE 7320Å VOLUME EMISSION RATE MODEL.....</b>	<b>103</b>
3.1 INTRODUCTION.....	103
3.2 PHOTOCHEMICAL MODELLING OF THE $[OII]$ 7320Å EMISSION .....	104
3.3 FOUR VERSIONS OF THE 7320Å VOLUME EMISSION RATE MODEL.....	109
3.3.1 Airglow Model .....	109
3.3.2 Aurora-Airglow Model .....	111
3.3.3 Maxwellian Model .....	124
3.3.4 Global 7320Å Model .....	124

3.4	RETRIEVING ATOMIC OXYGEN DENSITIES FROM [OII] 7320Å AIRGLOW .....	133
3.5	CONCLUSIONS .....	139
<b>4.</b>	<b>REMOTE-SENSING OBSERVATIONS OF F-REGION ION DRIFTS, ION TEMPERATURES AND BRIGHTNESSES USING DYNAMICS EXPLORER-2 DOPPLER MEASUREMENTS OF THE [OII] 7320Å EMISSION .....</b>	<b>141</b>
4.1	DE-2 FPI [OII] 7320Å EMISSION OBSERVATIONS.....	145
4.1.1	DE-2 FPI (7320Å) Spectrograms.....	145
4.1.2	Sample DE-2 FPI (7320Å) Brightness, Drift and Temperature Profiles.....	148
4.1.4	Meridional Ion Drift Additive Constant.....	152
4.1.5	Phenomena Affecting O <sup>+</sup> ( <sup>2</sup> P) Ion Drift .....	154
4.1.5.1	Transport .....	154
4.1.5.2	ExB Drift.....	156
4.1.5.3	Effects of Ion Pickup, Neutral Momentum and Neutral Winds on Ion Drifts .....	158
4.2	COMPARISONS BETWEEN FPI AND RPA ION DRIFT MEASUREMENTS .....	163
4.3	DE-2 FPI (7320Å) ION TEMPERATURES .....	170
4.3.1	Modification of the DE-2 Standard Analysis Software .....	171
4.3.1.1	Doublet Separation Determination .....	171
4.3.1.2	RPA vs FPI Ion Temperature Comparisons.....	174
4.4	VALIDATION OF THE 7320Å VOLUME EMISSION RATE MODEL AGAINST DE-2 FPI (7320Å) OBSERVATIONS .....	178
4.5	CONCLUSIONS .....	182
<b>5.</b>	<b>GROUND-BASED FPI (7320Å) OBSERVATIONS OF IONOSPHERIC DYNAMICS AND ENERGETICS FROM GREENLAND .....</b>	<b>184</b>
5.1	OUTLINE OF THE 7320Å ARCTIC CAMPAIGN .....	184
5.1.1	Thule AB, 8 - 15 January 1991 .....	185
5.1.2	Søndre Strømfjord, 16 - 21 January 1991 .....	185
5.1.3	Thule AB, 1 - 10 April 1991.....	187
5.1.4	Søndre Strømfjord, 3 - 10 September 1991 .....	188

5.2	FPI (7320Å) RESULTS AND ISR COMPARISONS FROM SØNDRE STRØMFJORD .....	189
5.2.1	FPI Retrieved Ion Drifts and Temperatures and ISR Comparisons.....	190
5.2.2	FPI vs VSH Ion Drifts and Temperatures.....	201
5.3	CONCLUSIONS.....	203
<b>6. DOPPLER IMAGING OF THE HIGH LATITUDE IONOSPHERIC CONVECTION PATTERN FROM SPACE: RESULTS OF A SIMULATION AND FLIGHT DEMONSTRATION STUDY.....</b>		<b>205</b>
6.1	DE-2 FPI (7320Å) SIMULATOR.....	206
6.1.1	Mathematical description of the DE-2 FPI (7320Å) Simulator .....	207
6.1.2	DE-2 FPI (7320Å) Simulator Examples.....	210
6.2	DE-2 FPI (7320Å) SIMULATION VALIDATION STUDIES.....	211
6.2.1	Orbit 1343 Simulation .....	213
6.2.2	Orbit 8000 Simulation .....	215
6.3	SIMULATED SATELLITE OBSERVATIONS OF THE HIGH LATITUDE ION CONVECTION PATTERN .....	216
6.3.1	CONVEX Geometry and Instrumentation .....	217
6.3.2	Determination of Spectrograms and Vector Ion Drifts.....	225
6.3.3	Simulation Results .....	227
6.3.4	Viewing At Different Elevation Angles to Produce Multiswaths of Ion Drifts.....	228
6.4	CONCLUSIONS.....	234
<b>7. CONCLUSIONS AND FUTURE WORK .....</b>		<b>237</b>
<b>APPENDICES.....</b>		<b>242</b>
<b>REFERENCES.....</b>		<b>278</b>

## LIST OF FIGURES

### **Figure**

- 1.1 Schematic of the solar atmosphere (adapted from Brasseur and Solomon, 1984) ..... 8
- 1.2 Three dimensional illustration of the solar equatorial current sheet and associated magnetic field lines. The current sheet is shown as lying near the solar equator with spiralled, outward pointing magnetic field lines lying above it and inward pointing field lines lying below it. The current sheet contains folds. When the sun rotates, an observer near the ecliptic plane will (alternately) lie above and below the current and will therefore see a changing sector pattern (from Kelley, 1989) ..... 10
- 1.3 Schematic representation of the magnetosphere (adapted from Kelley, 1989) ..... 12
- 1.4 Magnetospheric distortion caused by the solar wind (adapted from Lui, 1987). The magnetosphere is distorted because of its interaction with the solar wind; the magnetic field appears flattened on the dayside and elongated on the nightside. When the field has a southward component, there are enhanced magnetic storms, ionospheric storms and an increase in aurorae..... 13
- 1.5 Typical profiles of neutral atmospheric temperature and ionospheric plasma density with the layers designated (adapted from Kelley, 1989) ..... 20
- 1.6 Cycloidal trajectories described by ions and electrons in crossed  $\mathbf{E}$  and  $\mathbf{B}$ . Note that both electrons and ions drift in the  $\mathbf{E} \times \mathbf{B}$  direction with the ion's gyroradius much larger but the electrons gyrofrequency much greater, producing a drift velocity that is the same for both species. When both species drift together, ambipolar diffusion occurs..... 29
- 1.7 Schematic of ionospheric electric fields in the Northern Hemisphere polar cap and auroral zone in geomagnetic coordinates. The solid lines represent contours of electric potential, which act as streamlines to plasma flow - as denoted by the arrow ..... 32
- 1.8 Select OII transitions, modified from Seaton and Osterbrock (1957) and Yee, (1980). The  $7319.9\text{\AA}$  doublet separation ( $0.836\text{\AA}$ ) was determined by Meriwether et al. (1974) from a ground-based Fabry-Perot interferometer. In

this dissertation, the 7319.9Å doublet will be referred to as the 7320Å doublet. Optical instrumental resolution is usually too low to resolve the two components of the 7320Å doublet and most studies are the averaged wavelength. However, this quantity is heavily weighted in favor of the  $O^+(^2P_{3/2} \rightarrow ^2D_{5/2})$  component since the  $O^+(^2P_{3/2} \rightarrow ^2D_{5/2})$  component at ~7319.9Å is ~ 4 times stronger than the  $O^+(^2P_{1/2} \rightarrow ^2D_{5/2})$  component at ~7319.1Å.....37

- 2.1 A Gaussian distribution, such as the one pictured above, describes the intensity of an emitting species that is in thermodynamic equilibrium. The net shift of the emission line characterizes the bulk velocity ( $v_{bk}$ ); the width of the emission line characterizes the temperature of the emitting species. See text for variable definitions. Figure 3.1 Flow Diagram illustrating models used in producing the 7320Å volume emission rate profiles and contour maps.....55
- 2.2 An incident wave passes through the filter which eliminates most background; the incident wave undergoes multiple reflections within the etalon and produces the broadened fringe pattern. This fringe is a set of bright, concentric rings whose angular diameter is dependent on the gap spacing. The fringe width is a function of the reflectivity of the plates. The lens focuses the fringe on the IPD; the IPD samples the entire fringe simultaneously and yields a discretely sampled, instrument broadened Doppler profile (the spectrogram). Hence, the FPI transforms frequency ( $1/\lambda$ ) into angular displacement while adding instrument broadening.....56
- 2.3 DE-2 FPI (7320Å) spectrogram for orbit 7289 (FPI mirror position: 9.42°). The spectrogram shows the instrumental counts accumulated in 0.25s. Analysis of this by standard methods produces LOS drifts, temperatures and brightnesses. Channel 8 is ignored in all 6300, 5577 and 7320Å calculations since it had a large non-stochastic noise component.....59
- 2.4 Instrument transfer functions determined for the 12 channel FPI (7320Å) at Søndre Strømfjord, Greenland on 3 Sep 91. The free spectral range is the distance between successive channel one peaks. The integrated product of these instrument transfer functions and the observed 7320Å emission line produce the spectrogram - from this, LOS drifts, temperatures and brightnesses are determined. Note that as psi increases, frequency increases and wavelength decreases.....61



2.5	Schematic showing the physical interpretation of the instrument transfer functions. The channel response, $N_i = \int Y(\lambda) \Psi_i(\lambda) d\lambda$ , is produced by the portion of the emission line, $Y(\lambda)$ , that is allowed to pass through the etalon and onto the detector. Analysis of Ni produces LOS ion drifts, temperatures, brightnesses and continuum brightnesses, the topic of section 2.1.2. Figure adapted from Nardi (1991).....	62
2.6	Sample DE-2 FPI spectrogram for the conditions listed on the plot. Brightnesses were ~350R for both observations. See text for discussion.....	70
2.7	Optical schematic for the DE-2 FPI (after Killeen et al., 1983).....	72
2.8	Sample Søndre Strømfjord FPI (7320Å) spectrogram taken for the conditions listed in the figure. Peak sensitivity for this FPI is on channel 5, where the stronger line in the doublet is observed. The weaker line of the doublet <i>may</i> be seen ~channel 11. The intensity ratios of these two lines are ~3.78:1 in this figure.....	78
2.9	Schematic of the Søndre Strømfjord FPI system. Observations of ionospheric dynamics and energetics taken from this system are presented in Chapter 5.....	81
2.10	Schematic cross section of the RPA sensor (from Hoffman, 1981). Exposed surfaces and inner elements of the RPA sensor, except insulators, are gold plated. The nominal grid element separation is 2.5mm.....	84
2.11	DE-2 RPA meridional ion drifts (heavy solid line) for orbit 7438. Overplotted are meridional neutral winds (lighter dotted line) as recovered from DE-2 FPI (6300Å) measurements. Both neutrals and ions exhibit antisunward flow over the polar cap, bounded by local regions of more sunward flow at lower geomagnetic latitudes. In the dawn-side convection channel, intense frictional (Joule) heating occurs where the largest ion-neutral difference velocities occur (~500m/s at ~20.65UT) .....	85
2.12	Flow diagram illustrating models used in producing the 7320Å volume emission rate profiles and maps seen in Chapters 3 - 6.....	87
2.13	VSH ion drifts and temperatures for the given conditions. Solar terminator is the hatched line.....	88

2.14	Distribution of solar irradiance vs wavelength, and its variation with solar activity. Adapted from Smith and Gottlieb, 1974.....	91
2.15	Sample output from the SSFLUX model for relatively quiet (Ap: 10, F10.7: 140) and active (Ap: 50, F10.7: 240) conditions. SSFLUX uses an amalgam of sources to estimate the flux below 18Å (Solomon, 1987).....	92
2.16	Neutral number densities (MSIS) and plasma number densities (IRI) for varying conditions over Ann Arbor.....	97
2.17	The top panel represents neutral (MSIS) and plasma (IRI) temperatures for active conditions. The bottom panel are for quiet geomagnetic and moderate solar activity conditions.....	98
2.18	Solar photons, impacting a neutral atom or molecule, can either ionize, excite or dissociate that particle. If ionization occurs, a photoelectron is produced which can in turn ionize more neutrals, creating secondary electrons. As long as this secondary electron has more energy than the neutral's ionization energy threshold, it will continue to ionize all neutrals with which it collides. Once it has undergone sufficient collisions so further ionization is impossible, it is said to be "thermalized" .....	102
3.1	Sample 7320Å airglow volume emission rate profile for quiet conditions. The various components are plotted as part of the total. At this time, photoionization is the dominant source of the airglow emission. The volume emission rate reduction <i>below</i> the peak (at ~ 285km) is due to an increase in quenching. The volume emission rate decrease <i>above</i> the peak is due to the combination of decreasing electron and atomic oxygen number densities ...	110
3.2	Illustration of seasonal effects on the 7320Å volume emission rate. In the top panel (21 Nov, 12UT), the volume emission rate peaks near 7 ph/cc-s at ~350km. In the bottom panel (same conditions but for a summer day), the SZA is smaller and, therefore, EUV radiation penetrates is greater (deeper) and produces a larger volume emission rate (~16 ph/cc-s) .....	112
3.3	Example of 7320Å volume emission rates for various solar zenith angles during quiet (top panel) and active (bottom panel) conditions. See text for discussion.....	113

3.4	Illustration of the diurnal dependence of this emission. Top panel is for quiet conditions at noon near the summer solstice. Maximum production of the 7320Å emission is by photoionization. The bottom panel is for the same location, but at 8pm. At low altitudes, electron impact ionization is slightly dominant since the solar photon flux is rapidly diminishing but plenty of photo- and energetic secondary electrons remain. At higher altitudes, the sun has not set and photoionization remains the primary source of the emission.....	114
3.5	Illustration of the auroral electron energy flux that is added to the top of the atmosphere in the photoelectron model, thereby mimicking a diffuse aurora in the 7320Å volume emission rate model .....	116
3.6	Illustration of the LAPI addition to the airglow model. In the top panel, no LAPI data is added and the airglow model produces output smaller than expected. The bottom panel includes the added LAPI data and more accurately predicts results found in the literature (Smith et al., 1982; Rees et al., 1982).....	118
3.7	Magnetic and solar conditions are active and photoionization/electron impact ionization are nearly equal contributors to the 7320Å volume emission rate .....	119
3.8	Illustration of the auroral zone 7320Å volume emission rate during active times .....	119
3.9	O+(2P) production rates for 28 November at 11.16 local time and 48S latitude. The conditions were F10.7 = 89 and Ap = 5 (After Torr et al., 1990).....	121
3.10	O+(2P) production rates from the aurora-airglow 7320Å volume emission rate model for the same conditions as in Figure 3.10. Note the excellent agreement .....	121
3.11	7320Å volume emission rate profile for the same conditions as the previous two figures. The peak appears ~ 300km to be ~ 15 -16 photons per cm <sup>3</sup> s <sup>-1</sup> ; this compares extremely well with the 3-dimensional color plot in Figure 2 of Torr et al., 1990 .....	122
3.12	7320Å volume emission rate profile for 28 Nov at 11.16 local time and 68S latitude. The conditions were Ap = 8 and F10.7 = 89. The comparison with Figure 2 in Torr et al. (1990) is excellent .....	122

3.13	O+(2P) concentrations modelled during moderately quiet and active periods of solar activity.....	123
3.14	7320Å volume emission rate profiles using a Maxwellian distribution of auroral particles instead of the observed LAPI data. This version of the model consistently yielded larger high latitude 7320Å emissions than the airglow-only version, but less than the auroral-airglow version. It also took too much computer time to do global modelling .....	125
3.15	Three dimensional plot of the 7320Å volume emission rate. The conditions were 1 April at 12 UT, 0° longitude, Ap = 8, F10.7 = 140.....	126
3.16a	Global contour map of the 7320Å volume emission rate for day: 180, UT: 12 and the conditions listed on the figure. VSH ion drifts are overplotted. Latitudes are geographic with the outermost dial being ~45N latitude. The bottom of the dial, along the Greenwich Meridian, is 12LST (local solar time), while the top of the dial is 00LST. The right side of this dial (the duskside) is at 90° longitude (18LST), while the left side of the dial (the dawn side) is at -90° longitude (06LST).....	127
3.16b	VSH atomic oxygen concentrations ([O]) and ion drifts for the same conditions as Figure 3.17a. The 7320Å volume emission rate has a solar zenith angle dependence but is also strongly controlled by the pattern of [O] seen in this figure (compare to Figure 3.17a).....	128
3.17a	Global contour map of the 7320Å emission for day: 180, UT: 15 and the conditions listed on the figure. VSH ion drifts are overplotted. Figure 3.18b Global contour map of the 7320Å emission for day: 360, UT: 15 and the conditions listed on the figure. VSH ion drifts are overplotted.....	129
3.17b	Global contour map of the 7320Å emission for day: 360, UT: 15 and the conditions listed on the figure. VSH ion drifts are overplotted.....	130
3.17c	Global contour map of the 7320Å emission for day 90, UT: 15 (spring equinox) and the conditions listed on the figure. VSH ion drifts are overplotted. Volume emission rate and [O] for this date are the same as day 270 (autumnal equinox) .....	131
3.17d	Top panel: VSH [O] and ion drifts for day: 180, UT: 15. Middle panel: VSH [O] and ion drifts for day: 360, UT: 15.	

- Bottom panel: VSH [O] and ion drifts for day: 90, UT: 15. Compare these [O] patterns to the corresponding 7320Å volume emission rate patterns in Figures 3.17a-c..... 132
- 3.18 Top panel: VSH atomic oxygen number densities plotted for the following conditions - day 180, UT 12, Ap 10, F10.7 140. Bottom panel: plot of atomic oxygen number densities derived from the 7320Å auroral airglow model for the same conditions; good agreement between the two models exists ..... 138
- 4.1 Illustration of the two Dynamics Explorer satellites and their respective orbits. The DE program, sponsored by NASA, launched two spacecraft in August 1981; they were designed to study the coupling of the magnetosphere/ionosphere/thermosphere system. DE 1 and DE 2 were put into co-planar orbits inside common magnetic flux tubes, enabling measurements from the magnetosphere and ionosphere/thermosphere simultaneously. DE-2 instrumentation included the FPI and RPA, both of which sent data back to Earth until February 1983. The data system for the DE mission, similar to that of the previous AE (Atmospheric Explorer) mission, was designed to give investigators easy access to the incoming information. A central computer facility processed most of the data at Goddard Space Flight Center (GFSC), with remote terminals at the investigator's facilities. Solid lines in this figure represent the Earth's magnetic field (B); dashed lines represent the respective orbits..... 144
- 4.2 Examples of FPI measured [OII]  $\lambda 7320\text{\AA}$  Doppler spectrograms from DE-2 orbit 8227. The individual spectrograms depict the count rate (counts per second) measured at each channel of the instrument, with the exception of channel 8. The horizontal bar above each spectrogram denotes relative intensity. Each spectrogram is positioned in the plot at the location corresponding to the altitude and latitude of the tangent point to the Earth along the respective instrumental line of sight. Changes in ion drift velocity are seen in the evident variations in the peak centroid from spectrogram to spectrogram; this is most obvious in the enlarged two spectrograms from  $\sim 280\text{km}$  and  $-66.5^\circ$  geographic latitude. The free spectral range of the 7320Å FPI is  $0.21\text{\AA}$  and the spectral interval is  $\sim 0.018\text{\AA}$  per channel. Ion drifts are derived from the measured Doppler line centroid using the linear least squares fit technique of Killeen and Hays (1984)..... 147

- 4.3 Sample brightness profile for orbit 1098.1. Brightness units are in Rayleighs (R), where  $1R = 10^6 \text{ph/cm}^2\text{-s}$ . The brightness peaks at  $\sim 300\text{km}$ ; this was found to be true ( $\pm 50\text{km}$ ) with nearly all analyzed DE-2 FPI (7320Å) orbits..... 148
- 4.4 Meridional ion drift latitudinal profile for two successive orbits. Data are averaged in altitude from 200-500km. A value of 1604m/s was added to these drifts (see section 4.1.4 for explanation)..... 149
- 4.5 Two-dimensional plots of brightnesses and meridional ion drifts for orbit 8000. Three-dimensional plot in upper left hand corner is a sum of all brightness profiles for this orbit. Large drift errors were found *usually* to occur when the sun was too far below the horizon ( $\text{SZA} > 100^\circ$ ) to produce a strong 7320Å signal. When the 7320Å brightness was below 50R, accurate drifts could never be recovered. The large drift error positioned at  $\sim 56^\circ$  SZA and  $67^\circ$  geographic latitude was possibly caused by an aurora in the FPI's field of view as the DE 2 traversed the auroral zone ..... 150
- 4.6 Plots of brightnesses, drifts and temperatures for orbit 7439. Additive constant of 1602m/s is used to zero the ion drifts at the equator for this orbit. See text for further discussion of this figure ..... 151
- 4.7 VSH modelled ion drifts and  $\text{O}^+$  number density for the geophysical conditions listed in the diagram. Note the order of magnitude decrease of ion drifts going from high latitudes to mid- and low-latitudes..... 153
- 4.8 Ion collision frequency versus altitude. See text for discussion. Since ion densities are much less than neutral densities, distinguishing between day and night ionospheres is irrelevant..... 156
- 4.9 Trajectories for ions and electrons subject to **E** (in the plane of the paper) and **B** (out of the plane of the paper). Charged particles are assumed to collide with neutral species at regular intervals,  $1/v$  and to possess zero velocity after each collision. Numbers in brackets refer to approximate heights (km) at which conditions occur. Figure adapted from Rishbeth and Garriot (1969)..... 162
- 4.10a Meridional ion drifts measured by the FPI on DE 2 for four orbital passes at high geographic latitude. The FPI data are bin averaged for all tangent point altitudes between ~

- 200-500km. Errors are standard deviations from the mean. The remotely measured ion drifts are compared with *in situ* measurements by the RPA on DE 2. The FPI measurements have been adjusted in temporal phase to match the RPA measurements as discussed in the text. Compare to Figure 4.9b ..... 167
- 4.10b The FPI ion drifts in these plots are not bin averaged for all tangent point altitudes between ~200-500km, as in Figure 4.9a. Instead, these FPI ion drifts come from select mirror positions only (between tangent point altitudes of ~200-500km) in which the ion drift, temperature and brightnesses all rapidly converged to stable solutions in the standard analysis package. The agreement with RPA measurements is excellent ..... 168
- 4.10c Two orbits of FPI vs RPA comparisons using select mirror positions only. Agreement is excellent. Polar dials to the left of the drift comparisons are DE-2 RPA/IDM ion drift vectors plotted along the satellite track. The terminator is the hatched line. Times are local solar. The enhanced RPA and FPI LOS drifts are readily seen in the vector ion drifts on the polar dial ..... 169
- 4.11 FPI (7320Å) recovered ion temperature profile (using standard single-Gaussian analysis) plotted vs modelled VSH profile for the same geophysical conditions. A new method of determining FPI (7320Å) temperatures was devised to account for the doublet nature of this emission .... 170
- 4.12 Compare to Figure 2.1. In this case, the weaker component of the 7320Å doublet is superposed nearly on top (0.081 channels off - see Chapter 2.1.3) of the stronger component and has caused the Gaussian distribution to be wider than a single emission would be. Note that the temperature recovered from single-Gaussian analysis techniques will now be higher since the bandwidth is wider. By resolving the distance between the two emission peaks and applying a double-Gaussian source function to the standard analysis procedure, one can determine more accurate ion temperatures ..... 173
- 4.13 Figure 4.13 DE-2 FPI (7320Å) FPI vs RPA  $T_i$  comparisons for orbit 7289 using both the standard single-Gaussian (FPI 1G) and modified double-Gaussian (FPI 2G) version of the standard analysis package to account for the doublet nature of the 7320Å emission. FPI 1G is high since it cannot handle the wider bandwidth produced by the doublet emission (see Figure 4.12). Ion temperatures

	retrieved from this space-borne method must be viewed with caution. See text for discussion .....	176
4.14	In the top panel, the weaker doublet is shown to make the bandwidth wider than if it were not present. The double Gaussian software handles this adequately. But what if the intensity ratio fluctuates and becomes, for example, 4.5:1 (bottom panel) or 3.8:2? The double-Gaussian software, expecting the classic 3.8:1 ratio, will produce erroneous temperatures since its bandwidth does not represent the actual bandwidth.....	177
4.15	Plot of "observed" DE-2 7320Å volume emission rates for orbit 7125 obtained from the inversion of measured LOS brightnesses. The volume emission rate is seen to peak when the sun is at its highest point in the sky (maximum photoionization) and at ~300 km .....	179
4.16	DE-2 FPI (7320Å) "observed" volume emission rate profile for the same orbit as figure 4.14. Note the evident good agreement between the model and observation. Satellite altitude was 510km .....	180
4.17	Inverted 7320Å volume emission rate profiles for DE-2 orbits 1306 (top panel, Zsat=576km) and 8000 (bottom panel, Zsat=378km). The measured profiles are compared to the 7320Å aurora-airglow model presented in Chapter 3.3.2 for equivalent geophysical conditions. Note the peak emission altitude of ~300km. Low altitude DE-2 volume emission rates show large errors due to the severe quenching of O+(2P) ions below ~ 200km and contamination from Rayleigh scattering off cloud tops.....	181
5.1	Søndre Strømfjord FPI (7320Å) spectrogram for 9 Sep 91 at 4:29UT. The enhancement at channel 11 <i>may</i> be the weaker component of the doublet being resolved since it was shown in Chapter 2 that the weaker line of the doublet should be ~7 channels from the stronger one on this FPI.....	191
5.2	Søndre Strømfjord spectrogram; no intensification near channel 11 is seen, although it is visible in several individual spectrograms .....	192
5.3	Sample ISR data for 4 Sep 91. See text for discussion.....	193
5.4	Analyzed data from the Søndre Strømfjord FPI (7320Å) for 3/4 Sep 91. See text for discussion.....	195
5.5	Analyzed data from the Søndre Strømfjord FPI (7320Å) for 7/8 Sep 91 (Ap: 22, F10.7: 196). From ~01-04UT, electronic	



	interference from the ISR impacted the FPI's behavior <i>and</i> cloud coverage varied from 3/8 - 6/8. During this time, the background was too close to the actual signal and I was forced to ignore the data taken during that period.....	197
5.6	Analyzed data from the Søndre Strømfjord FPI (7320Å) for 9/10 Sep 91 (Ap: 32, F10.7: 185) .....	197
5.7	Polar dial plot for four nights of FPI (7320Å) ion drift observations. The two-celled ion convection pattern is visible, complete with antisunward flow seen in the center of the bottom dial and return flow seen on either side. The times on this dial are local solar and the latitudes are geographic. See text for discussion .....	199
5.8	FPI (with error bars) vs ISR (dash line) ion temperature comparison for 4 Sep 91. The integration period for the ISR was usually much shorter than that of the FPI, resulting in greater resolution in the ISR measurements. Generally, the agreement is good, suggesting future study of this emission at pre- determined times and seasons could prove eventful in understanding ionospheric energetics .....	200
5.9	ISR (with error bars) vs FPI (7320Å) drift comparisons. FPIE(W) indicates the FPI was looking eastward (westward). The ISR data were bin averaged so their lines-of-sight and integration times matched those of the FPI drifts. The comparison between the FPI and ISR drifts is good .....	201
5.10	VSH model output for the conditions occurring for the 4 Sep 91 FPI (7320Å) observations. The model shows drifts and temperatures to be ~ 700 m/s (southeastward) and 1320K respectively. The observations for this time (Figure 5.4) are ~ 725 m/s (southeastward) and $1300 < T_i < 1600$ K .....	202
6.1	Simulation for the conditions listed on the diagram. In the first two panels, solid lines represent VSH ion drifts and temperatures. Boxes (with error bars) represent the simulated 16 DE-2 FPI measurements. Agreement between the simulated values and the VSH "real atmosphere" values is excellent. In the far right panel, brightnesses (boxes) are simulated from the input 7320Å aurora-airglow volume emission rate model (solid line). The brightness scale is on top of this panel. These brightnesses will be compared to actual DE-2 brightnesses in Chapter 6.2 .....	212

6.2	Brightness profile, Orbit 1343. Peak brightness appears to be ~ 950R at 285km altitude. The satellite was at ~ 340km. Compare to Figure 6.3.....	213
6.3	Simulator plot with the contribution function plotted in the lower right panel. VSH drifts and temperatures in the first two panels (solid lines) are well simulated (boxes with error bars). The brightnesses in the right panel (boxes with error bars) were calculated from the 7320Å aurora-airglow volume emission rate model (solid line) and peak at ~ 285 km near 900R. This is very similar to the observed values in Figure 6.2. The contribution function in the lower right panel is the product of the volume emission rate and the pathlength of the line-of-sight through the 5km-thick layers. The functions have a sharp peak at the tangent height since the pathlength peaks there; hence, the information content of this simulated measurement is favored at the tangent height (~300km in this case).....	214
6.4	Orbit 8000 Simulation. Compare the simulated brightnesses (peak of ~ 450 - 475R at ~ 250km) to the observed brightnesses in Figure 6.5 .....	215
6.5	Orbit 8000 brightness profile. The peak is ~ 425R at ~ 250km. The comparison to the simulated brightnesses in Figure 6.4 is good.....	216
6.6	CONVEX FPI schematic.....	219
6.7	CONVEX geometry. The satellite is a polar orbiter at 600km. The four onboard FPIs look ahead and behind at +/- 45 and +/- 135° off-track. A RPA/IDM team determines <i>in situ</i> ion drifts. At this altitude, the FPI mirror elevation angle ( $\theta$ ) must be 16.87° in order to sample a tangent point altitude of 300km. The distance to the tangent point at this elevation angle is 2023km, which translates into 1432km (~130°) normal to the satellite track at the tangent point. In this configuration, a backward-looking FPI samples the same volume a forward-looking FPI did 5.9 minutes earlier.....	221
6.8	CONVEX footprint. At 600km, an FPI mirror elevation angle of 16.87° and a field-of-view of 1.5°, the diameter of the FPI's viewing cone at a tangent point 2023km away from the satellite will be ~ 52km. In this orbital configuration, the FPI will therefore be sensing the 7320Å emission from ~ 275-325km altitude. Hence, the well-	

- behaved (just one peak and wider in vertical extent than the FPI's field of view) 7320Å emission will be evenly distributed in the field-of-view; therefore, no distortion effects will occur. Note that the double peaked 5577Å emission has a ~10km thick peak in the lower thermosphere; hence, it is narrower than the DE-2 FPI field-of-view and distortion occurred since the outer channels were illuminated by 5577Å photons before the inner channels were (Nardi, 1991)..... 222
- 6.9 CONVEX pathlength. The dotted swath through the figure is the peak of the 7320Å emission layer. The maximum pathlength is through layer S(N-3); therefore, the information content of the FPI measurement is sharply favored at the tangent height (~300km in this case). In this configuration, the distance from CONVEX to the tangent point is 2023km. See text for further discussion ..... 223
- 6.10a VSH ion drifts vs simulated ion drifts from the DE-2 FPI (7320Å) Simulator - the Simulator used an IPD in this case. Conditions for the VSH model and the Simulator were: day: 180, UT: 18, Ap: 10, F10.7: 140 ..... 224
- 6.10b Similar to Figure 6.10a, but a CCD was used in the Simulator instead of an IPD. The addition of a CCD improves FPI sensitivity by a factor of 12..... 225
- 6.11 Three simulated ion drift velocity plots (left panels) vs the model that generated them (right panels). Simulated ion drifts are at tangent heights of 300km. Times on the polar dials are local solar; UT times represent the time CONVEX began its high-latitude pass. Conditions were day: 180, Ap: 10, F10.7: 140. Note that the areal coverage is ~26° latitude, enough to determine the two-celled convection pattern in a 16 minute polar pass by CONVEX. See text for discussion ..... 229
- 6.12 Recovered electric field vectors from the ion drift simulation. Conditions are the same as Figure 6.11 - day: 180, Ap: 10, F10.7: 140..... 230
- 6.13 The left panel is the ion drift pattern used as input to the convection-imaging simulation. The pattern is in geographic polar coordinates, with the outer circle at 40° latitude. The right panel shows the recovered ion drift vectors from the simulated FPI on the polar orbiting (dawn-dusk) spacecraft. Both the input model and simulation are for an altitude of 300km. Vector measurements from an *in situ* sensor are also assumed,

with these latter vectors being attached to the spacecraft orbit. The pattern provided by the simulated FPI measurements is in good agreement with the pattern used as input to the simulation, demonstrating the capability of the off-track imaging technique..... 233

- B.1 DE-2 FPI senses all emissions along the line-of-sight (LOS). LOS drifts are determined by the net Doppler shift of the spectrogram which is produced from these emissions occurring along the entire LOS. The largest contribution to the emission comes from the tangent point, depicted in this case at ~300km. With an auroral display in the instrument's field of view, the largest contribution may be coming from 382km, for example, instead of the actual 300km. However, most intense aurorae occur below ~200km and will therefore not affect spaceborne FPI observations. The same is not true for ground-based observations, the topic of Chapter 5 ..... 248
- B.2 Contribution functions for a model 7320Å volume emission rate profile produced for the conditions listed on the figure. The volume emission rate profile peaked at 293km and 18 ph/cc-s. Each kernel (there are 16 of them - one for each DE-2 mirror position) describes the contribution to a given measurement as a function of altitude. The maximum contribution occurs at the tangent height, denoted by the sharp peaks..... 249
- B.3 Sample plot of observed "line-of-sight" drifts (with errors) and inverted "true" drifts for the conditions listed on the diagram. Because of the localized emission source and sharply peaked contribution functions, no inversion of the line-of-sight drifts is necessary. The line-of-sight winds for DE-2 FPI (6300Å) were not inverted for similar reasons. The same was not true for the DE-2 FPI (5577Å) emission..... 252
- B.4 The standard analysis software package for analysis of DE-2 FPI (7320Å) data ..... 255
- C.1 Retrieved data from Søndre Strømfjord is placed on tape and brought back to the SPRL, where it is dumped onto the antiquated PDP11 and then downloaded to the VAX. Data are then analyzed by these programs ..... 258
- C.2 Diagram of the Søndre Strømfjord FPI (7320Å) data flow used in Chapter 5 ..... 259

C.3	Diagram of Søndre Strømfjord ISR Analysis Machinery used in Chapter 5. SRITAPE.FOR can be used for any tape in the new SRI tape-format.....	260
D.1	DE-2 FPI (7320Å) Simulator and datafile flow.....	262
D.2	Inner workings of the DE-2 FPI (7320Å) Simulator.....	263
E.1	Illustration of elevation angle calculation. See text for discussion .....	264
E.2	In this figure, CONVEX is moving to the right and its forward-sensing FPI is looking 45° off-track to the tangent point latitude/longitude. This distance is 2023km. The <i>normal</i> off-track distance to the FPI tp11 is readily seen to be 1432km .....	266
E.3	In this figure, the satellite is moving to the right of the page. The forward looking FPI looks off at a 45° angle to the satellite track and observes at a tp11 that is 2023km away or 1432km normal to the satellite track. The backward looking FPI does the same, only at -45°. At a satellite speed of 8km/s, it takes the backward looking FPI ~ 5.9 minutes before the satellite travels the 2864km and therefore allows it to sample the same volume the forward looking FPI did 5.9 minutes previously.....	267
E.4	Illustration of the method used to combine common-volume line-of-sight drifts to produce ion drift vectors. The vector ion drift velocity ( $V_i$ ) is the result of measurements taken by a backward looking FPI at time T(7) when the satellite is at 81° latitude and a forward looking FPI at T(1) when the satellite is at 55° latitude. See text for discussion ..	271
E.5	Assume the CONVEX is moving directly up the Greenwich Meridian. When it is at the point labelled 24.5° geographic latitude, its forward looking FPIs will be sensing locations in the ionosphere that are at 35.9° latitude and +/-13.9° longitude. Similarly, when the CONVEX is positioned at 50.5° geographic latitude, the backward looking FPIs will be sensing the identical regions. Combining the line-of-sight measurements allow one to determine the ion drift velocity vector (shown as $V_d$ in the diagram) at ~13° (1432km) off-track in this case .....	274
F.1	CONVEX Flow. The user is queried for Ap, F10.7, F10.7A, date, UT. CONVEX flies at 600km; this value is hardwired into the code but can easily be changed. The input UT	

specifies which one of the three telemetry tables will be used. VSH and the 7320Å aurora-airglow model, acting as the real atmosphere, feed the CONVEX machinery the desired values of ion drifts (meridional and zonal) and volume emission rates. The CONVEX code then outputs one swath of simulated zonal and meridional ion drifts at 13° off-track. This procedure is then repeated for the swath on the opposite side of CONVEX. If one wants swaths at, for example, 11 and 15° off-track (as seen in Figure 6.15), one can change the mirror position interactively, allowing the FPI to sense at varying distances from the satellite. The programs MERGE, ADDLINE and SAWTHPS are IDL routines that simply format the data and plot them.....277

## LIST OF TABLES

### **Table**

1.1	Flux (in units of $10^8$ ions/cm <sup>3</sup> -s), velocity, density, electron and proton temperature and magnetic field strength for solar wind minima and maxima (USAF MAC Course 2546, 1985).....	9
1.2	Fractional percentages of O <sup>+</sup> produced by electron impact ionization. The fourth column represents the threshold energy the electron must have in order to excite atomic oxygen to the state listed in column 2 .....	39
1.3	Some contaminating OH wavelengths.....	50
2.1	DE-2 FPI operating parameters (after Killeen et al., 1983). The last column (Sensitivity) has units of counts per Rayleigh per second per channel; the third column (#/fsr) indicates the number of channels per free spectral range.....	71
2.2	ISR sites and locations .....	82
2.3	VSH inputs and outputs .....	89
3.1	Atomic oxygen branching ratios into the O <sup>+</sup> ( <sup>2</sup> P) state at various EUV wavelengths (after Rees, 1989).....	106
B.1	If ion drifts, temperatures or brightnesses exceeded the values in this table, all data from that DE-2 FPI mirror scan are discarded.....	254
E.1	Sample CONVEX Telemetry .....	272

## LIST OF APPENDICES

### Appendix

A:	Spacecraft-Charging.....	243
B.1:	Inversion of DE-2 FPI (7320Å) LOS Parameters.....	247
B.2:	DE-2 FPI (7320Å) Software Flow .....	253
C:	Søndre Strømfjord Data Analysis and Flow .....	256
D:	DE-2 FPI (7320Å) Simulator Software Flow .....	261
E:	CONVEX Calculations.....	264
F:	CONVEX Simulation Software.....	275



## CHAPTER 1

### INTRODUCTION

#### 1.1 Dissertation Objective

*"To use the ionospheric [OII]  $\lambda 7320\text{\AA}$  emission to investigate F-Region dynamics, especially at high latitudes. Ground- and space-based observations, plus a considerable modelling effort, are combined to uniquely describe ion drifts, the  $7320\text{\AA}$  volume emission rate and the high latitude ion convection pattern".*

#### 1.2 Introduction and Organization

The near-space environment is dominated by solar energy that arrives at the top of the Earth's atmosphere as either *electromagnetic energy* or *plasma* contained within the solar wind. This energy interacts with the upper atmosphere and magnetosphere in a variety of ways. Much of the sun's electromagnetic energy is visible light, and as such, passes

through the atmospheric window to the surface. But some of this *electromagnetic energy* is in the extreme ultraviolet (EUV) and ultraviolet (UV) range and strongly interacts with the upper atmosphere to produce the ionosphere - a boundary between the Earth's neutral atmosphere and the sun's fully ionized atmosphere. The flow of solar wind *plasma* against the Earth's magnetic field puts plasma in motion around the Earth.

In addition to these interactions of solar energy with the near-space environment, there are complex processes that couple the thermosphere/ionosphere and magnetosphere. For example, the dynamics, energetics and composition of the neutrals in the upper thermosphere are strongly controlled by *ion-neutral collision processes*, especially at high geomagnetic latitudes. *Magnetospheric convection electric fields* map down into the high-latitude ionosphere along equipotential geomagnetic field lines and cause  $\mathbf{ExB}$  drift of the ions at F-Region altitudes, usually resulting in a two cell ion convection pattern with antisunward flow over the polar cap and return flow at lower latitudes. These convecting ions impart momentum to the neutral gas of the thermosphere through ion drag forcing that results in the neutral wind adopting a two cell pattern of its own that is similar to the ion convection pattern. In low- and mid-latitudes, the situation reverses and neutrals may drag ions since ionospheric currents are driven mainly by polarization electric fields which are generated by the *neutral* wind dynamo at ~120 km. The tightly coupled magnetosphere/ionosphere/thermosphere system is a complex one.

To this end, I have probed the ionosphere with models, remote sensing techniques from the ground and space and *in situ* techniques from space in an attempt to extend the current knowledge of ionospheric dynamics and energetics.

In Chapter 2, I present all research tools used in this dissertation. In Chapter 3, an existing airglow model is extended to produce both profiles and global contour maps of the [OII]  $\lambda 7320\text{\AA}$  emission. Inputs are date/time/geophysical conditions and geographic latitude and longitude. The model uses the two-stream approximation to the electron transport equation, known absorption cross sections for the various thermospheric and ionospheric species, a model of solar flux for various conditions and models for neutral and ion temperatures and concentrations. All known chemical processes creating and destroying the  $\text{O}^+(\text{}^2\text{P})$  ion are included in the model. This  $7320\text{\AA}$  volume emission rate model is validated against actual satellite measurements in Chapters 4 and 6 - agreement is good. The accuracy of this model is of the utmost importance since it will be the input "real" volume emission rate for a simulated satellite observing platform that is developed in Chapter 6.

In Chapter 4, I introduce the Dynamics Explorer 2 (DE 2) satellite. DE-2 instrumentation enabled measurements of the dynamics of both neutral (thermospheric) and ionized (ionospheric) constituents to be made during the satellite lifetime (August 1981 to February 1983). In addition to the *in situ* instruments capable of ion drift and temperature measurements, the Fabry-Perot interferometer (FPI) onboard DE 2 made routine observations of the Doppler line profiles of the ionospheric [OII]  $\lambda 7320\text{\AA}$  emission. The analysis of these line profiles enables height profiles of the ion drift, temperature and brightness component along the line-of-sight of the FPI to be determined. Temporal sequences of such measurements provide vertical profiles of the meridional ion drift, temperature and brightness for various geophysical conditions. These measurements are the first observations of ion drifts, temperatures and

brightnesses to be obtained using the spaceborne FPI technique. I compare these ion drifts to simultaneous *in situ* measurements using the DE-2 Retarding Potential Analyzer (RPA). Good agreement between the two exists. Using analyses similar to those of the DE 2, line-of-sight ion drifts and temperatures have been determined at Søndre Strømfjord (67.01N, 50.42W), Greenland. The results from these observations (Chapter 5) are compared to incoherent scatter radar (ISR) observations. For the period of study, reasonable agreement exists between the FPI-recovered drifts and temperatures and those observed by the radar.

A DE-2 FPI Simulator, previously used in red- and green-line studies, is extended to include the 7320Å emission in Chapter 6. This Simulator reincarnates the DE-2 FPI by imitating its optics. By using the Vector Spherical Model (VSH) as the true ionospheric drifts and temperatures and the 7320Å volume emission rate model as the true volume emission rate, the Simulator generates what the DE-2 FPI would have observed for meridional ion drifts, temperatures and brightnesses. These simulated results are validated by direct comparison to actual DE-2 measurements for similar geophysical conditions; agreement is excellent. The ability to model upper ionospheric drifts and temperatures by merely inputting today's date and geomagnetic conditions is very convenient and will have an immediate impact on future satellite and shuttle missions.

The validated performance of the DE-2 FPI as a remote spaceborne monitor of ionospheric convection opens the possibility that remote sensing methods can be used to image the quasi-instantaneous, high-latitude convection pattern. In order to demonstrate the potential of this imaging technique, I conducted a quantitative simulation study using a combination of the aeronomical model developed in Chapter 3, a model of polar

ionospheric convection (the Vector Spherical Harmonics Model) and an instrument function similar to that of the DE-2 FPI (the DE-2 FPI Simulator). Thus, the remainder of Chapter 6 is the development of this polar-orbiting satellite system in which the ionospheric convection and electric field pattern can be determined in one satellite pass. The motivation for the development of this satellite system is to routinely monitor ionospheric convection at high-latitudes, especially during times when the vertical component of the interplanetary magnetic field is oriented in a northward direction ( $B_z$ -north); the high latitude ion convection pattern is not well understood during  $B_z$ -north conditions. The name of this simulated satellite is CONVEX (*Convection Explorer*) - all instrumentation for CONVEX exists, as does the software to do data analysis. If deployed, the satellite system would be a relatively simple and inexpensive method of determining the ionospheric convection pattern, and phenomena associated with it.

The ionosphere is the zone of interest in this dissertation, especially the high-latitude ionospheric convection patterns. In the ionosphere, high latitude thermospheric and magnetospheric processes have a strong influence. The high-latitude ionosphere is coupled to the thermosphere via collisions between ions and neutrals. Likewise, the high latitude ionosphere is coupled with the magnetosphere in which electrical energy is generated and transmitted via highly conductive magnetic field lines into the ionosphere. Once there, the electric energy is converted into mechanical energy in the thermosphere via neutral gas collisions. To understand this coupling, one must understand the origins of, and interactions between, the solar wind and magnetosphere.

The rest of this chapter is a brief introduction to some of the terms found in this dissertation. I shall start with the origin of the energy which drives the magnetosphere/ionosphere/thermosphere system - the solar wind. I shall then introduce the magnetosphere, aurora, ionosphere, thermosphere and their peculiarities. Next, I shall discuss briefly why ions "drift" and the importance of this. The last sections of this chapter will cover electric fields, the airglow, and an introduction to the [OII]  $\lambda 7320\text{\AA}$  emission.

### 1.3 Solar Morphology

Energy radiated by the sun originates from nuclear reactions in the solar core. The most important process is the fusion of two hydrogen nuclei (protons) into one helium nuclei. To generate the observed luminosity ( $4 \times 10^{33}$  ergs/s), mass is devoured at a rate of 5 million tons/s (Wentzel, 1989). Energy released by nuclear reactions in the core moves outward by radiative transfer; photons are absorbed/emitted many times during this outward passage, resulting in the energy content of the photons cascading from gamma rays to visible light.

Temperature and density decrease outward from the core. At 0.86 solar radii, the temperature becomes low enough for a significant fraction of the free electrons to be recaptured by hydrogen or helium nuclei (Jursa, 1985). Photons can also be more easily absorbed. This increased opacity causes the temperature gradient to steepen, producing convective instability. A rising plasma parcel continues to rise until it reaches a level where the temperature and density are low enough so photons emitted outward have a small chance of being absorbed before they escape to space.

This level is the visible surface - the *photosphere*. It is not a distinct layer, but rather a range of depths from which visible radiation escapes; it is about 500 km thick.

The *chromosphere* occurs where the density of negative hydrogen ions has dropped to a value too low to result in appreciable opacity. In the chromosphere, density continues to decline but temperature rises again because of heating due to dissipation of sound, gravity and magnetohydrodynamic (MHD) waves generated in the convective zone. In the lower chromosphere, temperatures rise from 5000 - 20000K and continue to rise to nearly  $10^6$  K at the base of the corona. The chromosphere is about 3000km thick and most observations of it are made at 6563Å (H-alpha). The high temperature of the chromosphere makes it a good emitter in the UV and EUV (McCormac et al., 1991) and therefore, as will be discussed shortly, is one source of the Earth's ionospheric [OII]  $\lambda 7320$ Å emission.

The *corona* is the outermost part of the solar atmosphere and has an average temperature of  $1.5 \times 10^6$  K. Hence, except for a few heavy ions, the coronal plasma is fully ionized. Although the temperature is high, low density causes actual heat energy content to be low. In fact, it is only half as bright as the full moon (Wentzell, 1989) and is usually invisible in white light due to its overpowering photospheric neighbor. Figure 1.1 is a schematic diagram of the solar atmosphere.

#### 1.4 The Solar Wind and Interplanetary Magnetic Field

The *solar wind* is a continuation of coronal expansion and is therefore highly variable in space and time. The solar wind is a highly

conducting, tenuous plasma composed mainly of electrons and positive ions. The composition of the solar wind is similar to that of the sun's, ~ 10% alpha particles (helium nuclei) and 90% protons (Jursa, 1985).

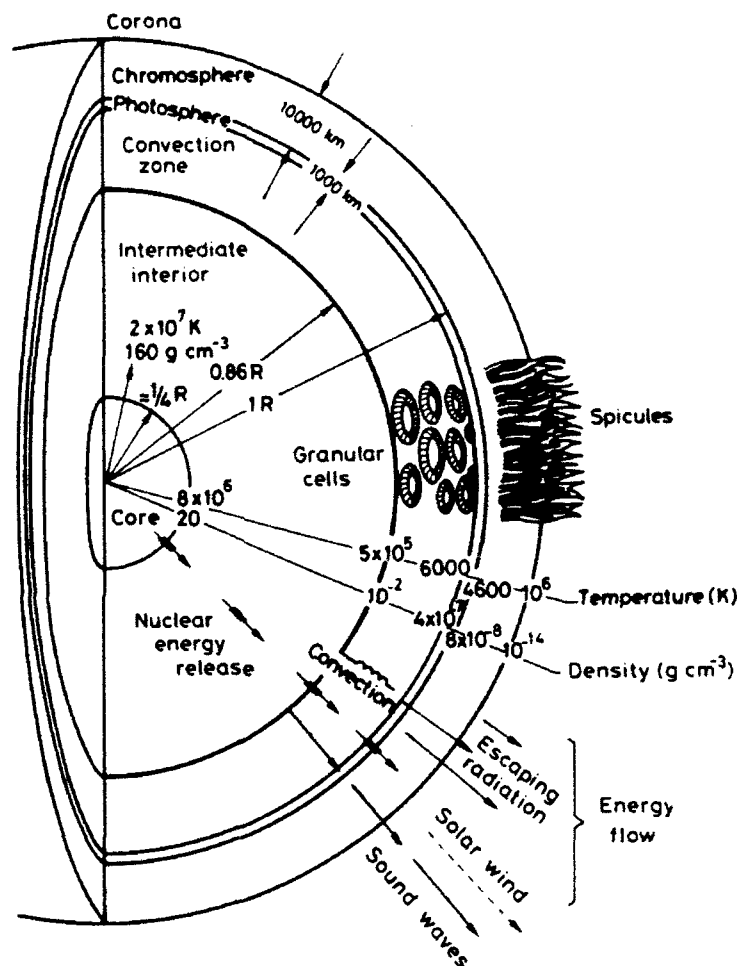


Figure 1.1 Schematic of the solar atmosphere (adapted from Brasseur and Solomon, 1984).

The expansion speed is low in the inner corona but increases outward, becoming supersonic and nonhydrostatic at 10 - 20 solar radii causing a radial plasma flux from the sun; nearly 600,000 tons of plasma leave the sun every second (Wentzel, 1989). General characteristics of the solar wind near the Earth's orbit (1AU) are listed in Table 1.



Parameter	Minimum	Maximum
$\phi$	1	100
$v$ (km/s)	200	1000
$\rho$ (ions/cm <sup>3</sup> )	0.4	100
$T_e$ (K)	5000	$10^6$
$T_p$ (K)	3000	$10^6$
$B$ ( $10^{-5}$ G)	0.2	80

Table 1.1 Flux (in units of  $10^8$  ions/cm<sup>3</sup>-s), velocity, density, electron and proton temperature and magnetic field strength for solar wind minima and maxima (Jursa, 1985).

Imbedded in the solar wind is a portion of the sun's magnetic field, particularly the photospheric field; this field, being dragged along by the solar wind, is referred to as the *interplanetary magnetic field* (IMF). The conductivity of the solar wind is high and the sun's magnetic field is frozen into the flow since there is essentially no diffusion of plasma transverse to the magnetic field (Nagy, p.c., 1990). As the solar wind drags the sun's magnetic field with it into space, the solar rotation causes the magnetic field to form an Archimedes spiral structure. As the solar wind expands and carries the sun's field into space, a *current or neutral sheet* is formed, separating adjacent yet antiparallel field lines from plasmas that flow from the two hemispheres of the sun. This ballerina skirt-shaped current sheet alternates above and below the ecliptic plane as the sun rotates. When the current sheet is above the plane, Earth experiences IMF lines that are *towards* the sun; when the sheet is below the ecliptic plane, Earth experiences IMF lines that are *away* from the sun. The IMF has values of  $\sim 5 - 20$ nT and varies with solar activity (Thayer, 1990). Figure 1.2 is a

schematic of the solar equatorial current sheet and associated magnetic field lines.

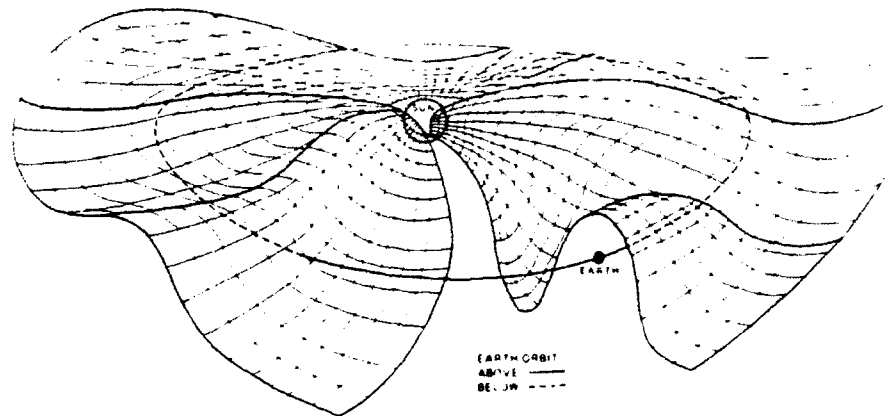


**Figure 1.2** Three dimensional illustration of the solar equatorial current sheet and associated magnetic field lines. The current sheet is shown as lying near the solar equator with spiralled, outward pointing magnetic field lines lying above it and inward pointing field lines lying below it. The current sheet contains folds. When the sun rotates, an observer near the ecliptic plane will (alternately) lie above and below the current and will therefore see a changing sector pattern (from Kelley, 1989).

Toward and away regions of polarity are called *sectors*. The IMF contains a 4 - 6 sector structure in which IMF polarity variations change 4 - 6 times during the sun's rotation period (~27 days). Away sectors contain a radial component directed away from the sun and an azimuthal component directed in an opposite sense to the sun's rotation. Toward sectors contain a radial component toward the sun and an azimuthal component directed in the same direction as the sun's rotation. The inclination of the current sheet with respect to the ecliptic plane creates an IMF component directed northward or southward of the ecliptic plane. The sector boundaries separating the fields of opposite polarity are thin and are swept past the

Earth in a matter of hours (Lethbridge, p.c., 1986). Using the geocentric solar magnetospheric (GSM) coordinate system, toward and away sectors are described in terms of  $B_x$  and  $B_y$  components. In an away sector,  $B_x$  is negative (directed away from the sun), while  $B_y$  is positive (directed towards dusk). In a toward sector,  $B_x$  is positive (toward sun) and  $B_y$  is negative (towards dawn). The  $B_z$  component may have either sign during these sectors with a  $+B_z$  labelled as northward IMF and a  $-B_z$  labelled as southward IMF. During magnetospheric storms, when  $B_z$  is southward, the IMF connects with the Earth's magnetic field and solar plasma can penetrate the magnetosphere by either sliding down a field line or entering from the tail. Thermospheric parameter variations at high latitudes, such as winds and temperatures, are directly related to IMF orientation (Thayer, 1990). Changes associated with the east-west, north-south and sun-earth components of the IMF are called  $B_y$ ,  $B_z$  and  $B_x$  effects respectively (McCormac, 1991).

The cavity in the solar wind created by the Earth's geomagnetic field is the *magnetosphere*; it is the volume in which the Earth's magnetic field is confined by the solar wind pressure (Hargreaves, 1979). Thus, the magnetosphere protects Earth from the solar wind, which stops at the bow shock and then sweeps around the magnetosphere. The *magnetopause* is the surface at which the particle pressure of the advancing solar wind plasma is balanced by the Earth's magnetic field pressure. On the sunward side, the magnetopause is about 10  $R_e$  (Earth radii) from the center of the Earth; it may be 6.5  $R_e$  if the solar wind has an unusually high velocity or density (Hargreaves, 1979). The magnetopause is about 200 km thick (Jursa, 1985). A collisionless *bow shock* is produced upstream from the magnetopause. The bow shock marks the transition from undisturbed

(supersonic) to disturbed (subsonic) solar wind. On the sunward side, it is about 15  $R_E$  from the Earth's center (Hargreaves, 1979). The *magnetosheath* is the region between the bow shock and magnetopause. It is a turbulent transition region containing post-shock solar wind plasma (which can be 10 times hotter than the solar wind since the velocity reduction leads to kinetic energy dissipating as thermal energy). The magnetopause does allow diffusion of some solar wind particles across the boundary from the magnetosheath. The *magnetotail* is the region where the Earth's magnetic field lines are drawn back in the antisolar direction by solar plasma motion. The tail extends to at least 1000  $R_E$  before it becomes indistinguishable from the IMF (Jursa, 1985). Figure 1.3 is a magnetospheric schematic and 1.4 is a magnetospheric schematic illustrating distortion caused by the solar wind.

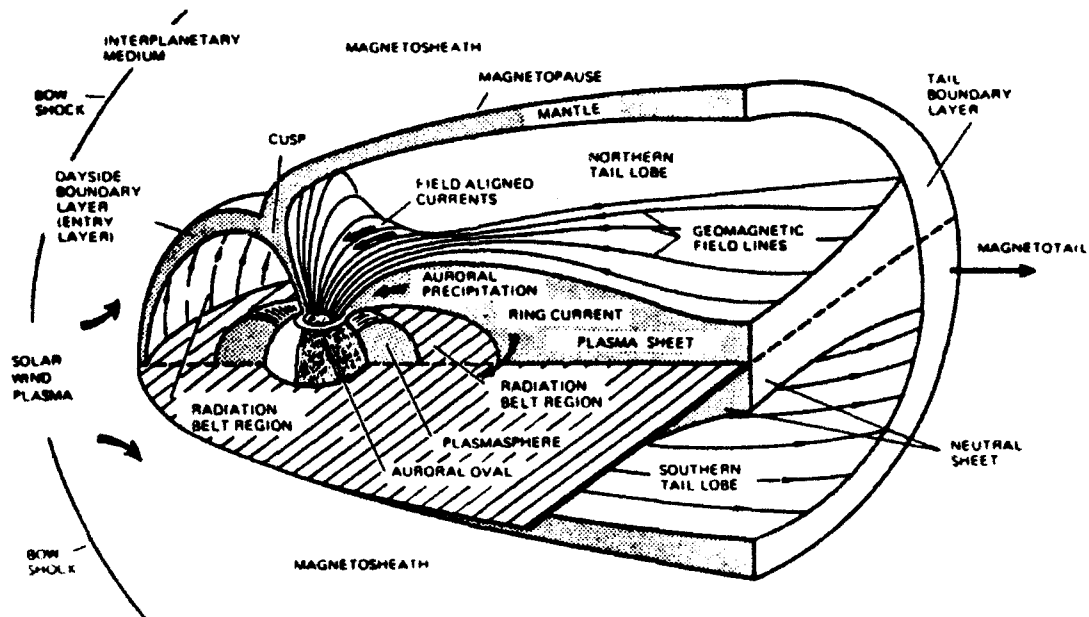


Figure 1.3 Schematic representation of the magnetosphere (from Kelley, 1989).

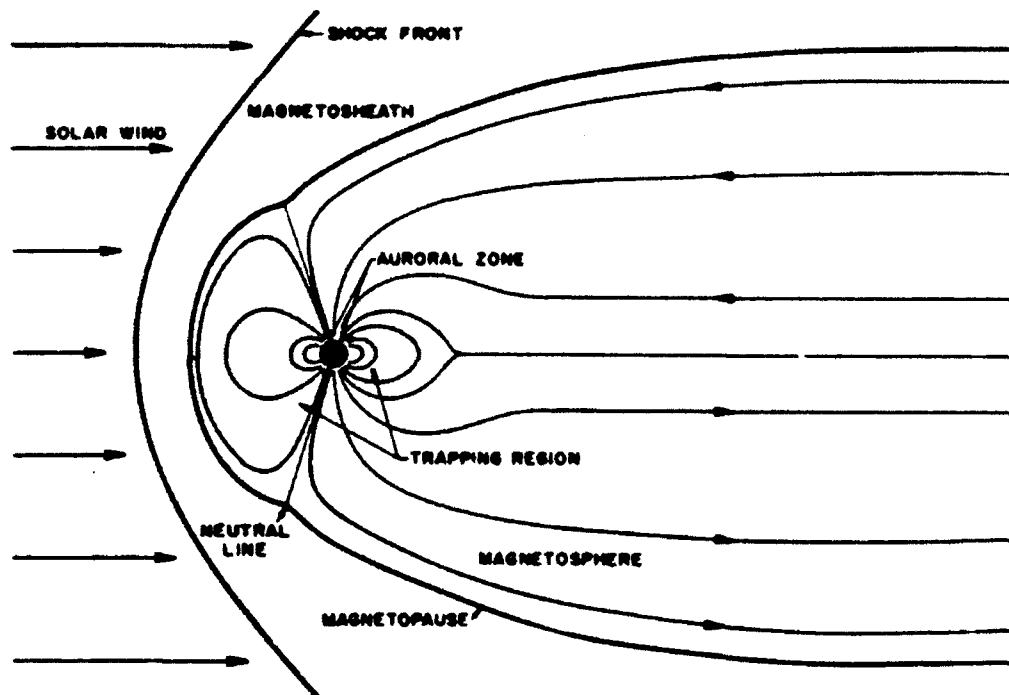


Figure 1.4 Magnetospheric distortion caused by the solar wind (adapted from Lui, 1987). The magnetosphere is distorted because of its interaction with the solar wind; the magnetic field appears flattened on the dayside and elongated on the nightside. When the field has a southward component, there are enhanced magnetic storms, ionospheric storms and an increase in aurorae.

## 1.5 The Aurora

Aurorae are created at high latitudes by the electrically charged particles in the solar wind that enter the Earth's magnetosphere and penetrate the atmosphere along magnetic field lines. There, these high

energy solar particles collide with numerous atmospheric atoms and molecules; the collisions excite these atmospheric ambients which then emit the light we perceive as aurorae. The aurora is highly structured in space and time. Auroral electrons have enough energy to overcome most excitation thresholds in the F-Region. Hence, it has a very complex emission spectra.

Electrons in the 1-10keV range cause visible aurora (Meng et al., 1991). The electron energy is lost through a cascading chain of ionization and excitation processes as the electrons collide with atmospheric atoms and molecules. Visible aurora are faint, luminous phenomena seen in the night sky at high geomagnetic latitudes. Aurorae occur simultaneously in both hemispheres with nearly identical time and space variations. The lower border of visible aurorae is in the E-Region (about 90 km) and may extend hundreds of kilometers upward. The energy emitted in the non-visible part of the spectrum exceeds that in the visible range. Optical aurora includes emissions in visible, ultraviolet and infrared; aurora also emit radio noise (Chamberlain, 1961) in VLF (<30kHz) and in the HF-VHF (3-300MHz). Aurora even emit in the X-ray bands; a continuous X-ray spectrum is produced as fast, energetic electrons are slowed by encounters with atmospheric particles (Bremstrahlung). Visible aurora rapidly change in form and intensity and are divided into two classes, diffuse and discrete. Diffuse aurora are faint, ill-defined, and have a width of tens of kilometers; discrete are curtain-like structures with a horizontal width of 0.1 - 10 km and extend from a continuous lower boundary upward along field lines for tens of kilometers (Chamberlain, 1961). The *auroral region* (60 - 90° geomagnetic latitude) is divided into three categories:

a. *oval*: the part of atmosphere that intersects the part of the magnetosphere from which auroral particles originate; it responds to geomagnetic activity. The oval's centroid is displaced  $\sim 30^\circ$  toward the night hemisphere. The aurora is generally strongest in the midnight sector since the particles causing them come from the magnetotail. As the Earth rotates, the oval moves around the geomagnetic pole. It stays furthest south (about  $23^\circ$  from the pole) near local midnight, and furthest north (about  $15^\circ$  from the pole) near local noon (Hargreaves, 1979).

b. *zone*: the area the oval sweeps out as the Earth rotates beneath it; it is the zone where aurorae are most frequent ( $55 - 75^\circ$  geomagnetic latitude).

c. *cap*: the area above the auroral zone in latitude where frequency of aurorae decreases. The polar cap is an area within  $15^\circ$  of the geomagnetic poles; it is susceptible to direct particle bombardment by high energy solar protons and alpha particles deflected by Earth's geomagnetic field and guided in through polar cusps. These particles can cause a weak diffuse auroral glow extending over a large part of the polar cap and can cause severe radiowave absorption, called polar cap absorption (PCA).

The auroral spectrum is complicated; auroral electrons are much more energetic than photoelectrons and therefore penetrate deeper into the atmosphere. This can be observed because the optical spectra reflect the change in composition at lower altitudes. Although these aurora are pleasing to the eye, they are usually viewed with angst by those who attempt to remotely sense the ionosphere with optical devices (see Chapters 4, 5).

## 1.6 Introduction to the Ionosphere

The portion of the upper atmosphere where ions and electrons are present in sufficient numbers to affect radiowave propagation is the *ionosphere*. The variation in electron density with height led to the subdivision of the ionosphere into the D (50 - 90km), E (90 - 140km) and F (140 - 1000km) layers. Note that the ionosphere is *not* composed mainly of plasma; neutrals outnumber charged particles by about 1000:1 at ~ 300 km.

The primary means of ionizing species X is photoionization,



where  $h$  is Planck's constant and  $\nu$  is the frequency ( $\nu = c/\lambda_t$  where  $c$  is the speed of light and  $\lambda_t$  is the minimum energy needed to create an electron with no kinetic energy).

A secondary means of ionization is electron impact ionization:



Loss of ion  $X^+$  or  $XY^+$  (the result of  $XY$  being ionized) is by quenching,



radiative recombination,



dissociative recombination,



or spontaneous emission (the major loss with which this work will deal)

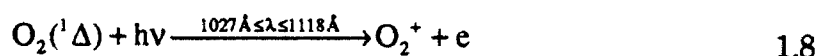




The "+low" indicates that an ion still exists after the emission but in a lower energy state.

Although the ionizing portion of the solar spectrum ( $<1800\text{\AA}$ ) represents a minute fraction of the total solar output, it has profound effects on the upper atmosphere because of the upper atmosphere's sensitivity to these wavelengths.

The *D-Region* exists from  $\sim 50 - 90$  km and is produced by the most penetrating of the ionizing radiations. Maximum electron densities occur  $\sim 75$  km. Densities range from about  $10^4/\text{cm}^3$  during the day to 0 at night; nighttime D-Region may exist at high latitudes where particle bombardment maintains the layer (Hargreaves, 1979; Chamberlain, 1961). The two major solar spectral regions affecting this layer are  $1027\text{\AA} - 1340\text{\AA}$  and  $1 - 10\text{\AA}$ . In the former,



produce the dominant ions. In the latter, X-rays easily penetrate the D-Region and ionize any ambient neutral. The sun does not emit much in this spectral region, but in random, infrequent spasms (flares, prominences), the concomitant enhanced X-ray flux will enhance D-Region ionization and produce copious amounts of radiowave absorption near the polar caps.

The *E-Region* lies between  $\sim 90 - 140$  km and peaks during daylight with maximum electron densities ( $10^5/\text{cm}^3$ ) occurring near 100 km

(Hargreaves, 1979; Chamberlain, 1961). This region, plus the F1-Region, form the central part of the ionosphere and are well understood by theory. Primary photoionization reactions in this layer are:



Note that  $\text{N}_2^+$  and  $\text{O}^+$  will quickly undergo the following charge exchange reactions:



Hence,  $\text{O}_2^+$  and  $\text{NO}^+$  are the dominant ions. The major ion sink is dissociative recombination.

The *F1-Region* (~140 - 200km) has two primary photoionization reactions:



Charge exchange reactions in the F1-Region are common and hence, the dominant ions are still  $\text{NO}^+$  and  $\text{O}_2^+$ . As in the E-Region, dissociative recombination is the major ion sink.

The *F2-Region* exists from ~200 - 1000km and is therefore the region of concern in this dissertation; the daytime electron number density is  $10^6/\text{cm}^3$  while the nighttime density is about  $10^4/\text{cm}^3$  (Hargreaves, 1979; Chamberlain, 1961). There is little diurnal dependence since one night is insufficient for a significant amount of ion-electron recombination to occur at such low densities. Also, the layer is maintained by other mechanisms, such as electron transport. The F2 layer electron density is greatest during sunlit hours and solar maximum years. This must be remembered during analysis of DE-2 data since the satellite flew during solar maximum. The primary photoionization reaction in the F2 layer is:



### 1.7 Introduction to the Thermosphere

The thermosphere begins at the mesopause (~85 km) and ends at the start of the exosphere (~600 km). Only homopolar molecules exist in this sphere and they do not have vibrational/rotational bands. Hence, these molecules do not emit infrared energy. They do, however, effectively absorb EUV and UV radiation which is then lost via downward heat conduction. This transport mechanism helps maintain thermospheric thermal balance. The energy input distribution into this sphere depends on the densities of atomic and molecular oxygen and nitrogen, cross sections for absorption as a function of wavelength, solar flux as a function of wavelength and chemical transformations. In addition to solar EUV and UV heating, there are strong high latitude heat sources due to auroral input. For example, the dissipation of electric fields in the ionosphere

provides a heat source known as Joule heating. Plus, direct insertion of energy occurs when energetic auroral particles precipitate into the atmosphere and produce particle heating. These sources are extremely variable and produce pressure gradients (thermospheric winds) because of the temperature gradients they can produce. Figure 1.5 is a typical temperature and plasma profile showing ionospheric and atmospheric layers.

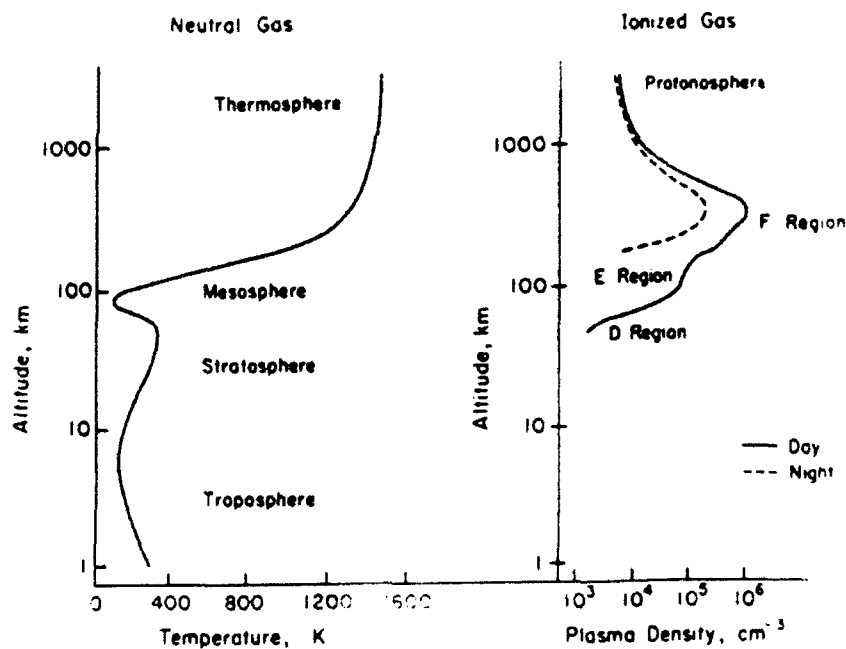


Figure 1.5 Typical profiles of neutral atmospheric temperature and ionospheric plasma density with the layers designated (adapted from Kelley, 1989).

## 1.8 Transport Equations of the Ionosphere and Thermosphere

Ions, electrons and neutrals in this dissertation will be considered as three intermingling fluids tightly coupled by collisions. Excellent treatments of the governing equations can be found in the literature (Rishbeth and Garriot, 1969 or Kelley, 1989 or references therein). At low- and mid-latitudes, the Earth's magnetic field may be assumed to be *dipolar*. As the latitude increases, the field lines extend into the magnetosphere introducing additional processes that must be included in the dynamics; at the polar cap, flux tubes can extend deep into the magnetosphere where thermal ions (such as  $O^+$  that are not gravitationally bound) may diffuse vertically along magnetic field lines and escape (Cannata, 1990). A fully self-consistent solution of thermospheric/ionospheric dynamics must include magnetospheric influences.

Physically significant information about a system is contained in the species velocity distribution function in phase space, given by

$$f_{\alpha}(\vec{r}, \vec{v}, t) \tag{1.19}$$

where  $\alpha$  represents the species of concern,  $\vec{r}$  is the position vector,  $\vec{v}$  is the velocity vector and  $t$  is time. All macroscopic variables of concern in the ionosphere and thermosphere, such as number density, temperature and mean velocity, can be determined if one knows the distribution function for the system. Theoretically, the distribution function can be determined by solving the Boltzmann Equation, given by

$$\frac{\partial f_{\alpha}}{\partial t} + \bar{V}_{\alpha} \cdot \bar{\nabla} f_{\alpha} + \bar{a} \cdot \bar{\nabla}_v f_{\alpha} = \left\{ \frac{\partial f_{\alpha}}{\partial t} \right\}_{\text{collision}} \quad 1.20$$

Note that  $\bar{V}_{\alpha}$  is the average drift velocity of species  $\alpha$ ,  $\bar{\nabla}$  is the space coordinate gradient,  $\bar{a}$  is the acceleration of  $\alpha$ ,  $\bar{\nabla}_v$  is the velocity space gradient and the right hand side of the equation is the time rate of change of the distribution function in phase space as a result of collisions. Solving this is no simple task. However, it is not necessary to solve this equation for the distribution function in order to determine the variables of interest. In fact, differential equations governing the time and space variations of these variables can be derived directly from the Boltzmann Equation without actually solving it. These equations are the macroscopic transport equations, and under appropriate boundary conditions, they can produce the desired macroscopic variables. The macroscopic variables of concern are related to the moments of the distribution function and the transport equations satisfied by these variables are obtained by taking the proper moments of the Boltzmann Equation. In this thesis, I shall only be concerned with the first three moments. These moments are obtained by multiplying the Boltzmann equation by  $m_{\alpha}$ ,  $m_{\alpha}v$  and  $m_{\alpha}v^2/2$  respectively and integrating over all velocity space, resulting in the conservation of mass (continuity), conservation of momentum and conservation of energy. Since the ionosphere and thermosphere consist of ions, neutrals and electrons, there is a system of transport equations for each species.

Consider the Boltzmann equation; multiplying each term by  $\chi(v)$  and integrating the resulting equation over all velocity space produces a general transport equation:

$$\frac{\partial}{\partial t}(n_\alpha \chi_\alpha) + \vec{\nabla} \cdot (n_\alpha \chi_\alpha \vec{V}_\alpha) - n_\alpha \vec{a} \cdot \vec{\nabla} \chi_\alpha = \left[ \frac{\delta}{\delta t}(n_\alpha \chi_\alpha) \right]_{\text{collision}} \quad 1.21$$

Hence, if one lets  $\chi(v) = m_\alpha$  or  $m_\alpha v$  or  $m_\alpha v^2/2$ , then the resulting equations are the continuity, conservation of momentum, and conservation of energy.

Assuming that  $\rho$  is mass density,  $U$  is the neutral velocity (wind),  $M_j$  is the mass of each species,  $P_j$  and  $L_j$  denote the rate of production of ions and electrons per cubic centimeter-second and the rate of loss respectively,  $n_j$  is the number density,  $k_B$  is the Boltzmann constant,  $p$  is the pressure,  $\pi_m$  is the momentum flux density tensor due to material motions,  $\pi_w$  is the momentum flux density tensor due to waves in the medium,  $\eta$  is the dynamic viscosity coefficient,  $g$  is gravity,  $v_{ni}$  is the neutral-ion momentum transfer collision frequency and  $\Omega$  is the Earth's constant angular velocity in a rotating reference frame, the neutral (thermospheric) fluid equations of continuity, momentum and state are (Kelley, 1989):

$$\frac{\partial \rho}{\partial t} = -\vec{\nabla} \cdot (\rho \vec{U}) \quad 1.22$$

$$\rho \frac{d\vec{U}}{dt} = -\vec{\nabla} p + \rho \vec{g} + \eta \nabla^2 \vec{U} - \vec{\nabla} \cdot \pi_w - 2\rho \vec{\Omega} \times \vec{U} - \rho v_{ni}(\vec{U} - \vec{V}_i) \quad 1.23$$

$$p = \rho k_B \frac{T_n}{m_n} = n_n k_B T_n \quad 1.24$$

and the corresponding equations for the ions in the ionosphere are:

$$\frac{\partial \rho_j}{\partial t} + \vec{\nabla} \cdot (\rho_j \vec{V}_j) = (P_j - L_j) M_j \quad 1.25$$

$$\rho_j \frac{d\vec{V}_j}{dt} = -\vec{\nabla} p + \rho_j \vec{g} + n_j q_j (\vec{E} + \vec{V}_j \times \vec{B}) - \sum_{k \neq j} \rho_j v_{jk} (\vec{V}_j - \vec{V}_k) \quad 1.26$$

$$p_j = \rho_j k_B \frac{T_j}{M_j} = n_j k_B T_j \quad 1.27$$

The following equation is the individual species form of the energy equation for the thermosphere/ionosphere system:

$$\begin{aligned} \frac{3}{2} \frac{dp_i}{dt} + \frac{5}{2} p_i \vec{\nabla} \cdot \vec{V}_i - \vec{\tau} : \vec{\nabla} \vec{V}_i + \vec{\nabla} \cdot \vec{q}_i + \rho Q = \\ \sum_j \frac{n_i \mu_{ij} v_{ij}}{m_i + m_j} \{ 3k(T_j - T_i) + m_j (\vec{V}_i - \vec{V}_j)^2 \} \end{aligned} \quad 1.28$$

where  $\tau$  is the viscosity tensor,  $q$  is the heat flux vector and  $Q$  is radiative heating.

Let us now use these facts to determine how ions *drift* under the influence of electromagnetic forces and collisions. The remainder of Chapter 1.8 is a review of ion drifts found in Hargreaves (1979) and Bittencourt (1986). An ion will feel all forces acting on neutrals, plus Lorentz forces. Considering a charged particle in the presence of electric and magnetic fields, the nonrelativistic momentum equation becomes:

$$m \frac{d\vec{V}}{dt} = q(\vec{E} + \vec{V} \times \vec{B}) \quad 1.29$$

Breaking this down further requires one to take components parallel and perpendicular to  $\vec{B}$ :

$$\vec{V} = \vec{V}_{\text{perp}} + \vec{V}_{\text{para}} \quad 1.30$$

$$\vec{E} = \vec{E}_{\text{perp}} + \vec{E}_{\text{para}} \quad 1.31$$



Hence, the momentum equation in two-component form becomes:

$$m \frac{d\tilde{V}_{\text{para}}}{dt} = q\tilde{E}_{\text{para}} \quad 1.32$$

$$m \frac{d\tilde{V}_{\text{perp}}}{dt} = q(\tilde{E}_{\text{perp}} + \tilde{V}_{\text{perp}} \times \tilde{B}) \quad 1.33$$

To solve 1.32 and 1.33, it is convenient to divide the perpendicular velocity vector into two components:

$$\tilde{V}_{\text{perp}}(t) = \tilde{V}'_{\text{perp}}(t) + \tilde{V}_d \quad 1.34$$

Note the last term on the right hand side (RHS) of 1.34 is the velocity vector in the plane normal to  $\mathbf{B}$ ; it is known as the *plasma drift velocity*. The first term on the RHS is the velocity of the particle as seen by an observer in a reference frame moving with constant drift velocity. By substituting 1.34 into 1.33, and writing the electric field component perpendicular to  $\mathbf{B}$  in the form:

$$\tilde{E}_{\text{perp}} = -[(\tilde{E}_{\text{perp}} \times \tilde{B}) / B^2] \times \tilde{B} \quad 1.35$$

one obtains:

$$m \frac{d\tilde{V}'_{\text{perp}}}{dt} = q[\tilde{V}'_{\text{perp}} + \tilde{V}_d - (\tilde{E}_{\text{perp}} \times \tilde{B}) / B^2] \times \tilde{B} \quad 1.36$$

Hence, in a coordinate system moving with a constant velocity,

$$\tilde{V}_d = (\tilde{E}_{\text{perp}} \times \tilde{B}) / B^2 \quad 1.37$$

and the particle motion in the plane perpendicular to  $\mathbf{B}$  is completely controlled by the magnetic field, according to

$$m \frac{d\vec{V}_{\text{perp}}}{dt} = q(\vec{V}_{\text{perp}} \times \vec{B}) \quad 1.38$$

By definition,

$$\vec{\omega}_c = -\frac{q\vec{B}}{m} \text{ and } \vec{v}_{\text{perp}} = \frac{d\vec{r}_c}{dt} \quad 1.39$$

where  $\omega_c$  is the gyrofrequency,  $m$  is the mass of the species,  $q$  is the charge and  $r_c$  is the particle position vector with respect to the center of gyration in the plane perpendicular to the magnetic field that contains the particle. The magnitude of  $\omega_c$  is always positive and is given by

$$\omega_c = \frac{qB}{m} \quad 1.40$$

Equation 1.38 can be re-arranged and integrated to eventually yield

$$\vec{V}_{\text{perp}} = \vec{\omega}_c \times \vec{r}_c \quad 1.41a$$

Equation 1.41a therefore shows that the velocity corresponds to a rotation of the position vector about the center of gyration in the plane perpendicular to  $\mathbf{B}$  with constant angular velocity. Thus, equation 1.38 implies that in a reference frame moving with constant drift velocity (equation 1.37), the particle moves in a circular motion at the gyrofrequency with radius  $r_c$ . Note that the radius of gyration is given by

$$r_c = \frac{mv_{\text{perp}}}{qB} \quad 1.41b$$

The instantaneous center of gyration of the particle is called the *guiding center*. Hence, as  $\mathbf{B}$  increases, the gyrofrequency increases and the radius decreases. Plus, the smaller the mass, the larger the gyrofrequency and the smaller the gyroradius. The particle velocity can therefore be expressed in vector form, independent of a coordinate system, as

$$\vec{V}(t) = \vec{\omega}_c \times \vec{r}_c + \frac{\vec{E}_{\text{perp}} \times \vec{B}}{B^2} + \frac{q\vec{E}_{\text{para}}t}{m} + \vec{V}(0) \quad 1.42$$

where the first term on the RHS of 1.42 represents the circular gyromotion, and the following ones represent, respectively, the guiding center drift velocity (perpendicular to both  $\mathbf{E}_{\text{perp}}$  and  $\mathbf{B}$ ), the constant acceleration of the guiding center along  $\mathbf{B}$  and the initial velocity parallel to  $\mathbf{B}$ .

The preceding discussion indicates that the resulting particle motion is described by the superposition of a circular motion in the plane normal to the magnetic field, with a uniform motion with constant drift velocity perpendicular to both  $\mathbf{B}$  and  $\mathbf{E}_{\text{perp}}$ , plus a uniform acceleration  $q\mathbf{E}_{\text{para}}/m$  along  $\mathbf{B}$ .

The drift velocity is independent of mass and the sign of the charge and is therefore the same for both negative and positive charges. Since the parallel component of the electric field crossed with the magnetic field is zero, the drift velocity takes on the more familiar look of

$$\vec{V}_d = (\vec{E} \times \vec{B}) / B^2 \quad 1.43$$

The resulting motion of the particle in the plane normal to the magnetic field is a cycloid. The explanation is as follows. The electric force acting simultaneously with the magnetic force, accelerates the particle so as to increase or decrease its velocity, depending on the relative direction of

the particle motion with respect to the direction of  $\mathbf{E}_{\text{perp}}$  and on the charge sign. The gyroradius increases with velocity and therefore the radius of curvature of the particle path will vary under the influence of  $\mathbf{E}_{\text{perp}}$ . This results in a cycloidal trajectory with a net drift in the direction perpendicular to both  $\mathbf{E}$  and  $\mathbf{B}$ . Since ions are much more massive than electrons, the gyroradius for ions is greater while the gyrofrequency is larger for electrons. Hence, the cycloid arcs are larger for ions, but there is a larger number of cycloid arcs per second for electrons, such that the drift velocity is the same for both species. Figure 1.6 shows trajectories described by ions and electrons in crossed  $\mathbf{E}$  and  $\mathbf{B}$  fields. Therefore, as long as the gyrofrequency of the charged particles exceed their collision frequencies (true above  $\sim 180\text{km}$ ), plasma will drift in the  $\mathbf{E} \times \mathbf{B}$  direction.

In a collisionless plasma, like the F2-Region in which this work resides, both positive and negative particles move together, implying no electric current. Below  $\sim 180\text{km}$ , collisions first become important since the ion's gyrofrequency ( $\omega_i$ ) begins to approach the value of the net ion momentum transfer collision frequency ( $\nu_i$ ).

In the collisional environment, let us consider the momentum equation in this form:

$$m \frac{d\vec{V}}{dt} = q(\vec{E} + \vec{V} \times \vec{B}) - m\nu(\vec{V} - \vec{U}) \quad 1.44$$

where  $\mathbf{V}$  is the ion velocity,  $\mathbf{U}$  is the neutral velocity,  $m$  is the mass (ion or electron) and  $\nu$  is a collision frequency. Assume that a collision brings a particle (either electron or ion) momentarily to rest at intervals of  $1/\nu$ ; thus, the trajectories are cycloidal and depend on  $\omega/\nu$ . As a positive ion begins to move in the electric field vector's direction, it begins to spiral about  $\mathbf{B}$ ; the ion is then successively stopped and then accelerated and drifts at some

angle inclined to  $\mathbf{E}$  with the classic spiral-helix motion. The electron mirrors the ion's motion, but with smaller spirals due to its smaller mass. In this collisional environment, the ion drift produces a current since the ion-neutral collision frequency is greater than the electron-neutral collision frequency, causing the ions to be more retarded than electrons. This current is normal to both  $\mathbf{E}$  and  $\mathbf{B}$  and is opposite to the drift velocity; it is called a *Hall current* and exists around  $\sim 120$  km. In general, motion of plasma is inclined to the direction of  $\mathbf{E}$  by the relation  $\arctan(\omega/\nu)$ .

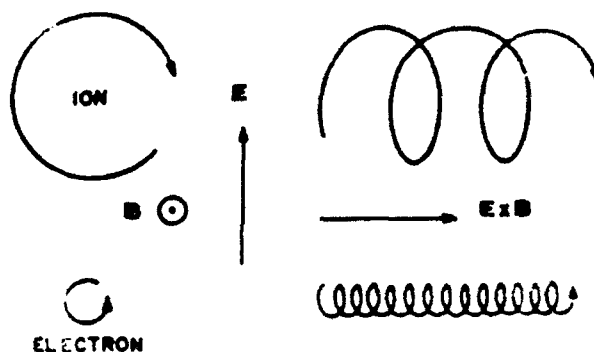


Figure 1.6 Cycloidal trajectories described by ions and electrons in crossed  $\mathbf{E}$  and  $\mathbf{B}$ . Note that both electrons and ions drift in the  $\mathbf{E} \times \mathbf{B}$  direction with the ion's gyroradius much larger but the electrons gyrofrequency much greater, producing a drift velocity that is the same for both species. When both species drift together, ambipolar diffusion occurs.

### 1.9 Electric Fields in the Upper Atmosphere

In the main *geomagnetic* field of the Earth, which originates within the Earth, there exist short term variations. Some occur regularly (related in frequency to the solar or lunar day); others are irregular and are

associated with disturbances (magnetic storms). This geomagnetic field extends outwards from the Earth to several Earth radii and can be assumed dipolar at low- and mid-latitudes (Chamberlain, 1961). By convention, the geomagnetic field is directed downwards into the Earth in the northern hemisphere and out of the Earth in the southern hemisphere.

*Electric fields* in the upper atmosphere are classified as either *external* or *internal*. External fields are large scale ionospheric electric fields that have magnetospheric origin, the two regions being coupled together by magnetic lines of force. This magnetospheric electric field is generated by the interaction of the solar wind and the Earth's magnetic field, causing electrons and ions to drift differently. The electric field for the solar wind (Kelley, 1989) is given by

$$\vec{E}_{sw} = -\vec{V}_{sw} \times \vec{B}_{sw} \quad 1.45a$$

where the "sw" subscript denotes solar wind parameters. This will generate a potential difference across the Earth's magnetosphere given by

$$V = \int_{\beta}^{\alpha} \vec{E}_{sw} \cdot d\vec{s} \quad 1.45b$$

where  $\alpha$  and  $\beta$  are points at the ends of the magnetosphere and  $s$  is the distance between them. Assuming a value of  $E_{sw} = 2.5$  mV/m (Kelley, 1989; Jursa, 1985) and integrating this electric field across the front of the magnetosphere ( $\sim 20$  Re in distance), one finds an available potential difference of  $\sim 320,000$  volts.

To get this energy into the magnetosphere, the electric circuit associated with the solar wind/magnetosphere interaction must be closed (Deng, p.c., 1992). This is done by connecting the open field lines of the

Earth with those of the IMF; since the magnetic field lines are equipotentials, electric fields can map great distances with no work being done. Hence, the interplanetary electric fields map into the magnetosphere and down into the conducting ionosphere, where this circuit is then closed. This connection occurs most easily when the IMF is southward ( $B_z$ -south). In this case, the dawn-dusk interplanetary electric field maps down into the polar cap ionosphere, causing plasma to flow in an antisunward direction. The electric field changes direction in the auroral zone creating a dusk-dawn electric field which causes plasma flow in the sunward direction. The two cell ion convection pattern pictured in Figure 1.7 is the result. Convecting ions impart momentum to the neutrals at high latitudes. There, these ion convection cells map themselves onto the neutral thermosphere, driving neutrals at auroral latitudes in the sunward direction opposite to the day-night pressure gradient. In the polar cap, ions convect in an antisunward direction and ion drag complements the day-night pressure gradient flow. Electric fields in the high latitude ionosphere may reach 50 mV/m, producing drifts in excess of 1000m/s (Kelley, 1989; Rees, 1989).

During positive  $B_z$  conditions (northward IMF or  $B_z$ -north), ion transport across the polar cap is reversed and sunward flow is observed. Our knowledge of the ion convection pattern during positive  $B_z$  conditions is limited and the current debate is whether or not the convection pattern is a four-celled or a distorted two-celled pattern (McCormac, 1991 and references therein). Understanding this ion convection pattern at high latitudes, especially during positive  $B_z$  conditions, is the motivation for development of the spaceborne ion drift observation platform in Chapter 6.

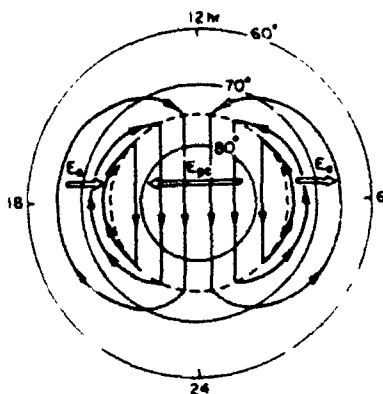


Figure 1.7 Schematic of ionospheric electric fields in the Northern Hemisphere polar cap and auroral zone in geomagnetic coordinates. The solid lines represent contours of electric potential, which act as streamlines to plasma flow - as denoted by the arrows.

Internal electric fields are caused by either polarization (small fields set up due to charge separation) or collisions (collisions between ions and neutrals couple their velocities resulting in the neutrals dragging the ions across geomagnetic field lines). The fact that ion temperatures can be greater than electron temperatures is evidence of large scale electric fields in high latitude regions.

Although the work in this dissertation is mainly done above the quenching zone (approximately  $> 180\text{km}$ ) where ions and electrons drift together (no current), I shall briefly discuss the currents in the collision environment (approximately  $< 180\text{km}$ ) for completeness.

Current ( $\mathbf{J}$ ) is carried by a flux of charged particles,

$$\vec{J}_i = en_i \vec{V}_i, \vec{J}_e = -en_e \vec{V}_e \quad 1.46$$



with ion flow being the current direction. Note that  $e$  is the charge, and  $n_i$  and  $n_e$  are the ion and electron number densities, respectively. Assuming charge neutrality,

$$n_e = \sum_i n_i \quad 1.47$$

the net current density is

$$\vec{J} = en_e(\vec{V}_i - \vec{V}_e) \quad 1.48$$

which, in an applied electric field measured in a reference frame moving with the bulk velocity of the gas, may be written as (Rees, 1989):

$$\vec{J} = \vec{\sigma}[\vec{E} + (1/c)\vec{V} \times \vec{B}] \quad 1.49$$

where

$$\vec{\sigma} = \begin{bmatrix} \sigma_p & \sigma_h & 0 \\ \sigma_h & \sigma_p & 0 \\ 0 & 0 & \sigma_0 \end{bmatrix} \quad 1.50$$

is the electrical conductivity tensor. The letter "p" stands for Pederson conductivity, "h" stands for Hall and "o" stands for Birkeland. In their full glory, the conductivities can be expressed as:

$$\sigma_0 = \sum_i n_i e^2 / m_i \nu_{in} \quad 1.51$$

$$\sigma_p = \sum_i \frac{en_i}{B} \left( \frac{\nu_{en} \omega_e}{\omega_e^2 + \nu_{en}^2} + \frac{\nu_{in} \omega_i}{\omega_i^2 + \nu_{in}^2} \right) \quad 1.52$$

$$\sigma_h = \sum_i \frac{en_i}{B} \left( \frac{\omega_e}{\omega_e^2 + \nu_{en}^2} - \frac{\omega_i}{\omega_i^2 + \nu_{in}^2} \right) \quad 1.53$$

where  $\nu_{in}$  and  $\nu_{en}$  are the ion-neutral and electron-neutral momentum transfer collision frequencies respectively and  $\omega_i$  and  $\omega_e$  are the ion or

electron gyrofrequencies. Note that Hall currents are in the  $\mathbf{E} \times \mathbf{B}$  direction, Pederson currents are in the  $\mathbf{E}$  direction and Birkeland currents are in the  $\mathbf{B}$  direction.

Hence, ionospheric plasma is subject to electromagnetic forces in addition to those felt by the thermospheric neutrals. The magnetic field creates geometric constraints on the plasma behavior which vary with geomagnetic latitude. Electric fields, however, are quite variable and put the plasma in motion perpendicular to  $\mathbf{B}$ . Electric fields play a large role in ionospheric dynamics and are therefore recovered by the simulated spaceborne observing platform developed in Chapter 6.

### 1.10 Airglow

Airglow is irradiance caused by atomic and molecular radiative transitions in the atmosphere. Quanta may be emitted in the visible, ultraviolet or infrared portions of the spectrum. Three categories of airglow exist: dayglow, twilightglow and nightglow. The emission of concern in this study (7320Å) is best observed from the ground at twilight (see section 1.11 and Chapter 5), is ubiquitous in the dayglow and therefore "easily" observed from space (see Chapter 4), and is nonexistent in the nightglow, except under sporadic conditions at high latitude when the emission may be generated by auroral electron impact ionization or when the conjugate point is in twilight. Airglow differs from aurora in that airglow covers all latitudes and longitudes, is unstructured and is often energized by the steady solar X-ray, EUV and UV emissions from the sun. Auroral emissions are superposed on these more omnipresent airglow emissions. It is very difficult to observe airglow from the ground by day because it is

overwhelmed by scattered sunlight. Most atmospheric spectroscopic emissions originate at thermospheric (or ionospheric) altitudes because this is where most of the solar EUV and UV energetic photons are absorbed and where energetic auroral particles stop. Above the thermosphere/ionosphere, hydrogen and helium are the dominant constituents and resonant scattering and fluorescence of solar photons produce the geocorona, in which the Earth is bathed.

### 1.11 The Ionospheric [OII] 7320-7330Å Airglow Emission

The 7320-7330Å *multiplet emission* that is produced in twilight airglow and aurora is the result of the metastable transition between excited  $^2P$  and  $^2D$  states of  $O^+$  ions. These transitions occur at thermospheric heights and are strictly forbidden by electric dipole radiation; the transition probabilities ( $A$ ) are finite because of the existence of electric-quadrupole ( $q$ ) radiation (Chamberlain, 1961). The 7320-7330Å emission multiplets were initially studied to understand gaseous *nebulae* (Bowen, 1928, 1935, 1955; Aller and White, 1949). The best wavelength determination of the forbidden  $O^+(^2P-^2D)$  emission available (Bowen, 1935) is from the Mount Palomar Observatory of galactic nebulae emissions. Unfortunately, these observations were incorrectly reported by Chamberlain (1961) and others; the errors have been repeated in several papers since. Meriwether et al. (1978) state that the correct results for the strongest component in each of the two *doublets* are:

$$O^+(^2P \rightarrow ^2D_{5/2}), \lambda = 7319.9\text{\AA} \pm 0.1\text{\AA} \quad 1.54$$

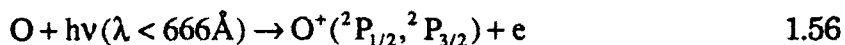
$$O^+(^2P \rightarrow ^2D_{3/2}), \lambda = 7330.4\text{\AA} \pm 0.3\text{\AA} \quad 1.55$$

These results will be used in this work. Doublet emissions in the  $O^+(^2P \rightarrow ^2D_{5/2})$  and  $O^+(^2P \rightarrow ^2D_{3/2})$  transitions will be rounded to 7320Å and 7330Å respectively, unless otherwise stated, to conform with the literature. The transition probability results of Seaton and Osterbrock (1957) are shown in Figure 1.8 (adapted from Yee, 1980) and are used herein. Theoretical transition probabilities were first given by Seaton and Osterbrock (1957); they found radiative lifetimes of 4.57s for  $O^+(^2P)$  ions and a branching ratio of ~0.78 for the emission of radiation in the 7320-7330Å multiplet. Since this emission lifetime is shorter than the diffusion lifetime in the F-Region (~10s-100s), the  $O^+(^2P)$  ions are believed to be in photochemical equilibrium.

Omholt (1957) was the first to detect these emissions in the atmosphere in an intense red *aurora*. He noted a broad feature at 7325Å and determined it to be the  $O^+$  multiplet; next, he assumed that this emission was quenched at low altitudes since the multiplet at low auroral altitudes was not detected. Since Omholt, others have studied auroral 7320-30Å emissions. Wallace (1960) resolved the 7320Å and 7330Å doublets and found line strengths close to Seaton's and Osterbrock's (1957) theoretical values. Meriwether et al. (1974) found the individual components in the 7320Å doublet to be separated by about 0.836Å (see Figure 1.8) in an auroral study using a ground-based FPI; this value is still quoted today, and will be reevaluated in Chapter 4. Photoionization leaves some  $O^+$  (~20%) in the excited, metastable  $O^+(^2P)$  state (Rees, 1989). The excess energy is lost by quenching or radiation.

### 1.11.1 Sources of $O^+(^2P)$ Ions

Metastable  $O^+(^2P)$  ions are *primarily* produced in our atmosphere by *photoionization* of neutral atomic oxygen by solar EUV radiation at wavelengths less than  $666\text{\AA}$ :



or photoionization of molecular oxygen by wavelengths less than  $1100\text{\AA}$ :

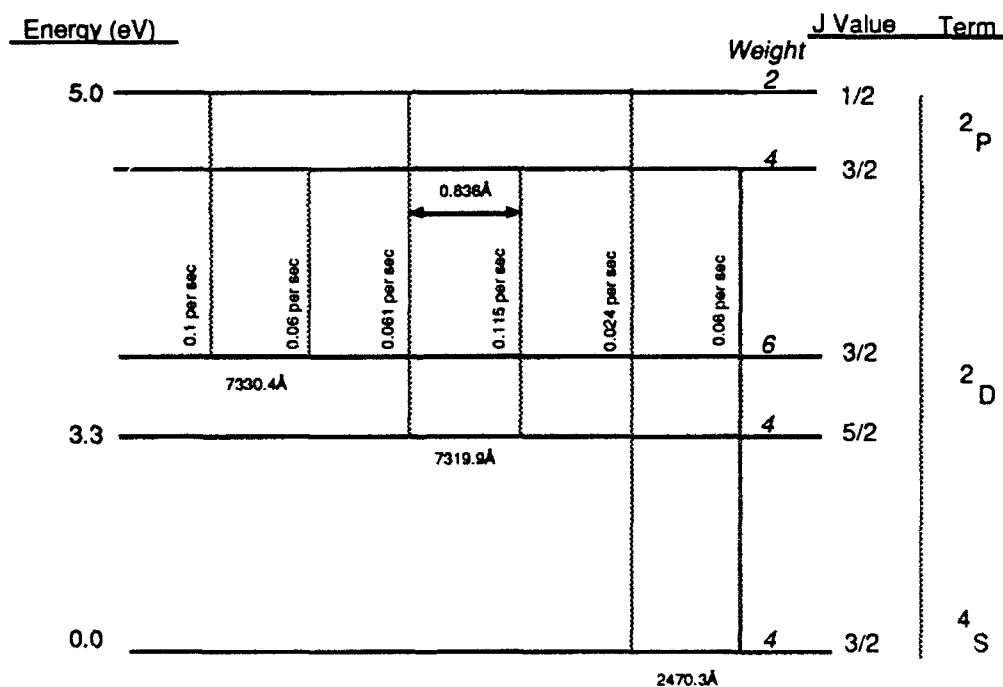
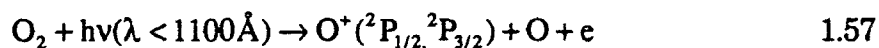


Figure 1.8 Select OII transitions, modified from Seaton and Osterbrock (1957) and Yee, (1980). The  $7319.9\text{\AA}$  doublet separation ( $0.836\text{\AA}$ ) was determined by Meriwether et al. (1974) from a ground-based Fabry-Perot interferometer. In this dissertation, the  $7319.9\text{\AA}$  doublet will be referred to as the  $7320\text{\AA}$  doublet. Optical instrumental resolution is usually too low to resolve the two components of the  $7320\text{\AA}$  doublet and most studies are the averaged wavelength. However, this quantity is heavily weighted in favor of the  $O^+(^2P_{3/2} \rightarrow ^2D_{5/2})$  component since the  $O^+(^2P_{3/2} \rightarrow ^2D_{5/2})$  component at  $\sim 7319.9\text{\AA}$  is  $\sim 4$  times stronger than the  $O^+(^2P_{1/2} \rightarrow ^2D_{5/2})$  component at  $\sim 7319.1\text{\AA}$ .

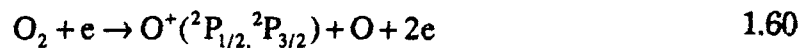
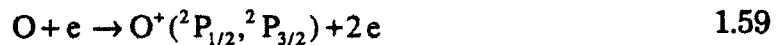
Equation 1.56 is by far the dominant source and 1.57 is frequently ignored, especially at F2 heights. Note that  $2P_{1/2}$  and  $2P_{3/2}$  are two substates of the  $O^+(2P)$  ions and the subscripts are the total angular quantum number (known as a J-value) associated with the particular substate.

A photoionization rate can be written

$$P_i = X \int_{\lambda_t}^{\lambda} F(\lambda) \xi(\lambda) \sigma_i(\lambda) d\lambda \quad 1.58$$

where  $P_i$  is the production rate of the  $i^{\text{th}}$  substate of the  $O^+(2P)$  ion,  $X$  is number density of atomic or molecular oxygen,  $\lambda_t$  is the ionization threshold wavelength,  $F(\lambda)$  is the solar EUV radiation,  $\xi$  is the quantum yield of the  $O^+(2P)$  ion, and  $\sigma_i(\lambda)$  is the photoionization cross-section.

A secondary source of  $O^+(2P)$  ions is *photoelectron impact ionization*, given by:



with equation 1.60 frequently ignored, especially at F2-Region heights.

Hays et al. (1975) and Swenson (1976) showed that the photoelectron source of  $O^+(2P)$  ions contributes less than 10% of the total  $O^+(2P)$  production. But Richards and Torr (1988) show that at large optical depths, the photoelectron source may exceed the direct photoionization rate. The importance of the photoelectron source depends on the attenuation of the solar EUV flux and the amount of local (conjugate) photoelectron transport into the zone of interest (McDade et al., 1991); they state that in the absence of conjugate flux, the photoelectron source contributes about 10-15% to the

total column  $O^+(2P)$  production rate during twilight; hence, photoelectron impact ionization is a neglected source in many studies.

Rees et al. (1982) studied a *minor source* of  $O^+(2P)$  formation: *auroral electron impact ionization*. They analyzed observations taken from the VAE instrument onboard the AE satellite and calculated a production efficiency of  $O^+(2P)$  by auroral electron impact ionization to be 18%. They stated that atomic oxygen ionization by (auroral) electron impact is the *main* source of  $O^+$  ions *only* during auroral particle precipitation. Low energy auroral particles (<1 keV) produce the 7320Å emission; the ionization cross section is maximized at ~100 eV (Smith, 1982). As the auroral particles become more intense, they penetrate deeper into the ionosphere and excite atoms and molecules there, including atomic oxygen. But most nighttime aurora deposit their energetic particles around 100 km, and at that altitude,  $O^+(2P)$  will be quenched before it can radiate. Table 1.2 (from Rees, 1989) illustrates branching ratios for electron impact ionization of atomic oxygen. The threshold energy is in eV; when atomic oxygen is impacted by an electron carrying at least 18.61 eV, 20% of the product will be  $O^+(2P)$ .

Ion	State	%	eV
$O^+$	4S	40	13.61
	2D	40	16.92
	2P	20	18.61

Table 1.2 Fractional percentages of  $O^+$  produced by electron impact ionization. The fourth column represents the threshold energy the electron must have in order to excite atomic oxygen to the state listed in column 2.

A more thorough discussion of production is presented in Chapter 3.

### 1.11.2 Sinks of O<sup>+</sup>(<sup>2</sup>P) Ions

O<sup>+</sup>(<sup>2</sup>P) ions are lost by quenching or spontaneous emission. Spontaneous *emission* of the ions to lower states is given by:



where  $A_\lambda$  is the Einstein coefficient, in units of s<sup>-1</sup>. Note that O<sup>+</sup>(<sup>2</sup>D) also has two substates, denoted O<sup>+</sup>(<sup>2</sup>D<sub>3/2</sub>) and O<sup>+</sup>(<sup>2</sup>D<sub>5/2</sub>). The ground state is simply O<sup>+</sup>(<sup>4</sup>S<sub>3/2</sub>). Therefore, there are six possible radiative losses from the O<sup>+</sup>(<sup>2</sup>P) state - three from O<sup>+</sup>(<sup>2</sup>P<sub>1/2</sub>) and three from O<sup>+</sup>(<sup>2</sup>P<sub>3/2</sub>). These losses can be written as:

$$L_{\text{O}^+(\text{}^2\text{P}_{1/2})} = \text{O}^+(\text{}^2\text{P}_{1/2}) \times A_{\text{}^2\text{P}_{1/2}} \quad 1.62$$

$$L_{\text{O}^+(\text{}^2\text{P}_{3/2})} = \text{O}^+(\text{}^2\text{P}_{3/2}) \times A_{\text{}^2\text{P}_{3/2}} \quad 1.63$$

where L is the loss of the respective ion, A is the proper Einstein coefficient and O<sup>+</sup>(<sup>2</sup>P<sub>1/2</sub>) or O<sup>+</sup>(<sup>2</sup>P<sub>3/2</sub>) are the number densities for the ion. Note that

$$A_{\text{}^2\text{P}_{1/2}} = A_{\text{}^2\text{P}_{1/2} \rightarrow \text{}^2\text{D}_{3/2}} + A_{\text{}^2\text{P}_{1/2} \rightarrow \text{}^2\text{D}_{5/2}} + A_{\text{}^2\text{P}_{1/2} \rightarrow \text{}^4\text{S}_{3/2}} = 0.185\text{s}^{-1} \quad 1.64$$

Similarly,

$$A_{\text{}^2\text{P}_{3/2}} = 0.236\text{s}^{-1} \quad 1.65$$

This substate population depends on the statistical weights (see Figure 1.8) as determined by Seaton and Osterbrock (1957). Hence,

$$\text{O}^+(\text{}^2\text{P}_{1/2}) = \frac{2}{6} \text{O}^+(\text{}^2\text{P}) \quad 1.66$$



$$O^+(^2P_{3/2}) = \frac{4}{6} O^+(^2P) \quad 1.67$$

where the number densities of the two states are equal to 0.33 or 0.67 of the total  $O^+(^2P)$  number density. Substituting 1.64 and 1.66 into 1.62, and 1.65 and 1.67 into 1.63 respectively gives

$$L_{O^+(^2P_{1/2})} = 0.061 \times O^+(^2P) \quad 1.68$$

$$L_{O^+(^2P_{3/2})} = 0.158 \times O^+(^2P) \quad 1.69$$

or the familiar:

$$L_r = 0.219 \times O^+(^2P) \quad 1.70$$

where  $r$  denotes the sum of radiative loss. Hence, equation 1.61 can be written as

$$O^+(^2P) \xrightarrow{A_\lambda} O^+(^2D, ^4S) + h\nu, A_\lambda = 0.219 s^{-1} \quad 1.71$$

The doublet emission at  $[OII] \lambda 7320 \text{\AA}$  is produced by the following radiative transitions:

$$O^+(^2P_{1/2}) \xrightarrow{A_\lambda} O^+(^2D_{5/2}) + h\nu, A_\lambda = 0.020 s^{-1}, \lambda = 7319.1 \text{\AA} \quad 1.72$$

$$O^+(^2P_{3/2}) \xrightarrow{A_\lambda} O^+(^2D_{5/2}) + h\nu, A_\lambda = 0.077 s^{-1}, \lambda = 7319.9 \text{\AA} \quad 1.73$$

with Equation 1.73 being ~3.8 times more intense than Equation 1.72 ( $0.077/0.02 \sim 3.8$ ). The doublet emission at  $7330 \text{\AA}$  is produced by:

$$O^+(^2P_{1/2}) \xrightarrow{A_\lambda} O^+(^2D_{3/2}) + h\nu, A_\lambda = 0.033 s^{-1} \quad 1.74$$

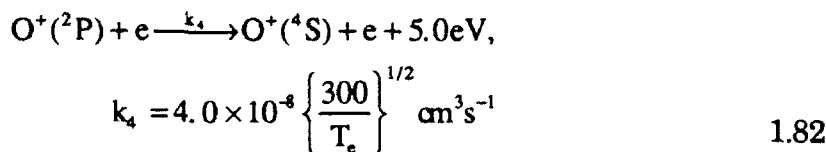
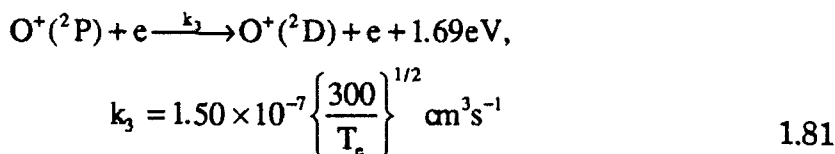
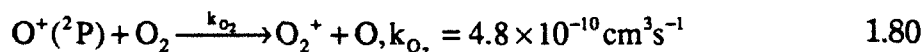
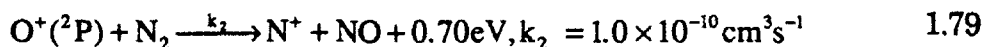
$$O^+(^2P_{3/2}) \xrightarrow{A_\lambda} O^+(^2D_{3/2}) + h\nu, A_\lambda = 0.040 s^{-1} \quad 1.75$$

These Einstein coefficients are determined by referring to Figure 1.8. For example, the transition probability from  $O^+(^2P_{1/2} - ^2D_{5/2})$  is  $0.061s^{-1}$ . But the determined weight is 2 (i.e.  $2/6$  or  $0.33$ ). Hence,  $0.33 \times 0.061s^{-1}$  produces the Einstein coefficient seen in equation 1.72. Mathematically, this is

$$A_{(^2P_{1/2} \rightarrow ^2D_{5/2})} \epsilon_{1/2} = (0.061s^{-1}) \left( \frac{2}{6} \right) \approx 0.020s^{-1} \quad 1.76$$

where  $\epsilon_{1/2}$  is the statistical weight for the  $O^+(^2P_{1/2} \rightarrow ^2D_{5/2})$  transition.

The following reactions are the major *quenching* losses of the  $O^+(^2P)$  ion. These equations are listed with excess kinetic energy of the reaction and the currently accepted rate coefficient.



The  $k$  parameters are the quenching rates for O, N<sub>2</sub> (Rusch et al., 1977; Rees, 1989), electrons (Henry et al., 1969; Rees, 1989) and O<sub>2</sub> (Solomon, p.c., 1991).

The loss equation for *quenching* is:

$$L_q = [O^+(^2P)]\{k_e[e] + k_{N_2}[N_2] + k_{O_2}[O_2] + k_O[O]\} \quad 1.83$$

where the terms within the square brackets ( $[e]$ , for example) are number densities, and  $k_{N_2}$  is  $k_1 + k_2$  and  $k_e$  is  $k_3 + k_4$ . Hence, the total loss equation becomes:

$$L_{total} = [O^+(^2P)]\{0.219 + k_e[e] + k_{N_2}[N_2] + k_{O_2}[O_2] + k_O[O]\} \quad 1.84$$

### 1.11.3 Number Densities and Emission Rates

Neglecting transport, since the lifetime of the  $O^+(^2P)$  ion is less than the diffusion time constant at F-Region altitudes (Yee, 1980), the continuity equation for the  $O^+(^2P)$  ion is:

$$\frac{\partial}{\partial t}[O^+(^2P)] = P - L \quad 1.85$$

where  $P$  and  $L$  are photoionization and electron impact ionization production and radiative and quenching loss rates as discussed previously. If one assumes steady state, the time derivative is zero and hence (re-arranging), the production rate of  $O^+(^2P)$  ions is

$$P = [O^+(^2P)]\{0.219 + k_e[e] + k_{N_2}[N_2] + k_{O_2}[O_2] + k_O[O]\} \quad 1.86$$

Re-arranging, the  $O^+(^2P)$  number density is

$$[O^+(^2P)] = \frac{P}{\{0.219 + k_e[e] + k_{N_2}[N_2] + k_{O_2}[O_2] + k_O[O]\}} \quad 1.87$$

The emission rate for any transition is defined as

$$\eta = A[X] \quad 1.88$$

where  $\eta$  is the emission rate,  $A$  is the Einstein coefficient and  $[X]$  is the concentration of species  $X$ . In this case, substitute 1.87 into 1.88 and get

$$\begin{aligned} \eta &= A*[O^*(^2P)] \\ &= \frac{AP}{\{0.219 + k_e[e] + k_{N_2}[N_2] + k_{O_2}[O_2] + k_O[O]\}} \end{aligned} \quad 1.89$$

The volume emission rate in the 7320Å doublet only is

$$\eta_{7320} = \frac{0.097P}{\{0.219 + k_e[e] + k_{N_2}[N_2] + k_{O_2}[O_2] + k_O[O]\}} \approx 0.44P \quad 1.90$$

where 0.097 is the sum of the two Einstein coefficients for the transitions in the 7320Å doublet (see Equations 1.72 and 1.73). Above the quenching zone (~180km), all terms in the denominator are small with respect to the quenching loss term (0.219), and one is therefore left with 0.44P. This volume emission rate equation will be discussed further in Chapter 3 and used in the 7320Å volume emission rate model calculations. Similarly, the volume emission rate in the 7330Å doublet above the quenching zone is

$$\eta_{7330} = \frac{0.073P}{\{0.219 + k_e[e] + k_{N_2}[N_2] + k_{O_2}[O_2] + k_O[O]\}} \approx 0.33P \quad 1.91$$

where  $0.073s^{-1}$  is the sum of the Einstein coefficients for the transition in the 7330Å doublet (see Equations 1.74 and 1.75). From equations 1.90 and 1.91, it is apparent that emission in the 7320Å doublet is 1.33 times stronger than emission in the 7330Å doublet. Emission in the 7320-30Å multiplet above the quenching zone is therefore written as  $\eta_{7320-30} \sim 0.78P$ .

#### 1.11.4 Other Previous Studies

Nebular and auroral 7320-7330Å emissions have been detected via ground-based means and thoroughly studied by many workers. But it was not until the advent of the Visible Airglow Experiment (VAE) onboard the AE satellite that the first attempts were made to measure *in situ* the *airglow* emission. Many studies of this VAE data have enhanced our understanding of the  $O^+(^2P)$  chemistry and physics and, hence, the dynamics and chemistry of the ionosphere. Confirming the auroral study of Omholt (1957) in which the  $O^+(^2P)$  ions were found to be efficiently quenched at low altitudes by collisions with neutral species, Walker et al. (1975) published the first 7320-30Å volume emission rate profile in the dayglow. Yee (1980) states that the 7320-30Å emission is mainly quenched at low altitudes by  $N_2$  and O, and by electrons at higher altitudes. Solar activity enhancements and the concomitant effects on the 7320-30Å emission have been studied. Torr et al. (1979) performed theoretical calculations that showed more than a factor of three increase in the  $O^+(^2P)$  photoionization rate within a solar cycle. Abreu et al. (1980) found the ionization rate of  $O^+(^2P)$  ions from measurements of the 7320-30Å emission during Solar Cycle 21. The F10.7 cm solar flux index and ionization rate varied in a similar fashion. The deduced ionization rate also compares favorably with the ionization rate computed using the solar EUV flux as measured by the EUV spectrometer on AE satellites. Yee et al. (1981) published averaged column emission rate profiles as a function of solar zenith angle and solar activity; they found that the rate of decreasing emission as a function of solar zenith angle agrees with the theoretical calculation based on MSIS (a neutral atmosphere model) and the solar spectrum as measured by the

EUV spectrometer on the AE. They also found emission brightness to increase as the solar F10.7cm solar flux increased with the solar cycle. Yee and Abreu (1982) monitored the exospheric temperatures from the 7320-30Å emissions by measuring the rate of decreasing  $O^+(^2P)$  vertical brightness after twilight. These exospheric temperatures, deduced from the VAE, agree well with temperature measurements made from the NATE (neutral atmosphere temperature experiment) on the AE.

Nighttime aurorae expend most of their energy around 110km (Rees et al., 1976) where the  $O^+(^2P)$  ion is severely quenched and therefore, the 7320Å emission is very weak ( $<10R$ , Sivjee, 1981). Hence, the sporadic nature and low intensity of nighttime auroral 7320Å emissions makes it difficult to study. In the daytime cusp, however, where low energy magnetosheath-like electrons excite the aurora above 200km (Deehr et al., 1980), the 7320Å emission is strong and stable, allowing ionospheric energetics and dynamics studies to take place. Smith et al. (1982) measured the 7320Å emission in Longyearbyen, Svalbard (Norway) during the 1980-81 winter in an attempt to deduce information about the ion convection pattern. This area is an excellent one in which to study aurorally induced 7320Å emissions since the emission is intense enough and stable enough for study. Hence, Smith et al. (1982) conclude that aurorally induced 7320Å emissions are best studied (from the ground) in the cusp regions where the soft electron flux necessary for formation is extensive enough to provide a source of this emission exceeding 20R for up to 10 hours. They also noted that 7320Å observations in the zenith indicate that vertical ion speeds are unimportant. This conclusion allows me to simplify ion drift calculations for the satellite observing platform proposed in Chapter 6.

Atmospheric trace constituents, such as  $O^+(2P)$ ,  $O(^1D)$  and  $O(^1S)$ , redistribute solar EUV energy in the thermosphere. These metastable species play a large role in this energy redistribution since they can act as temporary energy reservoirs which are eventually lost as radiation, or via collisional processes or transport (Torr and Torr, 1982). Radiative losses, such as  $O^+(2P) \rightarrow O^+(2D)$  represent an atmospheric cooling process. Torr et al. (1980) showed the ionospheric energy loss rate for  $O^+(2P)$  radiative emission (airglow) to peak at about  $60 \text{ eV cm}^{-3} \text{ s}^{-1}$  at 250 km. Torr et al. (1980) also showed that the major transfer of solar EUV energy to the neutral atmosphere as heat occurred by kinetic energy acquired by the products of exothermic reactions. They showed that the  $O^+(2P) + N_2$ ,  $O^+(2P) + O$  and  $O^+(2P) + e$  exothermic reaction heating rates peaked at about 170 km, 180 km and 240 km respectively and had values of about  $500 \text{ eV cm}^{-3} \text{ s}^{-1}$ ,  $100 \text{ eV cm}^{-3} \text{ s}^{-1}$  and  $10 \text{ eV cm}^{-3} \text{ s}^{-1}$  respectively.

Measurements of the 7320 Å-doublet emission may be used to determine the atomic oxygen concentration or the solar EUV ionization frequency (Meriwether et al., 1978). Torr et al. (1990a, 1990b) have recently developed a midlatitude interhemispheric model of the  $O^+(2P)$  airglow emission which computes volume emission rates as a function of altitude, latitude, longitude and time. Their model solves the coupled time dependent energy, momentum, continuity and photoelectron transport equations from 80 km in one hemisphere, along the field line, to 80 km in the conjugate hemisphere (Torr, 1990a). The MSIS-86 model (Hedin, 1987) supplies the Torr model with the concentration of the major neutral species. Other inputs are date and solar and magnetic indices. The semiglobal maps produced by this model show the diurnal, seasonal and solar variability of the 7320 Å-doublet emission; it also allows one to map the extent and the

longitudinal variability of conjugate photoelectron effects (Torr et al., 1990b). It is against this model that I compare my 7320Å volume emission rate model as one of its validation tests.

[OII]  $\lambda$ 7320Å emissions are relatively weak when compared to the red line emission of O(<sup>1</sup>D) at 6300Å or the green line emission of O(<sup>1</sup>S) at 5577Å. But intense 7320Å emissions observed by the *Intercosmos-Bulgaria-1300* satellite in the polar cap were reported by Israelevich et al. (1990). Emission intensities in some polar cap arcs were an order of magnitude larger than in the auroral oval, an observation that is not expected. Israelevich et al. (1990) discussed several possibilities which can lead to these emission enhancements; they conclude that these interesting observations of enormous 7320Å emissions need independent confirmation.

In the most recent study of the 7320Å emission, McDade et al. (1991) invert twilight observations of the 7320Å emission and obtain information about the thermospheric oxygen atom concentrations and the unattenuated O+(<sup>2</sup>P) ionization frequency. Their proposed observing strategy allows atomic oxygen concentrations to be recovered from twilight observations with greater precision and less error than previous methods. McDade et al. (1991) further show that 7320Å twilight observations, using their new method, can measure diurnal variations in the solar EUV flux at thermospheric atomic oxygen ionization wavelengths.

#### 1.11.5 Viewing Conditions

Twilight is the time when sunlight irradiates an emitting atmospheric layer from below, as opposed to daytime when the sun irradiates the emitting layer from above. At night, the emitting layer receives no solar illumination. Therefore, twilight marks the transition



between solar and photoelectron produced airglow to nighttime's auroral electron impact airglow. During twilight, the total sky brightness diminishes to a point where weaker radiation, like 7320Å, becomes easier to observe.

The [OII]  $\lambda$ 7320-7330Å emission in airglow is *best* observed from the *ground* at twilight (high solar zenith angle, long optical path) and above the quenching zone (~180km). The high solar zenith angle and long optical path mean that the background is depressed since most of the sky is already dark and the emission column path length is increased with longer optical path. The second best place to observe the 7320-30Å emission from the ground is the daytime polar cusp (photoionization, photoelectron and auroral electron impact ionization sources), where the emission is strong and stable - greater than 20 Rayleighs (R) for up to 10 hours (1R =  $10^6$  photons  $\text{cm}^{-2} \text{s}^{-1}$ ). The emission is also seen in nighttime aurora, but is sporadic and less intense than in twilight or the cusp since the ions are quenched at the lower auroral altitudes. Contamination by scattered sunlight and OH airglow can also make observations of the 7320Å emission difficult. Meriwether et al. (1978) showed that the Fraunhofer structure of the scattered light continuum near 7320Å can preclude accurate extraction of the 7320Å intensity unless appropriate techniques for the removal of this background emission are applied. Bass and Garvin (1962) and Krassovsky (1963) state that the P<sub>1</sub>(2), P<sub>2</sub>(3) and P<sub>1</sub>(3) rotational lines of the OH (8-3) molecular band occur approximately at 7316, 7330 and 7340Å. Ground-based observations (Meriwether et al., 1978) show that this OH 7316Å emission is ~2 times more intense than the 7320Å doublet emission in the O+(2P-->2D<sub>5/2</sub>) transition. Meriwether et al. (1978) also found that the O+(2P-->2D<sub>3/2</sub>) doublet at 7330Å blended nearly perfectly with the P<sub>2</sub>(3)

rotational component of the OH(8-3) P branch at  $7329.9\text{\AA} \pm 0.2\text{\AA}$ . They removed the contamination but found the intensity measurement of the unblended doublet at  $7320\text{\AA}$  stronger and more accurate. Table 1.3 shows *other* possible OH-contaminating lines. Because of the OH contaminant, most optical observations of OII  $\lambda 7320\text{\AA}$  discussed in the literature (and in this dissertation) are made with a narrow ( $\sim 3\text{\AA}$ ) filter such that only the  $7320\text{\AA}$  doublet is allowed to pass.

Space-based limb observations can be made during daytime and twilight hours and have the distinct advantages of being above contaminants (such as OH) and of having the Van Rhijn effect, which allows the optical instrument to scan along an enormous path length and detect more  $7320\text{\AA}$  photons.

Band	Line	Wavelength ( $\text{\AA}$ )
11,5	R2(9)	7311.732, 7211.812
8,3	Q1(4)	7312.800, 7313.353
11,5	R1(9)	7314.363, 7315.075
8,3	P1(2)	7318.268, 7318.337
11,5	P2(5)	7321.373, 7321.405
13,6	R2(10)	7326.437, 7326.442
8,3	Q2(5)	7327.698, 7327.739

Table 1.3 Some contaminating OH wavelengths.

Copeland and Slinger (1990) show that the DE-2 FPI ( $7320\text{\AA}$ ) spectrum below tangent heights of  $\sim 200\text{km}$  is due to the OH (11,5) Meinel band (P2(5) line) spacecraft glow. If true, this will not affect this dissertation since FPI

measurements below ~200km were ignored. Vehicle glow is an interaction of low orbit spacecraft with the atmosphere and is sometimes mistaken for airglow. Hence, understanding spacecraft glow is necessary for space-based observation of emissions, especially from large, low orbiters with multiple surfaces (Torr and Torr, 1988). For work on modelling spacecraft-atmosphere interaction, see Elgin et al. (1990a,b).

In conclusion, the remainder of this dissertation will deal with the emission in the 7320Å doublet only - *not* the 7330Å doublet. This is done for three reasons. First, the 7330Å emission is more difficult to measure than the 7320Å emission doublet because of contaminants (both the P<sub>2</sub>(3) rotational component of the OH(8-3) P branch and the N<sub>2</sub> 1PG (5,3) system have emissions at ~7330Å). Second, the 7330Å doublet emission is ~1.33 times weaker than emissions in the 7320Å doublet ( $\eta_{7320}/\eta_{7330} = 0.44P/0.33P = 1.33$ ). And third, the Thule AB, Søndre Strømfjord and DE-2 FPIs all contain filters that just measure emissions in the 7320Å doublet.

## **CHAPTER 2**

### **RESEARCH TOOLS**

#### **2.1 The Fabry-Perot Interferometer (FPI)**

At the end of the 19th century, two physicists (Charles Fabry and Alfred Perot) described a new and unique interference device which bears their name - the Fabry-Perot interferometer or FPI. The instrument makes use of interference phenomena due to waves successively reflected between two parallel, flat, semi-transparent mirrors separated by a fixed distance. Since its invention, the FPI has been used extensively as a passive, remote-sensing optical device, spectrally monitoring natural (in this case ionospheric) emissions. The FPI is a valuable tool for ionospheric studies since it allows one to determine the dynamics and energetics of the ionosphere by monitoring the 7320Å emission. The most current and thorough discussion of the FPI is in Nardi (1991); a review of winds and temperature measurements can be found in Hernandez and Killeen (1987) and references therein. To summarize, the Fabry-Perot etalon performs a wavelength analysis on the light observed from ionospheric emissions by scanning the interference fringe pattern with a detector. This analysis characterizes the Doppler line profile of the emitting species. An FPI

spectrogram (discretely sampled, instrument broadened Doppler profile) is produced by convolving a Gaussian source function (i.e the 7320Å dayglow emission) with the measured instrument transfer function (described by a Fourier series at each wavelength). Analysis of the spectrogram can produce line-of-sight (LOS) ion temperatures, brightnesses, continuum brightnesses and ion drifts. The method of actually determining the LOS parameters from the spectrogram by performing a four parameter least-squares fit (LSF) is explained in detail by Killeen and Hays (1984), and Nardi (1991) and is reviewed in section 2.1.2. The next section outlines the mathematical description (Killeen and Hays, 1984; Born and Wolf, 1980; Hernandez, 1961; Nardi, 1991; references therein) of the FPI.

### 2.1.1 Mathematical Description

FPI measurement processes impose distorting effects in observed emission lines. The optical components and detector may broaden the emission line; this is referred to as *instrument broadening* and must be properly characterized in the analysis procedure before any geophysical information can be extracted from the FPI observations. Field of view effects may also cause broadening, called *smearing* or *altitude averaging*. Geophysical parameters can be retrieved from the emission line profile if one considers the kinetic properties of a gas in thermodynamic equilibrium. An FPI only detects Doppler information along the line-of sight; this simplifies the following discussion since only one dimension needs to be considered. A gas in local thermodynamic equilibrium has the Maxwellian velocity distribution

$$f(v) = \left( \frac{2\pi kT}{m} \right)^{1/2} \exp \left[ \frac{-m(v - v_{bk})^2}{2kT} \right] \quad 2.1$$

where  $v$  is the particle velocity,  $v_{bk}$  is the bulk velocity,  $m$  is the mass of the emitter,  $k$  is the Boltzmann constant and  $T$  is the temperature. The intensity,  $Y(\lambda)d\lambda$ , is proportional to the number of particles associated with the velocity  $f(v)dv$ . Assuming a *Gaussian* expression for the normalized emission line profile in terms of Doppler shifts produces

$$\begin{aligned}
 Y(\lambda) &= \left( \frac{c^2}{\lambda_1^2} \frac{2\pi kT}{m} \right)^{1/2} \exp \left[ \frac{-m}{2kT} \left( \frac{\lambda - \lambda_1}{\lambda_1/c} \right)^2 \right] \\
 &\equiv \left( \frac{c^2}{\lambda_0^2} \frac{2\pi kT}{m} \right)^{1/2} \exp \left[ \frac{-m}{2kT} \left( \frac{\lambda - \lambda_0 - \Delta\lambda}{\lambda_0/c} \right)^2 \right]
 \end{aligned} \tag{2.2}$$

where  $\lambda_1$  is the spectral location of the shifted emission peak,  $\lambda_0$  is the spectral location of the unshifted peak,  $\Delta\lambda$  is the difference between the two and  $c$  is the speed of light. From Figure 2.1, it is apparent that the bulk *speed* corresponds to the mean *shift* of the emission line, the *temperature* of the emitter is related to the *width* of the emission line and the *density* is related to the *intensity*. The way in which drifts (ion winds), temperatures, brightnesses and background brightnesses are extracted from emission line measurements is in Section 2.1.1. Generally, the line-of-sight ion drift can be determined by detecting the Doppler shift

$$v = \frac{c(\lambda_1 - \lambda_0)}{\lambda_0} \tag{2.3}$$

In this dissertation, ionospheric temperature may be determined by detecting the FWHM (full width at half maximum) of the 7320Å source profile, which for a Doppler broadened line is

$$\sigma_{\lambda} = 2 \left\{ \frac{2kT \ln 2}{m} \right\}^{1/2} \frac{\lambda_0}{c} \quad 2.4$$

where  $k$  is Boltzmann's constant,  $c$  is the speed of light,  $m$  is the molecular weight, and  $T$  is the temperature of the emitting species.

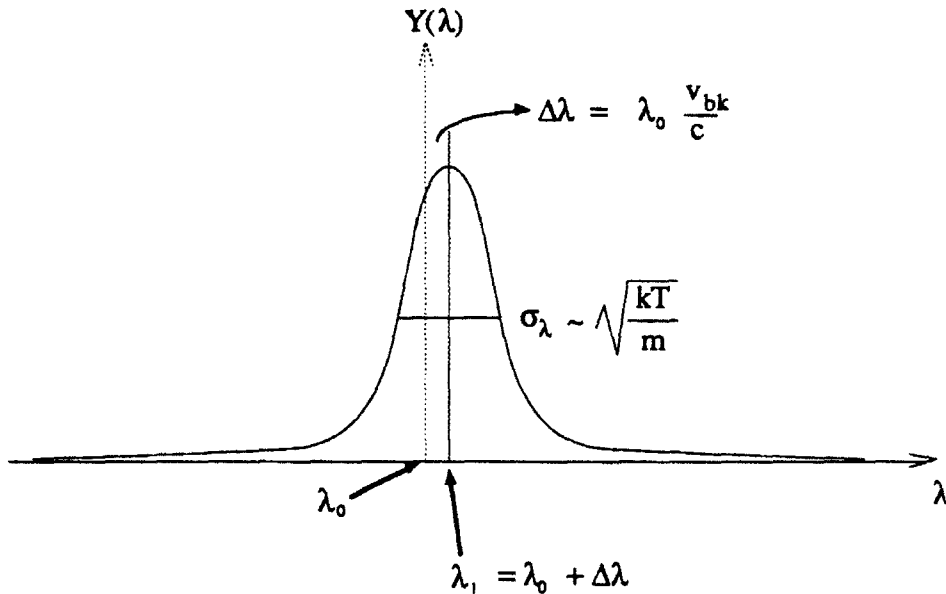


Figure 2.1 A Gaussian distribution, such as the one pictured above, describes the intensity of an emitting species that is in thermodynamic equilibrium. The net shift of the emission line characterizes the bulk velocity ( $v_{bk}$ ); the width of the emission line characterizes the temperature of the emitting species. See text for variable definitions.

The most important components of the FPIs used in this research are the *etalon* and the *IPD* (image plane detector). The etalon's objective is to modify the spectral distribution of an emission line into a radial distribution (the fringe pattern) so this spectral distribution can be measured by the IPD. The etalon is made of two silica plates separated by a certain distance (the gap spacing). These plates are coated with several reflective dielectric layers; the etalon is the primary optical component of the instrument and operates on the principle of constructive and

destructive interference of the light beams that are transmitted through it. See Figure 2.2 for details.

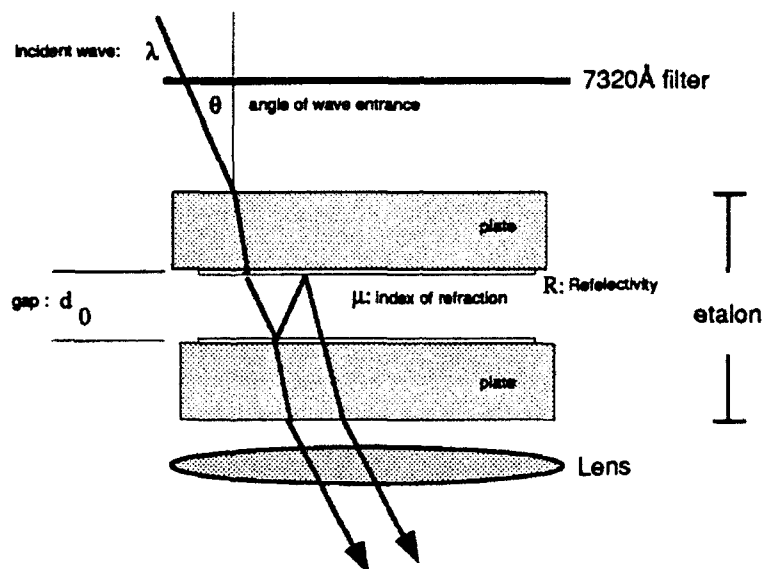


Figure 2.2 An incident wave passes through the filter which eliminates most background; the incident wave undergoes multiple reflections within the etalon and produces the broadened fringe pattern. This fringe is a set of bright, concentric rings whose angular diameter is dependent on the gap spacing. The fringe width is a function of the reflectivity of the plates. The lens focuses the fringe on the IPD; the IPD samples the entire fringe simultaneously and yields a discretely sampled, instrument broadened Doppler profile (the spectrogram). Hence, the FPI transforms frequency ( $1/\lambda$ ) into angular displacement while adding instrument broadening.

The degree of interference is determined by the phase shift of the light after reflecting between the etalon plates; this shift is given by

$$\delta = 2\pi \frac{2\mu d_0 \cos \theta}{\lambda} \quad 2.5$$

where  $\mu$  is the index of refraction of the gas in the gap ( $d_0$ ) and  $\lambda$  is the wavelength of the light entering the etalon at angle  $\theta$ . For a monochromatic incident beam, the transmitted light forms a series of concentric rings with each ring corresponding to the transmission maxima or constructive interference. In an ideal ionosphere, with a perfect FPI, the the fringe pattern formed by passing an emission line through the etalon is expressed



by the convolution of the emission profile with an etalon transmittance function; the transmittance function for this perfect or "ideal" etalon is given by the Airy function,

$$T_e(\lambda, \theta) = \frac{(1-R)^2}{1 - 2R \cos\left[2\pi \frac{2\mu d_0}{\lambda} \cos\theta\right] + R^2}$$

$$= \frac{1-R}{1+R} \left\{ 1 + 2 \sum_{n=1}^{\infty} R^n \cos\left(\frac{4\pi\mu d_0}{\lambda} n \cos\theta\right) \right\} \quad 2.6$$

This function is determined by the reflectivity ( $R$ ) of the etalon, the gap spacing, the index of refraction of the gas in the gap, the wavelength of the transmitted light ( $\lambda$ ) and the angle of incidence of the transmitted light. The fsr (free spectral range:  $\Delta\lambda_0$ ) is the distance between adjacent peaks of the Airy transmittance function and is defined as:

$$\Delta\lambda_0 = \frac{\lambda^2}{2d_0\mu} \quad 2.7$$

The finesse of the etalon,  $f=\Delta\lambda_0/\text{FWHM}$ , determines the spectral resolution of the measurements. The higher the finesse, the higher the spectral resolution. For example, in the Greenland ground-based observations, a finesse of 10-12 was desired.

The IPD is the multiple annular channel detector which simultaneously measures the intensity at 12 radial positions on the image plane. Figure 2.3 shows a spectrogram from the DE-2 FPI. Important geophysical parameters such as drifts, temperatures, surface brightnesses and continuum brightnesses can be obtained by the analysis of such a spectrogram. The number of detected counts in the  $i^{\text{th}}$  channel of a multichannel FPI over an integration time  $t$  can be written as

$$N_i = \frac{A_0 \Omega_i Q_i T_{0i} \cdot 10^6}{4\pi} \int_0^\infty T_F(\lambda) \psi(\lambda, \theta_i) Y(\lambda) d\lambda + B_i \quad 2.8$$

The terms in front of the integral represent constants of the instrument and define the sensitivity of the  $i^{\text{th}}$  channel in counts/R-sec, given as

$$C_{0i} = \frac{A_0 \Omega_i Q_i T_{0i} \cdot 10^6}{4\pi} \quad 2.9$$

where  $A_0$  is the working area of the etalon plates,  $\Omega_i$  is the field of view of the  $i^{\text{th}}$  ring detector,  $T_{0i}$  is the optical transmission of the instrument,  $Q_i$  is the efficiency of the  $i^{\text{th}}$  channel of the detector and  $10^6$  is the number of electrons generated by the detector per photon.  $T_F(\lambda)$  is the transmission function of the prefilter used to select the required line feature,  $\psi(\lambda, \theta_i)$  is the instrument function for the  $i^{\text{th}}$  channel and  $Y(\lambda)$  contains the spectral properties of the source function. The spectral distribution of light  $Y(\lambda)$  is comprised of two parts given by

$$Y(\lambda) = \frac{\Re_0 \exp\left(-\left(\frac{\lambda - \lambda_l}{\Delta\lambda_l}\right)^2\right)}{\sqrt{\pi} \Delta\lambda_T} + \left. \frac{\partial \Re}{\partial \lambda} \right|_0 \quad 2.10$$

where  $\Re_0$  is the surface brightness in Rayleighs,  $\lambda_l$  is the Doppler shifted wavelength and  $\Delta\lambda_T$  is the thermal width given by

$$\Delta\lambda_T = \left( \frac{2kT}{m} \right)^{1/2} \frac{\lambda_l}{c} \quad 2.11$$

The first term on the right of equation 2.10 is the normalized Gaussian corresponding to a thermal emission line of surface brightness  $\Re_0$  and the second term represents the continuum brightness underlying the emission line (Rayleighs/Angstrom). A complete discussion of the DE-2 IPD is found in Killeen et al., (1983); generally, it is an integrated 12

channel electric-optical device that converts the light intensity distribution of the fringe into a set of electron pulses. The output of electrons is then captured by an anode composed of 12 discrete concentric rings of equal area. Unfortunately, the ionosphere and the FPIs used in this study are not perfect. The instruments' transmission functions are broadened by several sources, usually coming from the etalon and IPD. The major broadening sources coming from the etalon are microscopic defect broadening, sagittal effect defect broadening and wedge defect broadening (Killeen et al., 1983); these defects tend to broaden the perfect Airy transmittance function. The broadening mechanisms associated with the IPD are blur spot, aperture, misalignment and quantum efficiency (Nardi, 1991). For descriptions of these broadening mechanisms, see Hernandez (1986) and Nardi (1991).

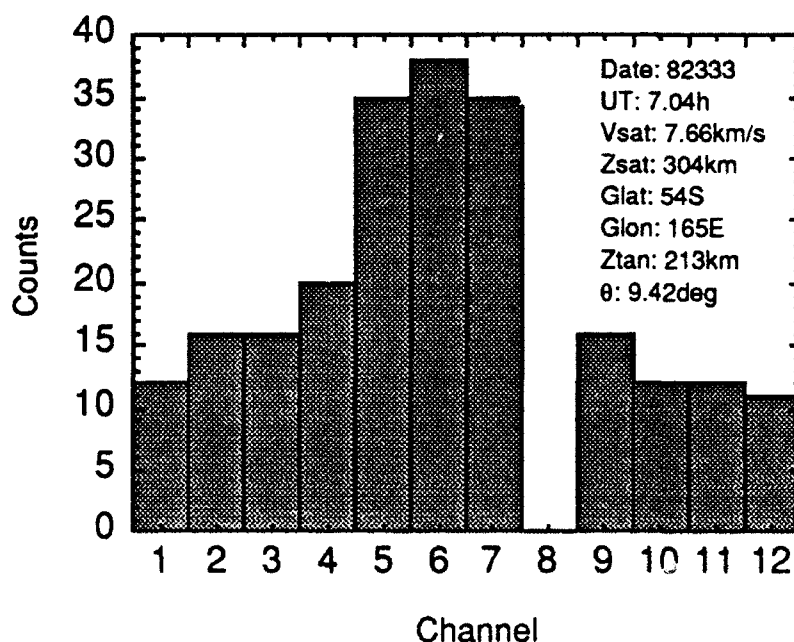


Figure 2.3 DE-2 FPI (7320Å) spectrogram for orbit 7289 (FPI mirror position: 9.42°). The spectrogram shows the instrumental counts accumulated in 0.25s. Analysis of this by standard methods produces LOS drifts, temperatures and brightnesses. Channel 8 is ignored in all 6300, 5577 and 7320Å calculations since it had a large non-stochastic noise component.

Instrument transfer functions ( $\Psi_i$ ) can be determined analytically or experimentally. For the two FPIs in this work, the experimental technique was used. The instrument transfer functions represent the sensitivity of each of the detector's channels, as a function of wavelength. The shape of this function for each channel can be determined by observing the channel response to an emission line profile as the etalon gap pressure is varied. This produces a variation in the index of refraction of the gas between the etalon plates, thus changing the optical path within the etalon. A frequency stabilized He-Ne laser at 6328Å is usually used as the calibrating laser source. The pre-DE 2 launch experimental setup of the pressure scan calibration is shown in Nardi (1991). The ground-based FPI "pscan" calibration for this work is done in a similar fashion, except that a Xe laser (7321.45Å) is used instead of the He-Ne. The laser is diffused by placing it within a spherical plastic globe at the entrance to the FPI. The response of each channel is recorded as the pressure between the plates is slowly increased. Since the channel response ( $N_i$ ) and emission source ( $Y(\lambda)$ ) are known, the instrument transfer functions can be determined from the following relation

$$N_i = \int Y(\lambda) \Psi_i(\lambda) d\lambda \quad 2.12$$

These instrument transfer functions are fit to a Fourier series and are expressed as

$$\Psi_i(\lambda) = a_{0i} + \sum_{n=1}^{\infty} \left[ a_{ni} \cos \frac{2\pi n}{\Delta\lambda_0} (\lambda - \lambda_r + \phi_i) + b_{ni} \sin \frac{2\pi n}{\Delta\lambda_0} (\lambda - \lambda_r + \phi_i) \right] \quad 2.13$$

where  $\phi_i$  gives the offset in phase between channel 1 and the  $i^{\text{th}}$  channel,  $\lambda_r$  is the arbitrary reference wavelength and the coefficients  $a_{ni}$  and  $b_{ni}$

contain all the necessary information to completely describe the instrument transfer functions, including sensitivity differences and all etalon and optical defects in the system (Killeen and Hays, 1984). Figure 2.4 represents the instrument transfer functions as a function of etalon pressure for the Søndre Strømfjord FPI (7320Å).

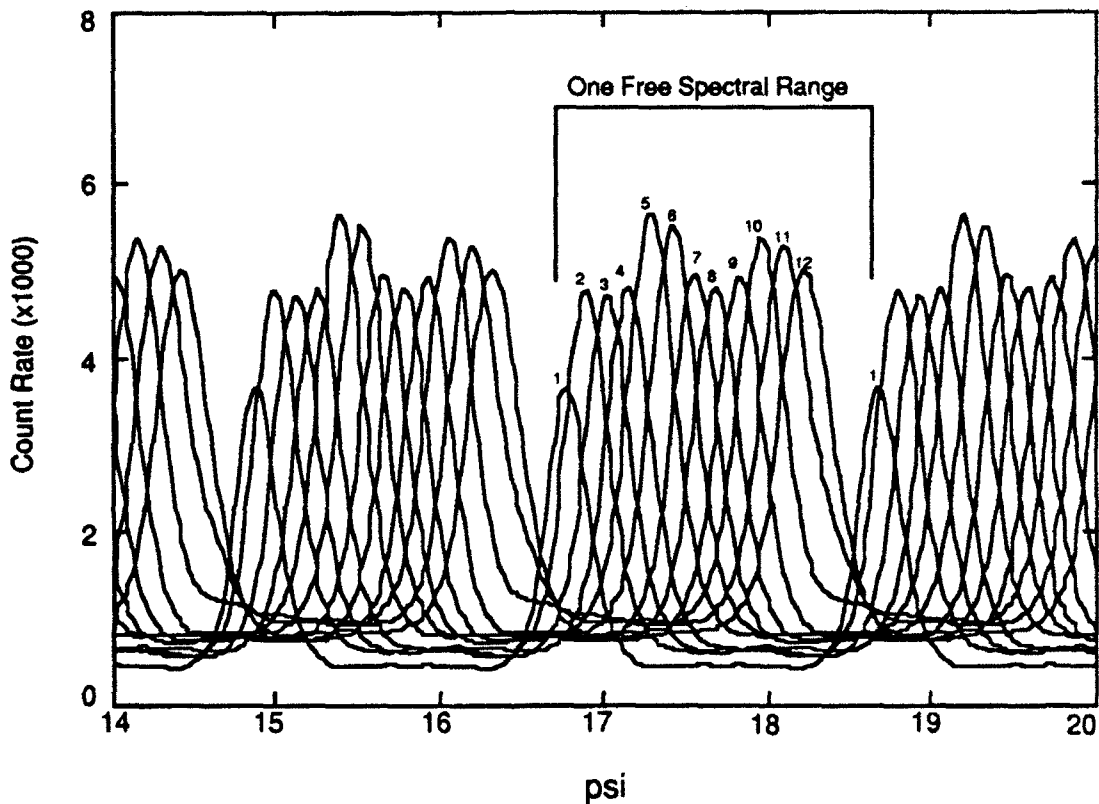


Figure 2.4 Instrument transfer functions determined for the 12 channel FPI (7320Å) at Søndre Strømfjord, Greenland on 3 Sep 91. The free spectral range is the distance between successive channel one peaks. The integrated product of these instrument transfer functions and the observed 7320Å emission line produce the spectrogram - from this, LOS drifts, temperatures and brightnesses are determined. Note that as psi increases, frequency increases and wavelength decreases.

The instrument transfer functions can therefore be thought of as the transmittance functions for each of the channels and the channel response,  $N_i$ , as the integrated product of its own transfer function and the emission line (or laser source) being measured. Armed with this knowledge, one

knows how the Doppler profile has been broadened by the instrument and has fully characterized it. Figure 2.5 illustrates the production of a spectrogram by the convolution of the source function (the 7320Å emission line) and the instrument transfer functions for the FPI being used.

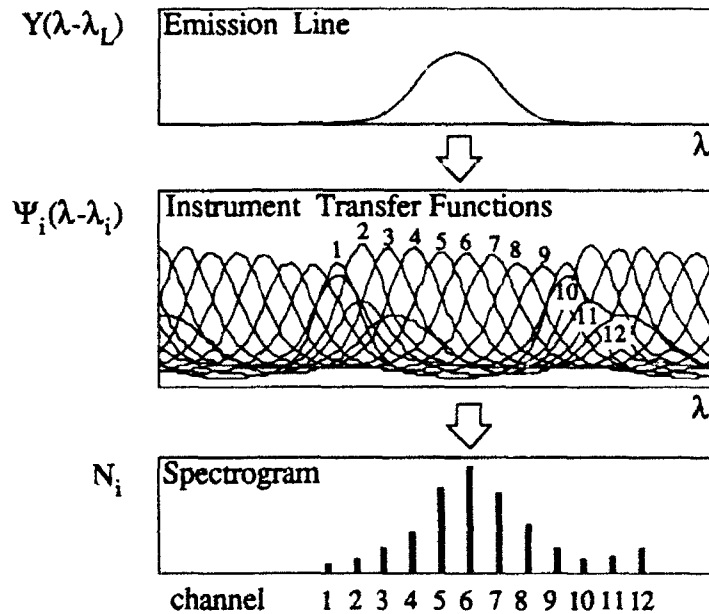


Figure 2.5 Schematic showing the physical interpretation of the instrument transfer functions. The channel response,  $N_i = \int Y(\lambda) \Psi_i(\lambda) d\lambda$ , is produced by the portion of the emission line,  $Y(\lambda)$ , that is allowed to pass through the etalon and onto the detector. Analysis of  $N_i$  produces LOS ion drifts, temperatures, brightnesses and continuum brightnesses, the topic of section 2.1.2. Figure adapted from Nardi (1991).

### 2.1.2 Recovery of Line of Sight Drifts, Temperatures and Brightnesses from the Spectrogram

This section demonstrates the recovery of LOS parameters from the spectrogram by performing a least squares fit. The standard analysis procedure (SAP) for the DE-2 FPI Doppler profiles is discussed in Killeen and Hays (1984) and Nardi (1991). The Søndre Strømfjord SAP is similar. The following discussion is a review.

All optical instruments transmit light with distortion. This distortion causes broadening of the emission line. Instrument broadening must be mathematically characterized (Chapter 2.1.1) by an instrument transfer function before geophysical information can be successfully extracted from the measurements. Once characterized, an FPI spectrogram can be produced by convoluting a Gaussian source function with the measured instrument transfer function (chosen by a Fourier series at each wavelength). Analysis of the spectrogram can produce drifts, temperatures, brightnesses and background brightnesses. The spectrogram (a discretely sampled, instrument broadened Doppler profile) is the basic unit of information from which geophysical information can be extracted. Once one has extracted the effects of instrument broadening by deconvolving the instrument function, one is left with a one-dimensional Doppler profile integrated along the LOS. Due to the direct correspondence between Doppler shifts/drifts and widths/temperatures of the emitter, knowledge of this Doppler profile is proportional to knowledge of the one-dimensional velocity distribution and temperature.

The numerical expression for the instrument response or spectrogram ( $N_i$ ) can be obtained by convolving the Fourier series (Equation 2.13) with the thermal emission line profile of Equation 2.2. Therefore, substituting equations 2.13 and 2.2 into 2.12 and solving eventually produces

$$N_i = C_{0i} T_F \mathcal{R}_{0i} \sum_{n=0}^{15} \left\{ \begin{array}{l} a_{ni} \exp[-n^2 G^2(T)] \cos n(X + \frac{2\pi M_0 v}{c}) \\ + b_{ni} \exp[-n^2 G^2(T)] \sin n(X + \frac{2\pi M_0 v}{c}) \end{array} \right\} + a_{0i} B_{BG} \cdot B_i \quad 2.14$$

where

$$G(T) = \frac{\pi}{c} \sqrt{\frac{2kT}{m}} \frac{\lambda_1}{\Delta\lambda_o} = \frac{\pi\Delta\lambda_T}{\Delta\lambda_o}$$

$$\Delta\lambda_o = \frac{\lambda_i^2}{2\mu d_o}$$

$$X = \frac{2\pi(\lambda_o - \lambda_i + \phi_i)}{\Delta\lambda_o}$$

$$B_{BG} = C_{oi} \overline{\Delta\lambda_F} \frac{\partial R}{\partial \lambda} \left( \frac{1-R}{1+R} \right)$$

$M_0$  is the integer part of the order of interference,  $\Delta\lambda_f$  is the filter integral width in Å and  $B_i$  is the background count due to the detector's thermionic emission (known as the Richardson Effect). Drifts, temperatures, brightnesses and background brightnesses may be calculated from the measured spectrogram using a non-linear least squares fitting technique. But with millions of spectrograms coming from the DE 2, Killeen and Hays (1984) conserved limited ground data system resources by linearizing the problem; they expanded Equation 2.14 about empirically determined approximations for the drift and temperature and used only first order terms in the expansion. Hence, linearly expanding  $N_i$  about  $T_0$  and  $v_0$  produces:

$$N_i(v_o + v, T_o + \Delta T) - B_i = C_{\alpha} T_{F_o} \mathcal{R}_o \left\{ \begin{array}{l} F_i^{(o)}(v_o, T_o) \\ + v F_i^{(1)}(v_o, T_o) \\ + \Delta T F_i^{(2)}(v_o, T_o) \end{array} \right\} + B_{BG} a_{\alpha} \quad 2.15$$

where



$$F_i^{(0)} = \sum_{n=0}^{15} \left\{ a_{ni} \exp[-n^2 G^2(T)] \cos n(X + \frac{2\pi M_o v}{c}) \right. \\ \left. + b_{ni} \exp[-n^2 G^2(T)] \sin n(X + \frac{2\pi M_o v}{c}) \right\}$$

$$F_i^{(1)} = \frac{\partial F_i^{(0)}}{\partial v} \\ = \frac{-2\pi M_o}{c} \sum_{n=0}^{15} \left\{ n a_{ni} \exp[-n^2 G^2(T_o)] \sin n(X + 2\pi M_o v_o) \right. \\ \left. - n b_{ni} \exp[-n^2 G^2(T_o)] \cos n(X + 2\pi M_o v_o) \right\}$$

$$F_i^{(2)} = \frac{\partial F_i^{(0)}}{\partial T} \\ = -\frac{G^2(T_o)}{T_o} \sum_{n=0}^{15} \left\{ n^2 a_{ni} \exp[-n^2 G^2(T_o)] \cos n(X + 2\pi M_o v_o) \right. \\ \left. + n^2 b_{ni} \exp[-n^2 G^2(T_o)] \sin n(X + 2\pi M_o v_o) \right\}$$

Equation 2.15 can be written in matrix form as:

$$\begin{bmatrix} N'_1 - B_1 \\ N'_2 - B_2 \\ \vdots \\ N'_{12} - B_{12} \end{bmatrix} = \begin{bmatrix} F_1^{(0)} & vF_1^{(1)} & TF_1^{(2)} & a_{01} \\ F_2^{(0)} & vF_2^{(1)} & TF_2^{(2)} & a_{01} \\ \vdots & \vdots & \vdots & \vdots \\ F_{12}^{(0)} & vF_{12}^{(1)} & TF_{12}^{(2)} & a_{01} \end{bmatrix} \begin{bmatrix} C_{01} T_{F0} \mathcal{R}_{0t} \\ C_{01} T_{F0} \mathcal{R}_{0tv} \\ C_{01} T_{F0} \mathcal{R}_{0tT} \\ B_{BG} \end{bmatrix} \quad 2.16$$

Assuming

$$N'_i = N_i - B_i \quad 2.17a$$

$$\chi_1 = C_{01} T_{F0} \mathcal{R}_{0t} \quad 2.17b$$

$$\chi_2 = v \cdot \chi_1 \quad 2.17c$$

$$\chi_3 = T \cdot \chi_1 \quad 2.17d$$

$$\chi_4 = B_{BG} \quad 2.17e$$

$$A_{ik} = F_i^{(k-1)}(v_o, T_o) \quad \text{for } 1 \leq k \leq 3 \quad 2.17f$$

$$A_{ik} = a_{0i} \quad \text{for } k = 4 \quad 2.17g$$

then Equation 2.16 becomes

$$N' = A \cdot \chi \quad 2.18$$

A *linear* least squares solution to this is

$$\chi = (A^T A)^{-1} A^T \cdot N' \quad 2.19$$

where  $T$  indicates the matrix transpose,  $\chi$  is the vector containing the unknowns and  $N'$  is the vector containing the counts  $N_i'$ . LOS parameters are then obtained from the equations 2.17(b-e). Because Equation 2.15 is a linear expansion,  $F_i^{(k)}(v_0, T_0)$  must be evaluated at  $v_0$  and  $T_0$  sufficiently close to the solutions,  $v$  and  $T$ . This was accomplished in the standard analysis software by storing a comprehensive set of pre-calculated matrices; the best-fit matrix for an individual spectrogram was automatically selected by an algorithm that provided approximate values for the initial temperatures and drifts (Hays et al., 1981). Iterating five times produces rapidly converging solutions (Killeen and Hays, 1984). If one defines an analysis matrix  $C$  as

$$C = (A^T A)^{-1} A^T \quad 2.20$$

one gets

$$\chi = C N' \quad 2.21$$

Statistical errors on the unknowns ( $\chi_k$ ,  $k=1,4$ ) can be determined if Poisson noise is assumed:

$$\sqrt{\delta x_k^2} = \sqrt{\sum_{i=1}^{Nch} (C_{ki})^2 N_i} \quad 2.22$$

where  $\sqrt{\delta x_k^2}$  is the standard deviation of the measurement  $x_k$ .

Note that a uniform emission must exist within the field of view in order for this analysis to work. The 7320Å emission, peaking at around 300km, is about 400 km thick (its volume emission rate profile extends from ~180 - 550km). The emission will illuminate the entire FPI field of view. The 6300Å emission has similar traits. However, the 5577Å emission, with a peak emission rate around 225 km, and another at 100km did not illuminate the FPI field of view. I shall now introduce the two FPIs used in this work.

### 2.1.3 DE-2 FPI

Meridional ion drift, temperature and brightness profiles were derived from DE-2 FPI (7320Å) measurements. The polar orbiting DE 2 sampled properties of the thermosphere/ionosphere at F-Region altitudes. A minor task was to remotely sense the 7320Å doublet emission (*not* the 7330Å doublet) with an FPI. This FPI had a twelve channel image plane detector (IPD) that had a quantum efficiency of ~5% at ~7320Å. At ~7320Å and 283K (the instrumental operating temperature), the O<sup>+</sup> filter had a peak transmission of 47%, a 10Å FWHM (full width, half maximum) bandpass, and an etalon gap-spacing of 1.26 cm. The working diameter of the fixed etalon plates was 3.3cm with a reflectivity (at 7320Å) of 73.9%. The instrument was oriented 15° off the RAM direction towards the Earth's limb so it could monitor atmospheric emissions ahead of (~500-1700km) and below (~25-225km) the spacecraft, depending on the mirror position.

The FPI viewed the atmospheric limb cyclically at various tangent points, using the onboard scanning mirror mechanism. Fringe patterns of the ionospheric 7320Å emission were recorded every 0.22s with an IPD dwell time between measurements of ~0.03s. The FPI performed a high resolution spectral analysis by measuring the geometry of these interference fringe patterns that were imaged onto the IPD; this analysis allowed the Doppler line profile of the  $O^+(^2P)$  emitting species to be characterized. The individual Doppler spectrograms obtained in this manner enable meridional ion drifts, temperatures, brightnesses and continuum brightnesses to be determined using the Killeen and Hays (1984) method reviewed in Chapter 2.1.2. The DE-2 FPI was designed to measure meridional ion drifts and temperatures to within 5 m/s and 10K respectively. Actual accuracies for individual measurements were dependent on the specific surface brightness of the emission and the integration time for the measurement.

The FPI consisted of three primary sections - the telescope, mirror and interferometer section. The telescope section contained a system of baffles (to preclude dayside sunlight from contaminating FPI observations) and the main objective lens. Light within this section passed through the lens which then focussed the rays at the sky stop (the mirror section entrance). This stop passed the image of the observation into the mirror section which was reflected by the scan mirror at the field stop. This field stop allowed about a  $2^\circ$  sector of the image to pass into the interferometer section. The emission that passed into this section was collimated (by one of the eight DE-2 filters in the filter wheel) and passed through the etalon where the resulting fringe was focussed on the IPD. Geophysical information is extracted from the channel responses (spectrogram).

Consider Figure 2.6. The free spectral range for the DE-2 FPI (7320Å) is:

$$\text{fsr} = \frac{\lambda^2}{2\mu d} = \frac{(7320\text{\AA})^2}{2 \times 1.26\text{cm}} \cong 0.21\text{\AA} \quad 2.23$$

One free spectral range shift is given by:

$$v = c \frac{(\lambda_1 - \lambda_0)}{\lambda_0} = c \frac{\text{fsr}}{\lambda_0} = 3 \times 10^5 \text{ km/s} \left( \frac{0.21\text{\AA}}{7320\text{\AA}} \right) = 8.5 \text{ km/s} \quad 2.24$$

which is about equal to the Doppler shift generated by the satellite's motion (~8 km/s). There are 11.59 channels per free spectral range at 7320Å (Killeen et al., 1983). The Doppler shift of one channel is therefore equivalent to a wavelength shift of ~0.018Å (0.21Å/11.59 channels per fsr); this directly corresponds to an ion drift shift of ~750m/s per channel (8.5km/s divided by 11.59 channels per fsr). In Figure 2.6, the dark spectrogram was observed at 28886.996 (s) UT during orbit 1387 at a tangent point latitude of -86.57°, tangent point longitude of 176.05° and tangent point altitude of 267.65km, corresponding to a scanning FPI mirror position of 9.42°. The peak 7320Å emission fell on channel 6.17. The shaded spectrogram was observed at the next 9.42° mirror position in the scanning cycle which was ~90s later (UT: 28976.996s) at a tangent point latitude of -87.42°, tangent point longitude of 355.75° and tangent point altitude of 283.51km. The peak 7320Å emission was observed on channel 5.88. Hence, the Doppler shift between spectrogram peaks is ~ 0.029 channels or 0.00522Å. Using Equation 2.13, one can determine an approximate ion drift of ~214m/s between the two measurements.

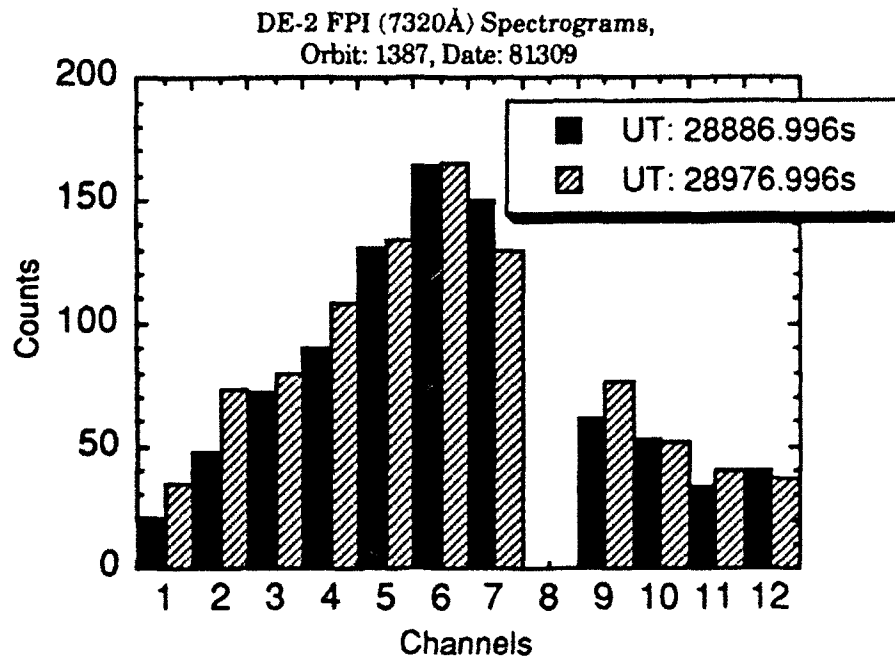


Figure 2.6 Sample DE-2 FPI (7320Å) spectrogram for the conditions listed on the plot. Brightnesses were ~350R for both observations. See text for discussion.

Note that the DE-2 FPI etalon gap spacing allowed the individual lines of the doublet emission to almost exactly overlap on the image plane. This poses problems in trying to extract meaningful temperatures since the temperature is related to the bandwidth of the spectrogram. With the lines overlapping, the Doppler profile becomes too wide, possibly leading to spurious temperature measurements. Chapter 4.3.1.2 of this dissertation deals with extracting ion temperatures from DE-2 FPI (7320Å) spectrograms. Ion drifts, related to the shift of the Doppler profiles, are not affected by this wide spectrogram. Assuming that the only known published value (Meriwether et al., 1974) for the doublet separation is correct ( $\sim 0.836\text{\AA}$ ), one can see that the overlap is nearly complete on the IPD by the following calculation. Dividing the doublet separation by the wavelength interval for each channel ( $0.836\text{\AA}/0.018\text{\AA}$  per channel) produces

~46.444 channels. Dividing this by the number of channels per fsr (11.59) produces ~ 4.007. Since the number of orders (4 in this case) is an unknown quantity with FPI spectra, the weaker component of the doublet is mapped almost exactly (0.007 orders or 0.081 channels) onto the same channel position as the stronger component. Hence, the DE-2 FPI measured both components of the 7320Å doublet, although the measurements were heavily weighted in favor of the  $O^+(2P_{3/2} \rightarrow 2D_{5/2})$  component at 7319.9Å since it is 3.8 times more intense than the  $O^+(2P_{1/2} \rightarrow 2D_{5/2})$  component at 7319.1Å. Table 2.1 lists the DE-2 FPI operating parameters. Figure 2.7 is an optical schematic of the FPI.

$\lambda(\text{\AA})$	Species	#/fsr	spectral range/ channel	Sensitivity (#/R-s-ch)
5200	N( $2D$ )	8.23	.0482	.215
5577	O( $1S$ )	8.83	.0449	.201
5896	Na( $2P$ )	9.34	.0425	.142
6300	O( $1D$ )	10.0	.0397	.098
7320	O $^+(2P)$	11.59	.0327	.050
7679	O $_2(^1\Sigma)A$	12.14	.0327	.035

Table 2.1 DE-2 FPI operating parameters (after Killeen et al., 1983). The last column (Sensitivity) has units of counts per Rayleigh per second per channel; the third column (#/fsr) indicates the number of channels per free spectral range.

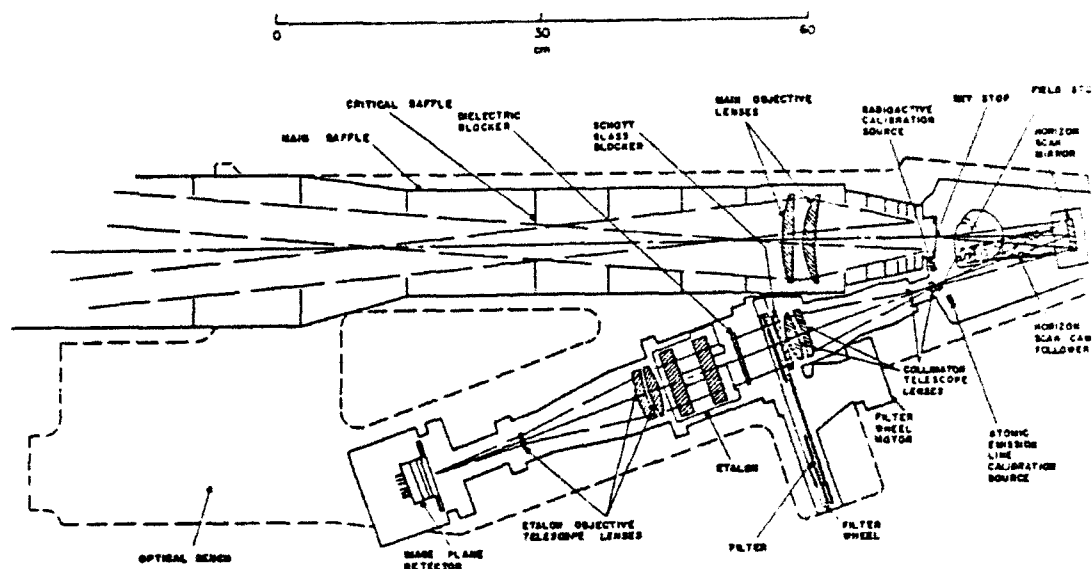


Figure 2.7 Optical schematic for the DE-2 FPI (after Killeen et al., 1983).

The DE-2 FPI had 24 scan mirror positions, 16 of which corresponded to science viewing positions (see Figure 2.7) and two of which corresponded to calibration positions which enabled the instrument to view one of two atomic line discharge lamps or a phosphor calibration source (Hays et al., 1981). The science view angles corresponded to tangent heights about 25 - 225 km ( $5 - 15^\circ$  below the satellite) and 500 - 1700 km ahead of the satellite. The minimum dwell time for each step was 0.5s and two complete 8 step horizon scans (one scanning up and one scanning down) were



accomplished for each rotation of the cam. The scan mirror could be stepped once per  $(2^n \cdot 0.25) + 0.25 \text{ sec}$  ( $n=0-7$ ). The volume of gas at the lowest altitude point along the view path where the LOS of the instrument is tangent to the Earth's surface is the *tangent point*; the *tangent height* refers to the altitude of this point. Emitting ions will be present along the entire LOS, but the dominant  $7320\text{\AA}$  contribution will normally come from a localized region around the tangent point since the contribution function (emission intensity per unit altitude) is a sharply peaked function of altitude. The reason for this is that the geometric path length of the LOS is greatest through a layer centered at the tangent point. A limitation with FPI measurements is the altitude resolution. If an aurora occurs well before the expected tangent point in the instrument's field of view, then an incorrect tangent height will be assigned to the placement of that observation since the peak emission will appear to the FPI to be coming from the aurora.

The DE-2 FPI had a field-of-view of  $\sim 2.74^\circ$  at  $7320\text{\AA}$ , defined by a doublet objective lens and a field stop (Hays et al., 1981). The radius of the roughly conical FPI field of view at the tangent point to the Earth's limb along the line-of-sight was in the 12 - 40 km range, depending on the zenith angle of the view direction. A filter wheel containing 8 spectral filters was used to select the spectral region to be sampled. The filter wheel could operate in four modes: fixed, cycling, sequencing or impulsive. In the cycling mode, the filter was stepped at once per  $2^n \cdot 0.5 \text{ sec}$  ( $n=0-7$ ) in the fast mode or once per  $2^n \cdot 0.5 \text{ sec}$  ( $n=3-7$ ) in the slow mode. The sequencing mode allowed the filter wheel to alternate between any two positions; the impulsive mode could be used if logic were lost. As discussed earlier, the tangent height varies in altitude and latitude; for each scan of 16 mirror

positions, a complete mirror cycle will cover a range of altitudes for many degrees of latitude. After a number of cycles, an altitude profile for a specific latitude can be obtained. FPI spectrograms were determined every 0.22s, and co-added to obtain a statistical uncertainty in the drift measurements of about 25m/s. Integration time for determining a meridional drift with an error of 25 m/s was 8s during the day and twilight and 32s during night observations. For a spacecraft velocity of 8km/s, the spatial resolution of the DE-2 FPI was between 64 - 272 km. Neutrals may not change much in the upper thermosphere in this distance, but ions can change dramatically in 272 km. Hence, the effect of this spatial averaging is to filter out some of the ion spatial resolution. Most models use a grid of  $5 \times 5^\circ$  (about 550 x 550 km); therefore, much more averaging is done in a model than in these DE-2 observations.

The standard analysis procedures of Killeen and Hays (1984) were developed to handle the millions of spectrograms obtained throughout the mission. Since the instrument transfer functions were calculated before launch, the ion drifts can be determined. These drifts have imbedded within them the satellite velocity vector ( $\sim 8$  km/s) and an error induced by temperature changes which causes the etalon gap to vary. The magnitude of the velocity shift caused by the satellite is dependent on the eccentricity of the orbit and the angle of the mirror position off the satellite's axis. An algorithm within the standard analysis procedure accounts for this satellite velocity correction ( $\sim -1$ km/s for the 7320Å emission) and the temperature correction ( $\sim +170$ m/s) and removes them from the measurement.

A zero reference drift is then determined by taking many equatorial passes and averaging the drifts about the equator, assuming they are zero;

this is a valid assumption since observations and models show ion drifts to approach zero near the equator. The actual meridional drifts can then be calculated from the FPI measurements by subtracting or adding the zero drift reference to the relative drifts determined from the analysis. See Chapter 4.1.4 for a thorough discussion of this 7320Å additive constant.

Of the 8000+ orbits that reside in the DE-2 database, ~1000 contain 7320Å data. Many are of poor quality for various reasons (a small 7320Å signal (brightness) due to a large solar zenith angle, for example). About 60 "choice" orbits do exist, and many will be analyzed in Chapter 4. There are other limitations to the DE-2 7320Å database, in addition to the fact that it looked at 6300Å most of the time. First, the 7320Å line is very weak (usually less than 1000R) compared to 6300Å and 5577Å, both of which frequently had signals greater than 5000R. Even though the 7320Å emission is ubiquitous in daylight, the DE-2 FPI mirrors frequently scanned too low in the atmosphere where  $O^+(2P)$  was quenched (below ~180km), resulting in no 7320Å measurements. Plus, the DE 2 was in orbit for a mere 18 months; thus it sampled during a solar maximum period (August 1981 - February 1983). Also, the DE 2 performed a yaw maneuver about its axis every 6 months for thermal control; hence, the FPI could only sense the thermosphere/ionosphere system 6 months per year. So, DE-2 FPI measurements were made from August 1981 - February 1982 and August 1982 - February 1983; this means drift measurements are basically from the solar maximum period and the winter solstice.

#### 2.1.4 Søndre Strømfjord FPI

Ground-based FPI observations have been used to determine the dynamic and energetic state of the thermosphere by measuring the red and

green lines routinely since 1984 at Thule and Søndre Strømfjord, Greenland. Hence, data have now been analyzed to obtain a record of the neutral wind of the Northern Hemisphere high-latitude thermosphere. The data cover nearly half a solar cycle. The system in Thule is similar to that in Søndre Strømfjord, Calgary and Arequipa, described in detail by Meriwether et al. (1983). The FPIs at Thule and Søndre Strømfjord use a 12 channel IPD, 10cm diameter etalon with a 1.116 cm gap, and a six filter interferometer that contains the necessary optics to view the thermosphere and ionosphere at various tangent heights. The instrument has a spectral resolution of  $0.01\text{\AA}$  with an instrumental drift less than  $0.0002\text{\AA}/\text{h}$  (or  $\sim 10\text{m/s}$ ). The  $7320\text{\AA}$  filter used in the arctic campaign has a bandpass of  $3.5\text{\AA}$  (thereby isolating the  $7320\text{\AA}$  emission from OH contamination) with a maximum transmission at  $7320.1\text{\AA}$  and peak transmission of 59%; the peak of the measured  $7320\text{\AA}$  profile is on channel 5 of the IPD at an etalon pressure of  $\sim 15.3$  psi.

Using the method presented before, the fsr at  $7320\text{\AA}$  for this FPI is  $\sim 0.24\text{\AA}$ . One complete shift in free spectral range is therefore equivalent to  $9.8$  km/s. From Figure 2.4, one sees there are 13 channels per free spectral range at  $7320\text{\AA}$  for this FPI. The construction of FPIs can be modified slightly so different studies can be undertaken. The DE-2 FPI's design enabled the  $7320\text{\AA}$  doublet components to nearly exactly overlap on the IPD. In the Søndre Strømfjord case, the FPI's design separated the doublet components for possible future analysis. Since there are 13 channels per free spectral range, the Doppler shift of one channel is therefore  $\sim 0.018\text{\AA}$ , which corresponds to an ion drift shift of  $\sim 750\text{m/s}$ ; these values are similar to those of the DE-2 FPI.

If one assumes the only reported value of the 7320Å doublet separation to be valid ( $\sim 0.836\text{\AA}$  by Meriwether et al., 1974), and if one knows that the fifth channel on this FPI is the most sensitive, then one can theoretically determine the channel on which the weaker component of the 7320Å doublet should fall. Since one channel is  $\sim 0.018\text{\AA}$  wide and the doublet separation is  $\sim 0.836\text{\AA}$ , then the weaker component should appear  $\sim 46.444$  orders away from channel 5. Since the integer number of orders in an FPI is unknown, the weaker component of the 7320Å doublet should appear 0.444 orders or  $\sim 6$  channels ( $0.444 \times 13$  channels per fsr  $\sim 5.8$ ) away from channel 5. Since the weaker component of the 7320Å doublet is known to be at a shorter wavelength (Smith et al., 1982) and since wavelength decreases as one moves to higher channels on the FPI, one notes that the weaker component of this doublet should appear at  $\sim$  channel 11. Thus, in contrast with the DE-2 FPI, the Søndre Strømfjord FPI *separated* the two components of the doublet on the image plane detector by  $\sim 6$  channels.

Figure 2.8 is a sample Søndre Strømfjord spectrogram showing an enhancement near channel 11. No enhancement was ever noted near channel 1. Three hundred forty spectrograms were observed during the September 1991 Greenland campaign. Very few (two) show the proper intensity ratio at channel 11 (3.8:1); when all spectrograms are averaged together, no enhancement is found near channel 11. This channel 11 enhancement may be due to auroral contamination, the appearance of the weaker 7320Å doublet component on the short wavelength side of the stronger 7320Å component or other factors (leakage from neighboring channels, instrumental design flaws etc.). Longer data campaigns at Søndre Strømfjord are necessary before this point is resolved (see Chapter 5 for more information on this topic).

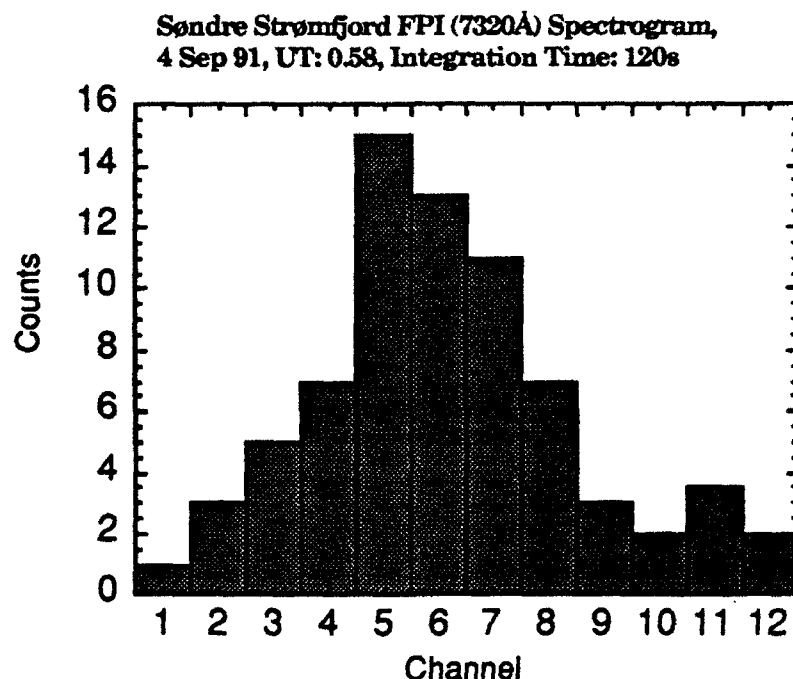


Figure 2.8 Sample Søndre Strømfjord FPI (7320Å) spectrogram taken for the conditions listed in the figure. Peak sensitivity for this FPI is on channel 5, where the stronger line in the doublet is observed. The weaker line of the doublet *may* be seen ~channel 11. The intensity ratios of these two lines are ~3.78:1 in this figure.

Presently, the FPIs at Thule and Søndre Strømfjord operate in a cyclic mode between 5577 and 6300Å in the zenith and the four geographic cardinal directions. There is also a calibration mirror position where a neon lamp is sampled once every cycle to record the behavior of instrument drift through the night. A 720s dark count is also recorded each cycle to account for background counts induced by electronic noise. Each patrol takes about 20 minutes to complete. The instrument function of the FPI is determined regularly by performing a pressure scan with a frequency stabilized He-Ne laser. This accounts for the broadening functions caused by the instrument and allows the source profile to be determined from the measured profile. The wind and temperature analysis is similar to that

described in the DE-2 standard analysis package. For these ground-based FPIs, the analysis is performed on every fringe retrieved during the night. Once this is complete, the ion drifts must be modified further to account for instrument drift during the night. The drift is removed from the derived ion drift by fitting a spline function through the calibration values for the entire night and subtracting off the calibration ion drift velocity corresponding to the time of the individual measurement. A reference wavelength of channel position corresponding to zero velocity is obtained empirically and depends on the assumption that over the period of a night the average of the derived vertical velocities is zero. By taking the average of the zenith ion drifts over the night, a reference for zero velocity is obtained and used to determine the actual drift velocities of the measurements made in the four cardinal directions. For results of Thule and Søndre Strømfjord ground-based measurements of ionospheric dynamics and energetics of the high latitude region, refer to Chapter 5. Figure 2.9 is a schematic of the Søndre Strømfjord FPI.

## **2.2 Søndre Strømfjord Incoherent Scatter Radar**

Co-Located with Michigan's FPI at  $66.59^{\circ}\text{N}$ ,  $50.95^{\circ}\text{W}$ , this incoherent scatter radar (ISR) site has a transmitting frequency of 1290MHz (23cm) and is fully steerable, allowing for a variety of operating modes. A number of pulse schemes can also be used; in this study, the long pulse (320 $\mu\text{s}$ ) scheme was used. The long pulse scheme is best suited for F-Region and topside plasma measurements because it provides the best signal to noise ratio. During my data campaigns, data were recorded with two different antenna modes. One mode was up-B (up the magnetic field line) for four

minutes and at two other positions for two minutes each; the other mode was dwelling up-B indefinitely. The data were integrated in time for as long as the antenna dwelled at a position in the three position mode or for 5 minutes if the antenna were in the up-B mode. The resulting range resolution, with a radar pulse length of 48km, was ~42km in the 200-400km zone of the ionosphere.

Plasma properties can be determined by examination of the backscattered radar signal. The backscattered power spread over a range of frequencies is caused by Doppler shifting of the radar wave as it is scattered by waves in the plasma. This return is the power spectrum. Analysis of this spectrum can directly yield electron density, line-of-sight ion velocity, electron temperature, ion temperature, ion-neutral collision frequency and ion composition. Many other geophysical parameters of interest can then be derived from these. ISR is one of the most powerful observational techniques used to remotely sense the F-Region ionosphere. An excellent review of the Søndre Strømfjord ISR is Wickwar et al. (1984). One drawback of ISR is that it is spatially limited, while the spaceborne DE-2 FPI is not. Other current ISR locations are in Table 2.2. Parameters that can be derived from ISR measurements are: vector ion velocity, meridional neutral wind, exospheric temperature, atomic oxygen density, Hall conductivity, Joule heating, optical emissions, electric field, vector neutral wind, neutral temperature, Pedersen conductivity, Birkeland current, ion-electron production rate and total neutral density.

ISR measurements from 3 - 10 Sep 91 will be used to verify co-located ground-based FPI (7320Å) drift and temperature measurements taken simultaneously in Chapter 5. While conditions for radar measurements and optical observations are often mutually exclusive, some good results



were obtained from this campaign. Once the final campaign was over and I was doing the analysis, I realized that the FPI measurements should have had the same integration times as the ISR measurements for better one-to-one comparisons. However, my main goal was to observe the 7320Å emission with an FPI, and therefore I used whatever integration time was necessary to achieve this.

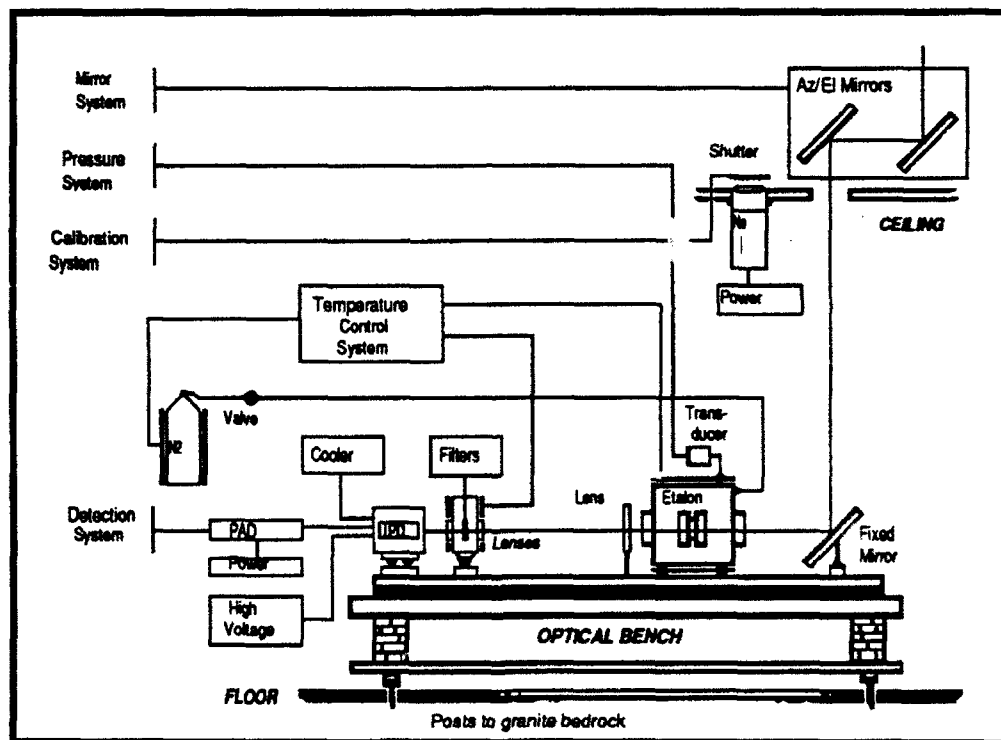


Figure 2.9 Schematic of the Søndre Strømfjord FPI system. Observations of ionospheric dynamics and energetics taken from this system are presented in Chapter 5.

ISR Site	Geographic Position
Arecibo	18N, 67W
Adelaide	35S, 140E
Fritz Peak	40N, 106W
Kiruna	67N, 21E
Kwajelein Atoll	9N, 168E
Jicamarca	16S, 72W
Laurel Ridge	40N, 79W
Millstone Hill	43N, 72W
St. -Santin	45N, 20E

Table 2.2 Some ISR sites and locations.

### 2.3 The DE-2 Retarding Potential Analyzer (RPA)

The RPA on the DE 2 provided data on ion composition, ion temperature, ion concentration and meridional ion bulk velocity (Hanson et al., 1981). Therefore, in conjunction with the onboard ion drift meter, the complete bulk ion velocity was measured. This is very important since ion motion can affect ion temperature and ion composition at high latitudes. The RPA's accuracy for meridional ion drift measurements was ~10%, while its accuracy for ion temperature and ion concentration measurements was ~ 5%. Figure 2.10 is a schematic cross section of the RPA sensor.

The RPA uses a planar retarding potential analyzer sensor that is oriented with its front normal to the vehicle velocity vector. Ions entering

the aperture in the sensor face pass through a region that is electrically segmented by a series of gold-plated tungsten grids before striking the solid collector. The collector ion currents are measured by a linear, automatic ranging electrometer. Two sensor entrance grids are grounded to the vehicle and surrounded by a conducting ground plane. The next grid inward is the double retarding grid, to which a time-varying electric potential is applied. The suppressor grid is held at a negative potential (-15V) to prevent low energy ambient electrons from reaching the collector and to prevent secondary electron escape from the collector. The function of the shield grid is to protect the electrometer connected to the collector from the electrical transients generated by changing potentials on the retarding grids. The measured ion current characteristics are fitted to theoretical curves using a least-squares technique. These fittings retrieve ion temperature, electron density, vehicle potential, some ion composition information and the component of the plasma drift velocity parallel to the sensor normal (i.e. meridional or line-of-sight drifts). This velocity component is extracted from the least squares fitting by determining the mean energy separation between ions of different mass and comparing that energy to that expected from the satellite velocity.

Measurements from this *in situ* device will be compared to nearly simultaneous FPI (7320Å) measurements; the results will be presented in Chapter 4. After a space and time correction is made to either the remote FPI measurements or *in situ* RPA measurements, good agreement between the two techniques result, validating the spaceborne interferometric technique and leading the way to the development of the CONVEX observing platform presented in Chapter 6. Figure 2.11 is a plot of meridional ion drifts (solid black line) as measured by the DE-2 RPA.

Overplotted are neutral winds (dotted line) as measured from the DE-2 FPI (6300Å). Note how the ions respond much more rapidly than the neutral gas to changes in magnetospheric electric fields.

A recent discovery (Anderson, p.c., 1992) points out that spacecraft charging may have contaminated some RPA measurements, especially those taken when DE 2 was in a low altitude orbit. This is similar to the possible contamination of FPI (7320Å) data by OH surface glow in that spacecraft charging contamination sources occur when the satellite is in relatively (<275km) low orbit. To preclude bad data usage, I use higher orbits when possible and make sure the data make sense before they are used. Appendix A contains an introduction to spacecraft charging.

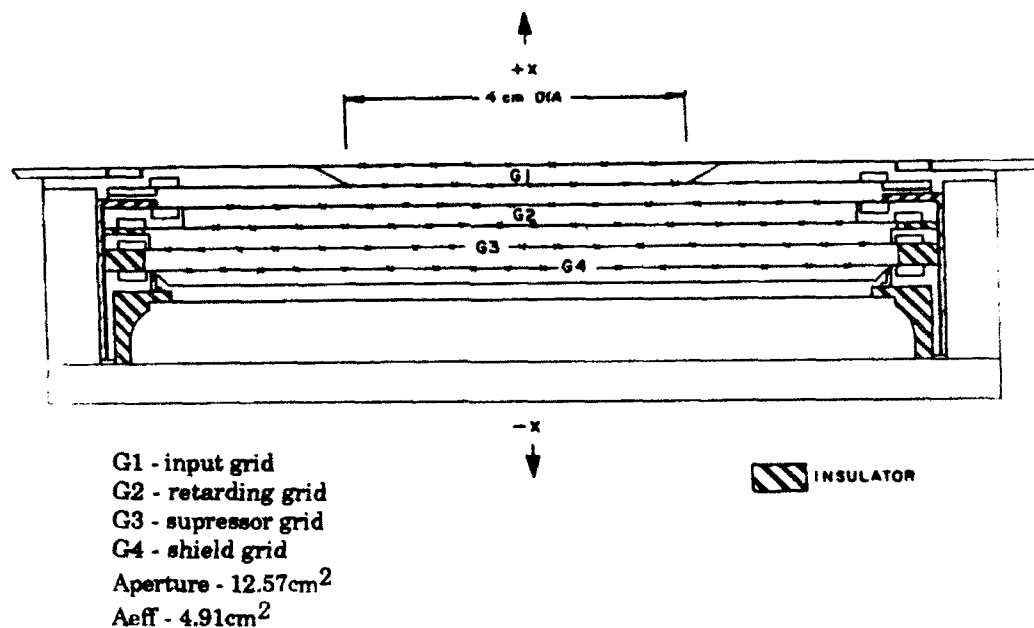


Figure 2.10 Schematic cross section of the RPA sensor (from Hoffman, 1981). Exposed surfaces and inner elements of the RPA sensor, except insulators, are gold plated. The nominal grid element separation is 2.5mm.

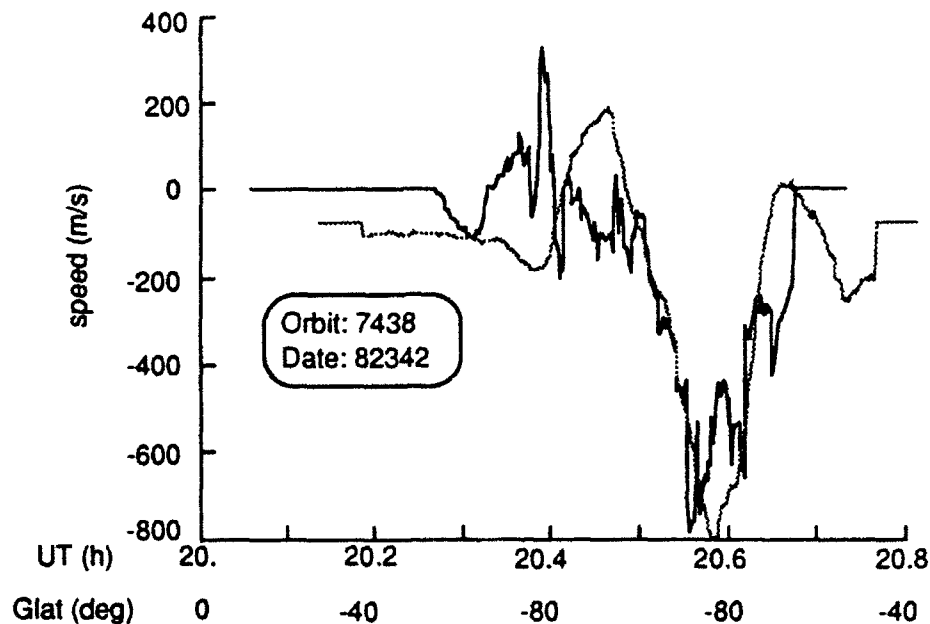


Figure 2.11 DE-2 RPA meridional ion drifts (heavy solid line) for orbit 7438. Overplotted are meridional neutral winds (lighter dotted line) as recovered from DE-2 FPI (6300Å) measurements. Both neutrals and ions exhibit antisunward flow over the polar cap, bounded by local regions of more sunward flow at lower geomagnetic latitudes. In the dawn-side convection channel, intense frictional (Joule) heating occurs where the largest ion-neutral difference velocities occur (~500m/s at ~20.65UT).

#### 2.4 Models Used in the [OII] $\lambda 7320\text{\AA}$ Volume Emission Rate Model

The aeronomical model of the ionospheric [OII]  $\lambda 7320\text{\AA}$  emission developed in Chapter 3, and the simulation study developed in Chapter 6, require inputs that are produced by other models. These inputs may be the solar flux spectrum or the plasma concentration during user-specified conditions. For example, Figure 2.12 is a flow diagram illustrating the models used in producing the 7320Å volume emission rate profiles and contour maps seen in Chapters 3 - 6. The five models outlined in this section have been used in many investigations of the thermosphere and ionosphere; output from these models supplement the modelling effort presented later in this dissertation.

#### 2.4a The Vector Spherical Harmonics (VSH) Model

The Vector Spherical Harmonics (VSH) model is a computer subroutine that describes the composition and dynamics of the thermosphere and ionosphere from ~130 - 600km. It is called VSH since it describes the wind field using vector spherical harmonics. Driving the model are two types of data - real time data and a coefficient library. The real time data consists of satellite measurements of composition, density and wind information plus geomagnetic indices. The coefficient library consists of output from a general circulation model of the thermosphere and ionosphere (NCAR-TIGCM). Hence, the description provided by VSH is determined by the physical, chemical and dynamic processes contained within the NCAR-TIGCM Model. For a detailed description of this model, see Killeen et al. (1987). This model is the first portable computer model of the thermospheric and ionospheric wind fields available to the scientific community. VSH input is time, location and the desired geophysical conditions. Two of the outputs are meridional ion drifts and ion temperatures. It is these two outputs that will be used as the "observed" atmosphere in the development of the DE-2 FPI (7320Å) Simulator and the spaceborne ion-convection pattern simulator developed in Chapter 6. Figure 2.13 is an example of VSH output. Table 2.3 illustrates VSH input and output.

#### 2.4b Solar Flux Model (SSFLUX)

At midlatitudes, during daytime, solar radiation is absorbed by upper atmospheric gasses, which are then either ionized, dissociated or excited.

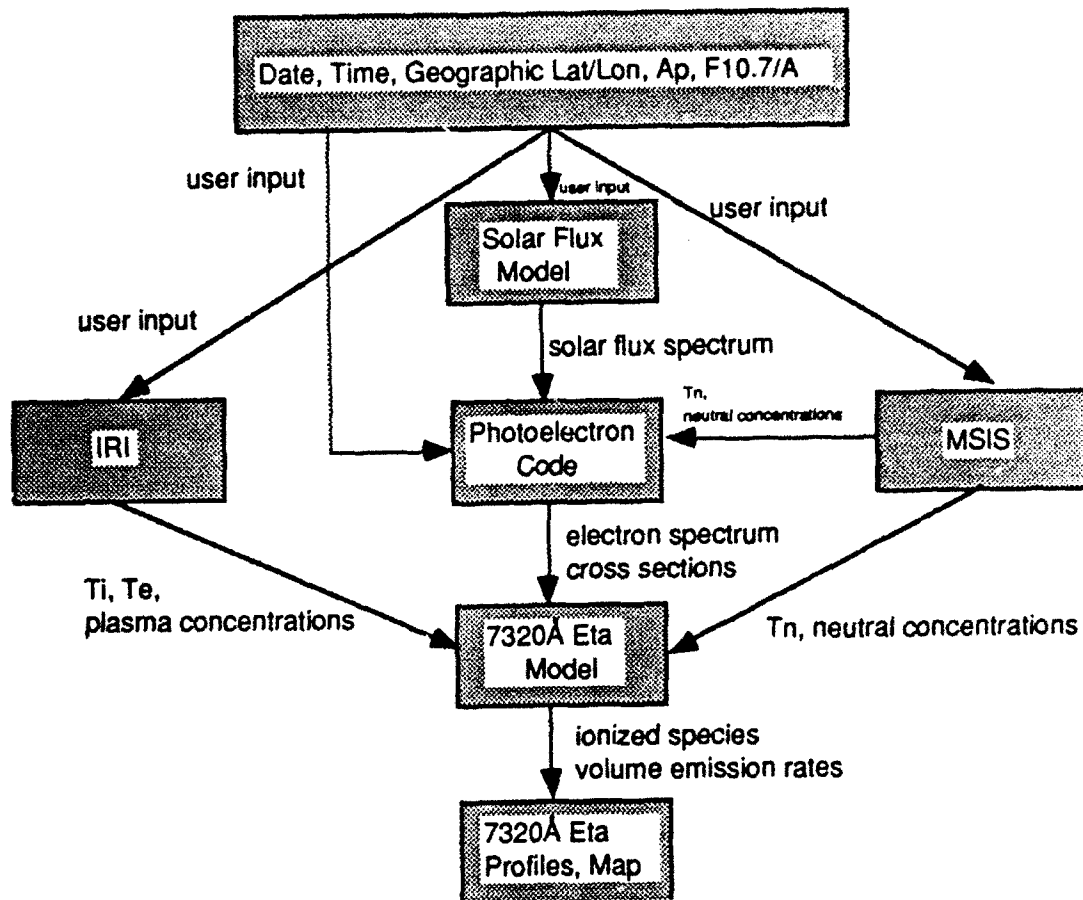


Figure 2.12 Flow diagram illustrating models used in producing the 7320Å volume emission rate profiles and maps seen in Chapters 3 - 6.

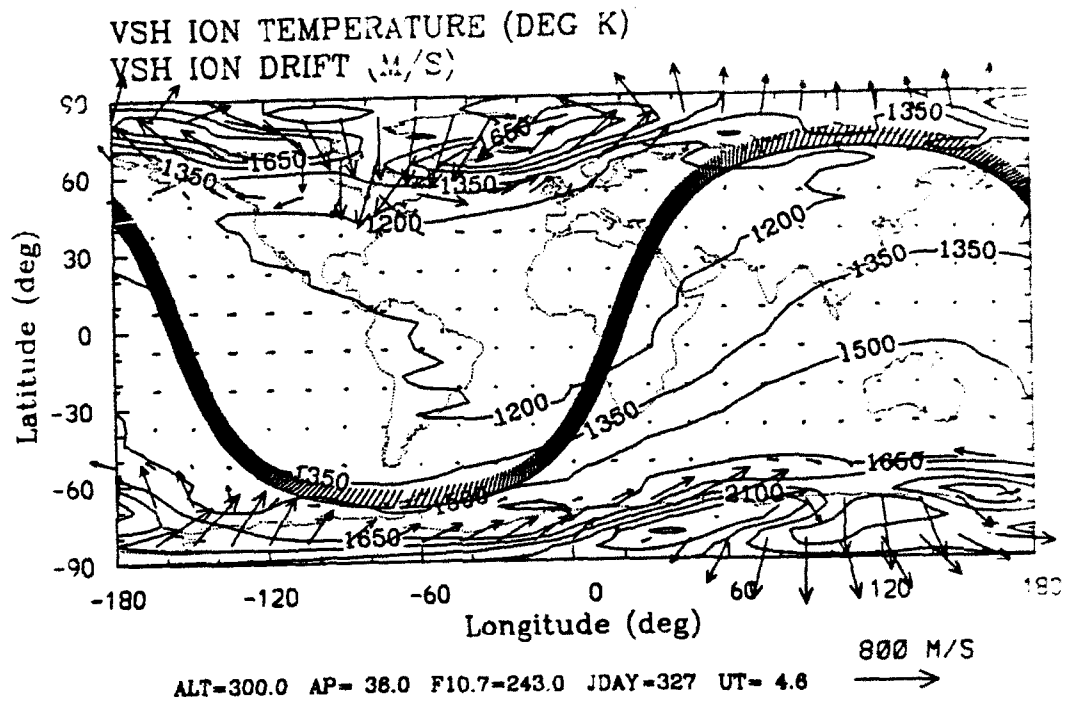


Figure 2.13 VSH ion drifts and temperatures for the given conditions. Solar terminator is the hatched line.



Input	Output
Day	Zonal Neutral Wind
Geographic Latitude	Meridional Neutral Wind
Geographic Longitude	Neutral Temperature
Altitude	Zonal Ion Drift
UT	Meridional Ion Drift
Ap	Pressure
F10.7	Vertical Neutral Wind
F10.7A	Atomic Oxygen Mass Mixing Ratio
	Mass Density
	Electron Density
	O <sup>+</sup> Density
	Ion Temperature
	O <sub>2</sub> Mass Mixing Ratio
	Atomic Oxygen Density
	O <sub>2</sub> Density
	N <sub>2</sub> Density
	Hydrogen Density
	N <sub>2</sub> Mass Mixing Ratio

Table 2.3 VSH inputs and outputs.

Most of this radiation is absorbed above 100km. The part of the solar spectrum that contributes the most to this phenomenon is radiation less than  $\sim 1900\text{\AA}$ . The result of this energy deposition is upper atmospheric heating. Solar radiation less than  $\sim 1027\text{\AA}$  has enough energy to ionize the

dominant thermospheric species; radiation between this and  $\sim 1900\text{\AA}$  is nearly completely absorbed in molecular photodissociation. Although this short wavelength radiation is a small part of the total flux from the sun, its energy input per unit mass is large since the mass of the absorbing part of the atmosphere is a small fraction of the total atmospheric mass. The energy input can become extremely large during solar disturbances when radiation less than about  $1027\text{\AA}$  can increase by several orders of magnitude. See Figure 2.14 for an example of this. Modelling the  $7320\text{\AA}$  airglow requires a solar flux as input so several photochemical reactions can occur. The SSFLUX model gives the solar flux at the top of the atmosphere between  $1 - 1750\text{\AA}$  based on the solar activity level. This solar flux is then used to calculate the photoionization of atomic and molecular oxygen as well as the photoelectron spectrum, all of which can be used to produce the  $7320\text{\AA}$  airglow emission. The solar flux is input to other models, as the flow diagram in Figure 2.12 shows, to produce the desired quantities for modelling this emission.

SSFLUX has several methods by which it can determine the solar flux based on input solar activity. The method used in previous modelling (Solomon, 1987; Hume, 1992) is the one used in this work and presented now. The flux is scaled using parameterization methods based on the daily  $10.7\text{ cm}$  solar radio flux ( $F_{10.7}$ ) and the 81 day average  $10.7\text{ cm}$  solar radio flux ( $F_{10.7A}$ ). For the ionizing EUV flux, Hinteregger's contrast ratio method (Hinteregger et al., 1981) and the Torr and Torr (1985) bin structure for a reference spectrum (SC#21REFW) are used.

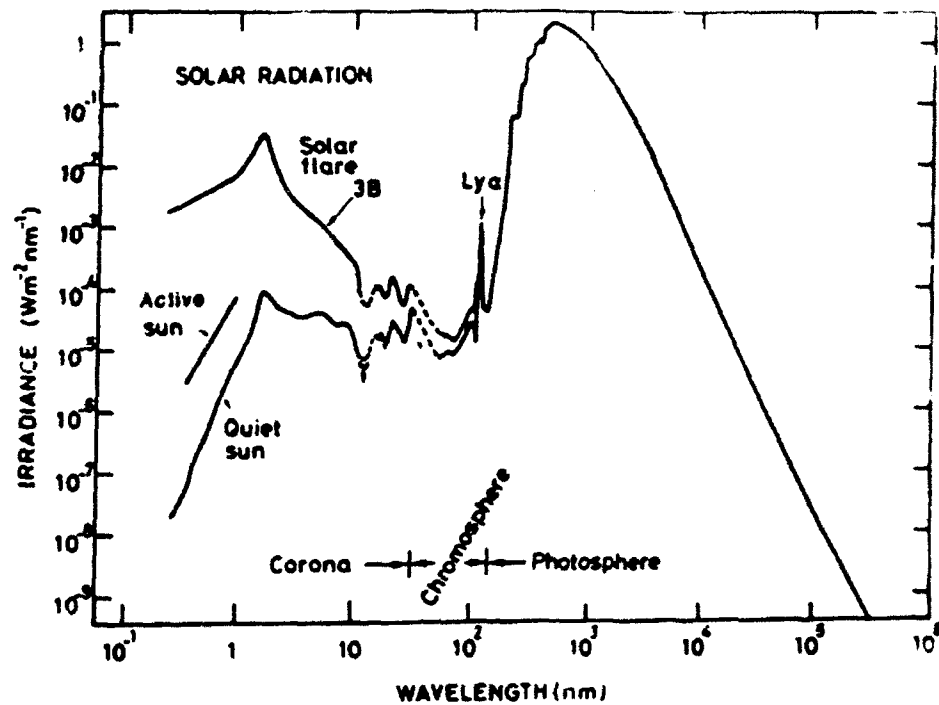


Figure 2.14 Distribution of solar irradiance vs wavelength, and its variation with solar activity. Adapted from Smith and Gottlieb, 1974.

The 1027Å (Ly-β) and 335Å (Fe XVI) enhancement ratios are found from Hinteregger's formula. The flux spectrum is then determined from these emissions using Hinteregger's method. For the 1216Å Ly-α line, the correlation relationship derived from SME data (Tobiska and Barth, 1990) is used. For the SRC (Schumann-Runge Continuum, ~ 1216-1750Å), the Torr et al. (1980) 50Å bin structure is used with the coefficients modified to reflect SME and LASP rocket data (Rottmann, 1981, 1988). Solar flux examples using this method for quiet and active times are presented in Figure 2.15.

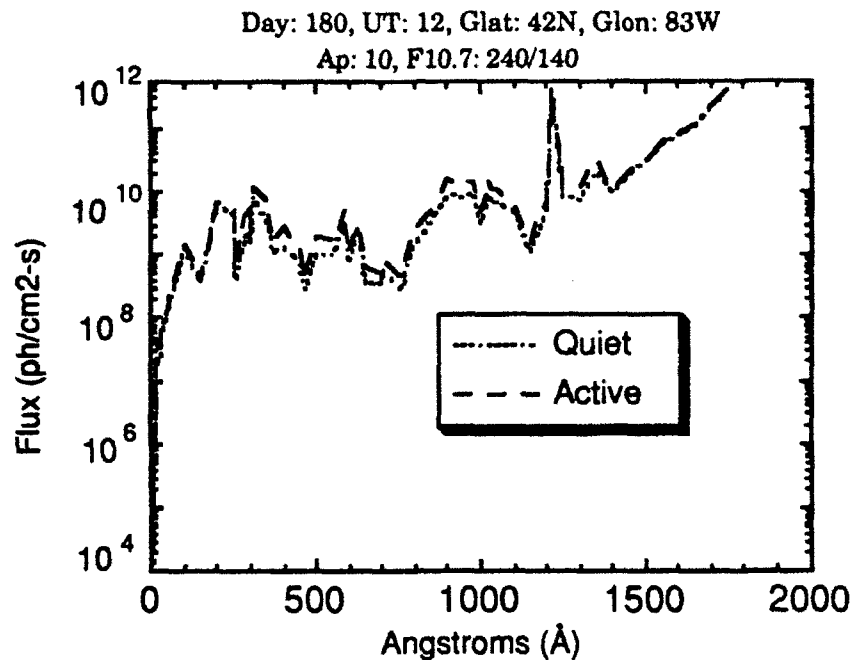


Figure 2.15 Sample output from the SSFLUX model for relatively quiet (Ap: 10, F10.7: 140) and active (Ap: 50, F10.7: 240) conditions. SSFLUX uses an amalgam of sources to estimate the flux below 18Å (Solomon, 1987).

#### 2.4c Mass Spectrometer and Incoherent Scatter Model (MSIS)

With the detection of atmospheric drag on satellites, Jacchia developed a series of models, the most widely used being J65 (Jacchia - 1965). This was the earliest comprehensive global model and had a lower boundary of 120km; height profiles of the principal constituents were calculated as a function of exospheric temperature assuming diffusive flux. The OGO-6 satellite mass spectrometer gave us the first extensive measurements of N<sub>2</sub>, O and He in the thermosphere. These measurements showed considerable variations in composition from J65 predictions - thus the production of the OGO-6 model. This model was based on J65, Bates temperature profiles (allows the hydrostatic equation to be explicitly

integrated), diffusive equilibrium and a lower boundary of 120 km. Hedin then developed the MSIS series of model (MSIS-77, 83, 86, 90). The MSIS-77 model followed the OGO-6 model but had an expanded database of composition and density from five satellites and temperature data from four ISR sites. MSIS-83 had an expanded database from seven satellites (temperature, density, composition) and five ISR sites providing lower thermospheric temperature and density; the lower boundary of this model was 85 km. MSIS-86 is based on data from the polar regions added from DE. It is the MSIS-86 model that provides VSH thermospheric data from 90 - 120 km. The 7320Å volume emission rate model requires knowledge of the neutral atmosphere. This neutral model must provide neutral temperatures and neutral number densities to the photoelectron model (see section 2.4d). The neutral atmosphere model used in the 7320Å model is MSIS-86.

In this MSIS-86 model, least squares methods fit data to equations for temperature and density. These fitting equations are spherical harmonic expansions in terms of local time and geographic latitude. Coefficients for these equations are dependent on seasonal effects, plus solar and magnetic activity. Temperature profiles are created by merging Bates (1959) temperature profiles for the upper thermosphere to an inverse polynomial profile for the lower thermosphere (Hedin, 1983). These profiles are joined near 117km by matching the temperature and temperature gradient. With the temperature profile determined and an average density that is dependent on solar and magnetic activity, the densities are then determined. The hydrostatic equation is integrated exactly to produce expressions for the density in terms of the average density. At the homopause, MSIS creates density profiles that are the sums of both mixed

and diffusive densities. Further discussion and detail can be found in Hedin (1983, 1987).

The MSIS model produces neutral densities for atomic and molecular oxygen, atomic and molecular nitrogen, helium, hydrogen and argon at a specific altitude. The temperatures it produces are the neutral temperature at the specified altitude, and the exospheric temperature. When using MSIS, modelers must be aware that an average error of ~10% in the densities and ~15K in the temperatures exists. Figures 2.16 and 2.17 show some modelled MSIS-86 densities and temperatures for various conditions.

#### 2.4d International Reference Ionosphere Model (IRI)

Ionospheric temperatures and densities are required for the 7320Å volume emission rate model to work. To satisfy this need, IRI-86 is used. Like the previous models, this model is a series of ever-improving models. The model describes monthly averages of electron density, electron temperature, ion temperature and ion composition (in percentages) from 50km to 1000km for *magnetically quiet conditions in the non-auroral zone*. Data sources for this model are: worldwide ionosonde measurements (peak plasma frequencies, peak densities), ISR measurements (E valley, F2 peak height, F2 bottomside, topside, ion temperature (Ti), electron temperature (Te)), Alouette 1 and 2 topside sounder measurements (topside), AE-C, ISIS 1 and 2 in situ measurements (Te), AEROS in situ measurements (Te, Ti, ion composition), rocket measurements (D and E electron density, ion composition), Beacon satellite data (total electron content for test purposes), and ground-based absorption measurements (E, F variability). For a

detailed discussion of the history and science behind this code, see Bilitza (1990).

The IRI model is partitioned into three segments - ion temperature profiles, ion density profiles and electron density profiles. The model uses several analytical functions and expressions to simulate density and temperature variations. Usually, the functions are spherical harmonics. A group of functions called the Epstein Family is used to simulate additional variations and special seasonal, diurnal and geographical features (Rawer, 1987). Booker's method (Booker, 1977) is used to determine altitude profiles.

Ion temperature profiles range from 120 - 1000km. At the base of the profile, thermal equilibrium is assumed between plasma and neutrals. As the profile increases in altitude, the temperatures are forced to maintain the  $T_e > T_i > T_n$  structure. The ion and electron temperature profiles are constructed by using the Booker functions. For further detail, see Bilitza (1984, 1990).

Ion density profiles are modelled as either percentages relative to the total electron density profile or the total ion density. Again, this segment of the code uses Booker's approach to determine atomic and molecular oxygen ion profiles; the rest of the profile is filled with  $NO^+$  at lower altitudes and  $H^+$  or  $He^+$ . Note that ion density parameters vary with solar zenith angle during daytime conditions. But due to size limitations, there is *no variation if the solar zenith angle is greater than 90 degrees*. See Bilitza (1990) for further details.

Electron density profiles extend from 60 (day) or 80 (night) to 1000km. These profiles are constructed from six regions which are joined via the Booker approach. The middle section of the ionosphere is determined by a

variety of parameters such as peak densities and valley parameters. See Bilitza and Rawer (1990) for a review on this topic.

Since the 7320Å model is taken to be the "real" volume emission rate in the atmosphere by the simulated satellite system in Chapter 6, it must be extremely accurate. IRI is known to give reasonable results for electron content at mid-latitudes and solar minimum, but overestimates this parameter during active conditions. Figures 2.16 and 2.17 illustrate some IRI parameters for various conditions. Note that the plasma concentrations have been modified with respect to total ion density and put into the usual units instead of percentages. Since IRI is only valid outside of the auroral zone and for quiet conditions, modifications had to be made to the 7320Å model to allow it to function properly in the auroral zone. This will be discussed further in the 7320Å volume emission rate model discussion (Chapter 3).

#### 2.4e Photoelectron Model

The upper atmosphere is driven by solar processes during the daytime. Solar flux can photoionize, photoexcite or photodissociate atoms and molecules. The photoelectrons produced by the ionization process may have sufficient energy to further ionize, excite or dissociate atoms and molecules in the thermosphere. This "energy-cascade" can be seen in Figure 2.18. Once an electron has lost so much energy via collisions that it can no longer cause ionization, dissociation or excitation, it is thermalized. To create, for example, an  $O^+(^2P)$  ion, an electron of at least 18.61 eV must impact an atomic oxygen.



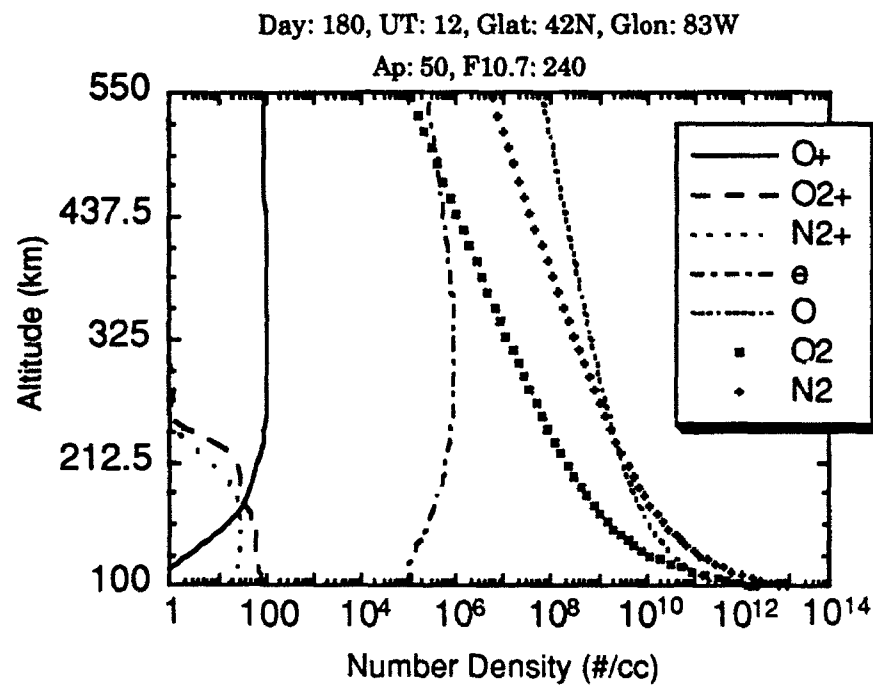
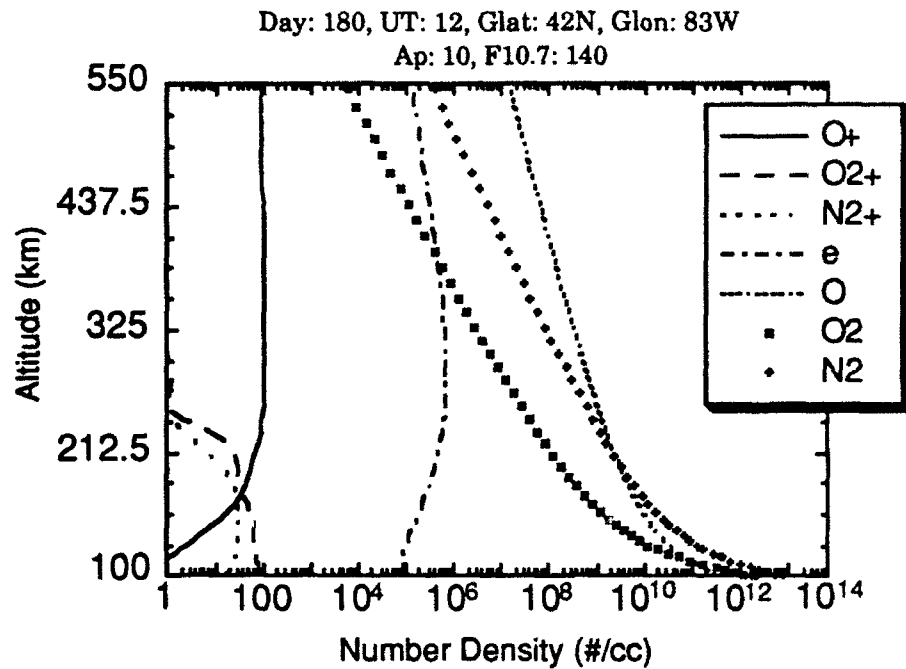


Figure 2.16 Neutral number densities (MSIS) and plasma number densities (IRI) for varying conditions over Ann Arbor.

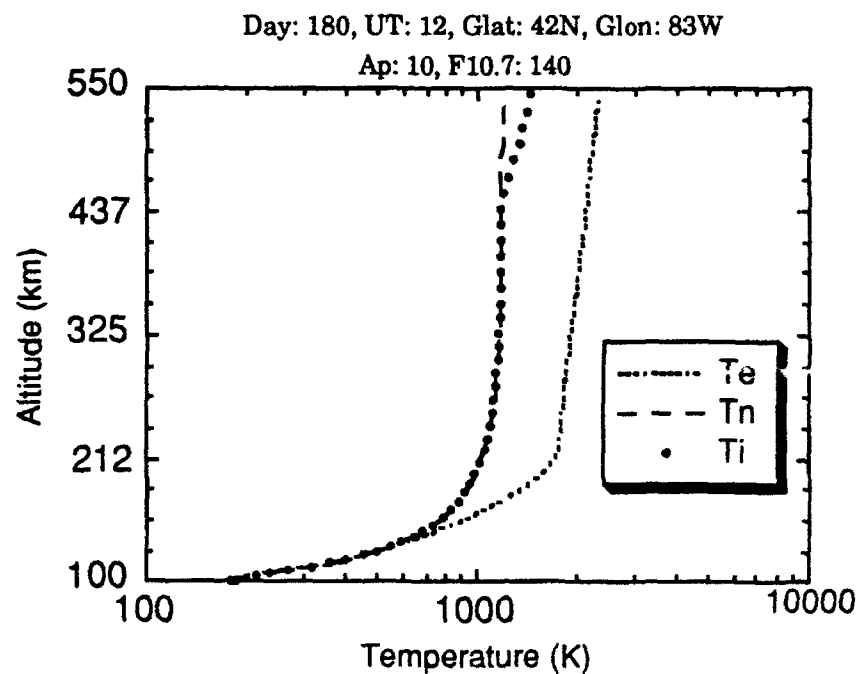
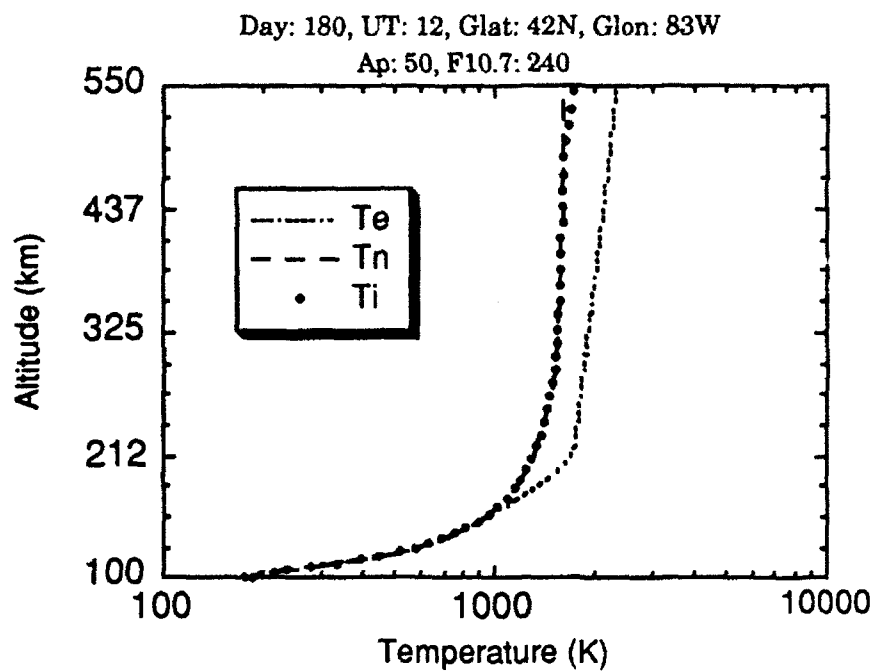


Figure 2.17 The top panel represents neutral (MSIS) and plasma (IRI) temperatures for active conditions. The bottom panel are for quiet geomagnetic and moderate solar activity conditions.

The photoelectron model used in this code is similar to that discussed in Solomon et al. (1988) and Solomon (1987). It uses the Banks and Nagy (1970) two stream electron transport model to calculate the photoelectron and secondary electron fluxes. The SSFLUX model discussed in Chapter is used as input to the top of the atmosphere and is attenuated to a given altitude. Conjugate electrons and auroral electrons as measured by the DE-2 LAPI (low altitude plasma instrument) are added to the top of the atmosphere in the same fashion; this makes the model more representative in auroral conditions. MSIS-86 generates the neutral density profiles for attenuation of the solar flux and for ionization, dissociation and excitation calculations. Photoionization and electron impact cross sections are those used by Solomon et al. (1988). The electron flux is calculated using the two-stream approximation (Banks and Nagy, 1970; Nagy and Banks, 1970; Banks et al., 1974) to the transport equations, solving for the upward and downward hemispherical fluxes along a magnetic field line as a function of energy.

Explicit solutions to these transport equations are obtained for a daytime sunlit exponential atmosphere in which local production occurs and for a twilight exponential atmosphere with an influx of photoelectrons arriving from the magnetic conjugate point. Gravity, parallel electric fields and magnetic field convergence are neglected. Elastic collisions with atomic oxygen, N<sub>2</sub> and O<sub>2</sub>, discrete energy losses from inelastic collisions resulting in excitation and ionization of these species and thermal excitation of the ambient electron gas are considered. From this model, the authors concluded elastic scattering significantly reduces the rate of photoelectron escape from a sunlit atmosphere while maintaining the up/down isotropy to higher altitudes than would be possible if elastic

scattering did not occur. They also found that in the twilight atmosphere, almost 50% of incoming photoelectrons are backscattered by means of elastic collisions. Hence, the model assumes that the photoelectron flux along a geomagnetic field line consists of an up-field line and down-field line component.

Photoelectrons are assumed to be created within the atmosphere by photoionization or other processes such that 50% contributes to the up component and 50% to the down. In traveling along the magnetic field lines, the photoelectrons are assumed to interact with the ions and neutrals through elastic and inelastic cross sections of various size. It is also assumed that elastic collisions do not result in appreciable photoelectron energy degradation. Inelastic collisions, however, cause cascading between the various photoelectron energy groups with photoelectrons absorbed at higher energies reappearing at appropriate lower energies. In determining the electron flux, first the highest energy electrons are considered, then the secondaries and degraded primaries created by this flux are computed and added to the flux at each altitude level and energy bin, and the excitation and ionization due to the top energy bin found. The next highest energy bin is considered, its effect on those below it calculated and so forth down to the lowest energy.

In this work, there are 58 energy bins in a discretely variable interval from 0.2 eV to 37keV; the altitude ranges from 90 - 550 km. As the electron transport model exists today, there are three sections. One calculates the transport of electrons, another the excitation and ionization and another is a look-up table of cross sections. Also, the model assumes a constant pitch angle ( $\mu=0.577$ ) to characterize transport. The model is widely accepted as the best available; it has one major criticism - it fails to conserve energy

when applied to keV fluxes. Fortunately, this occurs at altitudes below 120 km and therefore does not affect the emission of concern in this work. It is this model that performs the photoelectron transport and concomitant ionization/excitation for the 7320Å volume emission rate model about to be presented.

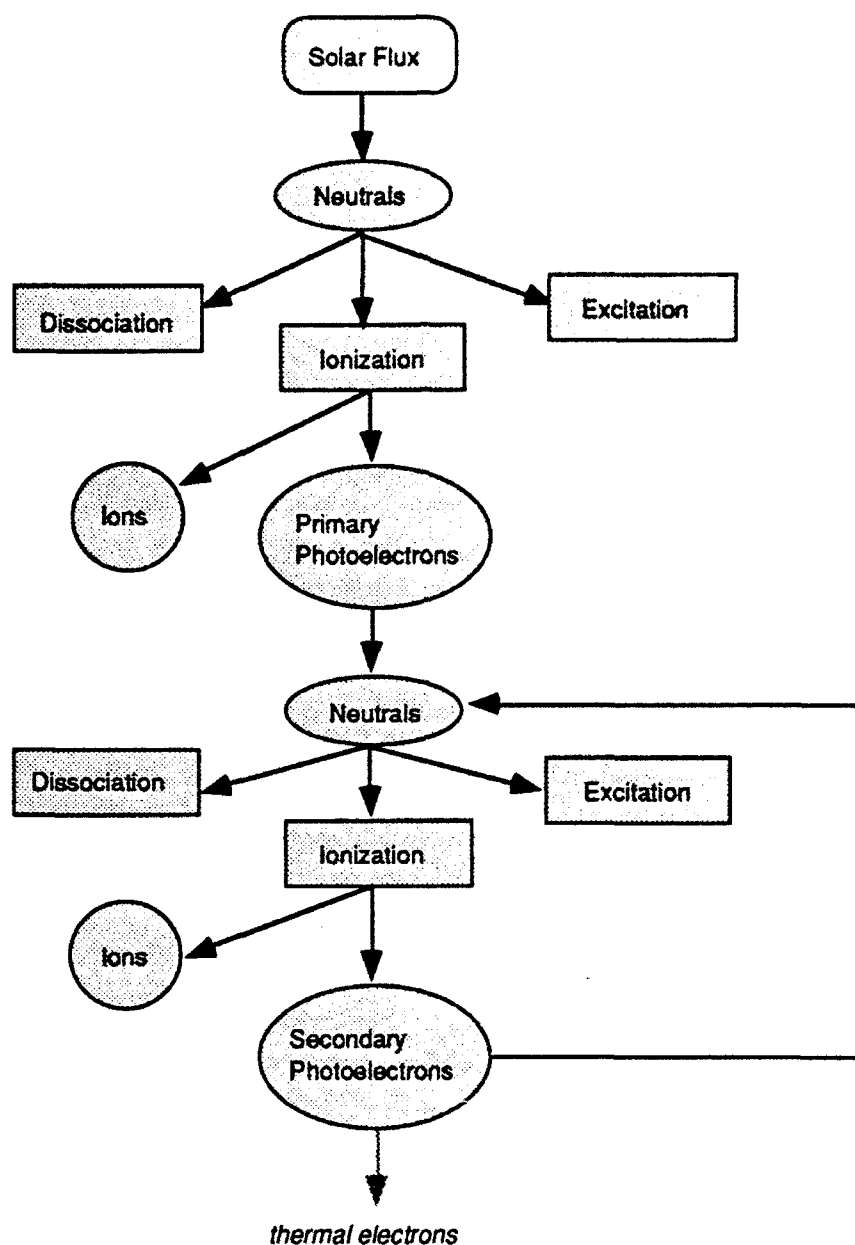


Figure 2.18 Solar photons, impacting a neutral atom or molecule, can either ionize, excite or dissociate that particle. If ionization occurs, a photoelectron is produced which can in turn ionize more neutrals, creating secondary electrons. As long as this secondary electron has more energy than the neutral's ionization energy threshold, it will continue to ionize all neutrals with which it collides. Once it has undergone sufficient collisions so further ionization is impossible, it is said to be "thermalized".

## CHAPTER 3

### THE 7320Å VOLUME EMISSION RATE MODEL

#### 3.1 Introduction

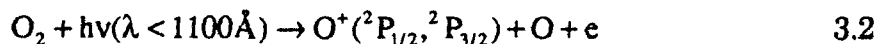
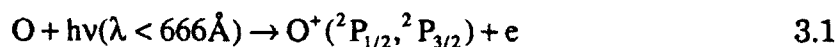
The 7320Å volume emission rate, produced by photoionization and electron impact ionization, has been modelled; the model and its results will be presented in this Chapter. Validation against other models will be done in this Chapter, but validation against actual DE-2 measurements will be done in Chapter 4. The accuracy of this model is critical to the remainder of this dissertation since it is taken to be the "observed" volume emission rate during the development of the new satellite-observing platform detailed in Chapter 6. The 7320Å volume emission rate model requires user input (date, UT, geographic latitude and longitude,  $A_p$ , F10.7, F10.7A) and the model inputs discussed in Chapter 2. Figure 2.12 is a flow diagram illustrating the logical progression one uses to model this emission rate.

The primary conclusion drawn from this modelling effort is that photoionization is by far the dominant source of the 7320Å emission in *dayglow*; not until *twilight* does electron impact ionization become nearly equally important. At *night*, electron impact ionization in the auroral zones, polar cusp areas and conjugate points (very minor) is the source of

the emission. The production of  $O^+(^2P)$  by photoionization or electron impact ionization of molecular oxygen was found to be small compared to that of atomic oxygen and could easily be ignored if one wanted to speed the model up in computing time. The model I am about to discuss is an extension of the Solomon et al. (1988) model made applicable to *only* the 7320Å emission. Emissions pertaining to the 7330Å transition are not included since this doublet is not of concern (the DE-2 FPI (Chapter 4), the Søndre Strømfjord FPI (Chapter 5) and the CONVEX FPIs (Chapter 6) only measure the 7320Å emission). To ignore the 7330Å emission, the Einstein coefficient I used was  $A_\lambda = 0.097$  for the  $O^+(^2P_{1/2,3/2}) - O^+(^2D_{5/2})$  transition (an  $A_\lambda$  of 0.171 would have included the entire 7320-30Å emission since this value pertains to the  $O^+(^2P_{1/2,3/2}) \rightarrow O^+(^2D_{5/2})$  transition at ~7320Å and  $O^+(^2P_{1/2,3/2}) \rightarrow O^+(^2D_{3/2})$  at ~ 7330Å transition). The most current chemistry, dynamics, transport and understanding of this emission has been placed in code. Four versions of the model exist and will be presented in a logical order.

### 3.2 Photochemical Modelling of the [OII] 7320Å Emission

An historical discussion of  $O^+(^2P)$  sources and sinks was presented in Chapter 2. The  $O^+(^2P)$  ion is *primarily* created by *photoionization*:



The second reaction (from Solomon, p.c., 1991) is very minor at the altitude of concern since molecular oxygen is nearly 1000 times less abundant than



atomic oxygen at 300 km (see Figure 2.16). A general photoionization equation may be written as:

$$P = X \int_{\lambda_t}^{\lambda} F(\lambda) \sigma_i(\lambda) \xi(\lambda) d(\lambda) \quad 3.3$$

where  $P$  is the photoionization production rate,  $X$  is the number density of the photoionizing species,  $\lambda_t$  is the threshold wavelength for photoionization (666Å in this case),  $\xi$  is the quantum yield for production of the desired ion,  $\sigma_i$  is the photoionization cross section of the photoionizing species and  $F$  is the attenuated solar flux (all wavelength dependent). This flux may be more clearly presented as:

$$F(\lambda) = F_{\infty} \exp \left\{ - \sum_i \int_0^s \sigma_i(\lambda) n_i(s) ds \right\} \quad 3.4$$

where  $s$  is the distance along the atmospheric path to the ionization point,  $F_{\infty}$  is the flux at the top of the atmosphere,  $\sigma_i$  is the photoionization cross section and  $n_i(s)$  is the number density of the  $i^{\text{th}}$  species along the path. Ionization cross sections and branching ratios for atomic and molecular oxygen, all with respect to wavelength, are taken from Appendix 2 in Rees (1989). For example, the atomic oxygen branching ratios at various wavelengths are illustrated in Table 3.1. Note that in no instance does the production of the  $O^+(^2P)$  ion exceed 26%; the rest of the ions are primarily in the ground state ( $O^+(^4S)$ ).

Hence, the photoionization production rates can be expressed as:

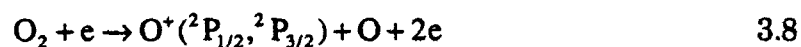
$$P_i = [O] \int_{666}^{\lambda} F(\lambda) \sigma_i(\lambda) \xi(\lambda) d\lambda \quad 3.5$$

$$P_2 = [O_2] \int_{1100}^{\lambda} F(\lambda) \sigma_1(\lambda) \xi(\lambda) d\lambda \quad 3.6$$

$\lambda(\text{\AA})$	Branching Ratio
50 - 314	.23
315 - 435	.26
436 - 666	.25

Table 3.1 Atomic oxygen branching ratios into the  $O^+(^2P)$  state at various EUV wavelengths (after Rees, 1989).

A secondary source for the production of the  $O^+(^2P)$  ion is *electron impact ionization*:



Equation 3.8 is much less important than 3.7 since  $[O_2] \ll [O]$  at 7320Å emission altitudes; therefore, it may be ignored in the model with no loss in accuracy. These electrons may be photoelectrons, auroral electrons, conjugate-point electrons or secondary electrons that have enough energy to ionize either atomic or molecular oxygen. Since these electrons do not have tags on them indicating their origin, any electron that has enough energy to ionize atomic and molecular oxygen will be included. Once an electron has lost too much energy via collisions and no longer has enough energy to ionize atomic or molecular oxygen, it is called a "thermal" electron and is

no longer considered in the model. Similarly, production via electron impact ionization is written:

$$P = X \int_{E_t}^E f(E) \beta(E) \sigma(E) dE \quad 3.9$$

where  $E_t$  is the threshold electron energy for ionizing species X,  $f$  is the electron flux,  $\beta$  is the branching ratio and  $\sigma$  is the ionization cross section (all dependent on electron energy). Hence,

$$P_3 = O \int_{18.61}^E f(E) \beta(E) \sigma(E) dE \quad 3.10$$

$$P_4 = O_2 \int_{12.63}^E f(E) \beta(E) \sigma(E) dE \quad 3.11$$

The loss mechanisms for the  $O^+(^2P)$  ion are spontaneous emission and quenching:

$$L_1 = O^+(^2P) \xrightarrow{A_\lambda} O^+(^2D, ^4S), A_\lambda = 0.219s^{-1} \quad 3.12$$

$$L_2 = O^+(^2P) + O \xrightarrow{k_0} O^+(^4S) + O + 5.0eV, k_0 = 5.2 \times 10^{-11} cm^3 s^{-1} \quad 3.13$$

$$L_3 = O^+(^2P) + N_2 \xrightarrow{k_1} N_2^+ + O + 3.02eV, k_1 = 4.8 \times 10^{-10} cm^3 s^{-1} \quad 3.14$$

$$L_4 = O^+(^2P) + N_2 \xrightarrow{k_2} N^+ + NO + 0.70eV, k_2 = 1.0 \times 10^{-10} cm^3 s^{-1} \quad 3.15$$

$$L_5 = O^+(^2P) + e \xrightarrow{k_3} O^+(^2D) + e + 1.69eV, \\ k_3 = 1.50 \times 10^{-7} \left\{ \frac{300}{T_e} \right\}^{1/2} cm^3 s^{-1} \quad 3.16$$

$$L_6 = O^+(^2P) + e \xrightarrow{k_4} O^+(^4S) + e + 5.0eV, \\ k_4 = 4.0 \times 10^{-8} \left\{ \frac{300}{T_e} \right\}^{1/2} cm^3 s^{-1} \quad 3.17$$

$$L_7 = O^+(^2P) + O_2 \xrightarrow{k_{O_2}} O_2^+ + O + 3.02\text{eV}, k_{O_2} = 4.8 \times 10^{-10} \text{cm}^3 \text{s}^{-1} \quad 3.18$$

The number density of a species, in steady state, is simply production divided by loss; the volume emission rate is the Einstein coefficient times the number density. Letting  $P = P_1 + P_2 + P_3 + P_4$  and  $L = L_1 + L_2 + L_3 + L_4 + L_5 + L_6 + L_7$  in the model, one has:

$$[O^+(^2P)] = \frac{P}{L} = \frac{P_1 + P_2 + P_3 + P_4}{L_1 + L_2 + L_3 + L_4 + L_5 + L_6 + L_7} \quad 3.19$$

which, above the quenching zone, reduces to

$$[O^+(^2P)] = \frac{P_1 + P_3}{0.219} \quad 3.20$$

Since  $\eta = AX$  and

$$A_{7320\text{\AA}} = (A_{^2P_{1/2} \rightarrow ^2D_{3/2}}) \epsilon_{1/2} + (A_{^2P_{3/2} \rightarrow ^2D_{3/2}}) \epsilon_{3/2} = 0.061 \times 0.33 + 0.115 \times 0.67 = 0.097 \text{s}^{-1}$$

then above the quenching zone:

$$\eta = 0.097 \left\{ \frac{P_1 + P_2 + P_3 + P_4}{0.219} \right\} = 0.097 \left\{ \frac{P_1 + P_3}{0.219} \right\} = 0.443(P_1 + P_3) \quad 3.21$$

or within the quenching zone:

$$\eta = 0.097 \left\{ \frac{P_1 + P_2 + P_3 + P_4}{0.219 + L_2 + L_3 + L_4 + L_5 + L_6 + L_7} \right\} \quad 3.22$$

The 7320Å volume emission rate model calculates the volume emission rate at 58 evenly spaced altitude points from ~ 90 - 550 km. MSIS provides neutral densities and temperatures, IRI provides plasma densities and temperatures. A solar flux spectrum based on the Hinteregger Reference Spectrum comes from the solar flux model (discussed in Chapter 2). The photoelectron spectrum is produced using the

photoelectron model based on the two stream approximation (Banks and Nagy, 1970). The photoelectron model calculates  $P_3$  and  $P_4$  due to photo-, auroral and conjugate electron impact ionization and the concomitant secondary electron ionization as the electron undergoes its energy cascade in both the upward and downward directions. Note that the 7320Å volume emission rate model combines loss Equations 3.14 and 3.15 into one loss equation and uses an  $N_2$  quenching rate of  $4.8 \times 10^{-10} \text{cm}^3 \text{s}^{-1}$  (after Rusch et al., 1977); similarly, loss Equations 3.16 and 3.17 are combined into one loss equation with an electron quenching rate (after Henry et al., 1969) of  $1.9 \times 10^{-7} (300/T_e)^{1/2} \text{cm}^3 \text{s}^{-1}$  (Solomon, p.c., 1991).

### 3.3 Four Versions of the 7320Å Volume Emission Rate Model

Four versions of the 7320Å volume emission rate model exist: *airglow*, *auroral-airglow*, *maxwellian* and *global*. These versions will be discussed in the following sections. In addition to volume emission rates, these versions of the model can quickly output  $O^+(^2P)$  number densities, production/loss rates for the  $O^+(^2P)$  ion and even collision frequencies and Joule heating rates, under appropriate boundary conditions.

#### 3.3.1 Airglow Model

This is the simplest version of the model. Auroral production of the  $O^+(^2P)$  ion is impossible since IRI does not provide a realistic estimate of the electron densities or ion composition under auroral conditions. Hence, it is found that this model creates very accurate profiles of the 7320Å emission rate at low- and mid-latitudes, but is frequently on the low side of 7320Å emission rates in the auroral zone (~17% less). Figure 3.1 is an

example of a volume emission rate profile on a quiet day. Note that the dominant reaction is the photoionization of atomic oxygen, as expected.

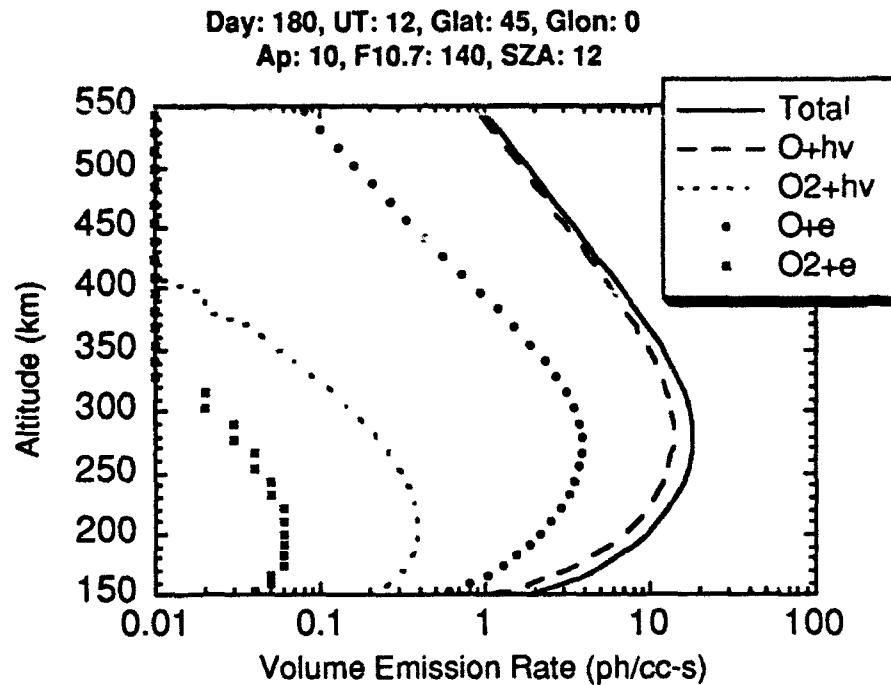


Figure 3.1 Sample 7320Å airglow volume emission rate profile for quiet conditions. The various components are plotted as part of the total. At this time, photoionization is the dominant source of the airglow emission. The volume emission rate reduction *below* the peak (at ~ 285km) is due to an increase in quenching. The volume emission rate decrease *above* the peak is due to the combination of decreasing electron and atomic oxygen number densities.

Volume emission rates will have a diurnal, seasonal and solar dependence. When the sun sets at a certain level, production of the 7320Å volume emission rate will be dominated by electron impact ionization. In different seasons, the solar zenith angle will be different at the same universal time, allowing for greater solar EUV penetration at, for example, 12 UT on 21 June versus 12 UT on 21 November over Ann Arbor (see Figure 3.2) and therefore creating different emission rates.

Substituting equation 3.4 into 3.3 and noting that  $ds = -\sec\theta dz$  where  $\theta$  is the solar zenith angle, one gets a general photoionization equation:

$$P = X \int_{\lambda_1}^{\lambda} F_{\infty} \exp \left\{ \sum_i \int_i^{\infty} \sigma_i(\lambda) n_i(z) \sec \theta dz \right\} \sigma_i(\lambda) \xi(\lambda) d\lambda \quad 3.23$$

This ionization rate is basically the integrated product of the neutral species, cross sections and the solar flux, with a solar zenith angle dependence. The greater the solar activity, the greater the ionizing flux. These dependencies are seen in Figure 3.3, an example of 7320Å volume emission rates for various solar zenith angles during quiet and active conditions. For both conditions, the altitude of the peak emission increases with the solar zenith angle due to the solar EUV attenuation. Also, for each individual solar zenith angle, this altitude increases with solar activity as a result of the neutral atmospheric expansion. It also means that during the high solar activity periods, solar EUV radiation cannot effectively penetrate the atmosphere as deeply as it does during low activity periods. Figure 3.4 illustrates the diurnal dependence of this emission.

### 3.3.2 Aurora-Airglow Model

The importance of auroral energy to the dynamics of the thermosphere/ionosphere has created great interest in the modelling of auroral particle influx, auroral impact ionization, the currents they induce and their effects on convection. Many new models analyzing ionization, excitation and heating in response to a flux of energetic electrons have been created. Some solve the Boltzmann equation for electron transport under the assumption that collisions with ambients dominate the energy cascade (degradation) process in the thermosphere. An iterative multistream method (Porter et al., 1987) was developed for auroral computations to describe laboratory beam injections. Rees and Lummerzheim (1989) and Lummerzheim et al. (1989) used the discrete ordinate method to solve a

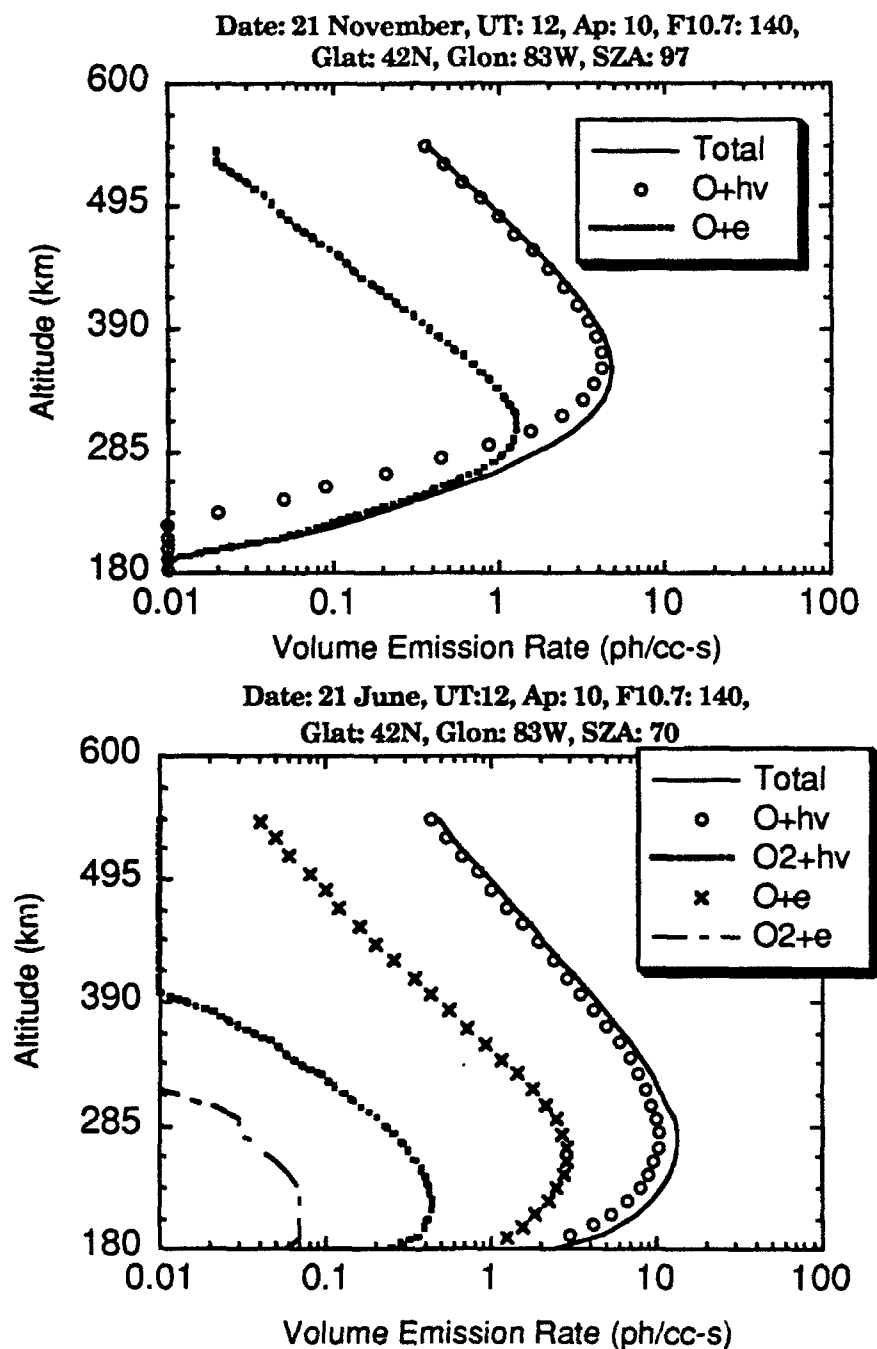


Figure 3.2 Illustration of seasonal effects on the 7320Å volume emission rate. In the top panel (21 Nov, 12UT), the volume emission rate peaks at  $\sim 7$   $\text{ph}/\text{cm}^3\text{-s}$  at  $\sim 350$  km. In the bottom panel (same conditions but for a summer day), the SZA is smaller and, therefore, EUV radiation penetration is greater and produces a larger volume emission rate ( $\sim 16$   $\text{ph}/\text{cm}^3\text{-s}$ ).



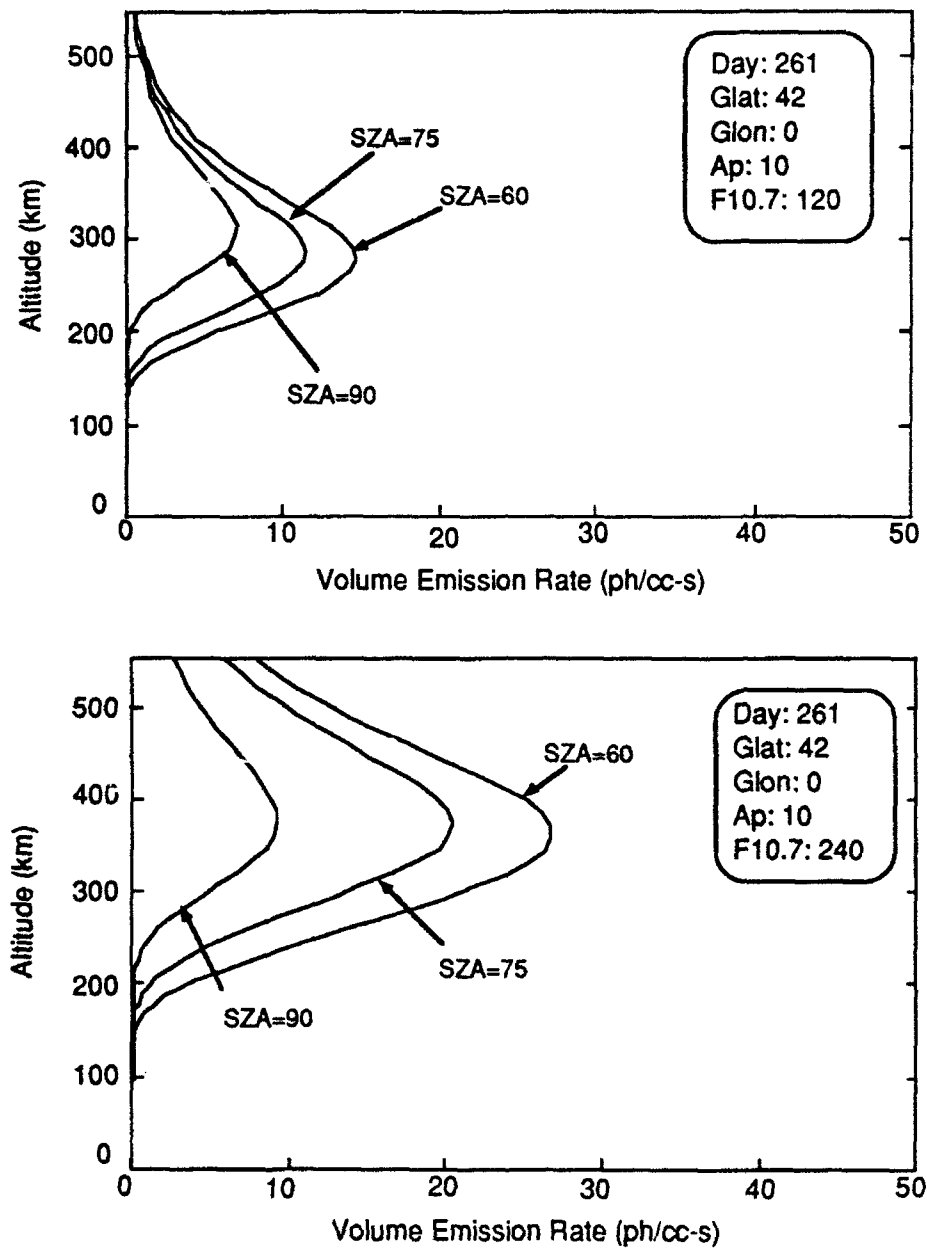


Figure 3.3 Example of 7320Å volume emission rates for various solar zenith angles during quiet (top panel) and active (bottom panel) conditions. See text for discussion.

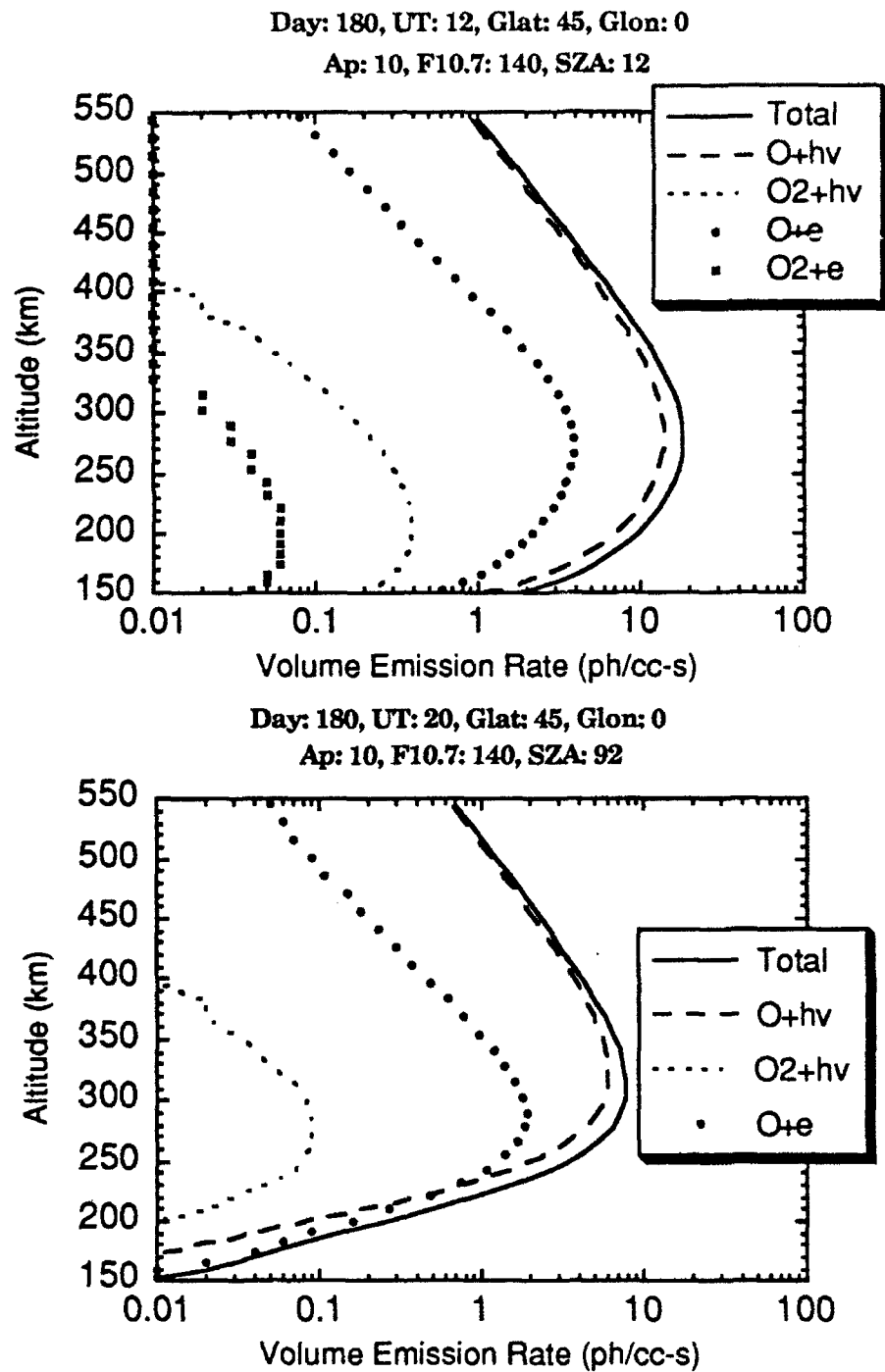


Figure 3.4 Illustration of the diurnal dependence of this emission. Top panel is for quiet conditions at noon near the summer solstice. Maximum production of the 7320Å emission is by photoionization. The bottom panel is for the same location, but at 8pm. At low altitudes, electron impact ionization is slightly dominant: since the solar photon flux is rapidly diminishing but plenty of photo- and energetic secondary electrons remain. At higher altitudes, the sun has not set and photoionization remains the primary source of the emission.

multi-stream formulation of the transport problem. Solomon et al. (1988) and Richards and Torr (1990) employed independent extensions of the two-stream method (Nagy and Banks (1970)) to high energies to calculate auroral fluxes. Link (1991) has applied the Feautrier solution technique to the electron transport equation. The *auroral electron energy flux* associated with optical features varies from  $\sim 0.1 - 10 \text{ ergs/cm}^2\text{-s}$ , with average energies ranging from  $\sim 0.2 - 2 \text{ keV}$  (Whalen et al., 1971; Winningham and Heikkila, 1974; Ismail et al., 1977; Hardy et al., 1982). Protons also create aurora, but proton modelling is curiously absent in the literature. Basu et al. (1987) describe a proton transport model and use it to model coincident satellite and radar measurements of a pure proton event. Whalen et al. (1971) and Niciejewski et al. (1989) found the upper limit of the *proton energy flux* to be less than  $0.01 \text{ ergs/cm}^2\text{-s}$  and  $0.04 \text{ ergs/cm}^2\text{-s}$ , respectively. Ismail (1977) observed the upper proton energy flux to be less than  $0.001 \text{ ergs/cm}^2\text{-s}$  in a polar cap satellite study. Hence, the aurora created in this model are considered electron aurora.

To include auroral precipitation in this model in order to make it more realistic, I used DE-2 LAPI (Low Altitude Plasma Instrument) data. DE 2 observed auroral electrons using the LAPI; I had access to several orbits of data all of which were observed during quiet times ( $A_p$  less than 18,  $F_{10.7}$  less than 170). I averaged the data from these orbits and produced the auroral electron spectrum shown in Figure 3.5. At 0215UT on 26 February 1987, the DMSP F6 satellite observed an electron flux (Niciejewski et al., 1989) near Søndre Strømfjord that closely resembled the LAPI spectrum in Figure 3.5; the LAPI flux was slightly higher (two times) than the DMSP-measured flux in the range of  $\sim 1 - 100 \text{ eV}$ . At 1249UT on 9

February 1988, the HiLAT satellite observed precipitating electrons from  $\sim 55^\circ - 77^\circ$  geographic latitude during its descending pass (Valladares et al., 1989). The flux spectrum (from near Søndre Strømfjord) published in that

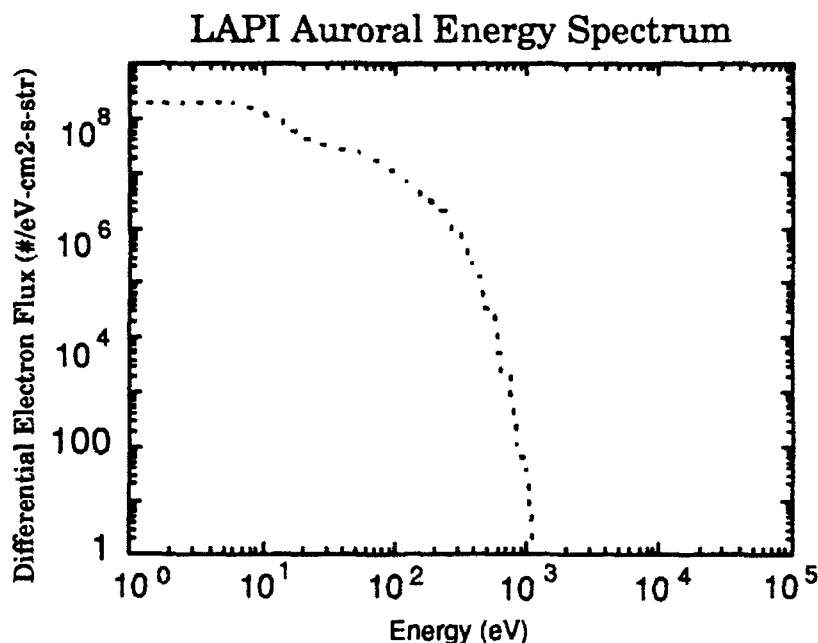


Figure 3.5 Illustration of the auroral electron energy flux that is added to the top of the atmosphere in the photoelectron model, thereby mimicking a diffuse aurora in the 7320Å volume emission rate model.

paper is nearly identical to the LAPI spectrum show in Figure 3.5. The HiLAT spectrum shows a flux of  $\sim 100$  electrons/cm<sup>2</sup>-s-ster-eV at 1000 eV,  $\sim 10^7$  electrons/cm<sup>2</sup>-s-ster-eV at 100 eV and  $\sim 10^8$  electrons/cm<sup>2</sup>-s-ster-eV at 10 eV. These values compare very favorably with those seen in Figure 3.5. Hence, when the 7320Å volume emission rate model is run between  $\sim 55 - 75^\circ$  geographic latitude, the LAPI spectrum is inserted into the electron transport code where it is treated the same as the photoelectron spectrum; the resulting energy cascade allows for considerably more 7320Å volume emission rate production than in the previously discussed version of the airglow model (Chapter 3.3.1). If profiles are created for areas outside this

55 - 75° auroral zone, this auroral-airglow model simply reduces to the airglow model. Figure 3.6 shows the airglow-only model of Chapter 3.3.1 in the auroral zone (top panel); note that photoionization is the dominant source at twilight. Figure 3.6 (bottom panel) shows this section's aurora-airglow model in the auroral zone for the same conditions. The bottom panel more nearly represents the observed 7320Å emission rate in the aurora (Smith et al., 1982). The long optical path in this case allows for enhanced electron impact ionization, relative to photoionization (Rees et al., 1982). Figure 3.7 is a model run for the same location but at active conditions.

One should note that the 7320Å emission peaks at a higher altitude during the active conditions since enhanced EUV/UV and energetic particle precipitation heat the thermosphere through absorption and collisions, causing the thermosphere to expand. This expansion means the atomic oxygen density will peak at higher altitudes, thereby meaning the 7320Å emission will peak at higher altitudes (recall that a Chapman layer is the integrated product of the ionizing flux and the neutral number density). Also, results from the auroral zone profiles (as opposed to the airglow-only ones) more closely match the profiles determined from much more sophisticated airglow models, such as the one created by Torr et al. (1990a,b).

Because of the conditions in which the auroral electrons were measured, this aurora-airglow model must be considered a diffuse auroral model. Low energy (20 - 100eV) electron precipitation is the source for the 7320Å volume emission rate since higher energy auroral particles do produce 7320Å, but the emission is masked by the lower and stronger N<sub>2</sub> 1P

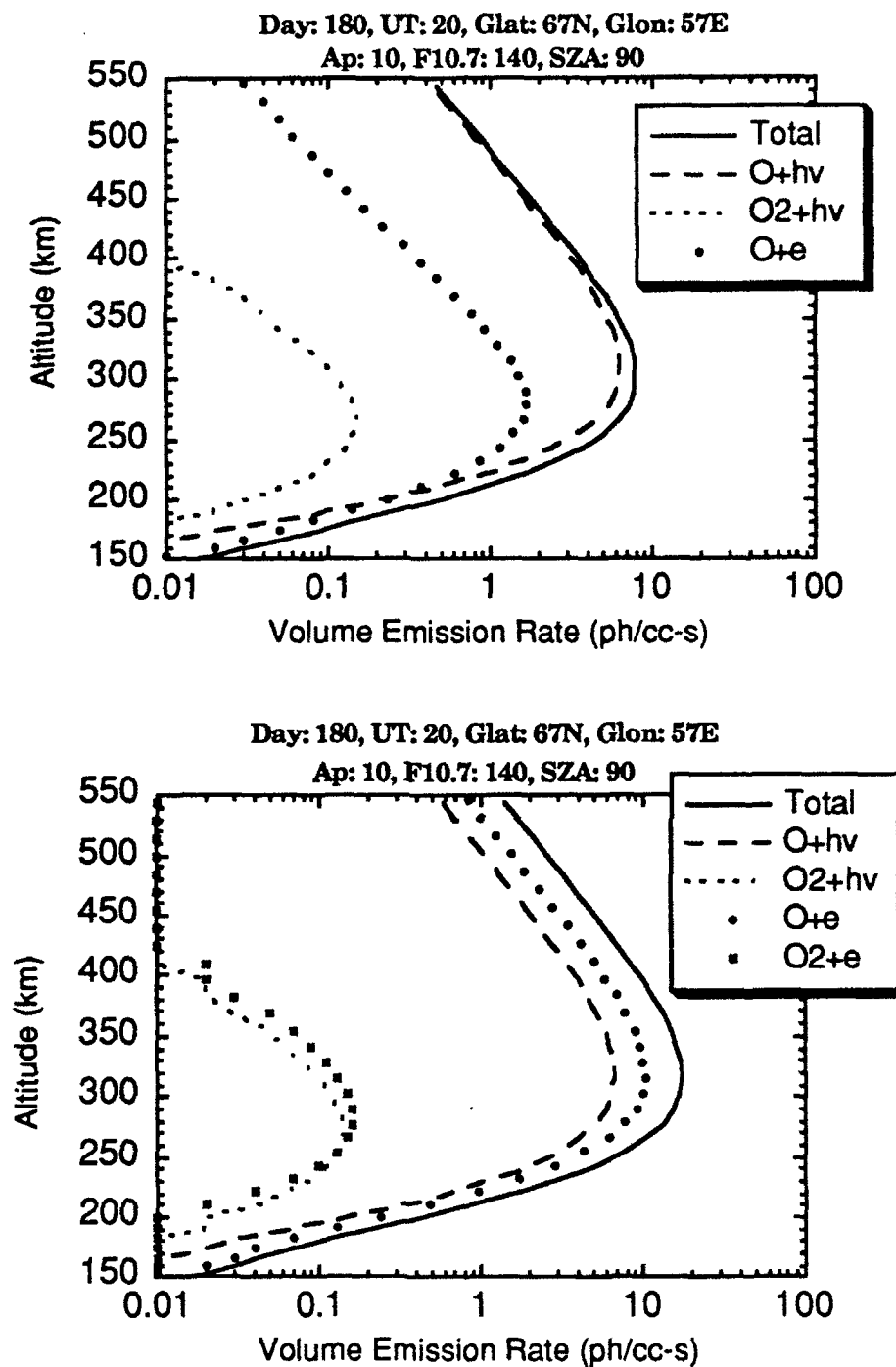


Figure 3.6 Illustration of the LAPI addition to the airglow model. In the top panel, no LAPI data is added and the airglow model produces output smaller than expected. The bottom panel includes the added LAPI data and more accurately predicts results found in the literature (Smith et al., 1982; Rees et al., 1982).

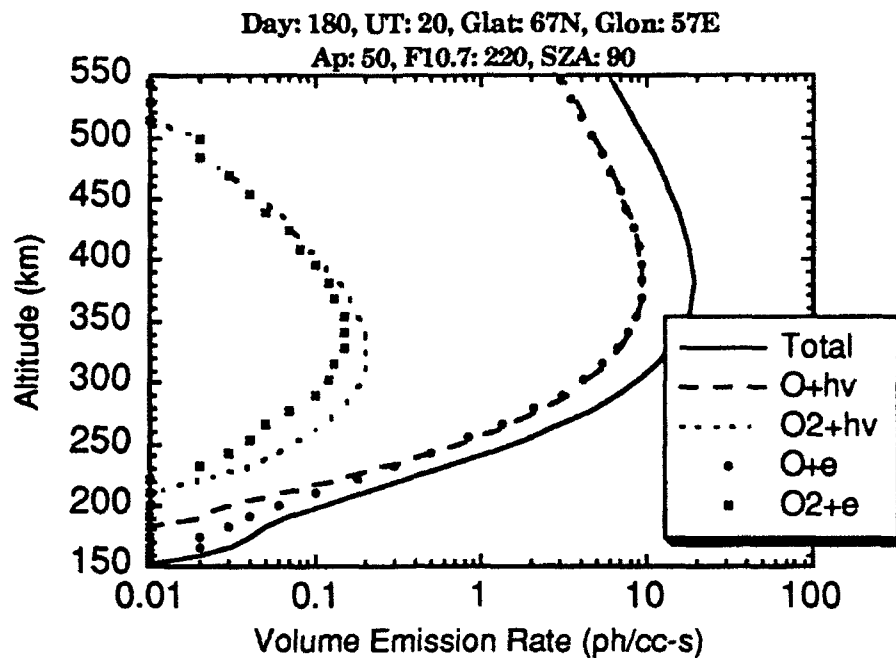


Figure 3.7 Magnetic and solar conditions are "active" and photoionization/electron impact ionization are nearly equal contributors to the 7320Å volume emission rate.

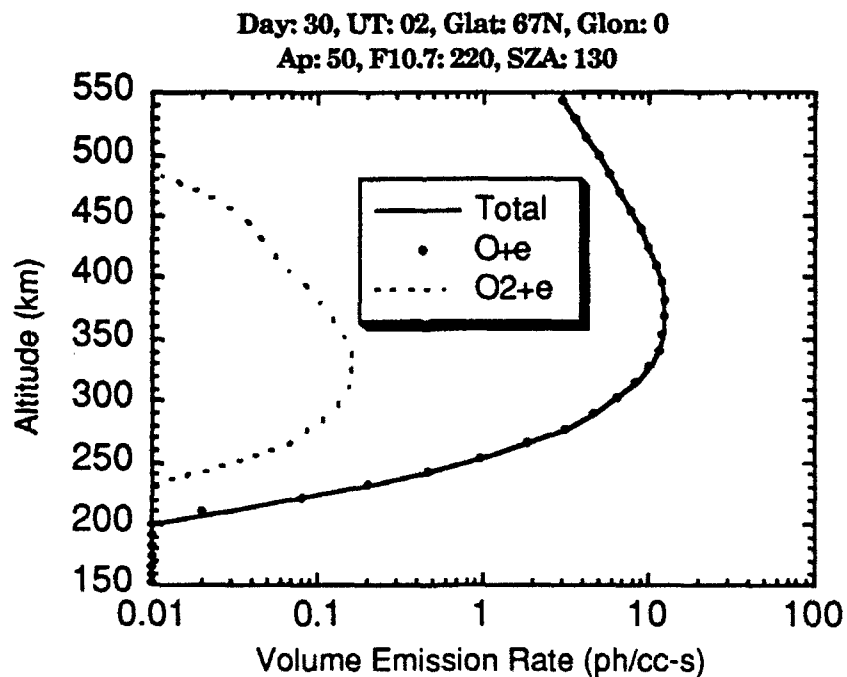


Figure 3.8 Illustration of the auroral zone 7320Å volume emission rate during active times.

system (Smith et al., 1982; Rees, 1989). Figure 3.8 illustrates auroral particle production of the 7320Å emission at high latitudes for active conditions. The profiles agree favorably with discussions in the literature (Smith et al., 1982; Rees, 1989; Torr et al., 1990a,b).

To show the accuracy of this model, I present the following three figures. Figure 3.9 is from Torr et al. (1990a); in this paper, they discuss a midlatitude interhemispheric model of the  $O^+(^2P)$  7320Å emission. They present  $O^+(^2P)$  production rates for 28 Nov at 11.16 local time and 48S geographic latitude. The conditions were  $A_p = 8$  and  $F_{10.7} = 89$ . As is customary in the aeronomy community, Torr et al. assumed  $O^+(^2P)$  losses to be by radiation and quenching due to atomic oxygen, molecular nitrogen and electrons. I did the same. Figure 3.10 is an example of the production rates from the aurora-airglow model. The comparison is quite good, except near 150km, where my model is slightly greater than the one of Torr et al. (1990a). This may be because I do not have all of their boundary conditions for the run they used. However, I am only concerned with the results above the quenching zone (>180km). Figure 3.11 is an example of the total 7320Å volume emission rate produced by the aurora-airglow model for the same conditions. It seems to peak ~300km with a value ~15 - 16 photons  $cm^{-3} s^{-1}$ , which are approximately the values Torr et al. (1990a) get in their Figure 2.

Figures 3.9 - 3.11 show profiles outside the auroral zone; hence, the aurora-airglow model reduces to the airglow-only model of Chapter 3.3.1. Torr et al. (1990a) explicitly state that their model is valid for  $\Lambda < 5$  (where  $\Lambda = 1/\cos(\theta)^2$ , where  $\theta$  = geomagnetic latitude), which may or may not contain auroral latitudes. In their Figure 2, auroral latitudes are included in the plot. Figure 3.12 is an example of auroral latitude output from my aurora-



airglow model. The conditions are the same, but in this case, I run the model at 68S. The Torr et al. (1990a) model predicts 7320Å volume emission rates at ~ 300 - 350 km to be between ~ 7.9 - 15.8 photons per  $\text{cm}^3 \cdot \text{s}$ . My model is within this range, and it only takes 53 seconds to run and produce the plot seen in Figure 3.12.

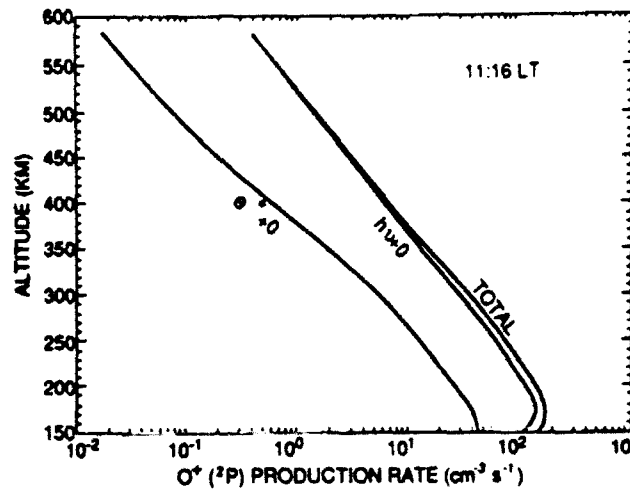


Figure 3.9  $\text{O}^+(2\text{P})$  production rates for 28 November at 11.16 local time and 48S latitude. The conditions were  $F_{10.7} = 89$  and  $A_p = 5$  (After Torr et al., 1990a).

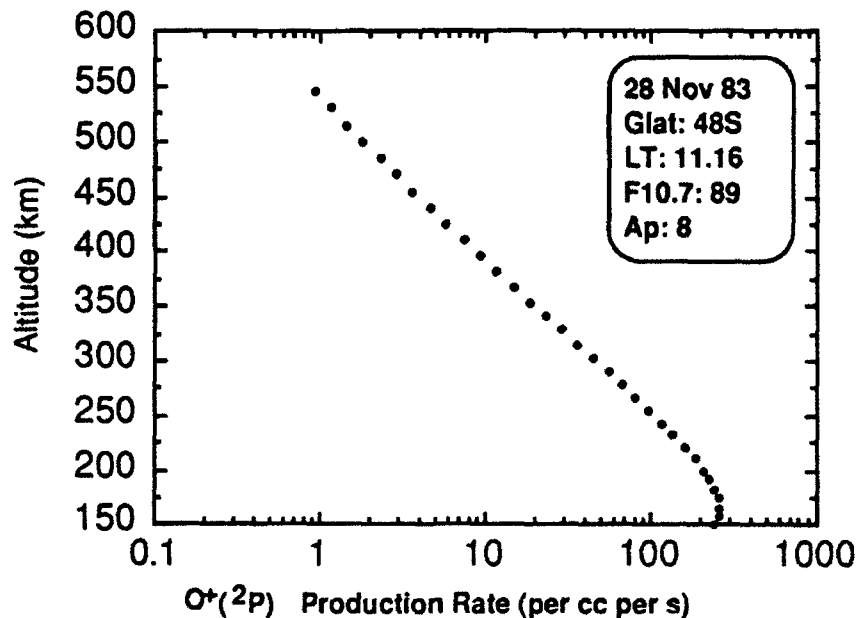


Figure 3.10  $\text{O}^+(2\text{P})$  production rates from the aurora-airglow 7320Å volume emission rate model for the same conditions as in Figure 3.10. Note the excellent agreement.

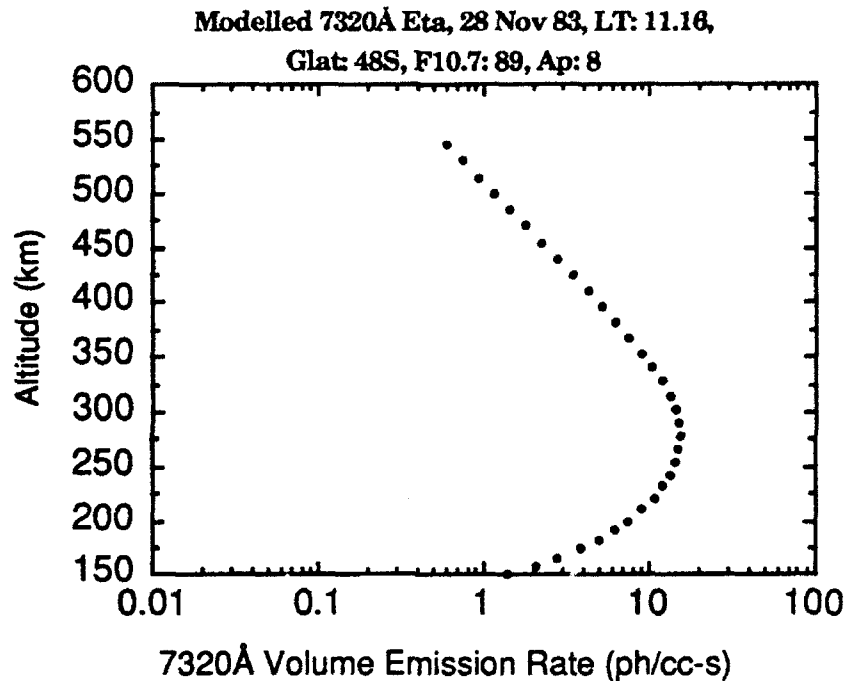


Figure 3.11 7320Å volume emission rate profile for the same conditions as the previous two figures. The peak appears  $\sim 300$  km to be  $\sim 15$  - 16 photons per  $\text{cm}^3 \text{ s}^{-1}$ ; this compares extremely well with the 3-dimensional color plot in Figure 2 of Torr et al., 1990a.

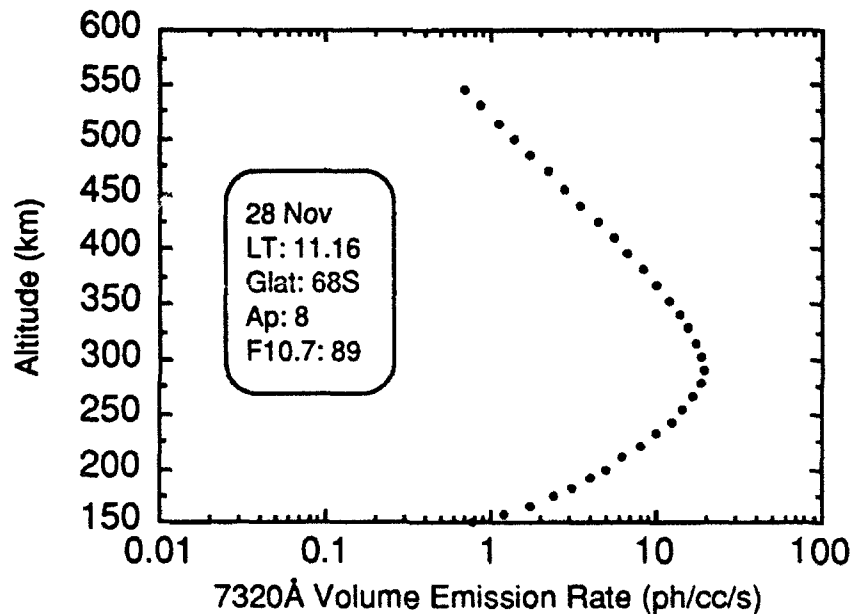


Figure 3.12 7320Å volume emission rate profile for 28 Nov at 11.16 local time and 68S latitude. The conditions were  $A_p = 8$  and  $F_{10.7} = 89$ . The comparison with Figure 2 in Torr et al. (1990a) is excellent.

The peak volume emission rate in Figure 3.12 is 18.9 - slightly higher than the Torr et al. (1990a) model. This is because of the addition of the LAPI data to simulate a diffuse aurora and the fact that the Torr et al. (1990a) model is designed to be a low- and mid-latitude model.

Figure 3.13 is an example of active and quiet  $O^+(^2P)$  concentrations. Again, as the activity increases, the thermosphere expands; this expansion allows the atomic oxygen, now existing at higher altitudes, to be ionized at those altitudes, thereby producing the  $O^+(^2P)$  number density enhancement. From the discussions and graphs in this section, it is apparent that this aurora-airglow version of the model agrees with theory, observations and other models. Therefore, this version of the model will be the one used throughout the remainder of the dissertation and will be referred to as the volume emission rate model.

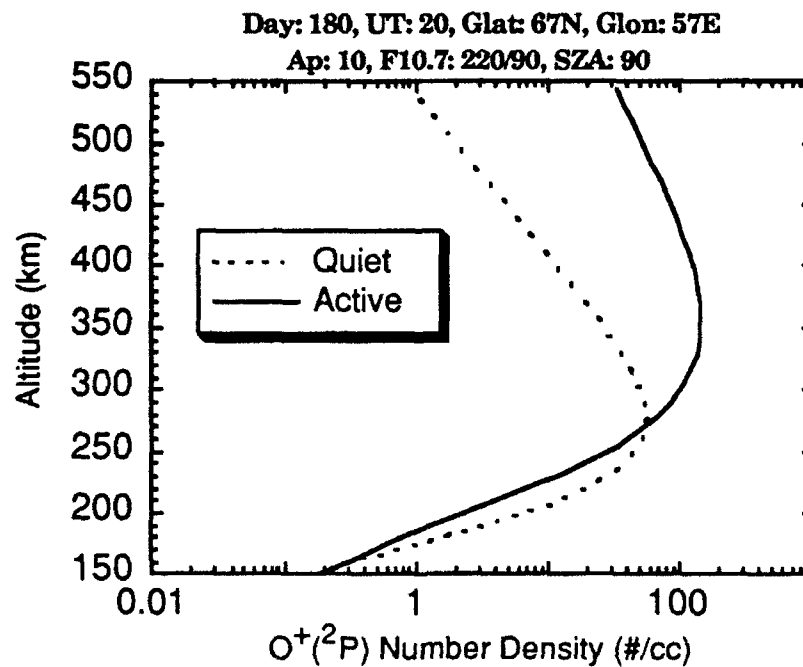


Figure 3.13  $O^+(^2P)$  concentrations modelled during moderately quiet and active periods of solar activity.

### 3.3.3 Maxwellian Model

In this version of the model, I add an auroral electron spectrum to the code in the same fashion the LAPI data is added in Chapter 3.3.2. Instead of using real data, however, I use a routine that generates a Maxwellian electron spectrum with a low energy tail that is supposedly representative of auroral electron energy distributions. To create the desired spectrum, the user inputs the desired auroral flux (i.e.  $1 \text{ erg cm}^{-2} \text{ s}^{-1}$ ) and the desired top range of energy (i.e. 1 keV). The spectrum is then added, along with the photoelectron spectrum, to the electron transport code, which feeds its results into the 7320Å volume emission rate model. This Maxwellian version of the model, while very accurate both inside and outside the auroral zone, is very time consuming - and when the model is made global, too much computer time is used. The aurora-airglow model in Chapter 3.3.2 is faster, is actual data and is usually more accurate when compared to other models or observations.

An example of the Maxwellian version of the 7320Å volume emission rate model is in Figure 3.14. Note that the Maxwellian model in this case slightly underestimates the impact ionization rate that the LAPI model determined in Figure 3.6. Of course, I can input any electron flux and energy with this version.

### 3.3.4 Global 7320Å Model

Instead of plotting 7320Å volume emission rate profiles, I devised a model (the aurora-airglow model version is usually used) that loops over latitudes and longitudes and outputs a global contour map of the 7320Å volume emission rate at a given height for a given date, time and

geophysical conditions. I binned the calculations by  $5^\circ$  geographic latitude and  $5^\circ$  geographic longitude and plot the volume emission rate at 300km (although any altitude range between 90 - 550 km could be used). I then plot the results in a variety of ways.

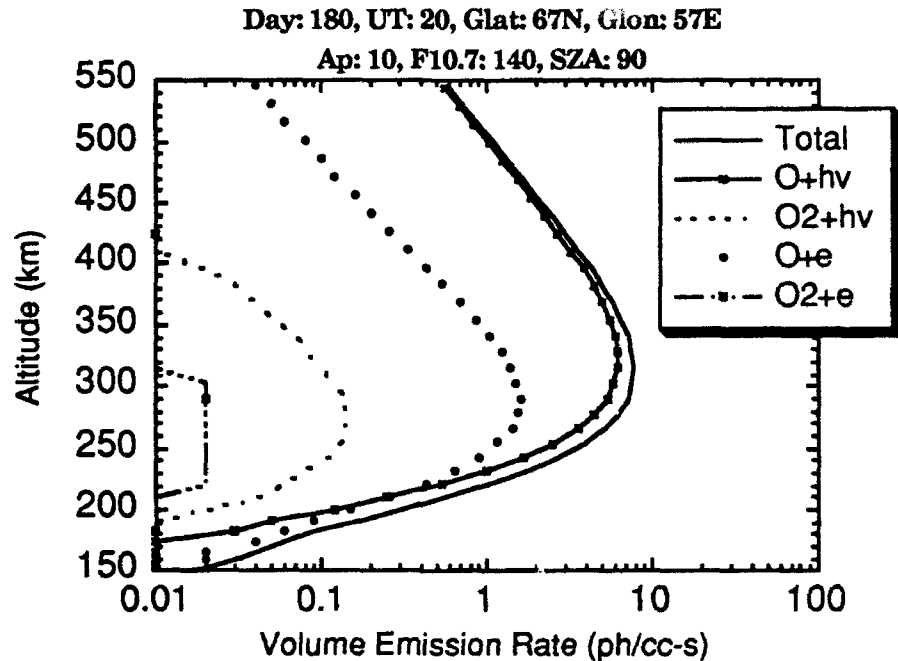


Figure 3.14 7320Å volume emission rate profiles using a Maxwellian distribution of auroral particles instead of the observed LAPI data. This version of the model consistently yielded larger high latitude 7320Å emissions than the airglow-only version, but less than the auroral-airglow version. It also took too much computer time to do global modelling.

Figure 3.15 is a 3-dimensional 7320Å volume emission rate plot. Note that the emission peaks where one would expect it - where the solar zenith angle is smallest and at ~300km. Figure 3.16a is a 7320Å contour map at 300km for day 180, UT 12 and the conditions listed on the figure; VSH ion drifts are overplotted. The 7320Å volume emission rate has an obvious solar zenith angle dependence, as expected; it also has a curious waveform appearance. Figure 3.16b is a VSH plot of atomic oxygen concentrations and ion drifts for the same conditions as Figure 3.16a. Note that the wavy contours in the 7320Å volume emission rate seen in Figure 3.16a are merely

following the troughs and ridges seen in the atomic oxygen number density of Figure 3.16b. Hence, the study of 7320Å volume emission rates, whether observed or modelled, will also give insight into the F2-Region's atomic oxygen concentration.

Figures 3.17a, b and c are contour maps of the 7320Å emission at 15UT for days 180 (~summer solstice), 360 (~winter solstice) and 90 (~spring equinox), respectively, with VSH drifts (for identical conditions) overplotted. Day 270 (autumnal equinox) results are exactly the same as those of day 90. For comparison, Figure 3.17d contains VSH plots of atomic oxygen concentrations corresponding to the days and conditions in Figures 3.17a, b, c. The accuracy of this model will help with the development of a new observing platform described in Chapter 6.

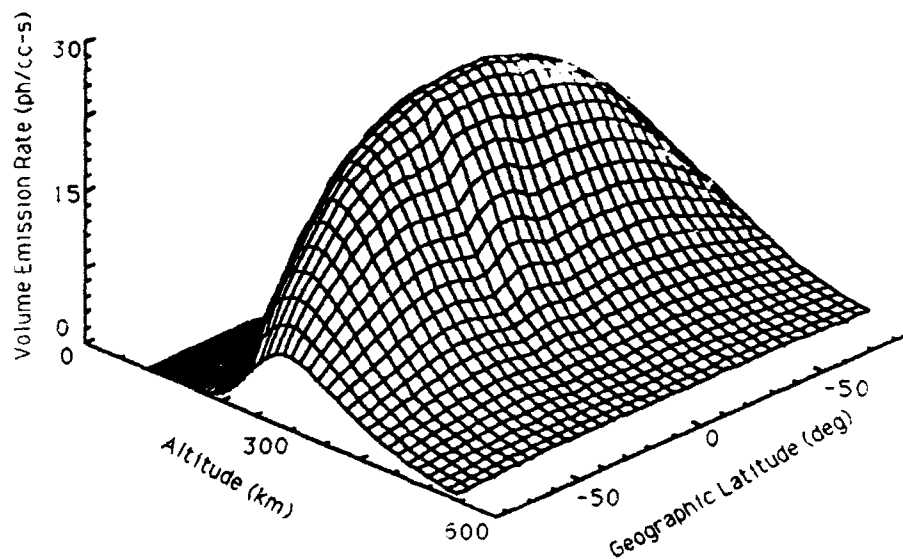
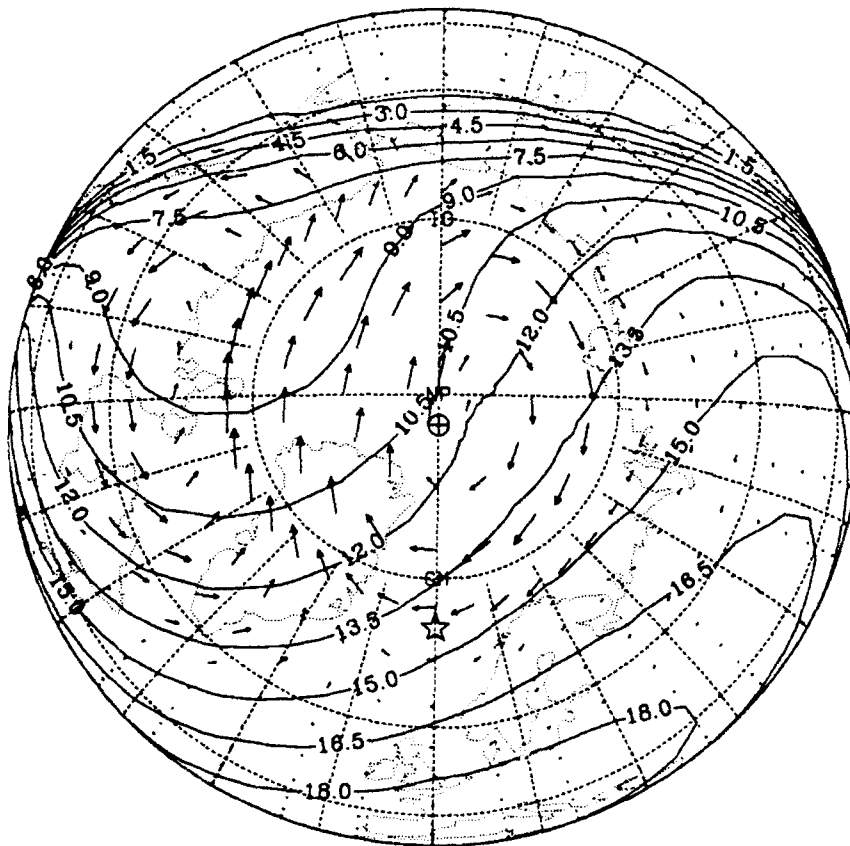


Figure 3.15 Three dimensional plot of the 7320Å volume emission rate. The conditions were 1 April at 12 UT, 0° longitude,  $A_p = 8$ ,  $F_{10.7} = 140$ .

[OII] 7320Å Eta (ph/cc-s)  
VSH ION DRIFT (M/S)

⊕ at ( 87.5, 0.0)  
( 2.0 earth radii)



### GEOGRAPHIC COORDINATES

ALT=300.0 AP= 10.0 F10.7=140.0 JDAY=180 UT=12.0

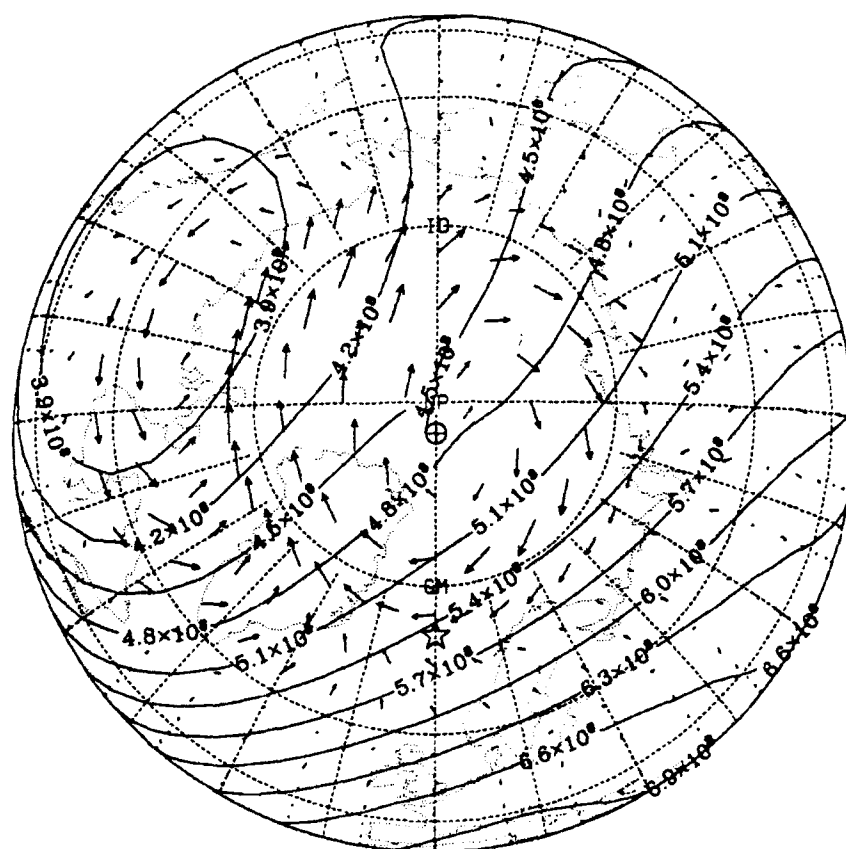
1000 M/S



Figure 3.16a Global contour map of the 7320Å volume emission rate for day: 180, UT: 12 and the conditions listed on the figure. VSH ion drifts are overplotted. Latitudes are geographic with the outermost dial being ~45N latitude. The bottom of the dial, along the Greenwich Meridian, is 12LST (local solar time), while the top of the dial is 00LST. The right side of this dial (the dusk side) is at 90° longitude (18LST), while the left side of the dial (the dawn side) is at -90° longitude (06LST).

VSH O NUMBER DENSITY (#/CM3)  
VSH ION DRIFT (M/S)

⊕ at ( 87.5, 0.0)  
( 2.0 earth radii)



GEOGRAPHIC COORDINATES

ALT=300.0 AP= 10.0 F10.7=140.0 JDAY=180 UT=12.0

1000 M/S

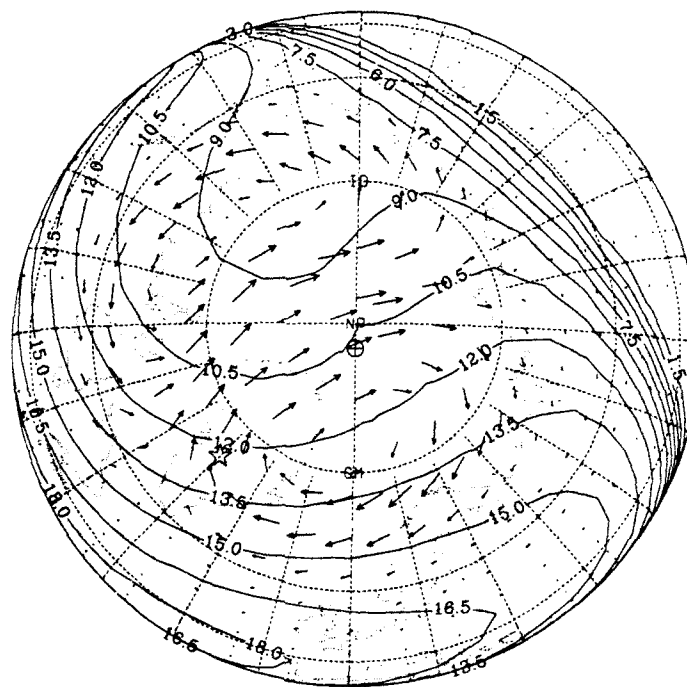


Figure 3.16b VSH atomic oxygen concentrations ([O]) and ion drifts for the same conditions as Figure 3.16a. The 7320Å volume emission rate has a solar zenith angle dependence but is also strongly controlled by the pattern of [O] seen in this figure (compare to Figure 3.16a).



[OII] 7320Å Eta (ph/cc-s)  
VSH ION DRIFT (M/S)

⊕ at ( 87.5, 00 )  
( 2.0 earth radii)



GEOGRAPHIC COORDINATES

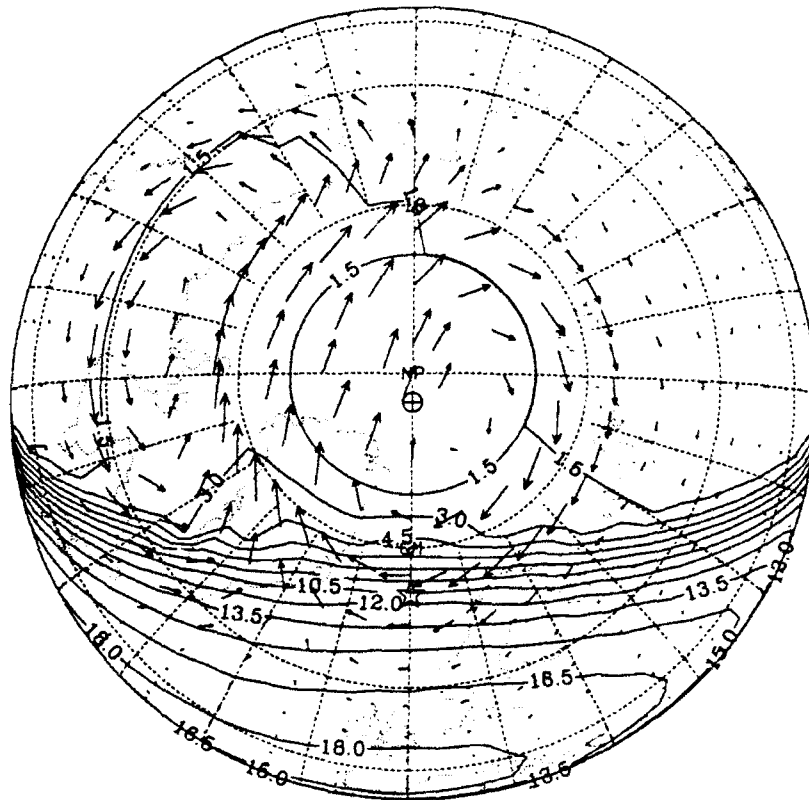
ALT=300.0 AP= 10.0 F107=140.0 JDAY=180 UT=15.0

1000 M/S  
→

Figure 3.17a Global contour map of the 7320Å emission for day: 180, UT: 15 and the conditions listed on the figure. VSH ion drifts are overplotted.

[OII] 7320Å Eta (ph/cc-s)  
VSH ION DRIFT (M/S)

⊕ at ( 87.5, 0.0)  
( 2.0 earth radii)



GEOGRAPHIC COORDINATES

ALT=300.0 AP= 23.0 F10.7=120.0 F10.7A=120.0 JDAY=360 UT=12.0

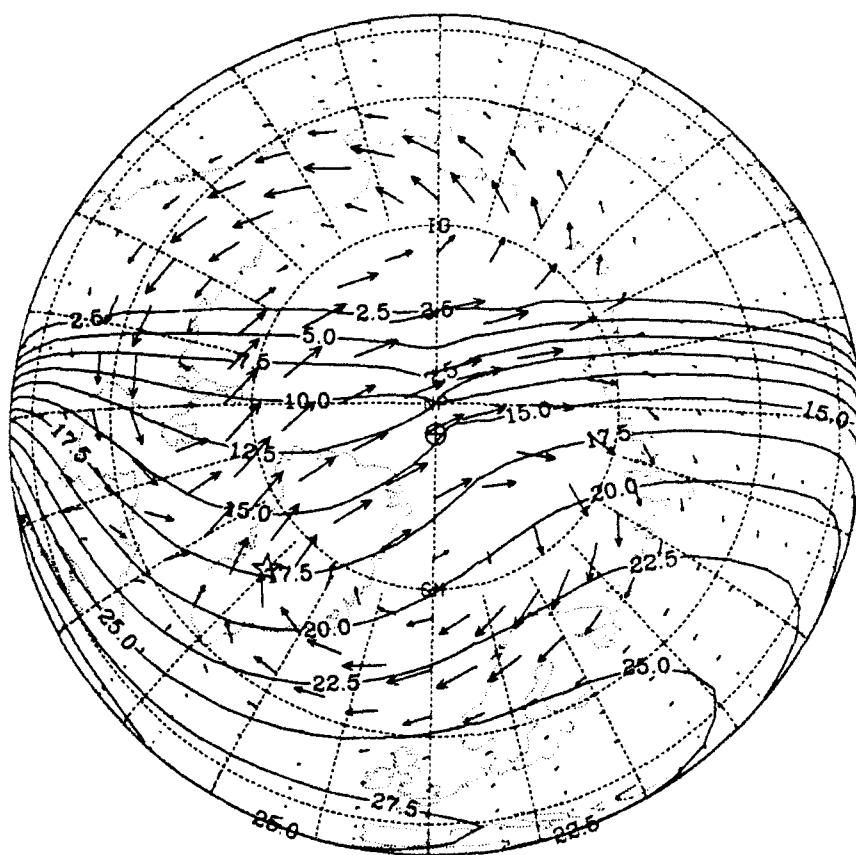
1000 M/S



Figure 3.17b Global contour map of the 7320Å emission for day: 360, UT: 15 and the conditions listed on the figure. VSH ion drifts are overplotted. Note auroral source of the 7320Å emission (via electron impact ionization) in the high latitude dawn and early morning sector.

[OII] 7320Å Eta (ph/cc--s)  
VSH ION DRIFT (M/S)

⊕ at ( 87.5, 0.0)  
( 2.0 earth radii)



# GEOGRAPHIC COORDINATES

ALT=300.0 AP= 23.0 F10.7=180.0 JDAY= 90 UT=15.0

1000 M/S



Figure 3.17c Global contour map of the 7320Å emission for day 90, UT: 15 (spring equinox) and the conditions listed on the figure. VSH ion drifts are overplotted. Volume emission rate and [O] for this date are the same as day 270 (autumnal equinox).

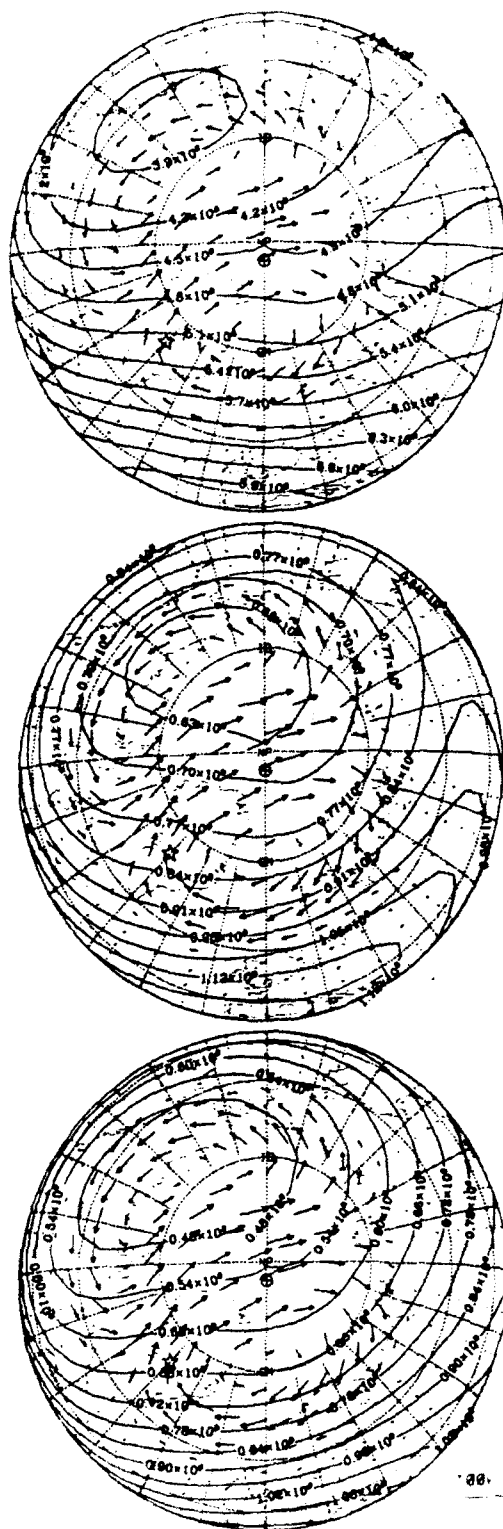


Figure 3.17d Top panel: VSH [O] and ion drifts for day: 180, UT: 15. Middle panel: VSH [O] and ion drifts for day: 360, UT: 15. Bottom panel: VSH [O] and ion drifts for day: 90, UT: 15. Compare these [O] patterns to the corresponding 7320Å volume emission rate patterns in Figures 3.17a-c.

### 3.4 Retrieving Atomic Oxygen Densities from [OII] $\lambda 7320\text{\AA}$ Airglow

Knowledge of thermospheric neutral concentrations is important for understanding thermospheric and ionospheric structure. This structure is primarily determined by atomic oxygen densities between  $\sim 225\text{km} - 500\text{km}$  since atomic oxygen is the dominant constituent in that region. In the aeronomy community, there is considerable interest in using ground- or space-based measurements of the  $7320\text{\AA}$ -doublet emission to routinely monitor atomic oxygen densities in the upper thermosphere. Since atomic oxygen plays a vital role in the dynamics and energetics of the thermosphere *and* is affected by human activity (Roble and Dickinson, 1989), more study of this atomic species is obviously necessary. From a practical standpoint, accurate knowledge of atomic oxygen concentrations is necessary for the calculation of atmospheric drag on satellites, for the estimation of deterioration of satellite surface materials due to oxidation (Fennelly et al., 1991) and for precision radar and radio communications. Also, large thermospheric and ionospheric empirical models can be improved if atomic oxygen densities can be consistently ingested for several years.

In a pioneering effort, Meriwether et al. (1978) showed that changes in the neutral thermospheric composition were reflected in the  $7320\text{\AA}$  emission. Fennelly et al. (1991) described an inversion technique for the extraction of thermospheric atomic oxygen concentrations from ground-based observations of the  $7320\text{\AA}$ -doublet emission. McDade et al. (1991) adopted a similar approach to that of Fennelly et al. (1991). These two inversion processes, described in this section, will enable the routine

monitoring of thermospheric atomic oxygen concentrations from the measurement of 7320Å emissions.

One limitation of atomic oxygen density retrievals from 7320Å emissions is that one needs information about the solar EUV flux at the time of the observation. This is a problem since there are only limited plans to resume EUV monitoring in the near future. The inversion technique of Fennelly et al. (1991) is very robust, and most promising, but information about the solar EUV flux at the time of observation is necessary.

Ground-based twilight observations are frequently made by viewing at a low angle and in the direction of the sun in order to maximize the airglow component and minimize the background component due to scattering in the lower atmosphere (Niciejewski, p.c., 1991). Brightnesses measured at a specific solar depression angle on the ground will therefore increase if the ionizing flux increases or if the atomic oxygen densities increase (McDade et al. 1991). Hence, it is difficult to determine if the large emission rate measured in the sunward direction is due to enhanced EUV flux or atomic oxygen abundances. Thus, one can only infer oxygen atom densities if the EUV flux is known. McDade et al. (1991) demonstrate that if twilight measurements are made toward the sun *and* in the zenith, then it is possible to recover information about both thermospheric oxygen atom densities and the unattenuated  $O^+(^2P)$  ionization frequency. Their proposal overcomes the need for solar EUV flux information.

According to the photochemistry outlined in Chapters 1.11 and 3.1, loss of the  $O^+(^2P)$  ion is primarily determined by molecular nitrogen, atomic oxygen and electron quenching, or radiation. At low altitudes, loss is dominated by atomic oxygen and nitrogen quenching; at higher altitudes, where electron quenching makes its contribution, radiation is the

dominant process. For simplicity, one can therefore neglect electron quenching. The 7320Å volume emission rate, at altitude  $z$  and solar depression angle  $\theta$  is:

$$\begin{aligned}\eta(z, \theta)_{7320\text{\AA}} &= \frac{(A_\lambda)(\gamma)(P(z, \theta))}{\{A_\lambda + k_O[O]_z + k_{N_2}[N_2]_z\}} \\ &= \frac{(0.097)(P(z, \theta))}{\{A_\lambda + k_O[O]_z + k_{N_2}[N_2]_z\}}\end{aligned}\quad 3.24$$

where the  $k$  terms are the quenching rate coefficients of the  $O^+(^2P)$  ion by atomic oxygen and molecular nitrogen,  $A_\lambda$  is the transition probability (Einstein coefficient or inverse radiative lifetime) of the  $^2P$  state ( $0.219s^{-1}$ ),  $\gamma$  is the branching ratio for the emission in the  $O^+(^2P_{1/2,3/2} - ^2D_{5/2})$  doublet at 7320Å ( $\sim 0.44$ ) and  $P(z, \theta)$  is the local  $O^+(^2P)$  production rate. The rate of  $O^+(^2P)$  production due to photoionization by EUV centered on wavelength  $\lambda_i$  is

$$P_i(z, \theta) = ([O]_z)(\kappa_i)(F_-)\exp[-\tau_i(z, \theta)] \quad 3.25$$

where  $\tau_i$  is the optical depth for the radiation at  $\lambda_i$ ,  $\kappa_i$  is the fraction of substate contribution in proportion to their statistical weights (i.e., 1/3 for  $O^+(^2P_{1/2})$ , 2/3 for  $O^+(^2P_{3/2})$ ), and  $F_-$  is the unattenuated solar EUV radiation. Hence, the total  $O^+(^2P)$  production rate is obtained by summing  $P_i(z, \theta)$  over all wavelength intervals that contribute to  $F_-$ . Since most EUV flux attenuation in the thermosphere is due to absorption by molecular nitrogen and atomic oxygen, the optical depth may be written as:

$$\begin{aligned}\tau_i(z, \theta) &= \{([O]_{min})(H_O)(\sigma_i^O)(Ch(\theta, H_O))\} \\ &\quad + \{([N_2]_{min})(H_{N_2})(\sigma_i^{N_2})(Ch(\theta, H_{N_2}))\}\end{aligned}\quad 3.26$$

where  $\sigma_1^{\text{O}}$  and  $\sigma_1^{\text{N}_2}$  are the total O and N<sub>2</sub> photoionization cross sections at  $\lambda_i$ ,  $\text{Ch}(\theta, H)$  is the Chapman function grazing incidence and  $[\text{O}]_{\text{min}}$  and  $[\text{N}_2]_{\text{min}}$  are the O and N<sub>2</sub> number densities at the minimum ray height of the grazing solar radiation.

By substituting Equations 3.25 and 3.26 into 3.24 and integrating the volume emission rate along the appropriate line-of-sight, the twilight 7320Å emission rates may be expressed in terms of  $F_{\infty}$ ,  $H_0$ ,  $[\text{O}]_{300}$ ,  $[\text{N}_2]_{300}$ , where 300km is an arbitrary reference altitude. McDade et al. (1991) used a standard nonlinear fitting routine to find the values of the four parameters that best reproduced a given set of twilight observations. Since most 7320Å emissions come from above ~200km, McDade et al. (1991) assumed that oxygen atom densities may be approximated by a single exponential profile and that the oxygen atom density at any altitude can therefore be expressed in terms of  $H_0$  and the oxygen atom density at a reference altitude (300km). They also assumed that N<sub>2</sub> may be expressed by an exponential profile whose scale height is  $16/28 H_0$ .

Inverse problems are extremely sensitive to noise in the data; this noise may be errors or uncertainties resulting from experimental procedures. A major experimental difficulty of ground-based 7320Å twilight FPI measurements is the problem of isolating the desired feature from (often dominant) Rayleigh scattered sunlight. Other uncertainties are the rate coefficients and cross sections. For example, note that  $k_{\text{N}_2} = (4.8 \pm 1.4) \times 10^{-10} \text{ cm}^3 \text{ s}^{-1}$  and  $k_{\text{O}} = (5.2 \pm 2.5) \times 10^{-11} \text{ cm}^3 \text{ s}^{-1}$  (from Rusch et al., 1977). The most commonly used cross sections for photoionization into  $\text{O}^+(^2\text{P})$  are found in Richards and Torr (1988); spectral shapes can be found in Hinteregger (1977).



Doing inversions on the 7320Å observations presented in Chapters 4 - 6 in order to retrieve thermospheric atomic oxygen densities is beyond the scope of this dissertation; but for completeness, it was necessary to mention what could be done in the future with these promising inversion techniques and routine 7320Å emission observations. Figure 3.18 is an example of atomic oxygen number densities derived from the aurora-airglow 7320Å volume emission rate model for the conditions listed in the figure (bottom panel). The top panel is VSH output for identical conditions. Agreement is good.

In their respective papers, McDade et al. (1991) and Fennelly et al. (1991) use *models* of the 7320Å emission. In Chapter 4, I present the first ever *space-based FPI (7320Å) observations*, and in Chapter 5, I present *ground-based FPI (7320Å) observations* from a high-latitude site. These high latitude ground-based FPI (7320Å) observations could be routinely made from ~ September - April every year. In Chapter 6, I introduce a *proposed space-based FPI (7320Å) system*. Hence, with these current and future databases of the 7320Å emission, a better understanding of upper thermospheric atomic oxygen concentrations can be developed.

The inversion technique of McDade et al. (1991) is a simple algorithm that neglects electron sources for the  $O^+(^2P)$  ion; the authors state it could be modified to include photoelectron sources. It now executes in several minutes on a personal computer and would therefore be ideal for use at a remote observing site like Søndre Strømfjord where computing facilities are limited. The similar but more complex algorithm of Fennelly et al. (1991) includes photoelectron sources but is very computationally demanding and needs solar EUV flux information at the observation time for reliable retrieval of oxygen atom densities. In the future, the robust system of

Fennelly et al. (1991) could be used to retrieve oxygen atom densities from the space-based FPI system proposed in Chapter 6 if a device were mounted on the satellite that routinely monitored solar EUV fluxes.

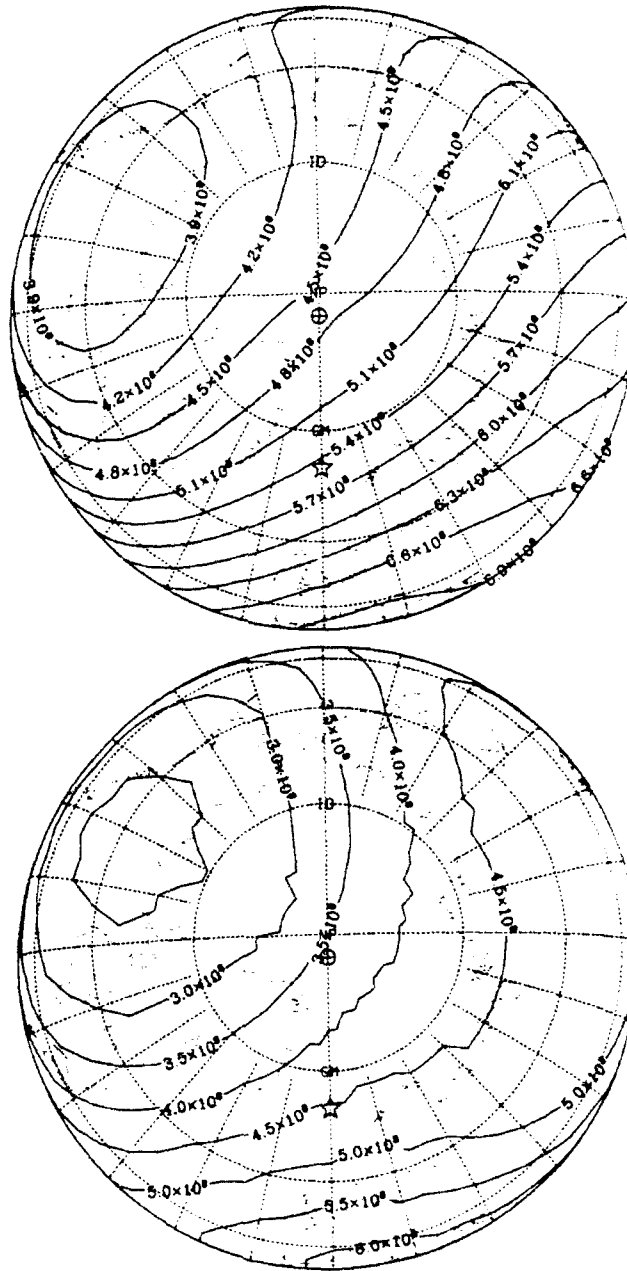


Figure 3.18 Top panel: VSH atomic oxygen number densities plotted for the following conditions - day 180, UT 12, Ap 10, F10.7 140. Bottom panel: plot of atomic oxygen number densities derived from the 7320Å auroral airglow model for the same conditions; good agreement between the two models exists.

### 3.5 Conclusions

Photoionization dominates electron impact ionization by about a factor of 10 as the primary source of the 7320Å emission in dayglow; not until twilight does electron impact ionization become an equally important source for this emission. At night, the 7320Å emission disappears, except in the auroral zones and polar cusp areas where electron impact ionization can be a source of the 7320Å emission. As the solar zenith angle decreases, the 7320Å volume emission rate increases and lowers in altitude due to an increase in solar EUV penetration and an increase in atomic oxygen number densities at lower altitudes. As solar activity increases, neutral atmospheric expansion occurs, enhancing atomic oxygen number densities at higher altitudes; this leads to a larger 7320Å volume emission rate at higher altitudes. The production of  $O^+(^2P)$  by photoionization or electron impact ionization of molecular oxygen was found to be small compared to that of atomic oxygen and can be ignored without noticeable loss in 7320Å modelling accuracy.

Four versions of the 7320Å volume emission rate model exist. The *airglow model* is the simplest of the four and is only valid outside of the auroral regions since it has no means by which to calculate the aurorally produced 7320Å volume emission rate. The *aurora-airglow model* includes a diffuse auroral electron spectrum (measured by the LAPI on DE 2) in its determination of the 7320Å volume emission rate if the user-desired latitude is between 55° - 75° geographic latitude. If the desired latitude is out of this range, this version of the model reduces to the airglow model.

The aurora-airglow model is the most accurate version and is used throughout the remainder of this dissertation. The calculated 7320Å

volume emission rate from the aurora-airglow model compares very favorably with the model of Torr et al. (1990a,b) at all locations and conditions. The accuracy of the aurora-airglow model is directly responsible for the success of the simulated satellite flight and FPI observations found in Chapter 6. The *Maxwellian model* adds a Maxwellian electron spectrum with a low energy tail (similar to auroral electron distributions) to the volume emission rate model in order to determine the aurorally-produced 7320Å volume emission rate. This model is accurate, but time-consuming, and is not used again in this work. The *global 7320Å model* simply uses the aurora-airglow model and loops over latitudes and longitudes for the user-desired conditions and produces global contour maps of the 7320Å emission, at a specified altitude.

-

## CHAPTER 4

### REMOTE-SENSING OBSERVATIONS OF F-REGION ION DRIFTS, ION TEMPERATURES AND BRIGHTNESSES USING DYNAMICS EXPLORER-2 DOPPLER MEASUREMENTS OF THE [OII] 7320Å EMISSION

There are three major sources of thermospheric and ionospheric energy input: solar EUV, energetic particle precipitation (and concomitant Joule heating) and wave energy transported up from the planetary boundary layer. Uncertainties about these energy sources, and their role in thermospheric and ionospheric dynamics and energetics, exist. A more complete understanding of ionospheric drift and temperature fields will give us more insight into the problem of understanding how heat deposited into the thermosphere is dissipated.

Limb-scan observations of Doppler line profiles from the [OII]  $\lambda 7320\text{\AA}$  emission at F-Region altitudes, made with the Fabry-Perot interferometer (FPI) on the Dynamics Explorer-2 (DE-2) spacecraft, have been analyzed to provide measurements of the meridional component of the ion convection velocity along the instrumental line-of-sight. The initial DE-2 results presented here demonstrate the first spaceborne use of the remote-sensing Doppler technique for measurements of ionospheric convection. The FPI meridional ion drift measurements have been compared with nearly simultaneous *in situ* ion drift measurements from the retarding potential

analyzer (RPA) on DE 2. Once allowance is made for the temporal lag between the *in situ* and remote measurements, the results from the two techniques are found to be in good agreement within specified experimental errors, giving confidence in the FPI measurements. The spaceborne interferometric technique has future utility for 2-dimensional imaging of polar ionospheric convection. Results of a simulation study based on the DE-2 technique are presented in Chapter 6 and demonstrate that a large fraction of the entire polar ionospheric convection pattern can be monitored from space during ~15-minute polar passes of a suitably-instrumented satellite.

The FPI on DE 2 (Hays et al., 1981; Killeen et al., 1982a,b) was the first spaceborne instrument with adequate spectral resolution to measure remotely thermospheric neutral winds and temperatures from the Doppler shift of atmospheric emissions. The Doppler line profile analysis technique used for the FPI wind measurements has been discussed by Killeen and Hays (1984) and Nardi (1991) and reviewed in Chapter 2. The neutral wind measurements, obtained between August 1981 and February 1983, have been used to provide a detailed experimental description of global thermospheric dynamics for the solar maximum period (Killeen and Roble, 1988, and references therein).

Smith et al. (1982) and McCormac (1984) used ground-based Fabry-Perot interferometer observations of the Doppler shifts of the [OII]  $\lambda 7320\text{\AA}$  emission in the northern-hemisphere polar cusp to determine the local F-Region vector ion drift at Svalbard. Ground-based interferometric measurements of ion drift are possible only when the  $\text{O}^+(^2\text{P})$  emission is sufficiently intense during twilight or nighttime hours. This condition is satisfied at times in the polar cusp, polar cap, and other high-latitude

auroral regions. Up to the present time, no spaceborne Doppler measurements of ion drift have been reported. The instrumental advantage of spaceborne measurements over ground-based measurements is twofold. Firstly, the large geometric limb-intensity enhancement (Van Rhijn effect) leads to improved sensitivity and/or smaller instruments with more modest optical throughputs for the same accuracy of measurement. Secondly, the ability of a baffled spaceborne limb scanner to discriminate against Rayleigh-scattered dayglow enables a daytime capability that takes advantage of the much brighter and ubiquitous daytime 7320Å emission.

One of the optical filters used in the DE-2 FPI instrument allowed Doppler measurements of the ionospheric [OII]  $\lambda 7320\text{\AA}$  emission. While the primary objective of the FPI was the measurement of *neutral* winds and temperatures, the 7320Å filter was used routinely in a background, time-shared mode during the DE mission and a large data base of ~1000 7320Å orbits exists. Much of these data have now been reduced to provide detailed Doppler-line-profile measurements of the daytime, twilight, and auroral [OII]  $\lambda 7320\text{\AA}$  emissions. The  $\text{O}^+(2P)$  Doppler line profile observations have been further analyzed to provide the ion drifts, ion temperatures and brightnesses along the instrumental line-of-sight. I present initial results of  $\text{O}^+(2P)$  Doppler line profile measurements and, in Chapter 6, evaluate the technique in terms of its capability as a remote-sensor of ionospheric convection. The results of a validation study, using nearly simultaneous ion drift measurements from the DE-2 RPA (Hanson et al., 1981: Chapter 2.3), demonstrate that reliable ion convection speeds are recoverable from the Doppler line profiles. With considerably more work, ion temperatures are also recoverable from the Doppler line profiles.

A review of the  $7320\text{\AA}$  emission was presented in Chapters 1.11 and 3.1. The rest of this Chapter discusses the following topics: the nature of the remote-sensing FPI technique, examples of FPI measurements, results of validation comparisons between the FPI and RPA, results of validation comparisons between the FPI and the  $7320\text{\AA}$  volume emission rate model. Figure 4.1 is an illustration of the DE satellites.

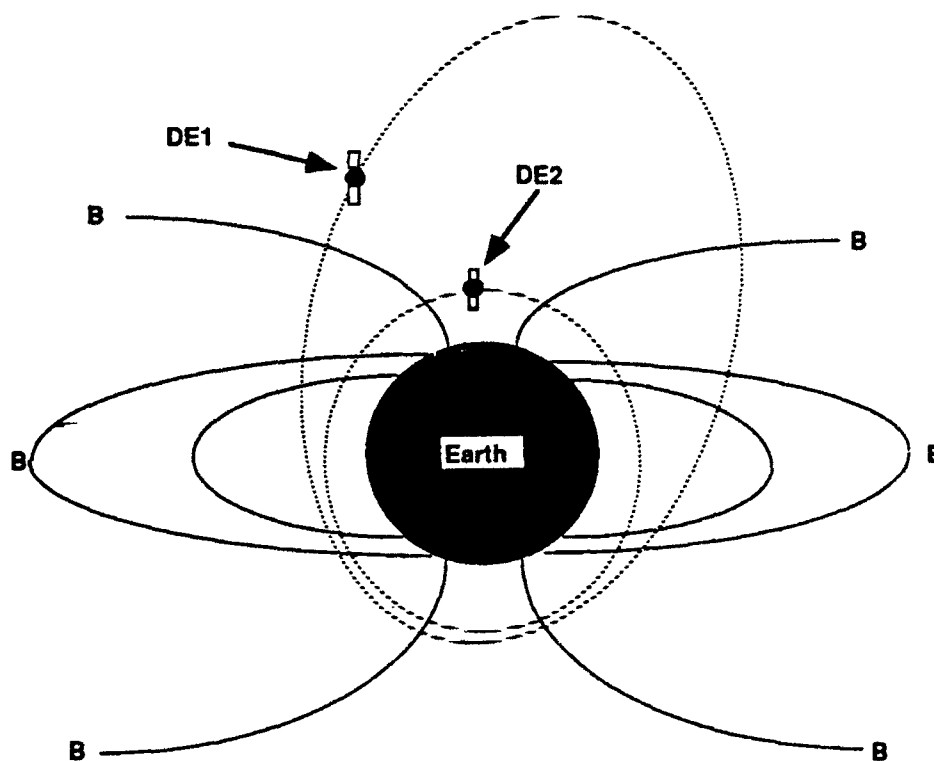


Figure 4.1 Illustration of the two Dynamics Explorer satellites and their respective orbits. The DE program, sponsored by NASA, launched two spacecraft in August 1981; they were designed to study the coupling of the magnetosphere/ionosphere/thermosphere system. DE 1 and DE 2 were put into co-planar orbits inside common magnetic flux tubes, enabling measurements from the magnetosphere and ionosphere/thermosphere simultaneously. DE-2 instrumentation included the FPI and RPA, both of which sent data back to Earth until February 1983. The data system for the DE mission, similar to that of the previous AE (Atmospheric Explorer) mission, was designed to give investigators easy access to the incoming information. A central computer facility processed most of the data at Goddard Space Flight Center (GSFC), with remote terminals at the investigator's facilities. Solid lines in this figure represent the Earth's magnetic field (**B**); dashed lines represent the respective orbits.



#### 4.1 DE-2 FPI [OII] $\lambda 7320\text{\AA}$ Emission Observations

The FPI observations were all carried out in the meridional (north-south) direction from the polar-orbiting DE-2 satellite. The DE-2 FPI had an etalon with a free spectral range of  $0.0021\text{\AA}$  (Killeen et al., 1982a) and a twelve-channel image-plane detector (IPD) that had a quantum efficiency of  $\sim 5\%$  at  $7320\text{\AA}$  (Killeen, p.c., 1992). At  $7320\text{\AA}$  and  $283\text{K}$  (the instrumental operating temperature), the  $\text{O}^+(^2\text{P})$  filter had a peak transmission of  $47\%$  and a  $10\text{\AA}$  FWHM bandpass. The FPI viewed the atmospheric limb cyclically at various tangent heights, using an on-board scanning mirror mechanism. The instrument performed a high-resolution spectral analysis of the ionospheric  $7320\text{\AA}$  emission by measuring the geometry of the interference fringe patterns imaged onto the IPD. This analysis allowed the Doppler line profile of the  $\text{O}^+(^2\text{P})$  emitting species to be characterized. The individual Doppler spectrograms obtained in this manner, in turn, enabled meridional ion drifts, ion temperatures, emission surface brightnesses, and continuum (background) brightnesses to be determined. The DE-2 FPI was capable of measurement accuracies of  $\sim 5\text{ m/s}$  and  $\sim 10\text{K}$  for meridional ion drift and ion temperature, respectively. Actual accuracies for individual measurements were dependent on the specific surface brightness of the emission and the integration time for the measurement.

##### 4.1.1 DE-2 FPI ( $7320\text{\AA}$ ) Spectrograms

Figure 4.2 depicts individual, bin-averaged, [OII]  $\lambda 7320\text{\AA}$  Doppler spectrograms obtained from DE-2 orbit 8227. The modulation seen in each

spectrogram represents the discretely-sampled Doppler line profile of the doublet emission at  $7320\text{\AA}$ . The spectrograms shown represent convolutions of the Doppler source function, characterized by the ambient ion drift and temperature, and the instrument function. These two functions were deconvolved during the analysis procedure and the resulting line-of-sight wind and brightness results inverted using the technique of Nardi (1991) to derive true altitude profiles. In practice, the "inverted" ion drifts were found to be almost indistinguishable from the line-of-sight drifts in the tangent-point altitude range  $\sim 200 - 500$  km due to the sharply peaked nature of the contribution functions (Killeen et al., 1982b; Nardi, 1991). Hence, inversions were not necessary to determine the true geophysical parameters from the line-of-sight parameters. See Appendix B.1 for a more thorough discussion.

Each spectrogram in Figure 4.2 is plotted in the appropriate location corresponding to the altitude and latitude of the tangent point to the Earth's surface along the instrumental line of sight for the respective measurement. Relative ion drifts can be discerned in Figure 4.2 by the evident sideways motion of the peak centroid from spectrogram to spectrogram; the enlargement of the two spectrograms from  $280$  km and  $-66.5^\circ$  geographic latitude enforces this point. The length of the horizontal bar given at the top of each spectrogram provides a relative (linear) intensity scale for the  $\text{O}^+(^2\text{P})$  emission. Channel 8 has been removed from all DE-2 spectrograms and analysis procedures since that channel developed a significant non-stochastic noise component.

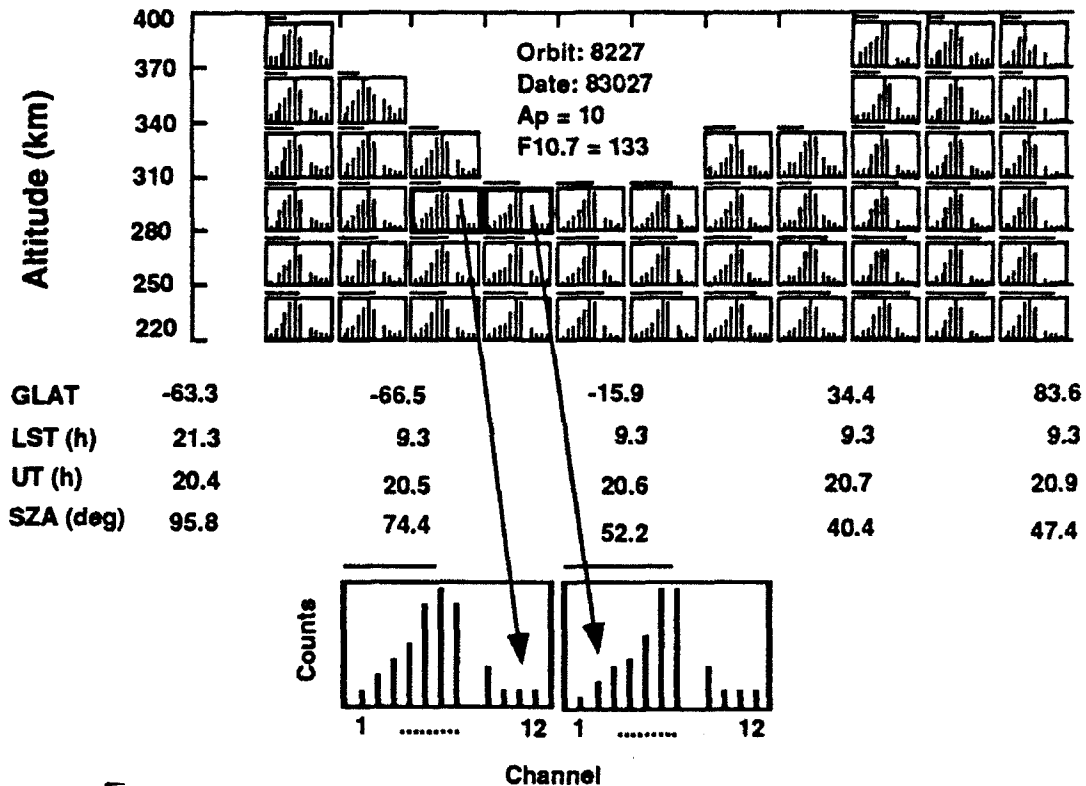


Figure 4.2 Examples of FPI measured [OII]  $\lambda 7320\text{\AA}$  Doppler spectrograms from DE-2 orbit 8227. The individual spectrograms depict the count rate (counts per second) measured at each channel of the instrument, with the exception of channel 8. The horizontal bar above each spectrogram denotes relative intensity. Each spectrogram is positioned in the plot at the location corresponding to the altitude and latitude of the tangent point to the Earth along the respective instrumental line-of-sight. Changes in ion drift velocity are seen in the evident variations in the peak centroid from spectrogram to spectrogram; this is most obvious in the enlarged two spectrograms from  $\sim 280\text{ km}$  and  $-66.5^\circ$  geographic latitude. The free spectral range of the  $7320\text{\AA}$  FPI is  $0.21\text{\AA}$  and the spectral interval is  $\sim 0.018\text{\AA}$  per channel. Ion drifts are derived from the measured Doppler line centroid using the linear least squares fit technique of Killeen and Hays (1984).

The elliptical nature of the DE-2 orbit 8227 (dropping to perigee at  $\sim 20.6$  hrs UT) is illustrated by the shape of the 2-dimensional swath of data. Above  $\sim 200$  km, the relative intensity of the [OII]  $\lambda 7320\text{\AA}$  emission increases up to peak at around  $300$  km (above the quenching zone but below the area where  $\text{O}^+(^2\text{P})$  decreases in concentration). Nearly 1000 DE-2 orbits of [OII]  $\lambda 7320\text{\AA}$  data are available and this dissertation presents a first analysis of a

subset of drift, temperature and emission brightness data. See Appendix B.2 for an overview of the software that produces the ion drift, temperature and brightness profiles. Appendix B.2 also has a table of constraints that FPI (7320Å) observations must satisfy before the data are processed.

#### 4.1.2 Sample DE-2 FPI (7320Å) Brightness, Drift and Temperature Profiles

A sample brightness profile is shown in Figure 4.3. Note that the brightness intensities increase with altitude and reach a maximum at ~300km. This phenomenon agrees with both observations and models of the 7320Å brightness and column emission profiles (Yee et al., 1981; Torr et al., 1990a,b; Solomon, p.c., 1991) since the two major sources (solar EUV and photoelectron impact ionization) of  $O^+(^2P)$  peak at ~300km ( $\pm 50$ km).

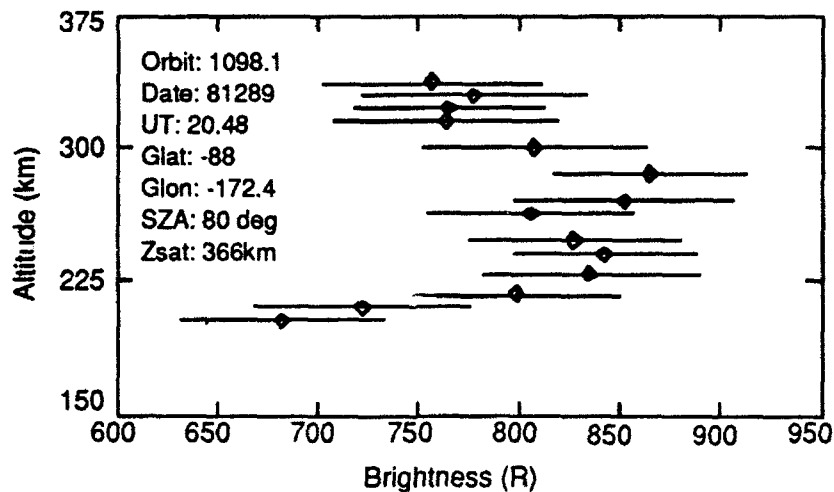


Figure 4.3 Sample brightness profile for orbit 1098.1. Brightness units are in Rayleighs (R), where  $1R = 10^6 \text{ph/cm}^2\text{-s}$ . The brightness peaks at ~300km; this was found to be true ( $\pm 50$ km) with nearly all analyzed DE-2 FPI (7320Å) orbits.

Figure 4.4 is a latitudinal profile of FPI (7320Å) recovered meridional ion drifts for orbits 1363 and 1364. Data from the two orbits were appended to one another for greater areal coverage. The data are averaged from 200-

500km in altitude. Latitudes are tangent point (geographic) latitudes. One immediately notes the increased drift speeds in the polar cap and auroral zone with small drift speeds ( $\sim 0$ m/s) at low latitudes, as expected.

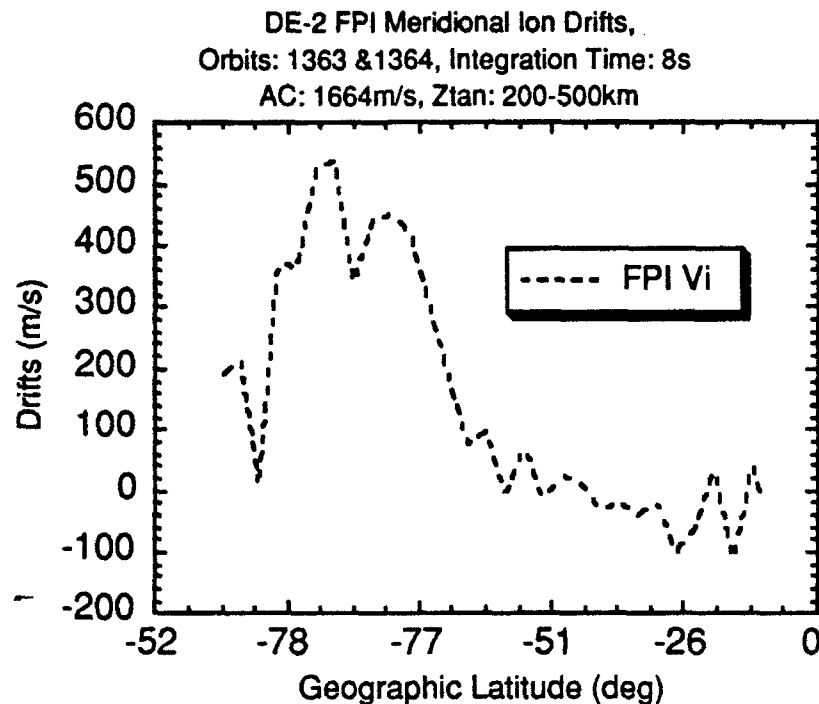


Figure 4.4 Meridional ion drift latitudinal profile for two successive orbits. Data are averaged in altitude from 200-500km. A value of 1604m/s was added to these drifts (see section 4.1.4 for explanation).

Figure 4.5 is a two panel plot of brightnesses (top panel) and meridional drifts (bottom panel). These data are from orbit 8000 and are from 300km tangent point altitudes only. UT, geographic latitude and longitude, local solar time and solar zenith angle are listed in the middle of the figure. The 3-D plot of brightness in the upper left hand corner is the sum of all brightness profiles for this orbit (*not* for 300km tangent point altitudes only); it shows brightness intensity increasing vertically, with altitude and UT (s) as the horizontal axes. Note the photoionization control of the brightness - as the solar zenith angle increases, so does the brightness. The drifts do not show much variation, ranging from near

600m/s to ~0m/s. A detailed validation of the FPI (7320Å) drifts is the topic of section 4.2.

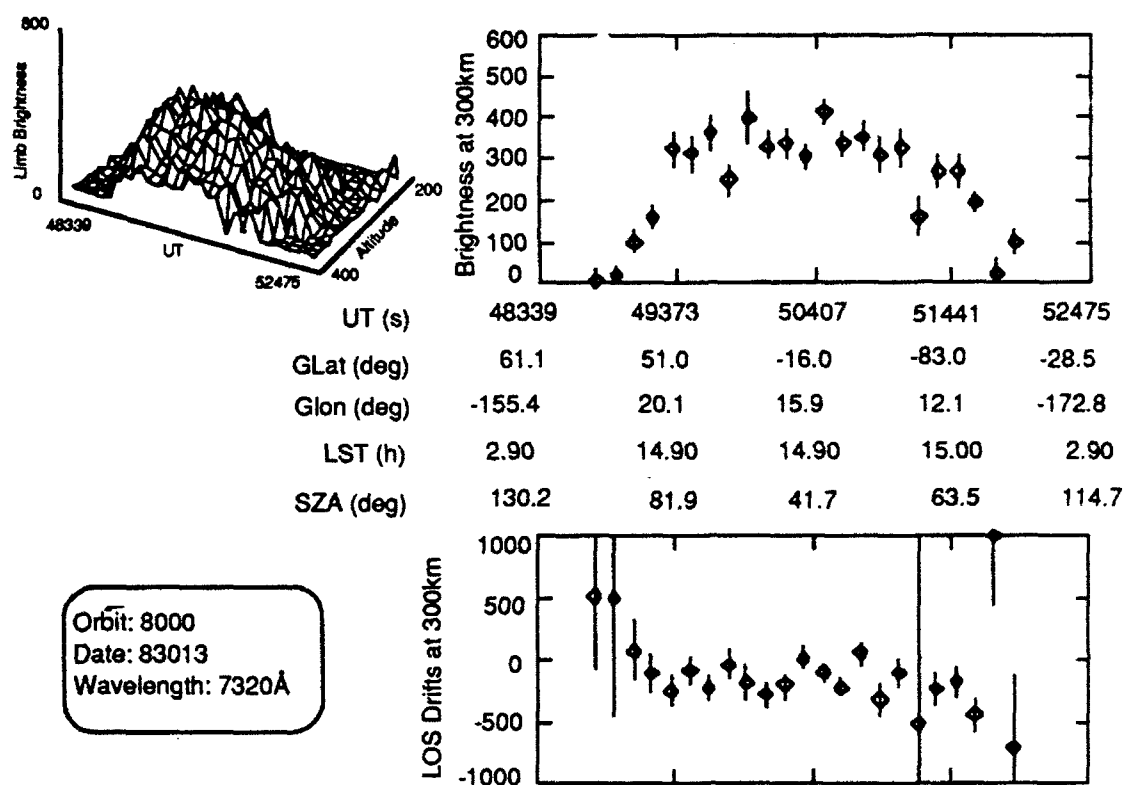


Figure 4.5 Two-dimensional plots of brightnesses and meridional ion drifts for orbit 8000. Three-dimensional plot in upper left hand corner is a sum of all brightness profiles for this orbit. Large drift errors were found *usually* to occur when the sun was too far below the horizon ( $SZA > 100^\circ$ ) to produce a strong 7320Å signal. When the 7320Å brightness was below 50R, accurate drifts could never be recovered. The large drift error positioned at  $\sim 56^\circ$  SZA and  $67^\circ$  geographic latitude was possibly caused by an aurora in the FPI's field of view as the DE 2 traversed the auroral zone.

Figure 4.6 is a three-panel plot of brightnesses, meridional ion drifts and ion temperatures for DE-2 orbit 7439; these data are from the 300km tangent point altitude only. The solar zenith angle is relatively constant in this example; hence, the 7320Å signal (brightnesses) remain relatively constant. But as the satellite crosses the pole and moves into the nighttime auroral sector, auroral heating increases (see relative ion temperature

increase in bottom panel after UT 79231s) which causes upwelling of nitrogen-rich and oxygen-poor air parcels. With less atomic oxygen to photoionize, the 7320Å brightnesses generally decrease after UT 79000s even though SZA remains nearly constant.

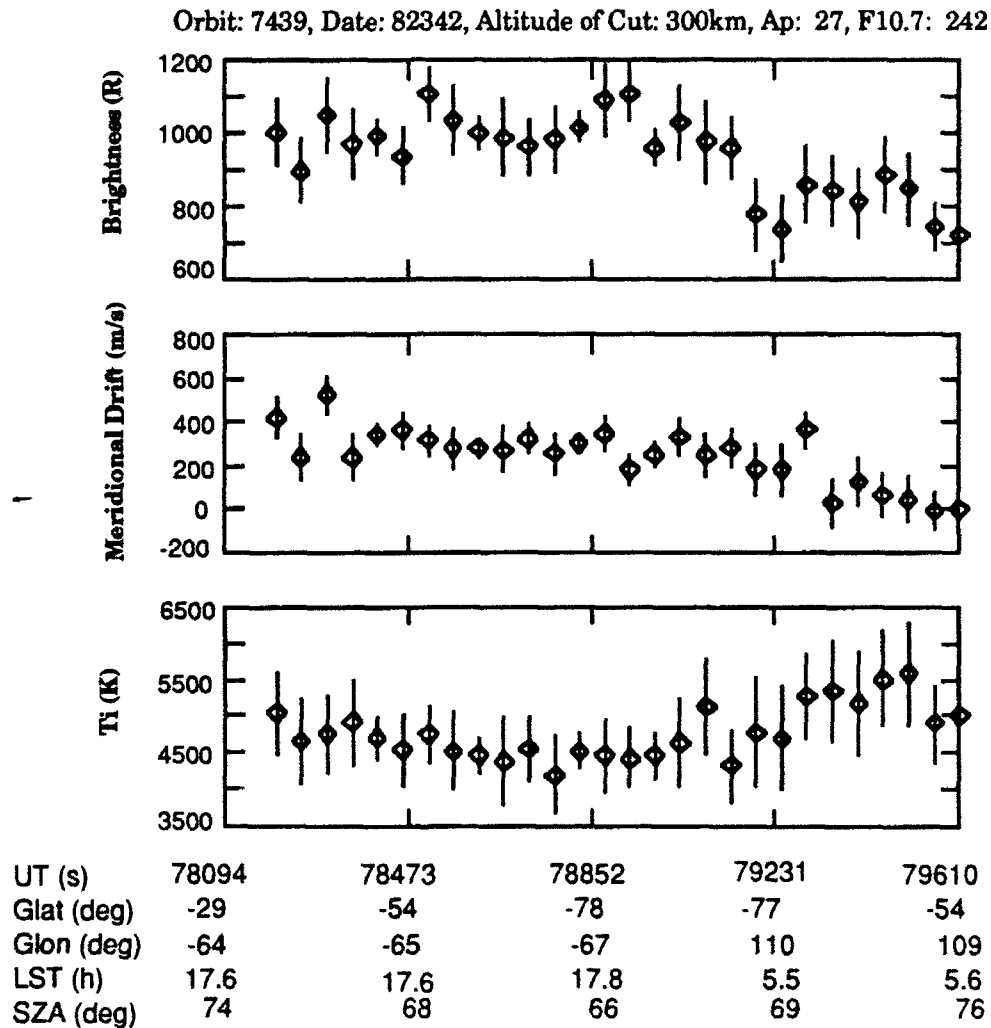


Figure 4.6 Plots of brightnesses, drifts and temperatures for orbit 7439. Additive constant of 1602m/s is used to zero the ion drifts at the equator for this orbit. See text for further discussion of this figure.

#### 4.1.4 Meridional Ion Drift Additive Constant

In Chapter 2.1.3, I mentioned that for the purposes of absolute ion drift measurements, a zero-velocity calibration is necessary. The coefficient translation scheme used to transfer instrument transfer functions from a wavelength where they are known (for example, 6328Å) to the new wavelength can only determine the spectral shapes and relative position of the new instrument functions and not the exact reference wavelength (Nardi, 1991; Thayer, p.c., 1991). This may result in large uniform shifts in the LOS velocity. Hence, a drift calibration was performed in order to obtain the effective shift that is inherent in the LOS drifts. I averaged drift observations at equatorial latitudes from 59 orbital passes and assumed near-zero low-latitude meridional ion drift (due to conservation of mass, the average neutral winds and ion drifts should be zero near the equator - Nardi, 1991). Models, such as VSH (discussed in Chapter 2.4a), show ion drifts approaching zero near the equator (see Figure 4.7). DE-2 RPA ion drift measurements also approach zero as the instrument observes in low latitudes. The DE-2 FPI (7320Å) equatorial crossings produced meridional ion drifts that averaged about -1600m/s. Nardi (1991) found greenline (5577Å) winds to average about -330m/s near the equator using an identical method. This deviation of the average drift is an artifact of the improperly referenced instrument transfer functions. Hence, I zeroed the drifts for each orbit studied by adding ~1600m/s to the retrieved drifts. The generally good level of agreement between the RPA and FPI drift measurements makes one believe this technique is valid. In addition, calibrations to correct for FPI instrumental drift were performed on a twice-per-orbital-pass basis using the on-board calibration lamp source. The offset error associated with



these calibrations is estimated to be  $\leq 15$  m/sec. The quoted statistical errors in the measured ion drifts are determined from the diagonal elements of the matrix used in the linear least squares fit technique. The overall systematic errors, instrument drift and offset errors are estimated to be  $\leq 25$  m/sec.

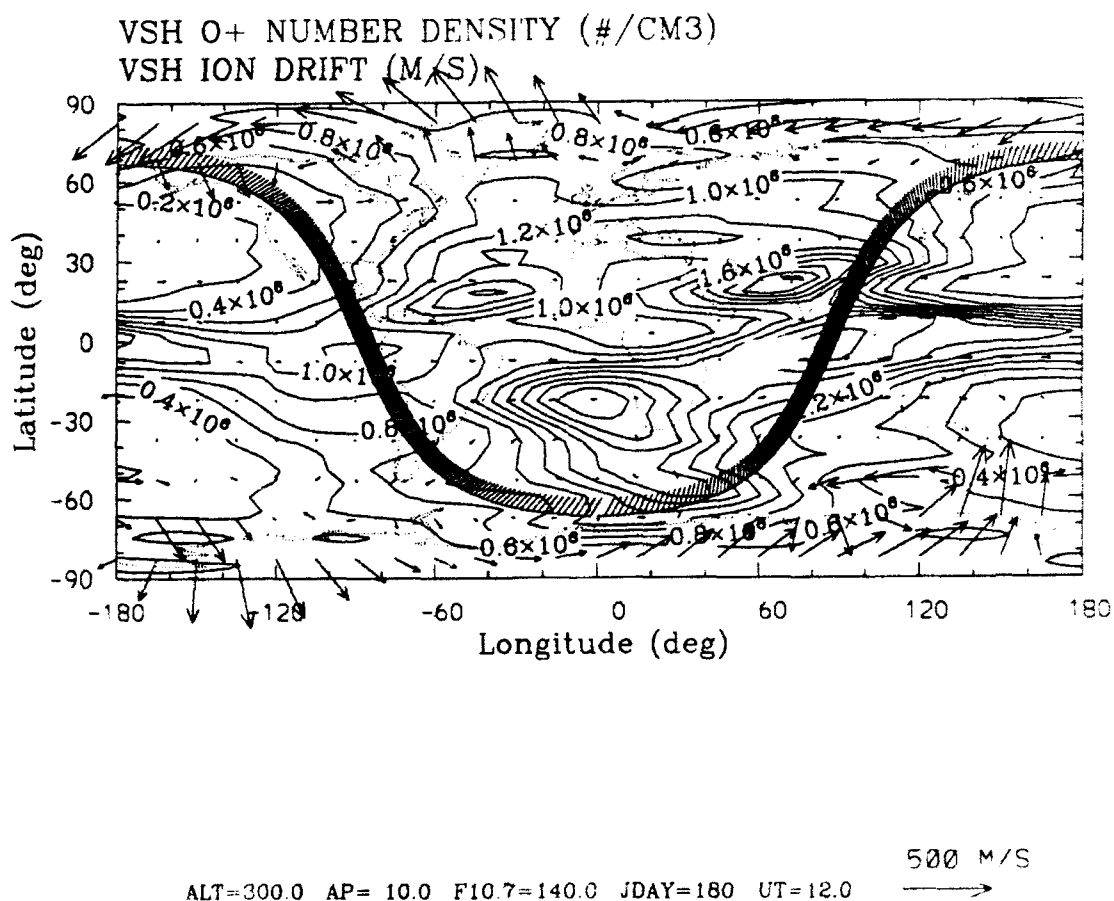


Figure 4.7 VSH modelled ion drifts and O<sup>+</sup> number density for the geophysical conditions listed in the diagram. Note the order of magnitude decrease of ion drifts going from high latitudes to mid- and low-latitudes.

#### 4.1.5 Phenomena Affecting $O^+(^2P)$ Ion Drift

##### 4.1.5.1 Transport

Metastable  $O^+(^2P)$  ions have a lifetime of 4.57s and a branching ratio of ~0.78 for the  $^2P$ - $^2D$  transition (see Chapter 1.11). The loss equation for this transition is (Chapters 1.11, 3.1):

$$L_1 = O^+(^2P) \xrightarrow{A_\lambda} O^+(^2D, ^4S), A_\lambda = 0.219s^{-1} \quad 4.1$$

Thus, if the ion has acquired a drift speed of 3000m/s (extremely high), it has, during its lifetime, been transported only ~13.7km.

The total ion collision frequency is given by:

$$v_i = v_{in} + v_{ie} = v_{in} \quad 4.2$$

where i, e and n denote ion, electron and neutral, respectively. Since electrons are (relatively) light, they have little effect on ions at ionospheric altitudes and therefore, their collision frequency is ignored. This total ion collision frequency can therefore be calculated by several methods. One way is via gas kinetics, in which

$$v_{in} = \frac{\bar{v}}{\lambda}, \bar{v} = \left( \frac{2kT}{m} \right)^{1/2}, \lambda = \sqrt{2}n\sigma \quad 4.3$$

where  $\bar{v}$  is the most probable velocity in the Maxwellian equilibrium velocity distribution, m and T are the mass and temperature of the species being analyzed ( $O^+(^2P)$  in this case),  $\lambda$  is the mean free path,  $\sigma$  is the collision cross section of the species being analyzed and n is the total number density. Another, simpler method, was derived by Chapman in 1956 and is written as:

$$\nu_{in} = (2.6 \times 10^{-9})(n_n + n_i)A^{-12} \quad 4.4$$

where  $n_i$  is the ion concentration,  $n_n$  is the neutral density and  $A$  is the mean molecular weight of the neutrals and ions. Using Equation 4.4, and number densities from Kelley (1989), the ion collision frequency at 300km was determined to be  $\sim 0.09$  collisions/second during solar minima. During solar maxima, the ion collision frequency at 300km is  $\sim 1$  collision per second (see Figure 4.8).

At F2-Region altitudes, let us assume that  $n_e = n_i$  and that  $O^+$  is the dominant ion (see Figure 2.16). Assuming an electron (and therefore atomic oxygen ion) concentration of  $\sim 10^6$  per  $\text{cm}^3$  for daytime solar maximum conditions, a collision frequency of  $\sim 1$  per second and a radiative lifetime of 4.57s for  $O^+(2P)$  ions, it is apparent that collisions are unimportant at these altitudes and most  $O^+(2P)$  ions will spontaneously emit.

Hence, the  $O^+(2P)$  7320Å-emitting ion, *above* the quenching zone, is destroyed in 4.57 seconds via *radiation*; this lifetime is much shorter than the time required to transport the ion out of the DE-2 FPI footprint. The DE-2 FPI (7320Å) had a field-of-view of  $\sim 2.7^\circ$  and scanned 500-1700km ahead of the satellite; therefore, the diameter of the footprint at the tangent point varied from  $\sim 24 - 80\text{km}$ . At the smallest FPI viewing angle (corresponding to 500km ahead of and below the satellite), an ion would have to maintain a speed of  $\sim 5250\text{m/s}$  for 4.57s to be transported out of the 24km footprint; the ion would have to be travelling in excess of  $17\text{km/s}$  to be transported out of the 80km-wide footprint. Since meridional ion drifts of this magnitude were not observed by the FPI (or RPA), transport is therefore unimportant and  $\mathbf{E} \times \mathbf{B}$  drift is the only motion that needs to be considered. Diffusion is

unimportant since at  $\sim 300\text{km}$ , the radiative lifetime of the  $\text{O}^+(2\text{P})$  ion ( $\tau_{7320\text{\AA}} = 4.57\text{s}$ ) is much less (Yee, 1980) than the diffusion time constant ( $\tau_{\text{diff}} \sim 10 - 100\text{s}$ ).

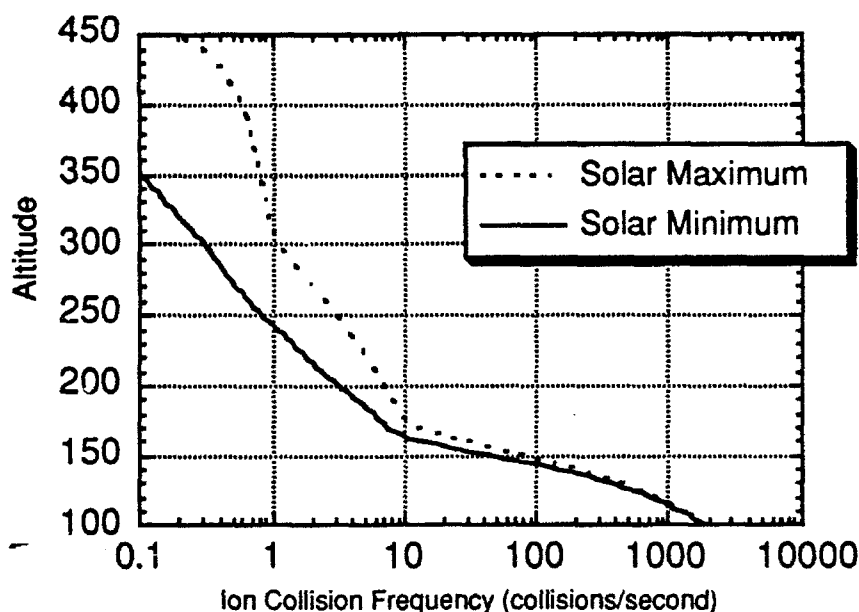


Figure 4.8 Ion collision frequency versus altitude. See text for discussion. Since ion densities are much less than neutral densities, distinguishing between day and night ionospheres is irrelevant.

#### 4.1.5.2 $\mathbf{ExB}$ Drift

The time taken for a newly created ion to drift with the bulk ion population in the  $\mathbf{ExB}$  direction is basically given by the gyroperiod ( $T_{\text{gyro}}$ ) at F-Region altitudes (Gaffey, 1988; Miller, p.c., 1992). If this gyroperiod is shorter than the  $\text{O}^+(2\text{P})$  ion's lifetime (4.57s), one may assume that the Doppler shift of the emitted  $7320\text{\AA}$  light is representative of the ion convection bulk velocity. The gyrofrequency is the product of electron charge and the magnetic field strength, divided by the mass of the species in question. Using generally accepted values, Equations 4.5a, 4.5b show the calculation of gyrofrequency ( $\omega$ ) and gyroperiod ( $T_{\text{gyro}}$ ).

$$\omega = \frac{qB}{m} = \frac{(1.6 \times 10^{-19} \text{ C})(0.5 \times 10^{-4} \text{ T})}{2.66 \times 10^{-26} \text{ kg}} \approx 300 \text{ s}^{-1} \quad 4.5a$$

$$T_{\text{gyro}} = \frac{2\pi}{\omega} \approx 0.02 \text{ s} \quad 4.5b$$

These values agree with those of Kelley (1989). Since the time taken for a newly created  $\text{O}^+(2\text{P})$  ion to drift with the bulk ion population in the  $\mathbf{E} \times \mathbf{B}$  direction is very nearly instantaneous (0.02s) relative to the ion's lifetime (4.57s), it may be assumed that the Doppler shift of the emitted light is representative of the ion convection velocity.

Consider solar maximum conditions at 300km (therefore imitating DE-2 conditions). Then

$$\frac{\omega}{v_i} \gg 1 (\approx 300) \quad 4.6$$

meaning there are ~300 gyrations about the field line before the  $\text{O}^+(2\text{P})$  ion experiences a collision. This illustrates the strong geomagnetic (rather than collisional) control on this ion. The effect of a collision is to momentarily bring the particle to rest at equal intervals given by the inverse of the collision frequency. This is why trajectories are cycloidal and dependent on the  $\omega/v$  ratio. Recall from Chapter 1.8 that the angle an ion ( $\text{O}^+(2\text{P})$  in this case) drifts relative to the electric field is given by

$$\theta = \arctan \frac{\omega}{v_i} = \arctan(300) = 89.81^\circ \quad 4.7$$

Hence, the  $\text{O}^+(2\text{P})$  ion drifts at an angle *almost exactly normal* to the fields, as expected. However, there *may* be other phenomena that affect the  $\mathbf{E} \times \mathbf{B}$ -drifting F2-Region  $\text{O}^+(2\text{P})$  ions.

#### 4.1.5.3 Effects of Ion Pickup, Neutral Momentum and Neutral Winds on Ion Drifts

A newly created F2-Region ion ( $O^{+}(^2P)$  ion in this case) must be accelerated from its parent's *neutral velocity* to that of the bulk ion flow in order for it to be assimilated into the bulk ion flow. This process is called *ion pickup*. Most articles in the literature deal with solar wind pickup of  $He^{+}$  or  $H_2O^{+}$ ; the parents of these ions come from neutral cometary exospheres. Clearly there are more ions in the ionosphere ( $\sim 10^6 \text{ cm}^{-3}$  at  $\sim 300\text{km}$ ) than in the solar wind ( $\sim 10 \text{ cm}^{-3}$ ), so one would think that there would be more interest in ion pickup in the ionosphere. But as I shall show in this section, ion pickup (and the concomitant newly created ion momentum) of newborn  $O^{+}(^2P)$  ions in the F2-Region is nearly instantaneous ( $\sim 0.02\text{s}$ ), while (for example)  $He^{+}$  pickup in the solar wind is at least 1000-10000 times longer (Gaffey et al., 1988). Since plasma properties are influenced and modified by the rate in which these newborn ions are picked up, the longer time scale for ion pickup in the solar wind makes the study of that process more intriguing than a study of the near-instantaneous pickup in the F2-Region.

The solar wind pickup process occurs in three stages: formation of an initial ring beam distribution, rapid pitch angle scattering of this initial distribution into a thin shell, and slow velocity diffusion that spreads out the shell (Gaffey et al., 1988). Time scales representing these stages are  $T_r$ ,  $T_s$  and  $T_d$  respectively. The time scale for the initial scattering has been shown to be related to the gyroperiod ( $T_r \sim T_{gyro}$ ) in the perturbed wavefield; hence, the gyroperiod is the bottom limit for ion pickup (Gaffey et al., 1988; Miller, p.c., 1992).

In the F2-Region (at 300km), a newborn  $O^+(^2P)$  ion must be accelerated from its initial velocity (that of its neutral parent - atomic oxygen) to that of the bulk ion flow in order to be picked up. According to Chapter 4.1.5.2, this assimilation of the ion will take  $\sim 0.02s$  (the gyroperiod). Assuming a characteristic neutral wind speed in the high latitude thermosphere of  $\sim 100m/s$  and an ion drift speed of  $\sim 1000m/s$ , the newborn ion must undergo a rapid acceleration of  $\sim 10^4 m/s^2$  in order for it to be assimilated into the bulk ion flow in  $0.02s$ . Hence, this newborn ion nearly instantaneously moves with the bulk ion population and, therefore, has a very short ( $0.02s$ ) memory of its parent's *neutral* momentum. Since the  $0.02s$  gyroperiod (and, therefore, pickup time and neutral momentum memory) is much shorter than the ion's lifetime ( $4.57s$ ), one can assume that DE-2 FPI observations of the Doppler shift of emitted  $7320\text{\AA}$  light is representative of the ion convection bulk velocity.

However, there *is* some component of the parent's *neutral velocity* imbedded within the observed ion motion. Recall that at high latitudes, the DE-2 FPI's line-of-sight (LOS) was *nearly perpendicular* to **B**. The question then becomes, will this neutral wind component contaminate DE-2 FPI LOS (meridional) observations of ion drifts? To answer this question, let us consider the equations of motion for the F2-Region. Accelerations acting on any charged particle in the presence of electric and magnetic fields can be written

$$\frac{d\vec{V}}{dt} = \frac{q\vec{E}}{m} + \frac{q\vec{V} \times \vec{B}}{m} - v(\vec{V} - \vec{U}) \quad 4.8$$

where accelerations due to gravity, pressure gradients and collisions have been ignored (Rishbeth and Garriot, 1969). **V** is the ion velocity, **U** is the

neutral wind velocity,  $q$  is the charge,  $\mathbf{B}$  is the magnetic field,  $m$  is mass and  $\nu$  is the effective collision frequency. If  $\mathbf{E}$  and  $\mathbf{B}$  are parallel, the charged particle motion is unaffected by the magnetic field. When  $\mathbf{E}$  and  $\mathbf{B}$  are perpendicular, the plasma motions are as shown in Figure 4.9. In this figure, it is assumed that the particles are brought to rest at equal time intervals of  $1/\nu$ . At the altitudes of concern in this work ( $\sim 180 - 500\text{km}$ ), both electrons and ions move in the  $\mathbf{E} \times \mathbf{B}$  direction. Assuming steady-state conditions, an average drift velocity can be determined from Equation 4.8. In a Cartesian coordinate system in which  $\mathbf{B}$  is directed along the  $z$ -axis,

$$F_x = m\nu V_x - qV_y B \quad 4.9$$

$$F_y = m\nu V_y + qV_x B \quad 4.10$$

$$F_z = m\nu V_z \quad 4.11$$

where

$$\vec{F} = q\vec{E} + m\nu\vec{U} \quad 4.12$$

is the applied force. The solution to this is written in terms of the tensor  $\vec{k}$  which satisfies the equation  $\vec{V} = \vec{k} \cdot \vec{F}$ , where

$$\vec{k} = \begin{bmatrix} k_p & \pm k_h & 0 \\ \mp k_h & k_p & 0 \\ 0 & 0 & k_d \end{bmatrix} \quad 4.13$$

The upper signs apply to ions and the lower signs to electrons. Each  $k$  component is the ratio of a velocity to a force and is referred to as a mobility per unit charge. These mobilities can be written as



$$k_d = \frac{1}{mv} = \frac{\omega}{qBv} \quad 4.14$$

$$k_p = \frac{1}{mv} \frac{v^2}{v^2 + \omega^2} = \frac{v\omega}{qB(v^2 + \omega^2)} \quad 4.15$$

$$k_h = \frac{1}{mv} \frac{\omega v}{v^2 + \omega^2} = \frac{\omega^2}{qB(v^2 + \omega^2)} \quad 4.16$$

where the d, p and h subscripts refer to direct, Pedersen and Hall, respectively. The direct component of mobility is aligned parallel to both **E** and **B**; the Pedersen component is aligned parallel to **E** but perpendicular to **B**; the Hall component is perpendicular to both **E** and **B**.

In the F2-Region of the high latitude ionosphere, the electric field is perpendicular to the magnetic field; let us assume a neutral wind at some angle to **B**. In this altitude region, the collision frequency will be much less than the gyrofrequency ( $v \ll \omega$ ) and therefore  $k_p \ll k_h \sim 1/qB$ . Thus, an electric field causes both electrons and ions to drift in the **E** $\times$ **B** direction with a speed of **E**/**B**. A neutral wind produces a Hall drift at speed  $(v/\omega)U$  in the **U** $\times$ **B** direction for positive ions and the opposite direction for electrons; this scenario applies to all charged particles above  $\sim 180$ km.

At any height, the *field-aligned* component of *plasma* drift due to *neutral* winds may be written as

$$\vec{U}_{\text{aligned}} = \frac{(\vec{U} \cdot \vec{B})\vec{B}}{B^2} \quad 4.17$$

Hence, there is a component of the neutral wind that affects the ion drift velocity. When one recovers ion drifts from DE-2 FPI observations, some

component of the neutral velocity is present in that measurement. The magnitude of this neutral wind component along the field line may affect

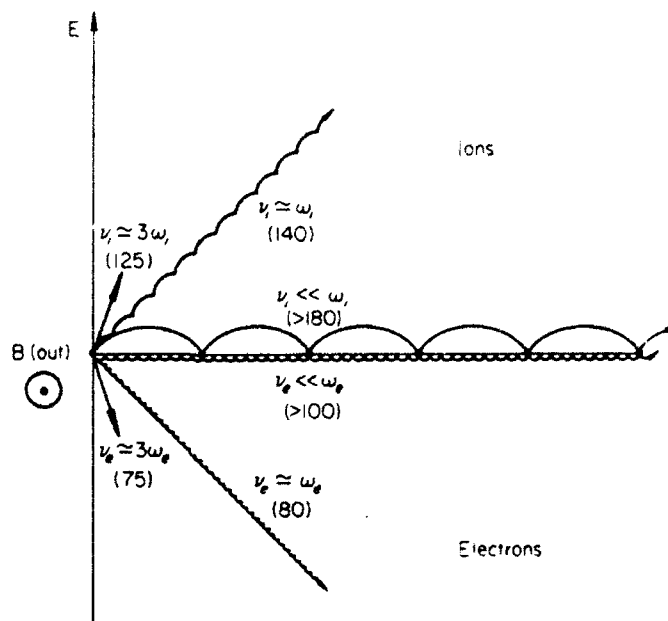


Figure 4.9 Trajectories for ions and electrons subject to  $E$  (in the plane of the paper) and  $B$  (out of the plane of the paper). Charged particles are assumed to collide with neutral species at regular intervals,  $1/\nu$  and to possess zero velocity after each collision. Numbers in brackets refer to approximate heights (km) at which conditions occur. Figure adapted from Rishbeth and Garriot (1969).

FPI retrievals of meridional ion drifts. To emphasize this situation, let us assume active conditions and a meridional neutral wind component in the high latitude ionosphere (at  $\sim 300$  km) of  $100$  m/s and a meridional ion drift speed of  $1000$  m/s (Burns, p.c., 1992). At high latitudes, with  $B$  nearly vertical, the horizontal winds will be at large angles to  $B$ . Taking magnitudes of Equation 4.17, one finds that  $U_{\text{aligned}} = U \cos \theta$  where  $\theta$  is the angle between the wind and  $B$  (basically  $\theta \sim$  latitude). At  $\theta = 45^\circ$ ,  $U_{\text{aligned}}$  is  $\sim 71$  m/s. This field-aligned component of plasma drift due to neutral winds is therefore only  $\sim 7\%$  of the meridional ion drift speed. Similarly, at  $60^\circ$ , the field-aligned component of plasma drift due to neutral winds is about  $5\%$ ; at

75°, it is ~2.5%. And when the neutral wind is perpendicular ( $\theta=90^\circ$ ) to  $B$ , no field-aligned component exists. Hence, the *field-aligned* component of plasma drift due to neutral winds is small relative to the meridional ion drift speeds. Therefore, in the high latitude polar ionosphere, the DE-2 FPI LOS measurements contained a small field-aligned component of ion drifts due to neutral winds; this component was only ~7% (or less) of the meridional ion drift speed for the situation presented. Since this value is small, and ion pickup is nearly instantaneous, we can assume that the measured ion drifts are representative of the bulk ion population.

Note that the average kinetic energy of the random ion motions satisfies the relation (Bittencourt, 1986)

$$\frac{3kT_i}{2} = \frac{m_i \langle v_i^2 \rangle}{2} \quad 4.18$$

where the  $\langle \rangle$  symbol denotes the average value with respect to velocity space for particles of type  $i$  (ions). If a component of the neutral velocity is imbedded within this ion velocity ( $v_i$ ), as shown in the previous paragraph, then ion temperature ( $T_i$ ) will increase according to Equation 4.18.

## 4.2 Comparisons Between FPI and RPA Ion Drift Measurements

Over 1000 DE-2 orbits contain FPI-sensed 7320Å data. However, many of these orbits have either limited 7320Å observation-time or poor observation quality (solar zenith angle too large resulting in too small a signal, scans too deep into the lower thermosphere where the ion is effectively quenched, etc.). About 10 orbits were found in which the FPI (7320Å), and RPA were both "on" and operating in very favorable

conditions. The FPI ion drift measurements were compared with simultaneous RPA (Hanson et al., 1981; Heelis et al., 1986) measurements in order to validate the remote-sensing technique at high geographic latitudes. The DE-2 RPA provided measurements of meridional ion drift velocity using a well-proven and more conventional *in situ* technique (see Chapter 2.3) and was typically "on" poleward  $\sim \pm 30$  geographic latitude. The stated accuracy for RPA meridional ion drift measurements was  $\sim 10\%$ . In order to make a comparison of FPI and RPA observed ion drifts, an adjustment was made to allow for the spatial difference between the physical volumes of space sampled by the remote and *in situ* techniques. The FPI mirror systems scanned from  $\sim 5^\circ$ - $15^\circ$  below the local horizontal. Hence, the distance from the spacecraft to the tangent point on the Earth's surface along the line of sight varied between  $\sim 500$ - $1700$  km. For each measurement, therefore, a separate temporal lag ( $\sim 1$ - $3$  minutes) was applied to the RPA measurements such that the comparison was always between RPA measurements made directly above the sampled volume of the (prior) FPI measurement. Inherent in this data handling approach is the assumption that no significant changes in meridional ion drift occur during the time delay for the RPA to reach the sampled volume of any given FPI measurement. While this assumption is questionable for ions at high latitudes and during disturbed conditions, the level of agreement seen between the two techniques demonstrates that the assumption is reasonable for the present validation purpose. A further assumption was necessary concerning the altitude invariance of the meridional ion drift. The FPI measurements were bin averaged using data obtained within the range of  $200$ - $500$  km tangent point altitudes (representative of the ion drift at  $\sim 300 \pm 50$  km, or near the peak of the [OII]  $\lambda 7320\text{\AA}$  emission layer). The RPA

measurements were made at satellite altitude. It was assumed that the magnetospheric convection electric field maps down along the nearly-vertical, high-latitude, equipotential magnetic field lines in such a way that the  $\vec{E} \times \vec{B}$  ion drift remains constant with decreasing altitude down to ~180 km where collisional effects become important. With this assumption, the remote FPI drift measurements may be directly compared with the *in situ* observations at satellite altitude.

Unfortunately, these RPA vs FPI comparisons were quite difficult to make. The RPA was frequently off when the FPI was observing strong 7320Å signals. Or when the RPA was taking ion drift and temperature measurements, the FPI was observing 6300Å or 5577Å. Also, the determination of similar atmospheric volumes that the two instruments were measuring was no trivial task. The FPI scanned in 16 science mirror positions, each one having a distinct tangent point altitude and latitude/longitude. The method of bin averaging the FPI data and applying the ~1-3 minute lag to the RPA measurements so they were directly above the sampled volume of the (prior) FPI measurement was done by a standard plotting routine.

Figure 4.10a shows four examples of "simultaneous" FPI and RPA ion drift measurements for selected polar passes of DE 2. The FPI data have been passed through a standard plotting routine and therefore represent bin-averaged ion drifts taken for tangent point altitudes between 200 and 500 km altitude. The independent measurements are in good agreement, for the most part within specified errors. Significant discrepancies may be ascribed to the tendency of the remote FPI measurement to smear out large shears due to the relatively long spatial integration path length of the

measurement (~300-500 km at the limb) and to possible temporal changes occurring on shorter time scales than the temporal lag already discussed.

It was found that the standard analysis package's fitting algorithm did not always produce stable solutions after five iterations, yet these solutions may have passed the error checking routines. To ensure only good FPI data points were plotted against RPA drifts, six orbits were analyzed by hand. During this hands-on work, it was noted that several FPI mirror positions frequently retrieved bad data. The two largest mirror angles looked ~215 and 225km beneath the DE 2; in these cases, the scans were often deep into the lower thermosphere where  $O^+(^2P)$  is severely quenched and 7320Å signals are, therefore, weak. The shallowest mirror angle looked only ~25km beneath DE 2; the standard analysis package seldom converged to reasonable solutions within five iterations at this mirror position when the satellite was at low altitude (<275km). This may be due to the OH surface glow contamination mentioned by Copeland and Slinger (1990). Thus, only those select science mirror positions that did not scan too deeply into the lower thermosphere or too closely to the DE 2 when it was at low altitude constantly produced reasonable drifts in these orbits.

In Figure 4.10b, I plot individual FPI drift measurements from *selected* mirror positions (those with rapidly converging, stable solutions in the standard analysis package); note that the ion drifts in Figure 4.10a are *averaged* from ~200-500km. The generally excellent level of agreement in Figure 4.10b gives confidence in the new remote technique. Knowledge from this analysis allowed me to design an improved space-based observing platform in Chapter 6 that focuses on ion drift observations only. Figure 4.10c is an example of two orbits of RPA vs FPI ion drift comparisons. The polar dial to the left of each drift figure shows the terminator and the ion

drift vectors along the satellite track from the DE-2 RPA/IDM (ion drift meter) team.

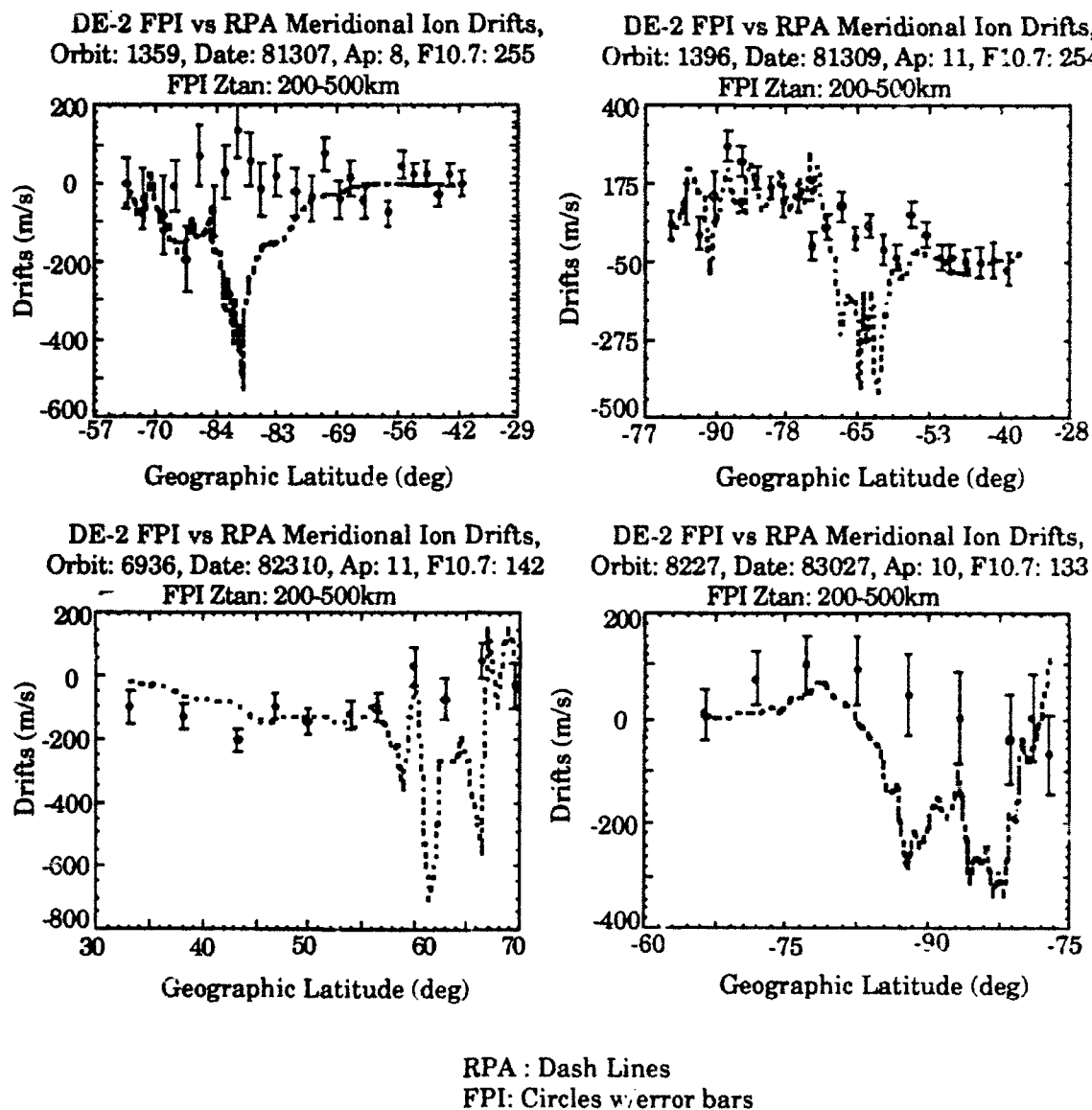


Figure 4.10a Meridional ion drifts measured by the FPI on DE 2 for four orbital passes at high geographic latitude. The FPI data are bin averaged for all tangent point altitudes between  $\sim 200$ -500km. Errors are standard deviations from the mean. The remotely measured ion drifts are compared with *in situ* measurements by the RPA on DE 2. The FPI measurements have been adjusted in temporal phase to match the RPA measurements as discussed in the text. Compare to Figure 4.10b.

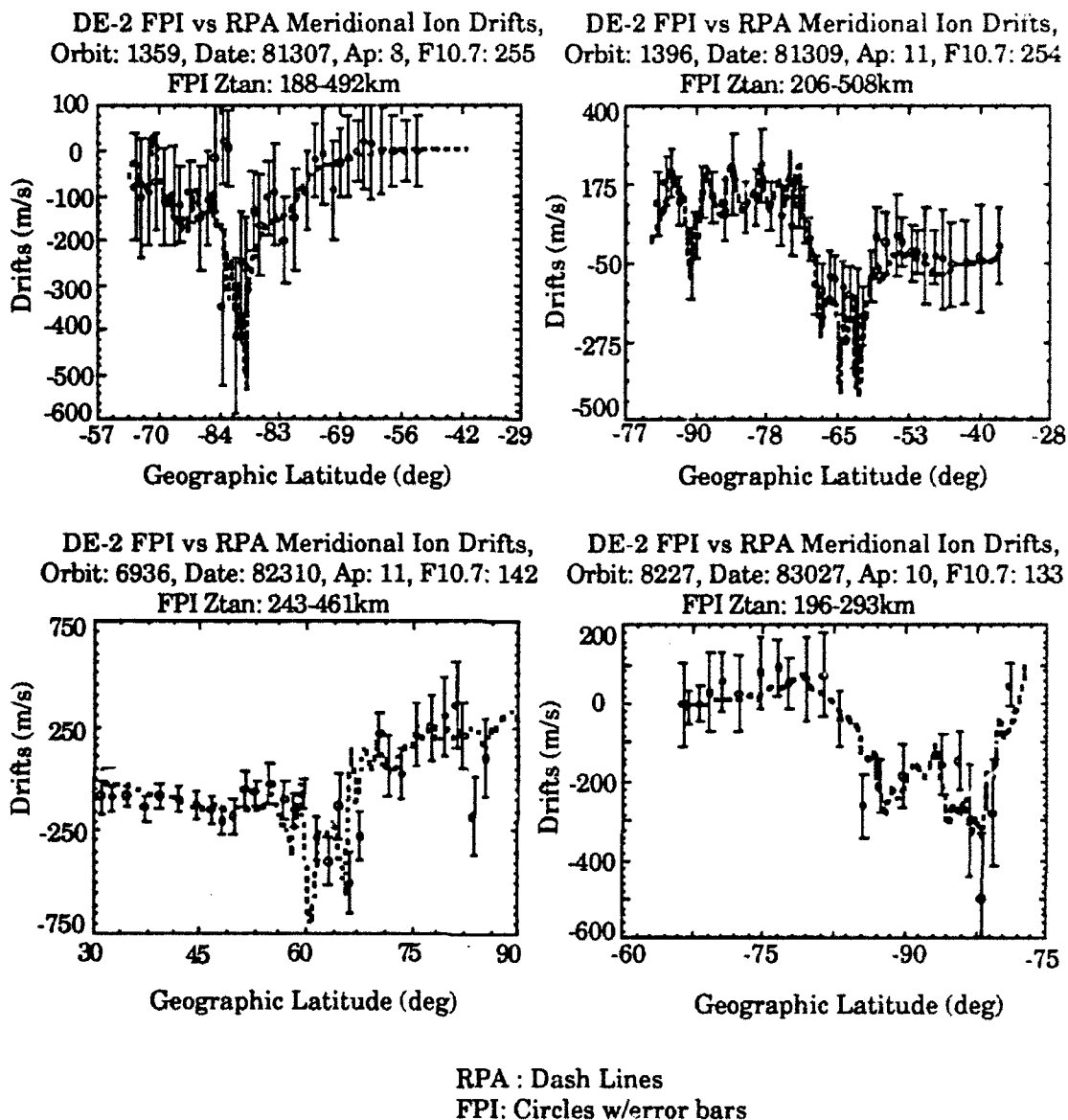


Figure 4.10b The FPI ion drifts in these plots are not bin averaged for all tangent point altitudes between  $\sim 200$ - $500$ km, as in Figure 4.10a. Instead, these FPI ion drifts come from select mirror positions only (between tangent point altitudes of  $\sim 200$ - $500$ km) in which the ion drift, temperature and brightnesses all rapidly converged to stable solutions in the standard analysis package. The agreement with RPA measurements is excellent.



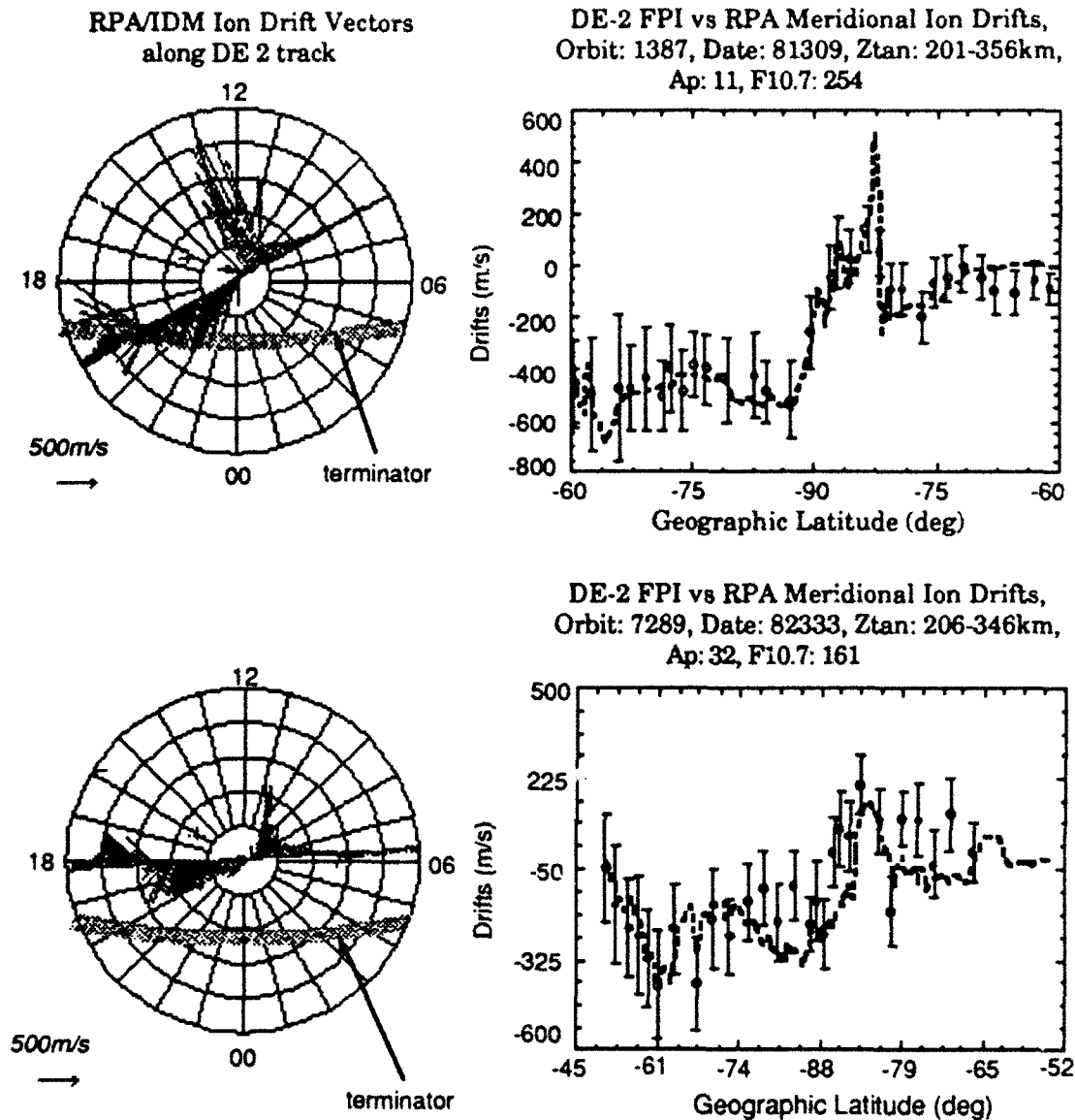


Figure 4.10c Two orbits of FPI vs RPA comparisons using select mirror positions only. Agreement is excellent. Polar dials to the left of the drift comparisons are DE-2 RPA/IDM ion drift vectors plotted along the satellite track. The terminator is the hatched line. Times are local solar. The enhanced RPA and FPI LOS drifts are readily seen in the vector ion drifts on the polar dial.

### 4.3 DE-2 FPI (7320Å) Ion Temperatures

The main thrust of this dissertation is to study ionospheric dynamics (ion drifts). However, as an aside (and for completeness), I attempted to retrieve ion temperatures from the 7320Å emission using DE-2 and ground-based observations; I had limited success. This section deals with DE-2 ion temperatures; ground-based ion temperatures are discussed in Chapter 5. The FPI (7320Å) ion temperature profiles are frequently much different than those measured by the RPA or output by the VSH model (see Figure 4.11). The standard analysis package that derived ion temperatures used a bandwidth analysis of a single-Gaussian spectrogram. The 7320Å emission is a doublet; modification of the analysis package to include deriving ion temperatures from a bandwidth analysis of a double-Gaussian spectrogram (thereby simulating the 7320Å doublet) somewhat improved the temperature comparisons. But DE-2 FPI recovered ion temperature problems still exist using the 7320Å emission.

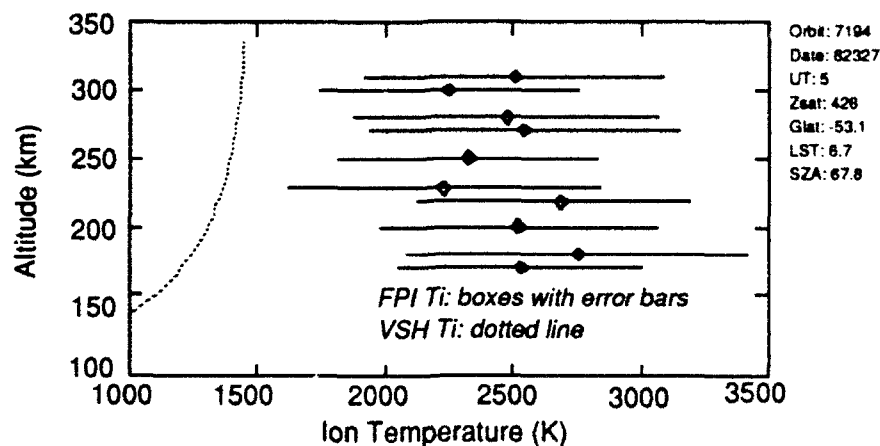


Figure 4.11 FPI (7320Å) recovered ion temperature profile (using standard single-Gaussian analysis) plotted vs modelled VSH profile for the same geophysical conditions. A new method of determining FPI (7320Å) temperatures was devised to account for the doublet nature of this emission.

#### 4.3.1 Modification of the DE-2 Standard Analysis Software

The temperature of an emitting species depends on the emission line width. Assuming the 7320Å emission to be a Gaussian distribution, the shift and width of the emission line contain the velocity and temperature information of the emitting species as discussed in Chapter 2.1.2. Since the 7320Å emission is a doublet with the  $O^+(^2P_{3/2} \rightarrow ^2D_{5/2})$  component at 7319.9Å being 3.8 times more intense than the  $O^+(^2P_{1/2} \rightarrow ^2D_{5/2})$  component at 7319.1Å, this single Gaussian approach will not work properly for temperature analysis. The addition of the second smaller Gaussian may cause the bandwidth to be too wide, possibly leading to temperature retrievals that are too high. The shift (drift speed) of the doublet using a single Gaussian analysis is not affected. To improve this situation and recover ion temperatures in an attempt to study ionospheric energetics, the DE-2 standard analysis package was modified to accommodate doublet species such as this one (the Sodium D lines are another example).

##### 4.3.1.1 Doublet Separation Determination

The precise doublet separation must be known *a priori* before code modification could begin. In 1974, Meriwether et al. reported an observed doublet separation of  $0.836\text{Å} \pm 0.004\text{Å}$  recovered from an FPI (7320Å) at College, Alaska. They state that the series of measurements was of low quality due to large temporal variation in the signal. Hence, their observed value is a "suggested" value. No where else in the literature have I seen another account of this doublet separation.

To determine this doublet separation, I left it as an unknown and made the single Gaussian standard DE-2 analysis software assume the emission was double Gaussian by specifying the brightness ratio as 3.8:1. I also knew what the temperatures should be for a particular orbit since I had RPA ion temperatures for select orbits and VSH model ion temperatures for orbits with no RPA data. I then ran FPI (7320Å) data through the double Gaussian software, varying the doublet separation from 0.001Å to 0.999Å, incrementing by 0.001Å. I did this for 10 orbits of data. The analysis would produce a file of FPI double Gaussian recovered ion temperatures created with the various doublet separations. Only temperatures that were between 500 - 6000K (with errors < 15%) were written to the datafile. I then compared the data in the datafile to what the RPA measured or VSH modelled. Surprisingly, this was easy to do since much of the data in the datafile was considerably different from the RPA or VSH values. What became immediately obvious was that a doublet separation of 0.210Å for the 10 orbits analyzed produced the best match to RPA and VSH values.

Note that the number of orders is unknown for FPI spectra. The DE-2 free spectral range is given by:

$$\text{fsr} = \frac{\lambda^2}{2d} = \frac{(7319.9\text{\AA})^2}{2(1.26 \times 10^{-8}\text{\AA})} = 0.213\text{\AA} \quad 4.19$$

where  $\lambda$  is the wavelength and  $d$  is the etalon gap.

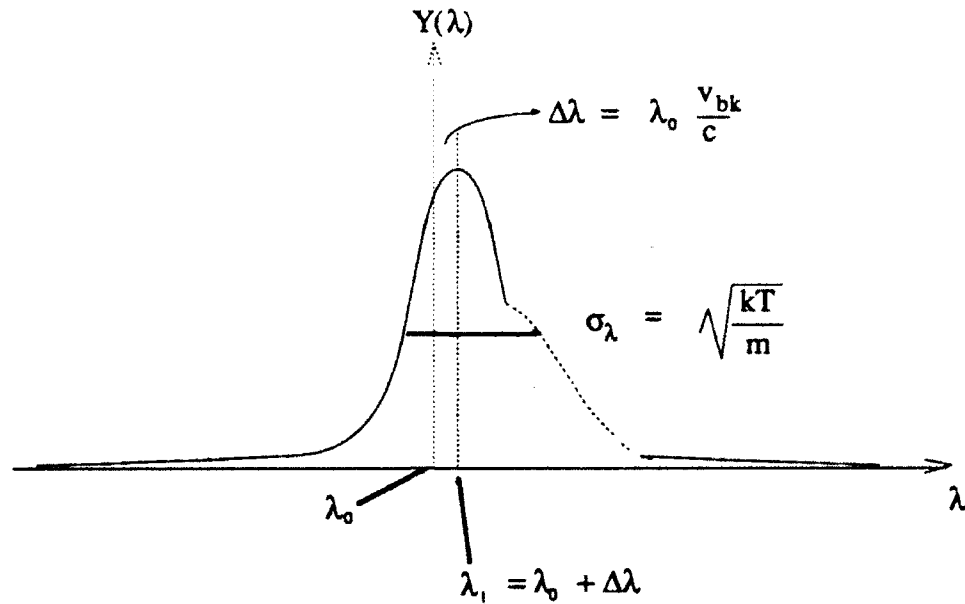


Figure 4.12 Compare to Figure 2.1. In this case, the weaker 7320Å doublet component is superposed nearly on top (0.081 channels off - see Chapter 2.1.3) of the stronger component and has caused the Gaussian distribution to be wider than a single emission would be. Note that the temperature recovered from single-Gaussian analysis techniques will now be higher since the bandwidth is wider. By resolving the distance between the two emission peaks and applying a double-Gaussian source function to the standard analysis procedure, one can determine more accurate ion temperatures.

Hence, one would expect the fit to repeat about every 0.213Å. Thus, 0.210, 0.423, 0.636 and 0.849Å are the obvious choices for doublet separation. I assume that a doublet separation greater than 1Å would be relatively easy to resolve and would have been published and known within the aeronomy community. Since 0.849Å is nearly identical to the observed values of Meriwether et al. (1974), I chose this to be the doublet separation to be used whenever determining ion temperatures. A month after this analysis machinery went into production, Meriwether (p.c., 1991) sent me a message stating that in 1979, he obtained a doublet separation of 0.859 +/- 0.004Å from one fringe at the Michigan Airglow Observatory in twilight. With his ground-based data, and this space-based data, the 7320Å doublet separation appears to be 0.836Å (+/-0.004Å) < Δλ < 0.859Å (+/-0.004Å). This

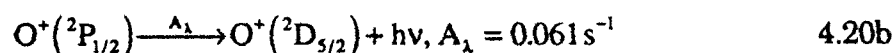
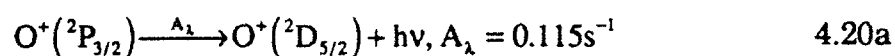
may help future researchers in their quest for determining F-Region plasma temperatures interferometrically.

#### 4.3.1.2 RPA vs FPI Ion Temperature Comparisons

Figure 4.13 shows "simultaneous" FPI (7320Å) ion temperatures compared with RPA temperatures for DE-2 orbit 7289. The FPI data are bin averaged for tangent point altitudes between 200 - 500km in the same fashion as the ion drifts in Figure 4.10a. The standard single-Gaussian (circles with error bars) fit threw many temperatures away because they were out-of-bounds. The double-Gaussian software (X with error bars) tossed out fewer temperatures and gives a better fit to the RPA measured ion temperatures. But problems still exist with ion temperature determinations in the double-Gaussian mode. When analyzing select mirror positions, as done with ion drifts in Figures 4.10b-c, it was noted that the temperatures vary considerably from mirror position to mirror position even when the iterations rapidly converged to a stable solution. Hence, the best method of displaying these ion temperatures was to average them, as shown in Figure 4.13. Large discrepancies, as with the drift profiles previously shown, may be ascribed to many factors. *First*, there is the tendency of the remote FPI measurement to smear out large shears due to the relatively long spatial integration path length of the measurement. *Second*, discrepancies may exist because of temporal changes occurring on shorter time scales than the temporal lag of ~1-3 minutes that was applied to the FPI measurements so the two instruments were measuring common volumes. *Third*, the RPA senses all ions at satellite altitude (mainly O<sup>+</sup>) while the FPI is only sensing the 7320Å emission from the O<sup>+</sup>(2P) ion, which is 5eV above ground state. *Fourth*, the standard analysis routine

assumes thermodynamic equilibrium; this may not be true, especially in auroral zones where precipitating energetic electron beams produce large electron and temperature gradients along the FPI LOS, causing non-thermal equilibrium. It has been shown (St-Maurice and Schunk, 1979) that the ion velocity distribution may not be Maxwellian at F2-Region polar latitudes when convection electric fields of  $\sim 10\text{mV/m}$  or greater are present. They went on to show that above  $\sim 180\text{km}$ , the ion velocity distribution may be characterized by *different* temperatures parallel and perpendicular to  $\mathbf{B}$ , with the perpendicular component larger than the parallel one. And *finally*, since there is a small field-aligned component (FAC) of the ion drift due to neutral winds (Chapter 4.1.5.3), ion temperatures may be affected by Equation 4.18 since the  $7320\text{\AA}$ -emission Gaussian source function will be broadened by this FAC.

Any of these complicated discrepancies will have an ill effect on the DE-2 FPI ( $7320\text{\AA}$ ) ion temperature retrievals by deforming the desired spectrogram's bandwidth. Measuring the shift of the spectrogram (ion drift) is a much simpler (relatively) task. Hence, Figure 4.13 should be viewed with very cautious optimism. The level of agreement seen in Figure 4.13, however, does give confidence in the remote technique of studying ionospheric energetics and forces one to consider suitably instrumenting a small satellite in the future so one can study ionospheric dynamics (drifts) and energetics (temperatures) using the  $7320\text{\AA}$  emission doublet as the *prime* emission to be observed. Unfortunately,  $7320\text{\AA}$ -deduced ion temperature recovery is more involved. The standard assumption that the strongest component in the doublet is 3.8 times more intense than the weaker component is not always true. This 3.8 value can be derived by recalling



The statistical weight for equation 4.20a is 4/6; the statistical weight for 4.20b is 2/6. Thus,

$$\frac{0.67 \times 0.116\text{s}^{-1}}{0.33 \times 0.061\text{s}^{-1}} \approx 3.8 \quad 4.21$$

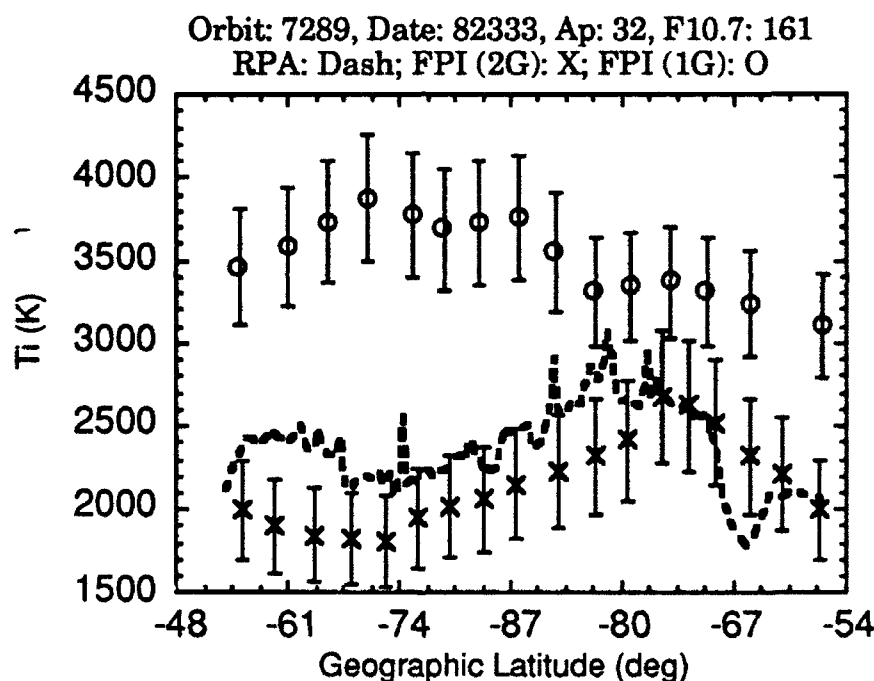


Figure 4.13 DE-2 FPI (7320Å) FPI vs RPA Ti comparisons for orbit 7289 using both the standard single-Gaussian (FPI 1G) and modified double-Gaussian (FPI 2G) version of the standard analysis package to account for the doublet nature of the 7320Å emission. FPI 1G is high since it cannot handle the wider bandwidth produced by the doublet emission (see Figure 4.12). Ion temperatures retrieved from this space-borne method must be viewed with caution. See text for discussion.

Hence, the transition in equation 4.20a is 3.8 times more intense than the transition in 4.20b. Torr (p.c., 1991) stated that laboratory measurements



indicate the two lines may vary in intensity ratio, with the most frequent ratio being the standard 3.8:1. Smith et al. (1982) have observed an enhancement of the weaker component of the 7320Å doublet during certain

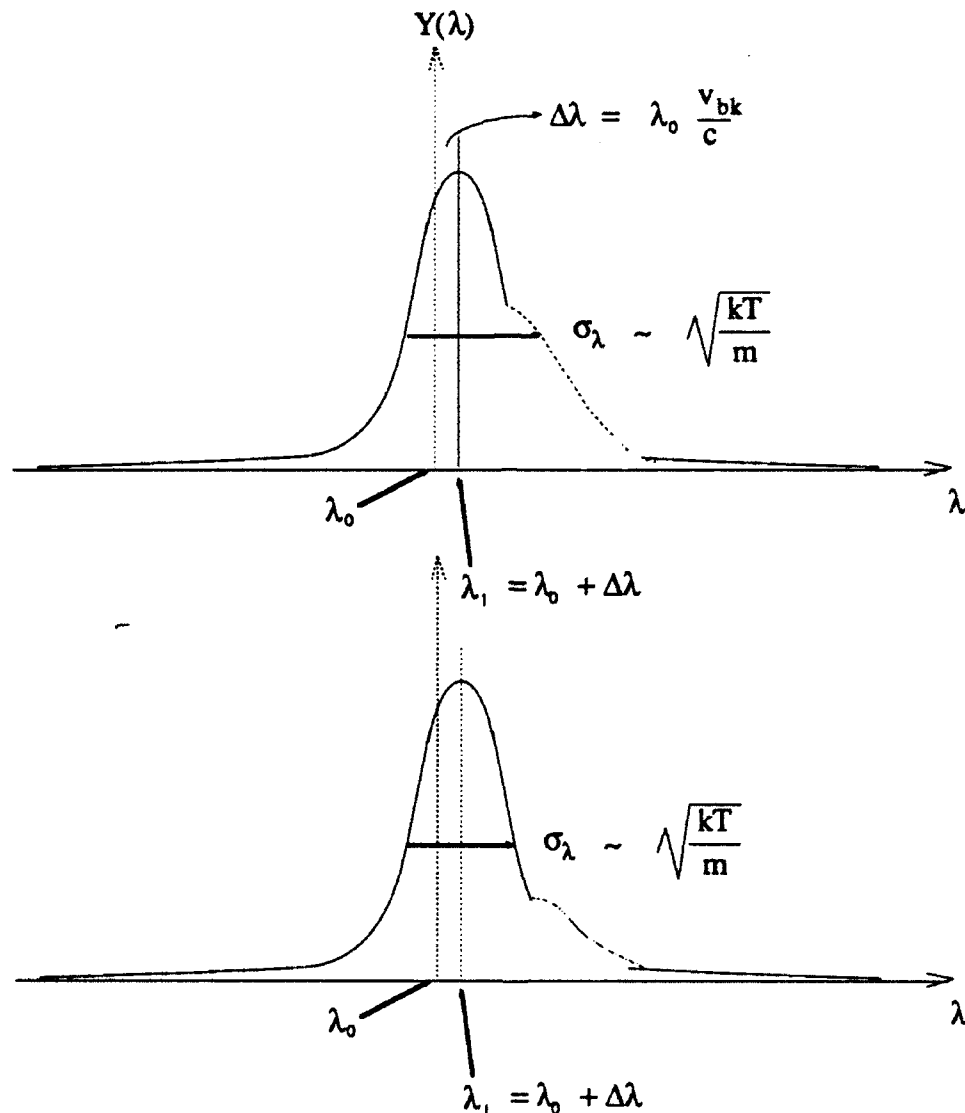


Figure 4.14 In the top panel, the weaker doublet is shown to make the bandwidth wider than if it were not present. The double Gaussian software handles this adequately. But what if the intensity ratio fluctuates and becomes, for example, 4.5:1 (bottom panel) or 3.8:2? The double-Gaussian software, expecting the classic 3.8:1 ratio, will produce erroneous temperatures since its bandwidth does not represent the actual bandwidth.

conditions using a ground-based FPI near Longyearbyen, Svalbard. If true, the double Gaussian analysis, built on the assumed 3.8:1 ratio, would frequently give erroneous results. Most double-Gaussian analyzed FPI ion temperatures seem very reasonable. But fewer FPI (7320Å) temperature measurements, even after the double-Gaussian analysis, compare as favorably with RPA measurements or modelled ion temperatures as do the FPI (7320Å) ion drift measurements. Perhaps this can be attributed to the fluctuating 3.8:1 ratio, or the five reasons listed previously. Figure 4.14 illustrates this point.

#### **4.4 Validation of the 7320Å Volume Emission Rate Model against DE-2 FPI (7320Å) Observations**

By inverting the line-of-sight brightnesses obtained from the DE-2 FPI (7320Å), altitude profiles of the 7320Å volume emission rate may be obtained. These "observed" volume emission rates can then be compared to the 7320Å volume emission rate model (Chapter 3) to validate the model. Figure 4.15 is a summation of all volume emission rate profiles taken along DE-2 orbit 7125. As expected, the volume emission rate peaks at ~300km. Figure 4.16 is a 7320Å DE-2 "observed" profile taken from this orbit for the conditions listed in the diagram. The volume emission rate data are compared with the calculated data from Chapter 3's [OII]  $\lambda$ 7320Å emission aurora-airglow model for equivalent geophysical conditions. The observed and modeled peak emission altitude in Figure 4.16 is seen to occur at ~300 km. The volume emission rate reduction below the peak is due to an increase in collisional deactivation caused by increasing ambient number

density with decreasing altitude. The volume emission rate decrease above the peak is due to a decrease in the production caused by the combination of decreasing electron and atomic oxygen number densities with increasing altitude.

In a series of tests, it was determined that for  $A_p$  values less than 50 and F10.7 values less than 220, the volume emission rate model accurately predicted what the DE-2 "observed" for a  $7320\text{\AA}$  volume emission rate. When

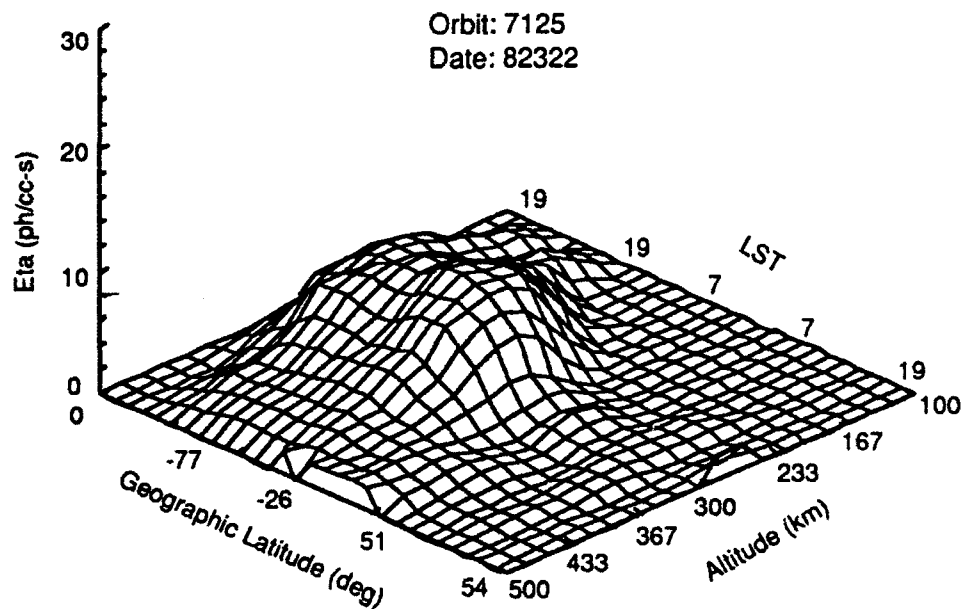


Figure 4.15 Plot of "observed" DE-2  $7320\text{\AA}$  volume emission rates for orbit 7125 obtained from the inversion of measured LOS brightnesses. The volume emission rate is seen to peak when the sun is at its highest point in the sky (maximum photoionization) and at  $\sim 300$  km.

the  $A_p$  and F10.7 values became greater than these values, the modelled volume emission rate was always less than the observations. This is due to

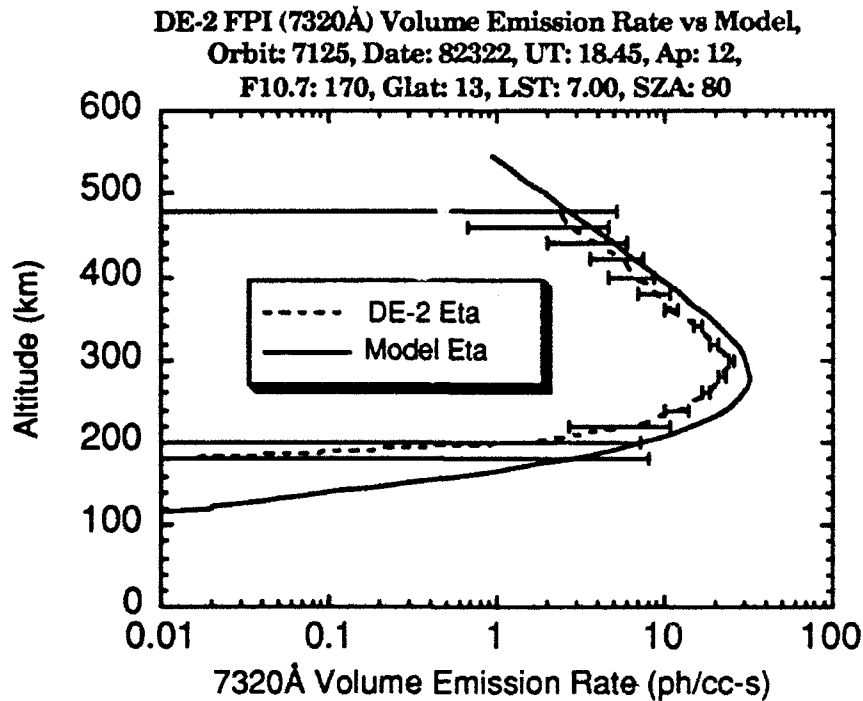


Figure 4.16 DE-2 FPI (7320Å) "observed" volume emission rate profile for the same orbit as Figure 4.15. Note the evident good agreement between the model and observation. Satellite altitude was 510km.

the fact that the LAPI data (Chapter 3.3.2), used to simulate aurora, is only a mirror of diffuse aurora (observations were made during quiet times). Plus, the photoelectron model (imbedded in the 7320Å volume emission rate model) used to produce photoelectrons (given a certain level of solar activity) and secondary electrons, underestimates the number of electrons that are created with energies greater than ~18eV (Hume, 1992). And it is these electrons that can produce the 7320Å emission via impact ionization.

It is not always possible to compare DE-2 volume emission rates with modelled volume emission rates. The model runs from ~ 100km - 550km while DE-2 observations are dependent on satellite altitude. In low altitude orbits, much of the observed volume emission rate will come from below 200km where the  $O^+(^2P)$  ion is severely quenched; errors in the volume emission rates in these cases are large since the 7320Å signal is weak and

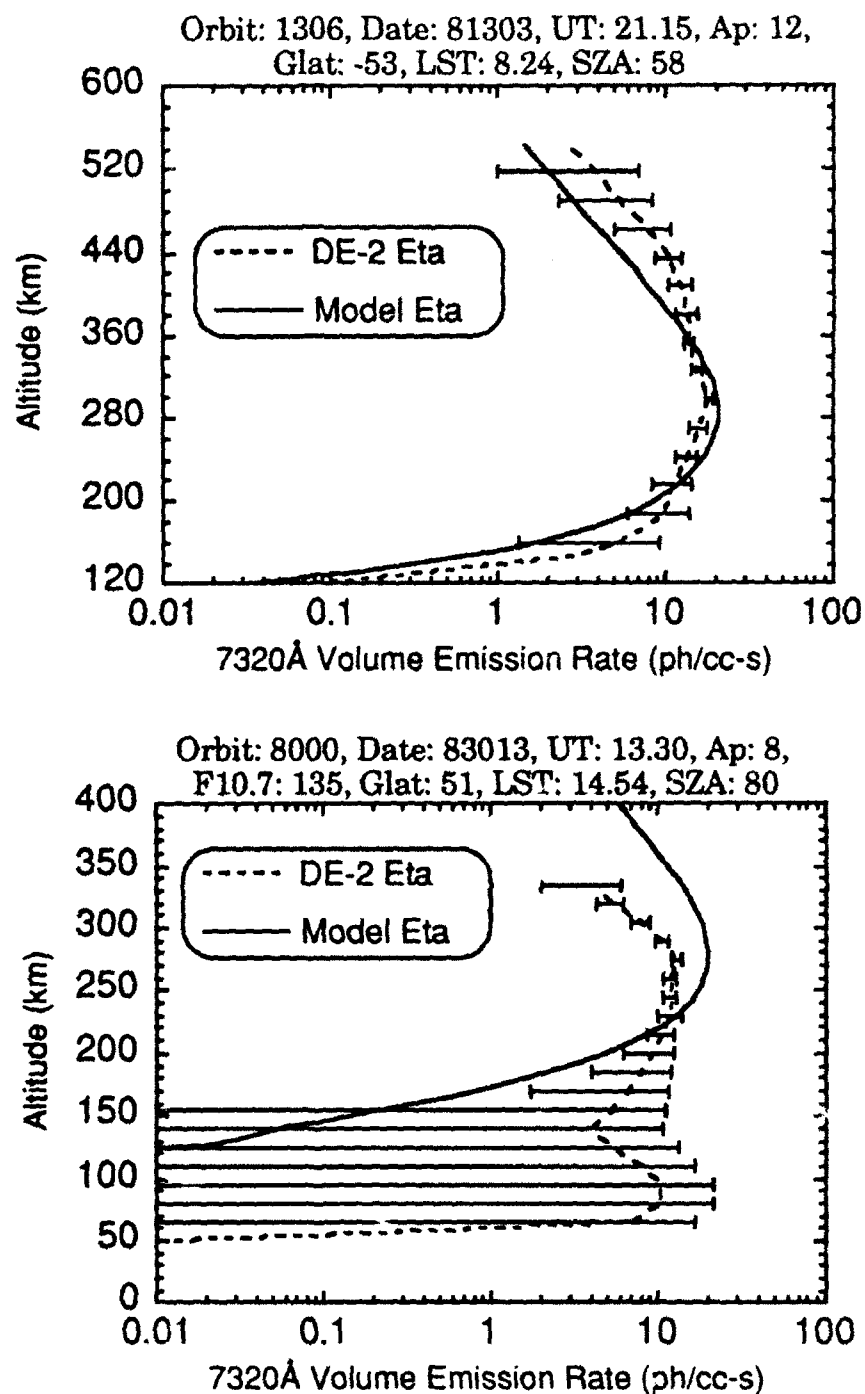


Figure 4.17 Inverted 7320Å volume emission rate profiles for DE-2 orbits 1306 (top panel,  $Z_{\text{sat}}=576\text{km}$ ) and 8000 (bottom panel,  $Z_{\text{sat}}=378\text{km}$ ). The measured profiles are compared to the 7320Å aurora-airglow model presented in Chapter 3.3.2 for equivalent geophysical conditions. Note the peak emission altitude of  $\sim 300\text{km}$ . Low altitude DE-2 volume emission rates show large errors due to the severe quenching of  $\text{O}^+(^2\text{P})$  ions below  $\sim 200\text{km}$  and contamination from Rayleigh scattering off cloud tops.

since Rayleigh scattering from cloud tops contaminates the measurements. Figure 4.17 is an example of this. In the top panel, the satellite is at 576km, and the agreement between model and observation is excellent for a full range of altitude. In the bottom panel, the satellite is at 378km, and much of the emission observation is from below 200km. Even in this case, however, the peak observed emission is similar to that of the model.

#### 4.5 Conclusions

First results of remote ion drift, temperature and brightness measurements from Dynamics Explorer-2 have been presented. The remotely-measured ion drift measurements have been validated against independent *in situ* observations. Volume emission rates have been produced from the remotely-measured 7320Å brightness and compared to a Chapter 3's 7320Å volume emission rate model; the results are favorable. The drift, temperature and brightness results demonstrate the utility of the new spaceborne technique, although ion temperature retrieval must be viewed with guarded optimism (see list of reasons in Section 4.3.1.2). Simulations in Chapter 6 will demonstrate the power of the technique for routine quasi-global-scale monitoring of ionospheric convection. While the statistical errors associated with the remote measurements are larger than those typically associated with conventional *in situ* techniques, the technique comes into its own in terms of its potential for remote imaging of the quasi-instantaneous polar ionospheric convection pattern. The determined doublet separation of 0.849Å favorably agrees with the value of ~0.836Å from Meriwether et al. (1974) and 0.859Å from Meriwether (p.c.,

1991). In the next Chapter, I discuss results of ground-based [OII]  $\lambda 7320\text{\AA}$  observations.

## CHAPTER 5

### GROUND-BASED FPI (7320Å) OBSERVATIONS OF IONOSPHERIC DYNAMICS AND ENERGETICS FROM GREENLAND

The purpose of this Chapter is to prove that ion drifts and possibly temperatures from a ground-based FPI (7320Å) can be recovered with confidence. To this end, I made the first-ever measurements of ion drifts and temperatures using the ground-based FPI technique *and* compared them to simultaneous incoherent scatter radar (ISR) measurements *and* model predictions for the same conditions. Agreement between the limited data sets is good. During my tenure at the University, I made three trips to Greenland for data-gathering campaigns. The first two trips resulted in low quality data, but introduced me to ground-based FPI studies of the 7320Å emission; the last trip produced excellent results. The resulting data will now be presented. Conclusions are in the final section of this Chapter.

#### 5.1 Outline of the 7320Å Arctic Campaign

Ground-based observations of the 7320Å emission are not possible during the *daytime* since this emission is overwhelmed by competing solar illumination. At *night*, when the photoionization source at F2-Region altitudes is gone, the 7320Å emission may be observed only if energized by



auroral electron impact ionization. At *twilight*, especially when the sun is  $\sim 1-14^\circ$  below the horizon, 7320Å emission observations are ideal since the F2-Region is still being photoionized, yet the ground is in darkness. Thule and Søndre Strømfjord, Greenland offer the experimenter both long hours of twilight and aurorally-induced observations of the 7320Å emission.

#### 5.1.1 Thule AB, 8 - 15 January 1991

Located at  $\sim 76.34^\circ\text{N}$  geographic latitude and  $\sim 68.47^\circ\text{W}$  longitude, Thule AB is north of the auroral zone and in the polar cap. The FPI here is similar to the one in Søndre Strømfjord (Chapter 2.1.4). During this week of near total darkness, I became familiar with this FPI and determined the best observing times and look directions for the twilight campaign scheduled for April 1991.

#### 5.1.2 Søndre Strømfjord, 16 - 21 January 1991

From 16-21 January 1991, the Michigan Airglow Observatory ground-based FPI at the Søndre Strømfjord ( $69.15^\circ\text{N}$ ,  $53.3^\circ\text{W}$ ) ISR site made observations of Doppler line profiles of the ionospheric [OII]  $\lambda 7320\text{\AA}$  emission. The FPI at Søndre Strømfjord is a 10cm single etalon, six filter interferometer employing a 12 channel image plane detector (IPD); its spectral resolution is  $0.01\text{\AA}$  and the instrument drift is  $0.0002\text{\AA}/\text{h}$  (about 10m/s; see Chapter 2.1.4 for more details of this FPI). The ISR at Søndre Strømfjord has a transmission frequency of 1290MHz and is fully steerable. During the observation period, the ISR operated in the up-B mode (looking straight up the magnetic field lines) and the long pulse scheme. Due to instrumental and weather related problems, simultaneous FPI (7320Å) and ISR observations of line-of-sight ion drifts and ion temperatures only

occurred at ~ 21.47UT and 23.56UT on 19 Jan 91. These  $O^{+}(^2P)$  7320Å fringes collected at twilight (21.47UT) and in aurora (23.56UT), coupled with the magnetic field-aligned ISR measurements, made these the first-ever ion drift and temperature comparisons using these two instruments. During three evenings, (17-19 Jan 91), I observed aurorally produced  $[OII] \lambda 7320\text{\AA}$  emissions near local midnight. In each case, low energy (<200eV) diffuse aurora was overhead. This agrees with Rees (1989) who states that in hard aurora, produced by keV electron precipitation, the OII lines are masked by strong emissions from the  $N_2$  1P system. This is because keV electrons penetrate down to ~ 100km where OII lines are severely quenched and strong  $N_2$  1P system emissions dominate.

However, the ground-based FPI (7320Å) observations taken during this period were of low quality (background nearly equal to signal) since I was unsure of the exact place and time to be looking for this emission at this location. Clouds on several nights and windy conditions precluded routine ISR and FPI comparisons. Plus, due to the weakness of the emission (frequently ~20-50R), the IPD required very long integration times before good fringes could be measured and later analyzed for drifts and temperatures. Of course, none of this was known until about 30 days *after* the data campaign was over and the analysis had begun. By the end of February, 1991, the best times and FPI-look directions were calculated, and the 7320Å emission observation patrol was determined to have integration periods ranging from ~ 120s to 720s. Armed with this knowledge, a new data gathering campaign for Søndre Strømfjord, complete with radar time, was then scheduled for September 1991.

### 5.1.3 Thule AB, 1 - 10 April 1991

During my second and final trip to Thule AB, the conditions were ideal for twilight 7320Å emission observations the first night I was there. But by the time I calibrated the instrument and began taking data, clouds rolled in, making twilight observations impossible. This was then followed a 72 hour-long arctic blizzard. When the weather cleared, I had to recalibrate the instrument due to the severity with which the winds had buffeted the trailer in which the FPI was housed. Once that was complete, I cleared all snow and ice from the viewing dome on top of the trailer. I had one night left for observations. However, when twilight came, so did the clouds. No ion drift or temperature data were ever retrieved at Thule AB.

Normally, Thule should be an ideal place for ground-based FPI (7320Å) twilight observations. Twilight is defined as the period when an emitting layer is illuminated by the sun from below. For ~ 60 days/year (late March/early April or late August/early September), Thule has about 12 hours of twilight since the sun is just beginning to skirt the horizon. Since it is north of the auroral zone, 7320Å emission observations after twilight (solar depression angle  $> 14^\circ$ ), when the photoionization source is gone, will be nearly impossible (especially with an IPD detector in the FPI). During the daytime, competing solar illumination overwhelms the 7320Å emission at the ground. Therefore, future 7320Å emission observation attempts at Thule should be made during March/April and August/September twilight periods when the sun is ~  $1 - 14^\circ$  below the horizon.

#### 5.1.4 Søndre Strømfjord, 3 - 10 September 1991

During this data campaign, I retrieved drifts and temperatures from twilight and aurorally produced 7320Å emissions. Unlike Thule AB, Søndre Strømfjord is in the auroral zone; hence, 7320Å emissions may be detected from dusk through dawn since the energetic electron impact ionization from the auroral electrons may be a source for the 7320Å emission all through the night.

The FPI (7320Å) operated in a cyclic patrol observing just 7320Å emissions at mirror positions in the zenith and in the four geographic cardinal directions (North, South, East and West at an elevation angle of 45°). There was also a calibration mirror position in which a Xenon lamp was sampled once every patrol to record the behavior of the instrument drift through the night of observations. A six minute dark count was recorded during each patrol to account for the background counts induced by electronic noise. Each patrol took ~30 minutes. The ISR ran during the nights I was looking for twilight and aurorally produced 7320Å emissions. The desired conditions for making the FPI (7320Å) emission observations at Søndre Strømfjord are twilight conditions with the solar depression angle between ~ 1 - 14 degrees, clear skies (scattering from clouds may alter the spectral information of the emission) or nighttime (Rayleigh scattered light must be avoided since it obscures the airglow) with no discrete aurora in the field-of-view. Discrete aurora originate from various heights; hence, the resulting FPI measurements cannot be attributed to a certain altitude. The condition necessary for ISR measurements is that there must be at least ~ 10<sup>5</sup> electrons/cm<sup>3</sup> at F-Region altitudes.

The night of 3/4 September 91 was the best observational period, with ideal conditions existing for both FPI and ISR measurements. The skies were clear and low energy electron precipitation was occurring between the evening and morning twilight periods. This night turned out to be the best night of the campaign. The night of 4/5 Sep 91 was completely overcast and no FPI observations were made. The night of 5/6 Sep 91 had a windstorm with gusts to 65 mph and steady winds > 40 mph most of the evening; no ISR or FPI observations were made. The night of 6/7 Sep 91 began well and ended well, but from ~02-05UT, intense pulsating green aurorae were seen overhead and the analysis run on these data produced low quality spectrograms from which no reliable information could be retrieved. The night of 7/8 Sep 91 was a good night with partly cloudy skies and low energy electron precipitation. However, I had to limit the ISR observations because every time the radar was turned on, electronic interference upset the FPI measurements. The final night, 9/10 Sep 91, was an excellent night with clear skies and low energy electron precipitation between the twilight periods. The electronic interference with the ISR was fixed; this was the second best night of observations and FPI/ISR comparisons.

The next section presents this unique data set and validates the FPI (7320Å) drifts and temperatures against the ISR.

## **5.2 FPI (7320Å) Results and ISR Comparisons from Søndre Strømfjord**

ISR data were recorded with an antenna mode which dwelled up-B and at two other positions. This is known as the three position mode. Vector information can be extracted from the measurements since the first position is antiparallel to the magnetic field, and with the other two

components being more or less eastward and northward (with negative values being westward and southward). The ISR data for this period was shipped to SRI (Stanford Research Institute) where it was processed and then sent to me on tape. The tape consisted of data under various headings, a few of which were altitude, ion temperature and line-of-sight ion velocity components. Appendix C illustrates the software used to extract the ISR encoded data from tape and then to manipulate them into the form seen in this Chapter. Appendix C also illustrates the software and dataflow used in the FPI analysis and plotting routines.

### 5.2.1 FPI Retrieved Ion Drifts and Temperatures and ISR Comparisons

One of my goals for the September 1991 campaign was to resolve the weaker component of the 7320Å doublet ( $O^+(^2P_{1/2} \rightarrow ^2D_{5/2})$  at  $\sim 7319.1\text{\AA}$ ). See Figure 2.8 for an example. Figure 5.1 is sample spectrogram, taken at 4:29UT on 9 Sep 91. FPI (7320Å) calibration was done so that channel 5 was the most sensitive channel. The smaller secondary peak on  $\sim$ channel 11 *may* be the weaker component of the 7320Å doublet. I averaged all 340 spectrograms from this campaign in an attempt to determine if the weaker component of the doublet were resolved near channel 11, as predicted in Chapter 2. This averaging, covering a seven day period with varying geophysical conditions, smoothed the data too much; consequently, no enhancement was detected near channel 11. But by inspecting the spectrograms individually, a near-channel 11 enhancement was seen in  $\sim 25\%$  of the spectrograms. The enhancement was usually during twilight when the the 7320Å signal was strong (see Figure 2.8) or during nighttime with aurora present and long integration times (Figure 5.1). When the enhancement was detected, however, it was always  $\sim$ channel 11 and did not

vary much in relative intensity; when compared to channel 5 counts, channel 11 counts only showed the theoretical 3.8:1 intensity ratio in two of the 340 spectrograms. Smith et al. (1982) and Torr (p.c., 1991) have both stated that this ratio varies in 7320Å-doublet emission observations.

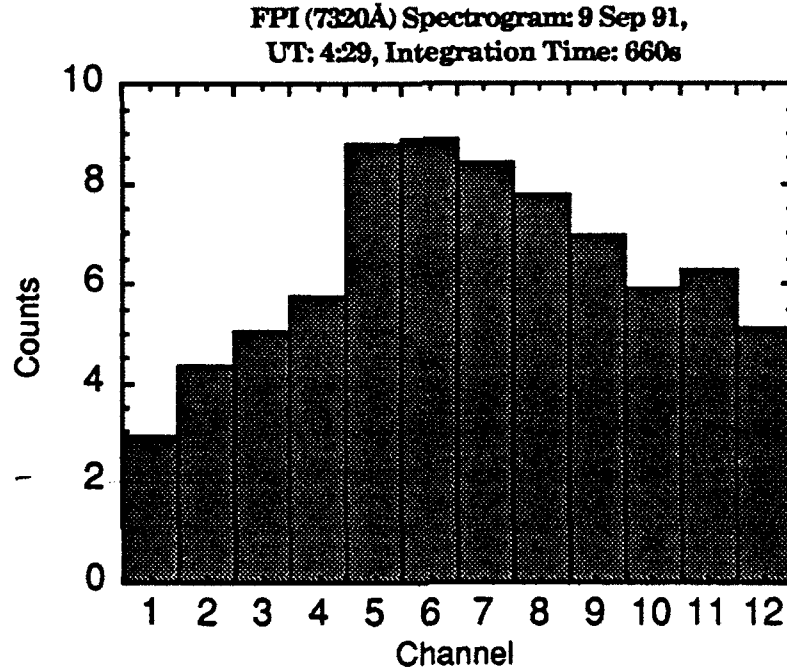


Figure 5.1 Søndre Strømfjord FPI (7320Å) spectrogram for 9 Sep 91 at 4:29UT. The enhancement at channel 11 *may* be the weaker component of the doublet being resolved since it was shown in Chapter 2 that the weaker component of the doublet should be ~6 channels from the stronger one on this FPI.

Currently, this near-channel 11 enhancement could be *detector sensitivity problems* (most probable), *OH contamination* (possible during twilight only since OH has no auroral source), *auroral contamination* (strong band emission from the N<sub>2</sub> 1P may mask the 7320Å lines) or the *weaker component* of the 7320Å doublet (possible after twilight and during soft (<200eV) particle precipitation). Hence, a more sensitive (CCD) detector and a longer data-gathering campaign, with the accumulation of millions of spectrograms (like DE 2), is needed to determine if the weaker component

of the doublet is resolved. Figure 5.2 is a more typical Søndre Strømfjord spectrogram, with no ~channel 11 enhancement seen.

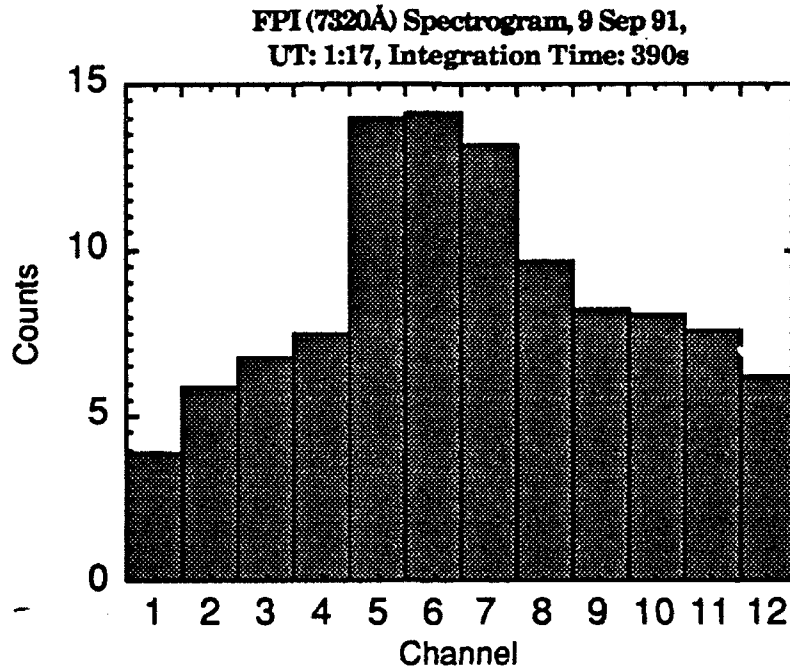


Figure 5.2 Søndre Strømfjord spectrogram; no intensification near channel 11 is seen, although it is visible in several individual spectrograms.

Figure 5.3 is a sample of ISR data observed on 4 Sep 91. The upper left panel contains the ion and electron temperature profiles observed ~00.03 UT. The panel on the right are line-of-sight velocities for the same date and time. The bottom panel is a stack plot of ion drift velocity vectors with time as the abscissa and altitude as the ordinate. The wind barb on the right of the bottom panel denotes 600 m/s. In Chapter 4, I assumed that the ion drift velocity vectors did not change in magnitude from ~ 200 - 500km; this assumption helped me compare the RPA and FPI (7320Å) drift measurements. In Figure 5.3 (bottom panel), it becomes obvious that this assumption is valid - little direction or magnitude change is seen in the drift vectors from ~ 200 - 500 km.



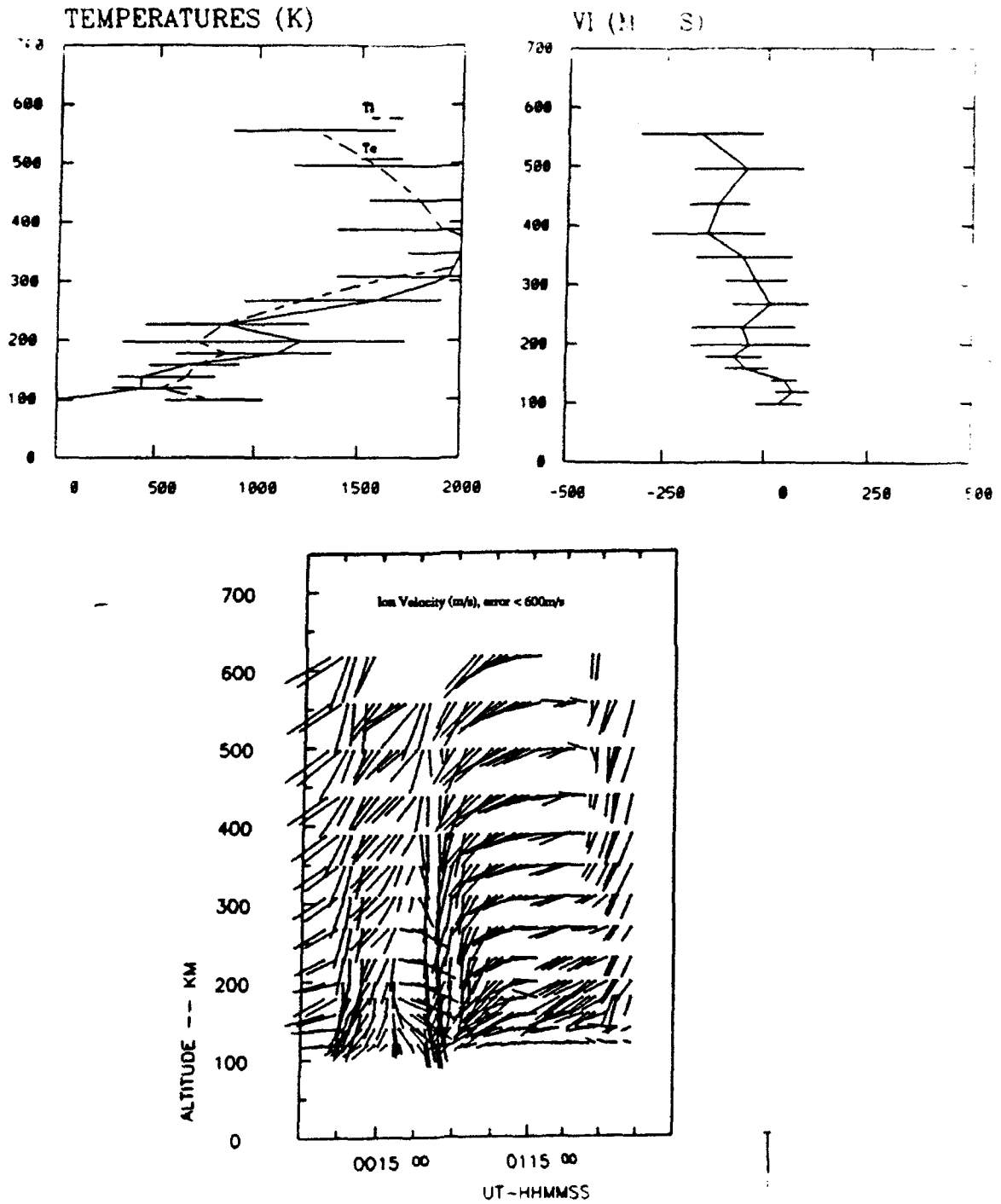
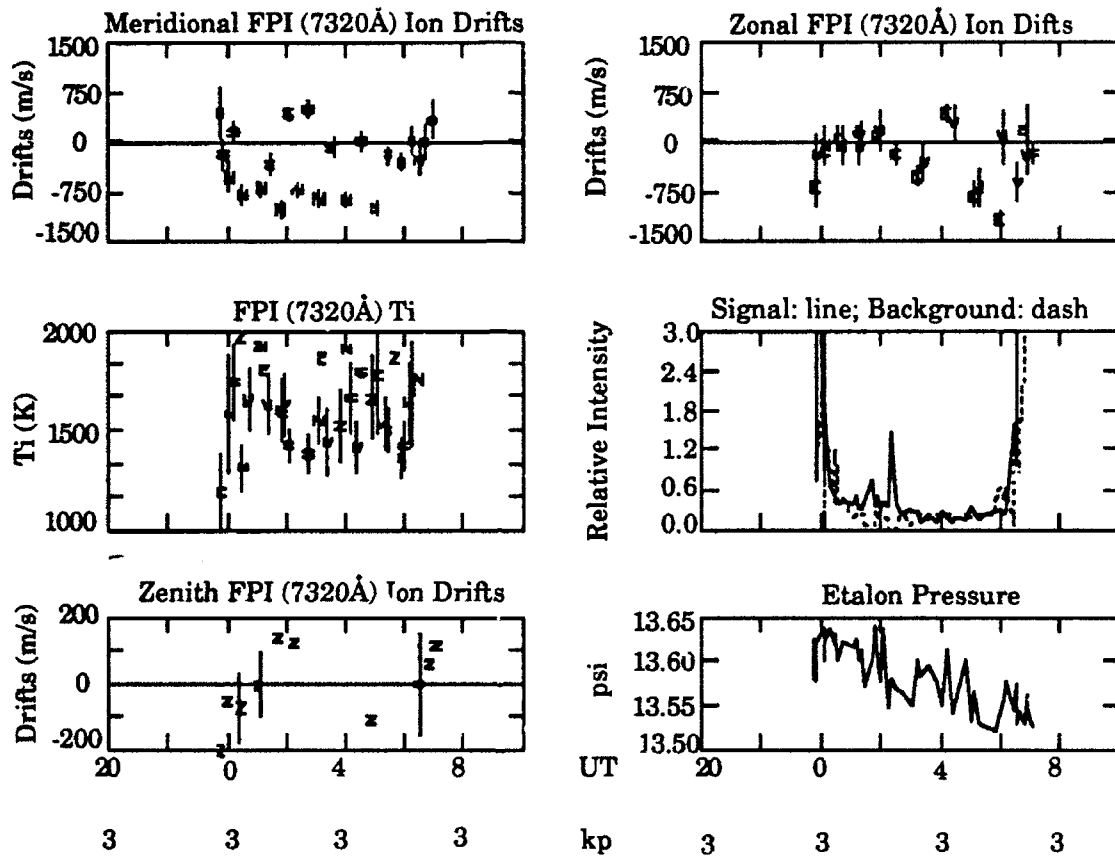


Figure 5.3 Sample ISR data for 4 Sep 91. See text for discussion.

Figure 5.4 is an illustration of analyzed data from Søndre Strømfjord's FPI (7320Å) for the night of 3/4 Sep 91. Universal Time and the appropriate 3-hourly *kp* is the abscissa for all panels. Observations began once the solar depression angle exceeded  $10^\circ$ , which for this time of year was from  $\sim 20$ UT to 08UT. Each measurement is indicated by its corresponding first initial (N  $\sim$  north) along with its error bar in each of the panels. Universal Time and the *kp* index are listed on the bottom of the Figure as the X-axis. The upper two panels contain the retrieved FPI (7320Å) meridional and zonal ion drifts in m/s, after accounting for elevation angle, instrument drift and the zero wind reference as discussed in Chapter 2. Positive is the standard convention: north and east. Since the FPI had an elevation angle of  $45^\circ$ , the north and south measurements are therefore separated by  $\sim 500$ km, assuming an emission altitude of  $\sim 250 - 300$ km. This distance corresponds to  $\sim 5^\circ$  in latitude.

Unlike neutral winds, these ion drifts show considerable fluctuation between the north/south (meridional) and east/west (zonal) measurements, indicating that the ion drifts in the high latitude ionosphere change significantly over  $5^\circ$  of latitude. Redline (6300Å) measurements show the north/south and east/west measurements to be nearly identical (Thayer, 1990; Won, p.c., 1992). In *these* ion measurements, the drifts change considerably in  $5^\circ$  of latitude and strong areas of plasma convergence and divergence are seen in Figure 5.4. Referring to Figure 5.4, the left middle panel contains the FPI (7320Å) ion temperatures for each measurement with its corresponding error bar. The Søndre Strømfjord IPD has a quantum efficiency of  $\sim 5\%$  meaning that only 5% of the 7320Å photons striking the IPD start the electron cascade that is ultimately registered as

the spectrogram. A CCD will increase the sensitivity by a factor of 12 (Killeen and Niciejewski, p.c., 1992).



F10.7: 171  
Ap: 15

Figure 5.4 Analyzed data from the Søndre Strømfjord FPI (7320Å) for 3/4 Sep 91. See text for discussion.

The middle right panel is the relative surface brightness of the emission determined from the analysis for each direction which are connected by the solid line. The dash line in this panel is the continuum background for the emission. When clouds exist in too great a quantity, the background signal strength increases substantially. For the  $7320\text{\AA}$  emission, I found that sky cover had to be 2 octa or less or the background would become intolerable. During two nights of observations, the sky cover increased to greater than this value, and I was forced to ignore the data during those periods. The lower left panel contains the vertical winds after the removal of instrument drift and the reference zero drift value. The lower right panel contains the etalon pressure and its variation during the period of observation.

Figure 5.5 is analyzed Søndre Strømfjord data from 7/8 Sep 91. Cloud cover made accurate retrieval of ion drifts and temperatures impossible from ~ 01 - 04 UT. Figure 5.6 is from the night of 9/10 Sep 91. Conditions during this night were nearly ideal; only some slight hardware problems made the evening less than perfect. Figure 5.7 is a sum of the FPI ( $7320\text{\AA}$ ) drift components combined into vector form and plotted on a geographic polar dial. The drift barb on the lower left corner of the plot represents 500 m/s. Times are local solar and the circles start at  $60^{\circ}\text{N}$  geographic latitude and move inward to the North Pole. I have assumed that the  $7320\text{\AA}$  emissions originate from ~ 300 km. Observation times were limited to twilight and nighttime due to the ill-effects solar illumination on the FPI. Recall from Chapter 1 that the solar wind's electric field is mapped into the polar cap ionosphere along geomagnetic field lines of equipotential, where a dawn-dusk electric field will result. This electric field drives the polar

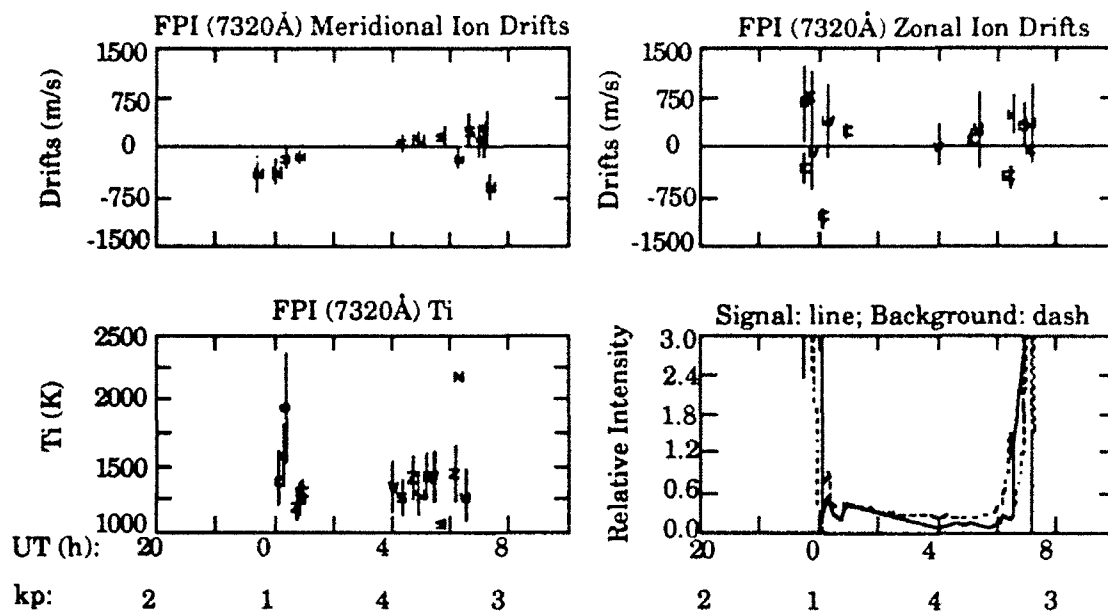


Figure 5.5 Analyzed data from the Søndre Strømfjord FPI (7320Å) for 7/8 Sep 91 (Ap: 22, F10.7: 196). From ~01-04UT, electronic interference from the ISR impacted the FPI's behavior *and* cloud coverage varied from 3/8 - 6/8. During this time, the background was too close to the actual signal and I was forced to ignore the data taken during that period.

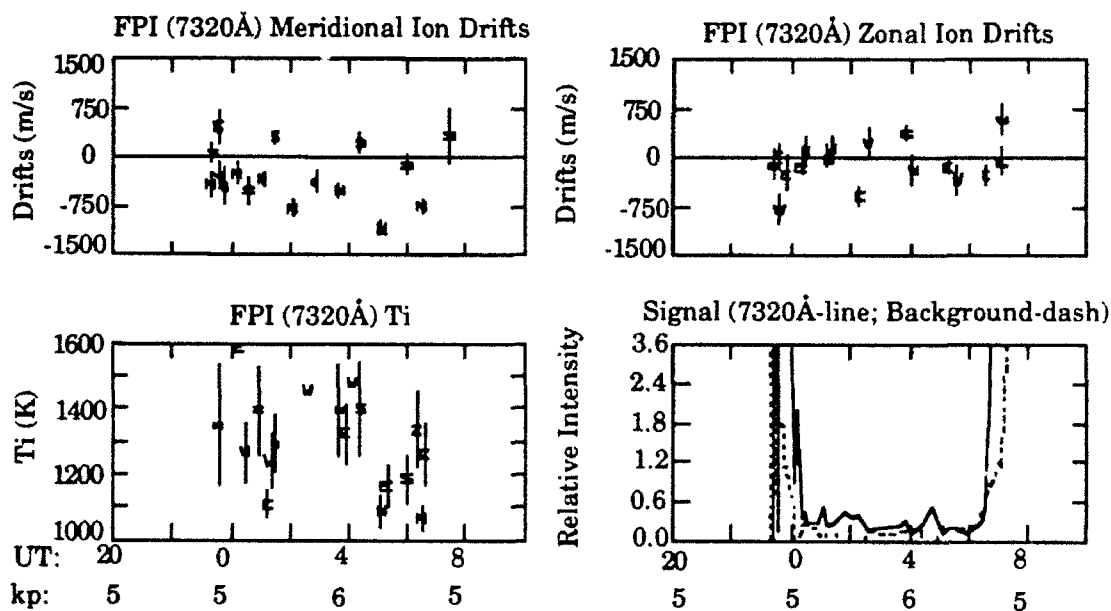


Figure 5.6 Analyzed data from the Søndre Strømfjord FPI (7320Å) for 9/10 Sep 91 (Ap: 32, F10.7: 185).

ionospheric F-Region plasma in the antisunward direction at a drift velocity given by

$$\vec{V}_d = \frac{\vec{E} \times \vec{B}}{B} \quad 5.1$$

where the geomagnetic field is directed into the page in Figure 5.7. The sign of the electric field is reversed in the auroral zone; there, due to equation 5.1, the resulting ion flow is sunward. The two-celled ion convection pattern in Figure 5.7 is visible from just four nights of ground-based observations. Antisunward flow is seen in the center of the bottom dial, with the beginnings of return flow on either side.

Comparisons between the ISR and FPI were difficult to make, mainly because of the different integration times and sensing locations. The FPI patrols consisted of integration times varying from ~ 120 to 720 seconds. The ISR normally had integration times of about 120 seconds. Since temperatures are scalars, the direction in which the FPI was scanning should make no difference to the observed ISR temperatures. Hence, I overplot ISR and FPI temperature values in Figure 5.8. Agreement is reasonable. Note that in Figure 5.8, single-Gaussian software was used to determine the FPI-recovered temperatures. Since the Søndre Strømfjord FPI separated the 7320Å doublet components by ~ 6 channels, the single-Gaussian analysis retrieved accurate (relative to the ISR temperatures) ion temperatures for the 7320Å doublet emission. Double-Gaussian analyses, accounting for the weaker component in the 7320Å doublet, made no noticeable improvement. Separating the doublet components in this fashion should be noted for future FPI work.

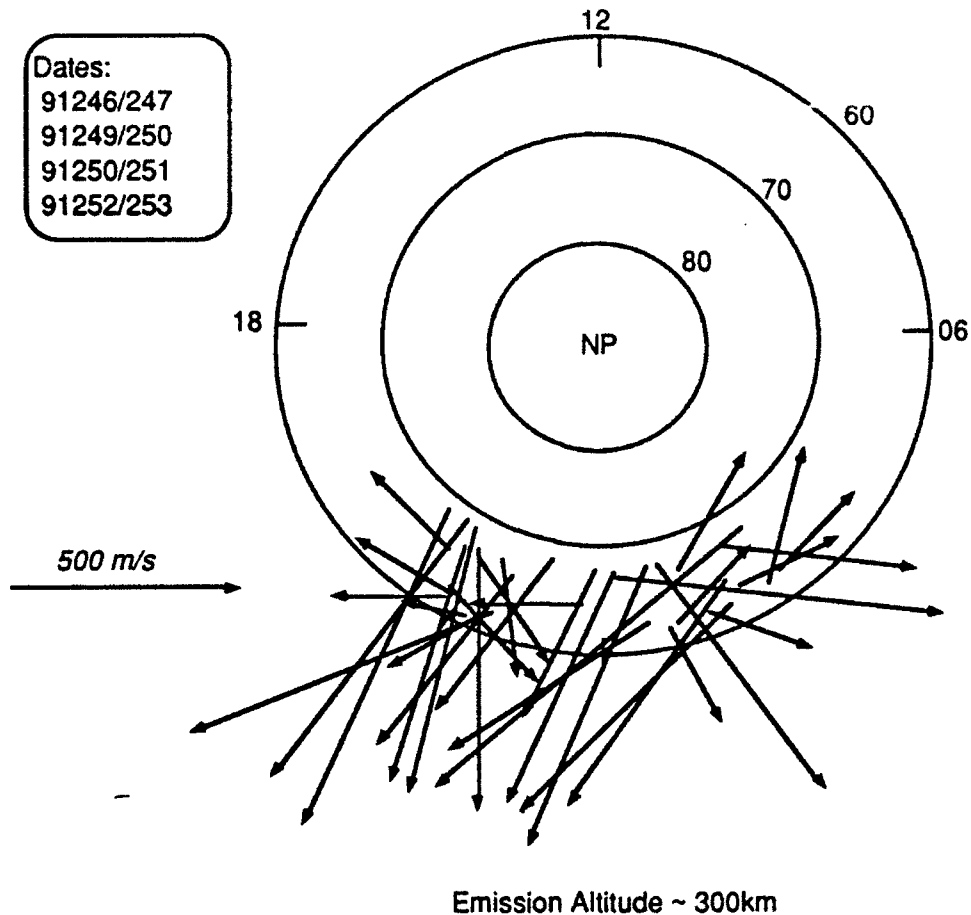


Figure 5.7 Polar dial plot for four nights of FPI (7320Å) ion drift observations. The two-celled ion convection pattern is visible, complete with antisunward flow seen in the center of the bottom dial and return flow seen on either side. The times on this dial are local solar and the latitudes are geographic. See text for discussion.

For ion drift velocity components, the ISR data were bin averaged so their lines-of-sight and integration times matched those of the FPI drifts. I then plot an ISR error which is simply a standard deviation about the mean. From Figure 5.9, one can see that the drift comparison (zonal, in this case) seems to be reasonable. FPI-North and FPI-South measurements were sometimes found to be considerably different from ISR measurements. This was probably due to the fact that as the auroral oval moves over Søndre Strømfjord during the evening, spatial and temporal

changes in the oval are occurring quicker than the FPI integration times. A CCD, allowing for shorter integration times, could remedy this problem.

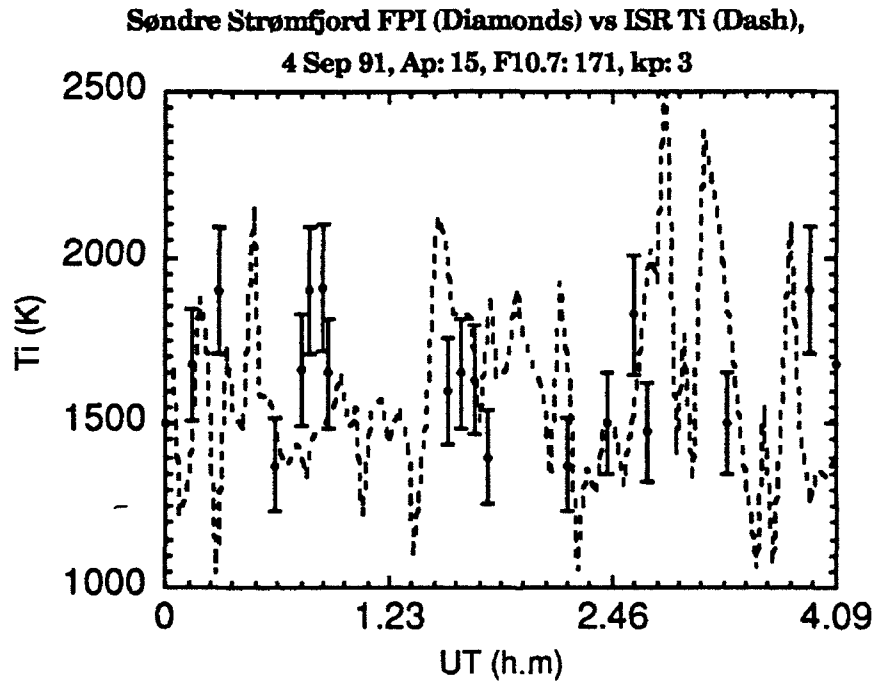


Figure 5.8 FPI (with error bars) vs ISR (dash line) ion temperature comparison for 4 Sep 91. The integration period for the ISR was usually much shorter than that of the FPI, resulting in greater resolution in the ISR measurements. Generally, the agreement is good, suggesting future study of this emission at pre-determined times and seasons could prove eventful in understanding ionospheric energetics.



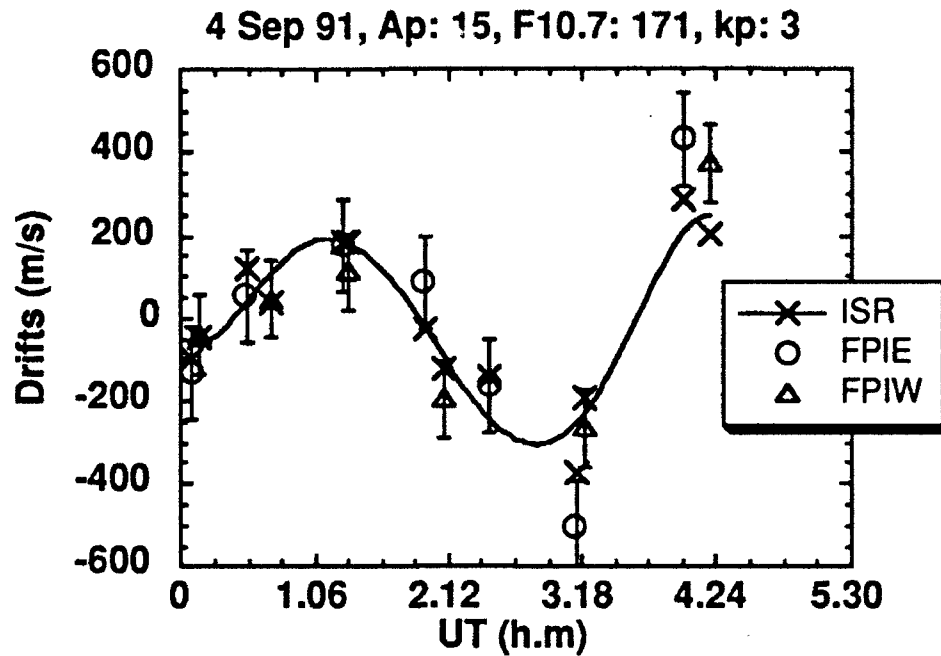


Figure 5.9 ISR (with 5th-order polynomial curve fit through points) vs FPI (with error bars) ion drift comparisons. FPIE(W) indicates the FPI was looking eastward (westward). The ISR data were bin averaged so their lines-of-sight and integration times matched those of the FPI (7320Å) drifts. The comparison between the FPI (7320Å) and ISR drifts is good.

### 5.2.2 FPI vs VSH Ion Drifts and Temperatures

Further validation of the high latitude ion drift convection pattern made by a ground-based FPI can be done by comparing results to model output. In Figure 5.10, I have run the VSH model for the exact geophysical conditions that took place on 4 Sep 91 at 01 UT at Søndre Strømfjord. The Figure is a satellite view of the earth from two earth radii; a cross hair is placed near Søndre Strømfjord for identification. The drift barb in the bottom right corner represents 1000 m/s. One can see that a southeastward flow of ion drifts of about 700 m/s and an ion temperature of about 1320K is

the output near Søndre Strømfjord. Referring to Figure 5.4, one sees an observed meridional (south) flow of  $\sim 700\text{--}750\text{ m/s}$  (these speeds straddle 01UT), an observed zonal (east) flow of  $\sim 10\text{ m/s}$  and an observed temperature of  $\sim 1300\text{--}1600\text{K}$  (these temperatures straddle 01UT). The resultant velocity flow is southeastward at  $\sim 725\text{ m/s}$ . These observed values favorably agree with the VSH output.

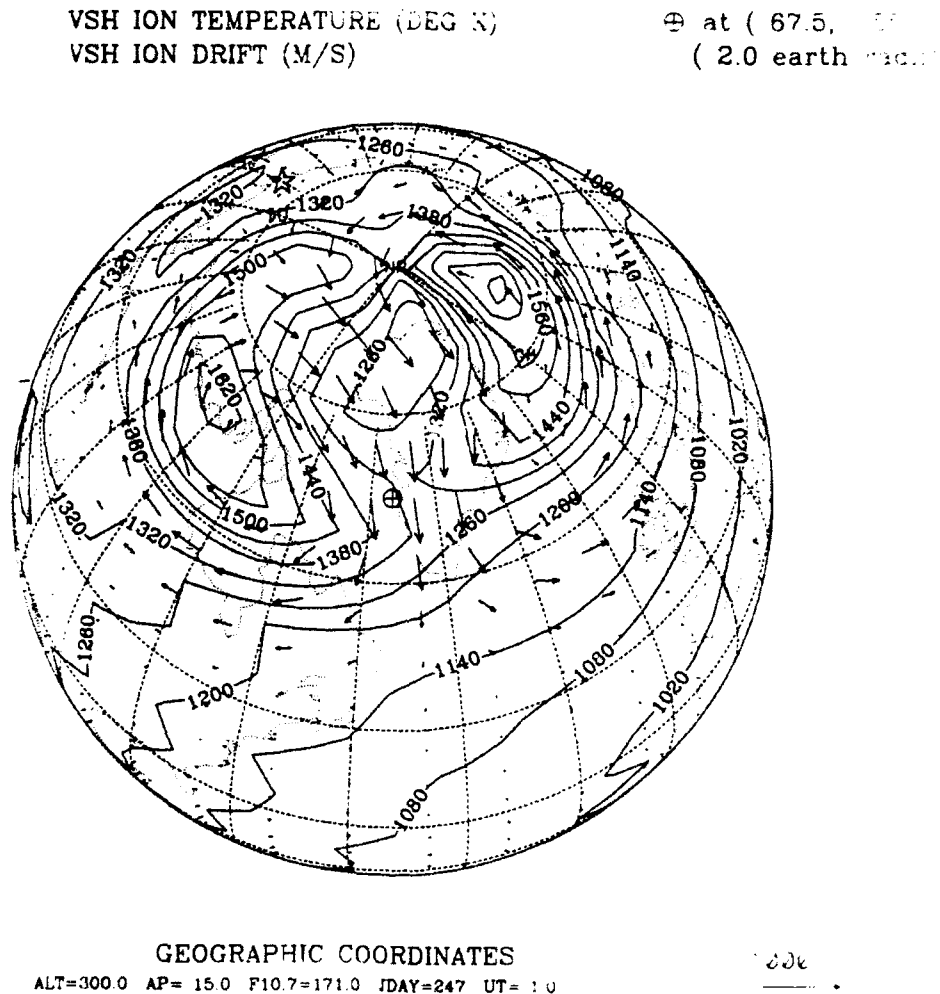


Figure 5.10 VSH model output for the conditions occurring for the 4 Sep 91 FPI ( $7320\text{\AA}$ ) observations. The model shows drifts and temperatures to be  $\sim 700\text{ m/s}$  (southeastward) and  $1320\text{K}$  respectively. The observations for this time (Figure 5.4) are  $\sim 725\text{ m/s}$  (southeastward) and  $1300 < T_i < 1600\text{K}$ .

### 5.3 Conclusions

The first ion convection pattern measurements and ion temperature measurements using an FPI (7320Å) from Søndre Strømfjord have been presented and compared to simultaneous ISR measurements. The agreement is good (although a limited dataset of four nights exists), giving us confidence in this ground-based technique. I suggest that the 7320Å doublet lines be separated (by as great a distance as possible) on future FPI detectors to ease ion temperature recovery. Overlapping the 7320Å-doublet components on the IPD made ion temperature extraction very difficult with the DE-2 FPI; separating them, as in the Søndre Strømfjord FPI, made ion temperature retrieval (relatively) simpler. Comparisons to the VSH model are good, but the grid size of the model is too large and four nights of FPI data are too sparse to give precise comparisons. Making these 7320Å emission observations on a regular basis will provide needed information on the high latitude ion convection pattern, ion outflow, and ionospheric energetics. The method of observation is simple, inexpensive and proven.

Using the methods outlined in Chapter 3.4, the detection of the 7320Å-doublet emission by a ground-based FPI opens the possibility that these emissions can be used to monitor thermospheric atomic oxygen concentrations. Ionospheric and thermospheric structure is largely determined by atomic oxygen between ~225 - 500km. With few (if any) aeronomy satellite programs projected for the next several years that can provide the necessary measurements, ground-based FPI and other optical remote sensing systems will have to play a major role in determining thermospheric atomic oxygen concentrations. Important practical needs for knowledge of thermospheric atomic oxygen concentrations are for

satellite drag calculations and for providing new compositional data to large, thermospheric/ionospheric empirical models.

Note that VSH predicts the total  $O^+$  number density near Søndre Strømfjord to be  $\sim 2 \times 10^5/\text{cm}^3$  at 00UT in early September during quiet conditions. Some of these ions will be in the  $O^+(^2P)$  state and will emit at 7320Å. The low intensity ( $\sim 20\text{-}100R$ ) and sporadic nature of the 7320Å emission in nighttime aurorae currently limit ground-based FPI observations. However, the addition of a CCD detector would enhance the Søndre Strømfjord capabilities immensely. With a CCD, one could more easily resolve this weak emission and, possibly, the weaker component of the 7320Å doublet. But more importantly, one could use shorter FPI integration times, thereby generating more spectrograms and hence, more frequent drift and temperature measurements. The resulting larger database of ion drifts and temperatures will give us a more complete understanding of ionospheric and thermospheric dynamics and energetics.

## CHAPTER 6

### DOPPLER IMAGING OF THE HIGH LATITUDE IONOSPHERIC CONVECTION PATTERN FROM SPACE: RESULTS OF A SIMULATION AND FLIGHT DEMONSTRATION STUDY

Limb scan observations of Doppler line profiles from the [OII]  $\lambda 7320\text{\AA}$  emission at F-Region altitudes, made with the FPI on the DE-2 spacecraft, were analyzed to provide measurements of ion drift velocity in Chapter 4. These DE observations represent the first spaceborne use of the remote sensing Doppler technique for measurements of ionospheric convection. The FPI measurements were validated against *in situ* RPA drift observations. The spaceborne interferometric technique demonstrated by this work has future utility for the two dimensional imaging of polar ionospheric convection. The motivation for a routine, spaceborne monitor of ionospheric convection via FPI ( $7320\text{\AA}$ ) observations is to enhance our understanding of the ion convection pattern, auroral physics, phenomena associated with the convection electric field, magnetospheric/ionospheric coupling and upper-thermospheric atomic oxygen concentrations. This routine monitoring of the polar ionosphere will be especially valuable during  $B_z$  positive ( $B_z$ -north) conditions, since it is not yet known if the polar ionospheric convection pattern is a four-celled pattern, a distorted two-celled pattern or some permutation. Results of a simulation study,

based on the DE-2 technique of Chapter 4 and the full aurora-airglow model developed in Chapter 3 are presented to demonstrate that a large fraction of the entire polar ionospheric convection pattern can be monitored from space during ~ 16 minute polar passes of a suitably instrumented satellite.

Section 6.1 will introduce the DE-2 FPI (7320Å) Simulator; this simulator mimics an instrument function similar to that of the DE-2 FPI. Section 6.2 validates the DE-2 FPI Simulator against actual observations. Section 6.3 introduces the FPI-system onboard the CONVEX (*Convection Explorer*) satellite. The four FPIs onboard CONVEX will have an instrument transfer function similar to that of the DE-2 FPI. This polar-orbiting satellite is then flown through a model atmosphere of VSH ion drifts and temperatures, and volume emission rates from the aurora-airglow model. The simulated spaceborne FPI-system integrates the 7320Å emission contributions along each field of view and produces spectrograms. These spectrograms are then analyzed using the standard DE-2 methods to recover the high latitude ion convection pattern and electric field vectors.

### 6.1 DE-2 FPI (7320Å) Simulator

The DE-2 FPI (7320Å) Simulator consists of two parts: raw spectrogram simulation and spectrogram analysis to obtain line-of-sight drifts, temperatures, brightnesses and background signals. The spectrogram synthesis is done with an algorithm that uses the instrument transfer functions to predict the instrumental response for given limb observations of a "model" atmosphere. The DE-2 standard analysis procedures outlined in Chapter 2 are used to extract line-of-sight drifts, temperatures, brightnesses, and background signals from the

spectrogram. A thorough discussion of the DE-2 FPI (5577Å) Simulator can be found in Nardi (1991). This version is similar, but is modified for 7320Å use. The wavelength, etalon reflectivity, filter transmissivity, filter width, detector sensitivity, free spectral range, number of channels/free spectral range etc. were changed to match the DE-2 FPI (7320Å) values.

Hence, the Simulator reincarnates the DE-2 FPI. A "model" atmosphere consisting of meridional ion drift, temperature and volume emission rate profiles for a desired set of geophysical conditions is fed into the Simulator. These data pass through simulated DE-2 optics and generate a synthetic spectrogram; the standard analysis is run on this spectrogram, and the resulting line-of-sight drifts, temperatures and brightnesses are retrieved. Previous workers have used "model" atmospheres that were observed wind, temperature and volume emission rate profiles. In the DE-2 FPI (7320Å) Simulator, the "model" atmosphere consists of VSH meridional ion drift and ion temperature profiles and volume emission rate profiles from the 7320Å aurora-airglow model for chosen conditions. This "model" atmosphere is assumed to be the precise atmospheric conditions during the simulated conditions.

A review of the Simulator's mathematics can be found in Killeen and Hays (1984) and Nardi (1991). A summary follows in the next section.

#### 6.1.1 Mathematical description of the DE-2 FPI (7320Å) Simulator

Killeen and Hays (1984) showed that the spectrogram,  $N_i$ , for an instrument with an infinitely narrow (or bore-sight) field of view in a spatially uniform atmosphere is the integrated product of the emission line profile,  $Y(\lambda)$ , and the instrument transfer function ( $\Psi_i$ ). Mathematically, this is written as:

$$N_i = C_{oi} \int_{\lambda=0}^{\infty} T_F(\lambda) \Psi_i(\lambda, \theta_i) Y(\lambda) d\lambda \quad 6.1$$

where

$$C_{oi} = \frac{Q_i A_o \Omega_i T_{oi} t 10^8}{4\pi} \quad 6.2$$

$Q_i$  is the quantum efficiency of the  $i^{\text{th}}$  channel of the detector,  $A_o$  is the area of the etalon plates,  $\Omega_i$  is the field of view of the  $i^{\text{th}}$  ring detector,  $T_{oi}$  is the optical transmission of the instrument,  $t$  is the integration period,  $T_F(\lambda)$  is the transmission function of the filter and  $\Psi_i(\lambda, \theta_i)$  is the instrument transfer function for the  $i^{\text{th}}$  ring detector (dependent on wavelength and angle of incidence).  $Y(\lambda)$  is the spectral distribution of the Gaussian emission line source and may be written as:

$$Y(\lambda) = \frac{\mathcal{R}_o \exp\{-(\lambda - \lambda_1) / \Delta\lambda_T\}^2}{\sqrt{\pi} \Delta\lambda_T} + \frac{\partial \mathcal{R}}{\partial \lambda}_o \quad 6.3$$

The thermal line width is

$$\Delta\lambda_T = \left\{ \frac{2kT}{m} \right\}^{1/2} \frac{\lambda_1}{c} \quad 6.4$$

where  $\lambda_T$  is the thermal line width,  $k$  is the Boltzmann constant,  $T$  is the kinetic temperature,  $c$  is the speed of light,  $m$  is the mass of the emitting species,  $\mathcal{R}_o$  is the surface brightness and  $\lambda_1$  is the centroid wavelength of the emission line.

However, the atmosphere is not spatially uniform; in the Simulator, the atmosphere is assumed to be multilayered since the model atmosphere of VSH drifts and temperatures and 7320Å modelled volume emission rates



have layered profiles. Since the FPI integrates all emissions along the line-of-sight, the instrumental response produced by each layer is calculated, one layer at a time, and then summed to produce the total instrument response. In the DE-2 FPI (7320Å) Simulator, atmospheric shells are 5km thick; hence, if the satellite is at 400km and is sensing the 7320Å emission at a tangent height of ~ 300km, the instrumental response from all layers above the tangent height is summed to produce the total spectrogram. Of course, the 7320Å emission is strongly peaked at ~ 300km and the dominant contribution will come from that tangent point. The expression for the line source function,  $Y(\lambda)$ , is therefore given by summing all Gaussian emission line profiles within the field of view. This can be done by integrating along the line-of-sight to produce:

$$Y(\lambda, z_t) = \int_s \eta(\lambda, s) ds \quad 6.5$$

where  $s$  is the coordinate along the line-of-sight and  $z_t$  is the tangent height. The instrumental response is then written as:

$$N_i(z_t) = C_{oi} \int_{\lambda=0}^{\infty} T_F(\lambda) \Psi_i(\lambda, \theta_i) \int_s \eta(\lambda, s) ds \quad 6.6$$

Now that one has an infinitely narrow instrument field of view scanning an altitudinally variable atmosphere, the Simulator algorithm is improved to include a conical field-of-view. Thus, an integration must be performed with the angular range of the cone-of-view to obtain the line function  $Y(\lambda)$ :

$$Y(\lambda, z_t) = \int_{\alpha_{\min}}^{\alpha_{\max}} \int_s \eta(\lambda, s) d\alpha ds \quad 6.7$$

where  $\alpha$  is the angle between the instrument axis and a ray within the cone-of-view. The spectrogram may now be written as:

$$N_i(z_t) = C_{\alpha} \int_{\lambda=0}^{\infty} T_F(\lambda) \Psi_i(\lambda, \theta_i) \int_{\alpha_{\min}}^{\alpha_{\max}} \int_s \eta(\lambda, s) d\alpha ds \quad 6.8$$

In this case, all detector rings are assumed to have an identical cone-of-view; hence, if any spatial structure in the emission source does exist, it is not imaged onto the detector. The final part of the Simulator algorithm accounts for the distinct field-of-view of each detector channel, as characterized by weighting functions  $W_i(\alpha, z_t)$ . With this addition to the Simulator, the line source function becomes ring dependent. For programming purposes, the discretized form of the channel response is therefore written as:

$$N_i(z_t) = C_{\alpha} \sum_{k=1}^{30} W_{ik}(z_t) \left\{ \sum_{j=1}^N S_{jk}(z_t) \Delta z \left[ \sum_{l=1}^L Y_{jl} \Psi_{il} \Delta \lambda \right] \right\} \quad 6.9$$

where  $i$  is the detector channel,  $j$  denotes the altitude layer,  $k$  denotes the angle within the field of view, index 1 denotes wavelength,  $z_t$  is the tangent height and  $S$  is the pathlength of the line-of-sight through layers of thickness  $\Delta z$ . Analysis of this simulated spectrogram by the standard analysis package produces LOS drifts, temperatures, brightnesses and continuum brightnesses.

### 6.1.2 DE-2 FPI (7320Å) Simulator Examples

In this section, I present a sample from the DE-2 FPI (7320Å) Simulator. In Figure 6.1, I have the satellite positioned at 400km altitude. The local time is 12UT and the conditions are quiet ( $A_p = 10$ ,  $F10.7 = 120$ ).

The satellite is assumed to be over  $67^{\circ}\text{N}$  geographic latitude and  $0^{\circ}$  longitude. The satellite velocity is assumed to be 7.5 km/s and the FPI integration time is 30s. These geophysical conditions are fed into VSH and the  $7320\text{\AA}$  aurora-airglow model, which then produce the "real" meridional ion drifts, temperatures and volume emission rates. The Simulator then integrates all contributions along the line-of-sight down to the tangent point of the emission. Spectrograms are produced in each layer with an algorithm that uses the instrument transfer functions and the field of view weighting functions to predict the instrumental response for given limb observations of a model atmosphere. The standard DE-2 analysis routines then retrieve the line-of-sight ion drifts, temperatures and brightnesses at each altitude increment. In Figure 6.1, the solid lines are the model input while the boxes (with error bars) are what the simulated DE-2 FPI observed for drifts, temperatures and brightnesses. There are sixteen boxes with error bars since the DE-2 FPI had 16 mirror positions and therefore observed  $\sim 25\text{-}225\text{km}$  beneath the satellite. Appendix D describes the Simulator methodology in much greater detail. In the next section, I validate the Simulator by comparing the brightnesses that it calculates to actual DE-2 measured brightnesses at the same time and conditions.

## 6.2 DE-2 FPI ( $7320\text{\AA}$ ) Simulation Validation Studies

In this section, I shall take two representative DE-2 orbits (one from early in the satellite's lifetime when the orbit was elliptical; one from late in its lifetime when the orbit was nearly circular) and plot vertical profiles of line-of-sight brightnesses and calculated DE-2 volume emission rate profiles. I then shall run the DE-2 FPI ( $7320\text{\AA}$ ) Simulator for the exact same

conditions as during the chosen two orbits. Finally, I shall compare the simulated brightnesses to the actual brightnesses measured by the DE-2 satellite at the corresponding time and place and under the proper conditions.

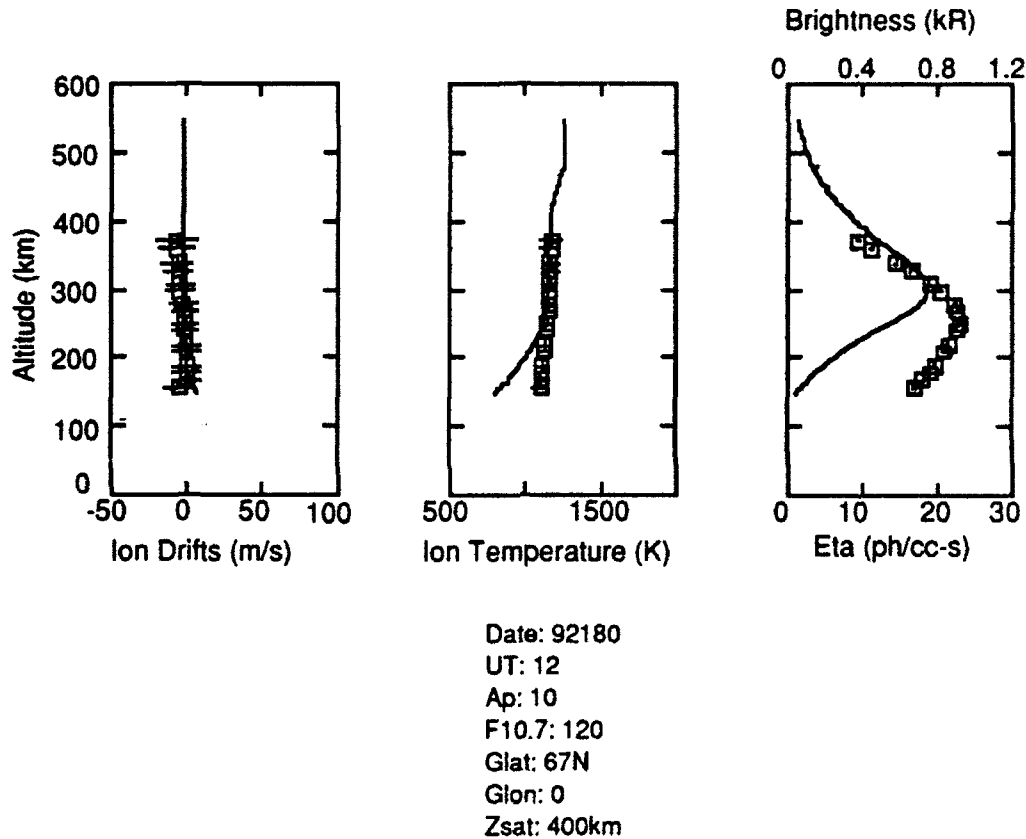


Figure 6.1 Simulation for the conditions listed on the diagram. In the first two panels, solid lines represent VSH ion drifts and temperatures. Boxes (with error bars) represent the simulated 16 DE-2 FPI measurements. Agreement between the simulated values and the VSH "real atmosphere" values is excellent. In the far right panel, brightnesses (boxes) are simulated from the input 7320Å aurora-airglow volume emission rate model (solid line). The brightness scale is on top of this panel; the volume emission rate scale is on the bottom. These brightnesses will be compared to actual DE-2 brightnesses in Chapter 6.2.

### 6.2.1 Orbit 1343 Simulation

Figure 6.2 is an actual DE-2 profile of measured 7320Å brightnesses for the conditions shown in the figure. The brightnesses are seen to peak at  $\sim 275\text{km}$  with values  $\sim 950R$ . Figure 6.3 is a DE-2 FPI (7320Å) Simulator plot modelling the conditions of Figure 6.2. The contribution function is plotted in a separate panel in the lower right hand corner. The 7320Å emission is strongly peaked at  $\sim 300\text{km}$ , allowing one to assume that the line-of-sight drifts are the real drifts, with no inversions necessary. The VSH drifts in the first panel of Figure 6.3 are well simulated above 200km by the DE-2 FPI (7320Å) Simulator, as are the VSH ion temperatures in the second panel. The line-of-sight brightnesses in the third panel (boxes) peak at  $\sim 285\text{km}$  with a value near 900R (see top of panel 3 for the brightness scale). Hence, the agreement between observed and simulated brightness is quite good.

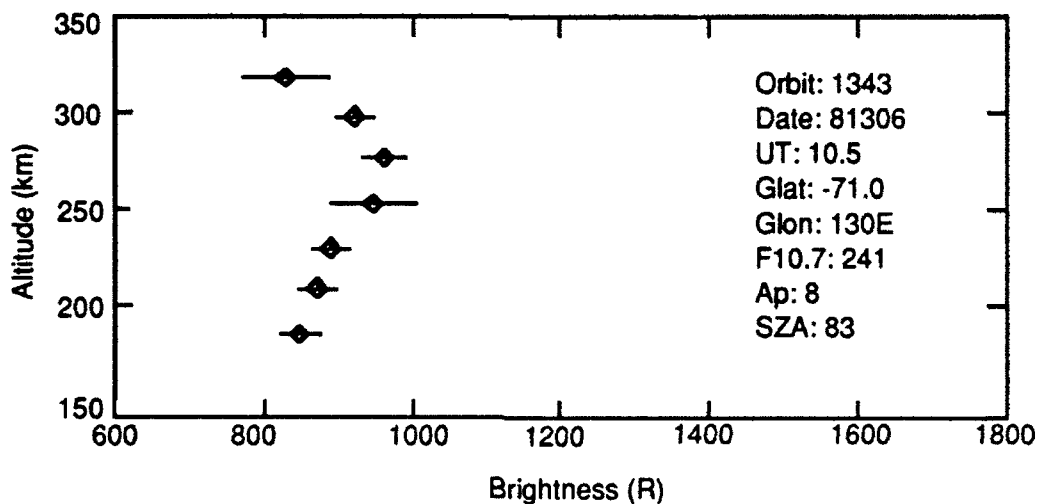


Figure 6.2 Brightness profile, Orbit 1343. Peak brightness appears to be  $\sim 950R$  at 285km altitude. The satellite was at  $\sim 340\text{km}$ . Compare to Figure 6.3.

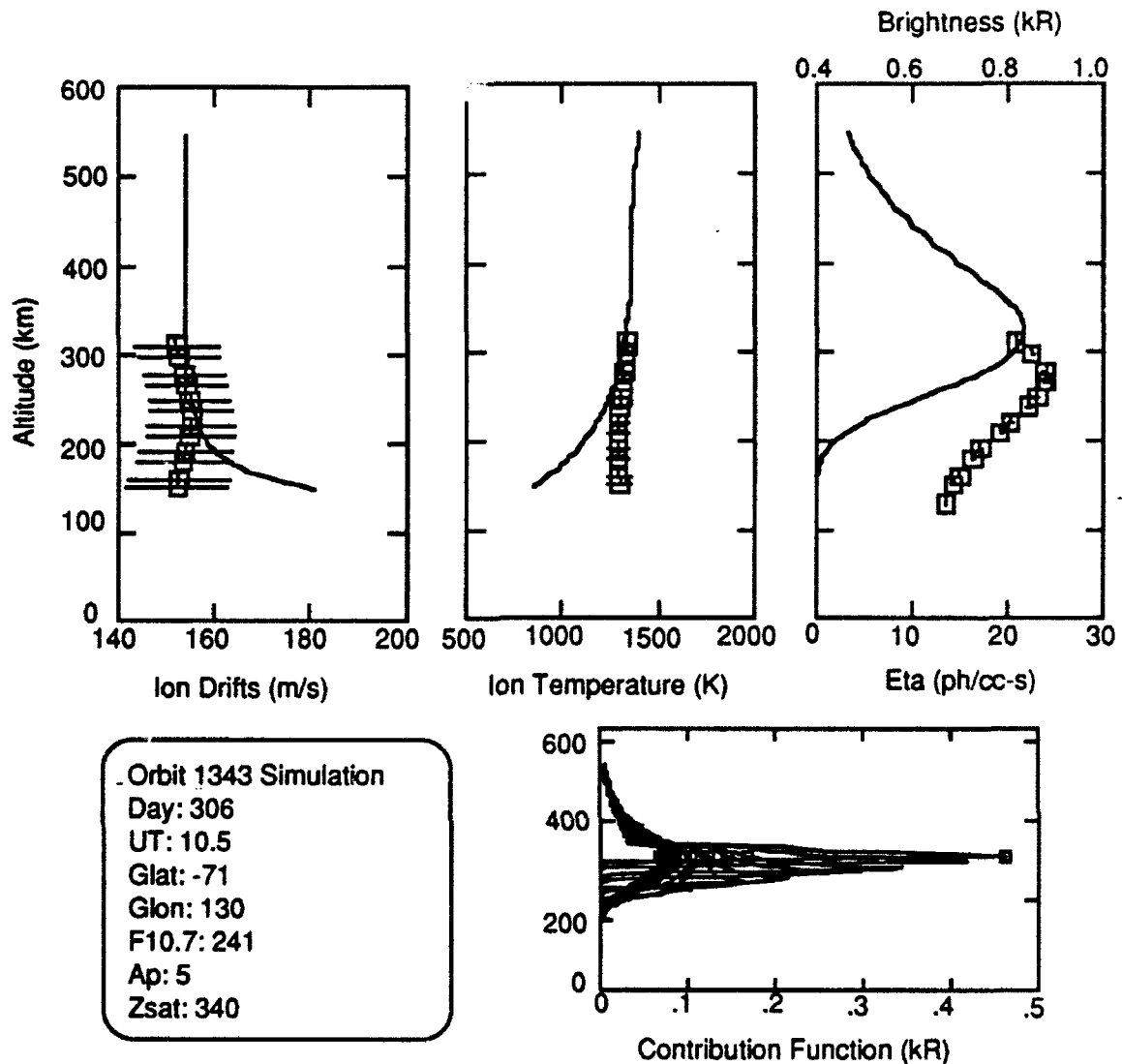


Figure 6.3 Simulator plot with the contribution function plotted in the lower right panel. VSH drifts and temperatures in the first two panels (solid lines) are well simulated (boxes with error bars). The brightnesses in the right panel (boxes with error bars) were calculated from the 7320Å aurora-airglow volume emission rate model (solid line) and peak at ~ 285 km near 900R. This is very similar to the observed values in Figure 6.2. The contribution function in the lower right panel is the product of the volume emission rate and the pathlength of the line-of-sight through the 5km-thick layers. The functions have a sharp peak at the tangent height since the pathlength peaks there; hence, the information content of this simulated measurement is favored at the tangent height (~300km in this case).

### 6.2.2 Orbit 8000 Simulation

The profile randomly selected from this orbit occurred at mid-latitudes in quiet conditions ( $F_{10.7} = 135$ ,  $A_p = 8$ ,  $Z_{\text{sat}} \sim 380\text{km}$ ). Figure 6.4 is a standard DE-2 FPI ( $7320\text{\AA}$ ) Simulator plot. In the third panel, the simulated brightness appears to be  $\sim 450R$  near  $250\text{km}$ . Figure 6.5 is the observed DE-2 FPI ( $7320\text{\AA}$ ) brightness profile for the same time and place, and under the same conditions, as in Figure 6.4. At  $250\text{km}$ , the observed brightness is  $\sim 425R$ .

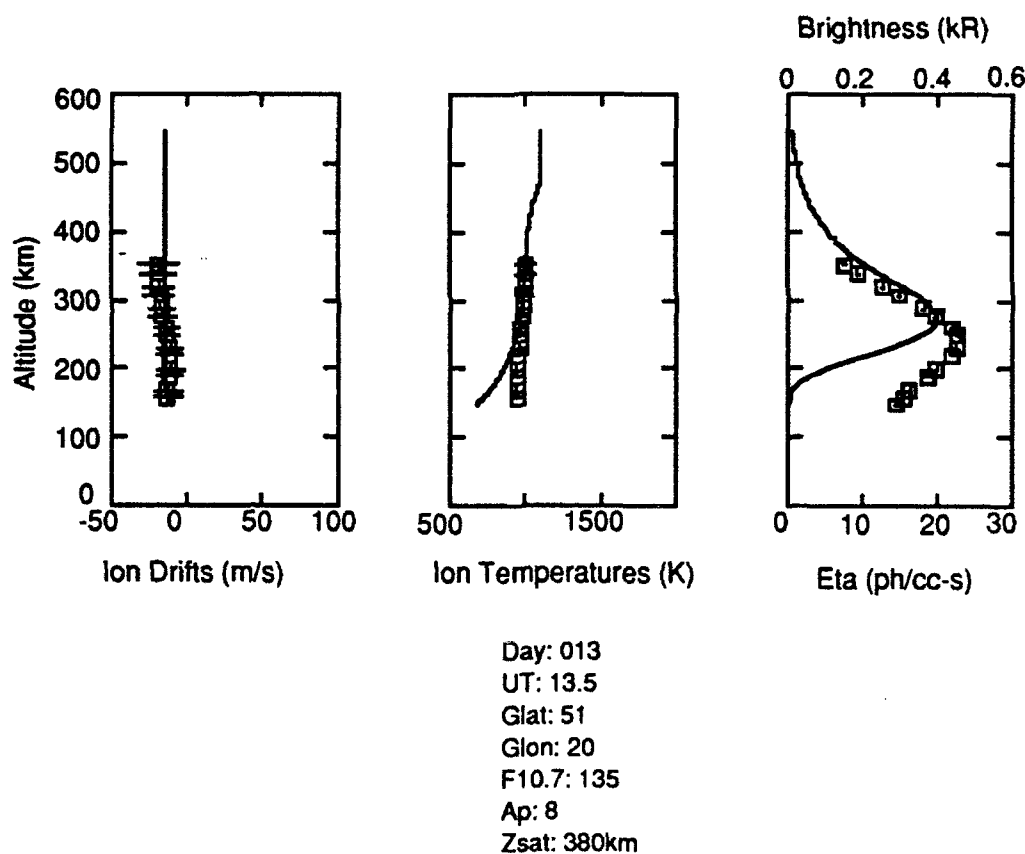


Figure 6.4 Orbit 8000 Simulation. Compare the simulated brightnesses (peak of  $\sim 450 - 475R$  at  $\sim 250\text{km}$ ) to the observed brightnesses in Figure 6.5.

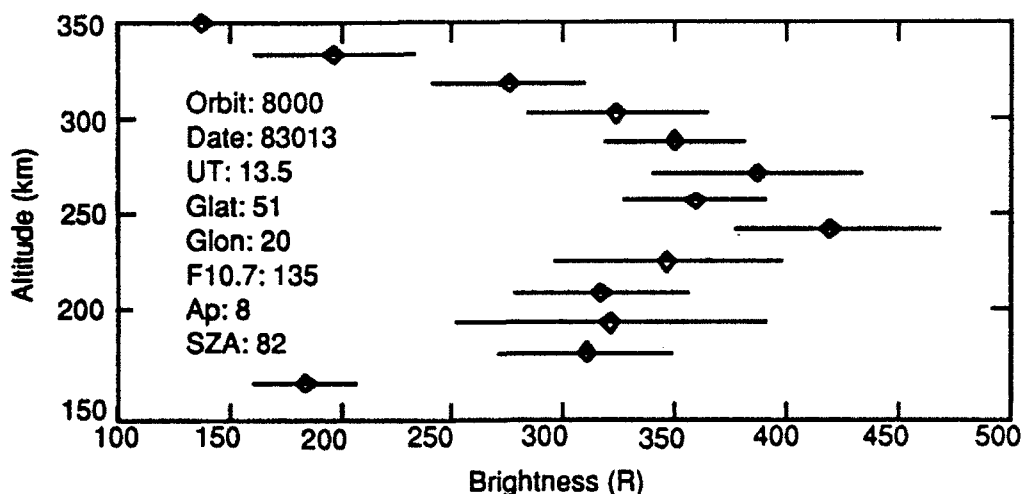


Figure 6.5 Orbit 8000 brightness profile. The peak is  $\sim 425R$  at  $\sim 250km$ . The comparison to the simulated brightnesses in Figure 6.4 is good.

In conclusion, by inputting the known DE-2 satellite altitude, position, F10.7, Ap, UT, FPI integration period, VSH meridional ion drifts and temperatures and 7320Å aurora-airglow volume emission rate model profiles, the DE-2 FPI (7320Å) Simulator accurately predicts what the DE-2 actually observed for brightnesses. This gives confidence to the simulation about to be performed, and indirectly illustrates the accuracy the 7320Å aurora-airglow volume emission rate model below extremely active ( $Ap > 50$ ,  $F10.7 > 220$ ) conditions.

### 6.3 Simulated Satellite Observations of the High Latitude Ion Convection Pattern

The performance of the DE-2 FPI as a remote spaceborne monitor of ionospheric convection opens the possibility that remote sensing methods can be used to image the high-latitude convection pattern over a large fraction of the polar region. Minow and Smith (1990) have recently suggested that the two-dimensional high-latitude ionospheric convection



pattern can be imaged using a satellite-borne FPI. In order to demonstrate the potential of this 2-dimensional imaging technique based on the results of this work, I have conducted a quantitative simulation study using combination of the *7320Å aurora-airglow volume emission rate model* (Chapter 3), a model of polar ionospheric convection (VSH, Chapter 2.4a), and an instrument transfer function similar to that of the DE-2 FPI (the *DE-2 FPI Simulator*, Chapter 6.1).

### 6.3.1 CONVEX Geometry and Instrumentation

NASA's Small Explorer (SMEX) program is designed to give scientists easy access to space by using expendable vehicles that provide frequent and (relatively) inexpensive launches of scientific satellites. These smaller missions allow specialized investigations that can apply state-of-the-art technological innovations and provide hands-on experience for many scientists and students. A noteworthy feature of SMEX programs is that one principal investigator (PI) proposes an entire mission and its experiments; hence, the PI is in complete charge of the SMEX mission. The SMEX program will also create a new generation of scientists and engineers knowledgeable with the space exploration program. The CONVEX satellite mission (Convection Explorer) about to be discussed will hopefully be a SMEX mission with a possible launch date ~1996. This date is important since it occurs during solar minimum. Atmospheric drag is known to increase with solar activity. Jachia (1965) showed that a significant variation in density and pressure is associated with the F10.7cm flux. This flux is used as a monitor of solar energy output since it originates in the chromosphere - the same region from which UV and EUV emissions originate. As solar activity increases, the F10.7cm flux increases and,

therefore, more UV and EUV energy is absorbed in the upper atmosphere. This absorption and concomitant heating leads to an outward expansion of the upper atmosphere, bringing increased densities to higher altitudes. A low altitude orbiter (i.e. DE 2) will therefore experience more drag during active solar conditions. Hence, a CONVEX launch during solar minimum will prolong its lifetime.

In the convection-imaging simulation study, I assumed a polar-orbiting satellite at an altitude of 600 km equipped with four FPIs with similar characteristics to the DE-2 FPI, but viewing the [OII]  $\lambda 7320\text{\AA}$  emission at various tangent point altitudes in four azimuthal directions at  $\pm 45^\circ$  and  $\pm 135^\circ$  to the satellite velocity vector. Figure 6.6 is a CONVEX FPI schematic and Figure 6.7 illustrates the CONVEX geometry. Recall that the  $7320\text{\AA}$  doublet components nearly overlapped on the DE-2 FPI's IPD, causing great difficulty in retrieving ion temperatures. The Søndre Strømfjord FPI separated the  $7320\text{\AA}$ -doublet components by  $\sim 6$  channels; single-Gaussian software retrieved accurate ion temperatures in this case. Hence, the CONVEX FPI should also separate the  $7320\text{\AA}$  doublet components.

The FPI integration time can be anything, but by using experience gained from the DE-2 observations of this emission, I shall use 30 seconds. A retarding potential analyzer (RPA) and ion drift meter (IDM) team will also be on the spaceborne observation platform to measure *in situ* ion drift velocities. With a polar-orbiting satellite at  $\sim 600\text{km}$  altitude, the mirror elevation angle for the FPI system must be  $16.87^\circ$  if the  $300\text{km}$  altitude range is to be sampled. Of course, any elevation angle can be selected, but for this introduction, I chose this angle for simplicity. Later, I shall vary this angle, and therefore sample different altitudes at varying lateral

distances from the satellite. With a satellite velocity of  $\sim 7.5$  km/s, the orbital period for CONVEX will be  $\sim 97$  minutes. Assuming the high-latitude ionosphere is the zone of interest ( $60^\circ - 90^\circ - 60^\circ$  geographic latitude), it will therefore take CONVEX  $\sim 16$  minutes to pass over this region; hence, both high latitude zones can be sensed in  $\sim 1$  hour. Note that the orbit altitude and FPI mirror elevation angles of CONVEX were chosen so as to eliminate many of the problems that DE 2 had (spacecraft charging, contaminating OH surface glow and FPI scans deep into the lower thermosphere, where the  $O^+(2P)$  ion is severely quenched - all because of low altitude orbits).

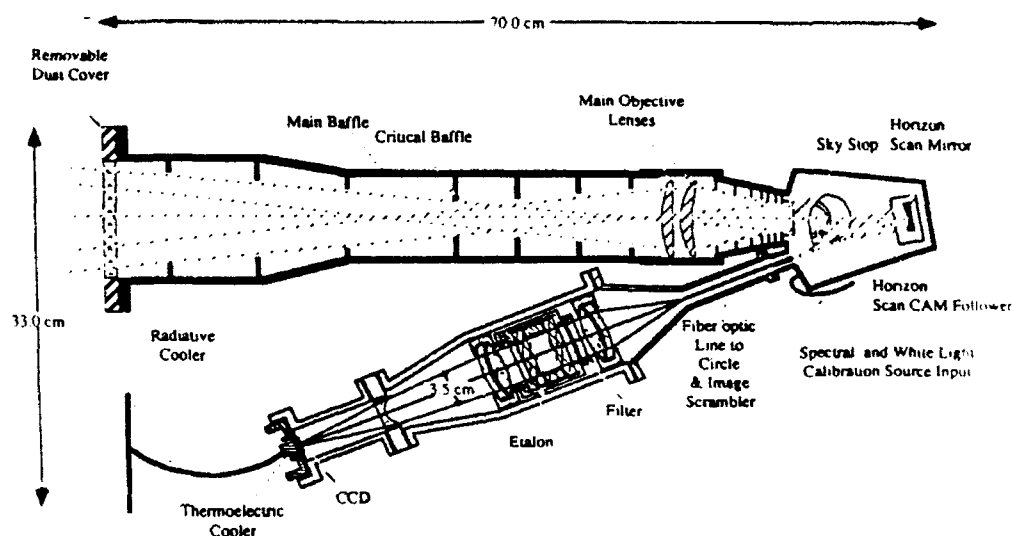


Figure 6.6 CONVEX FPI schematic.

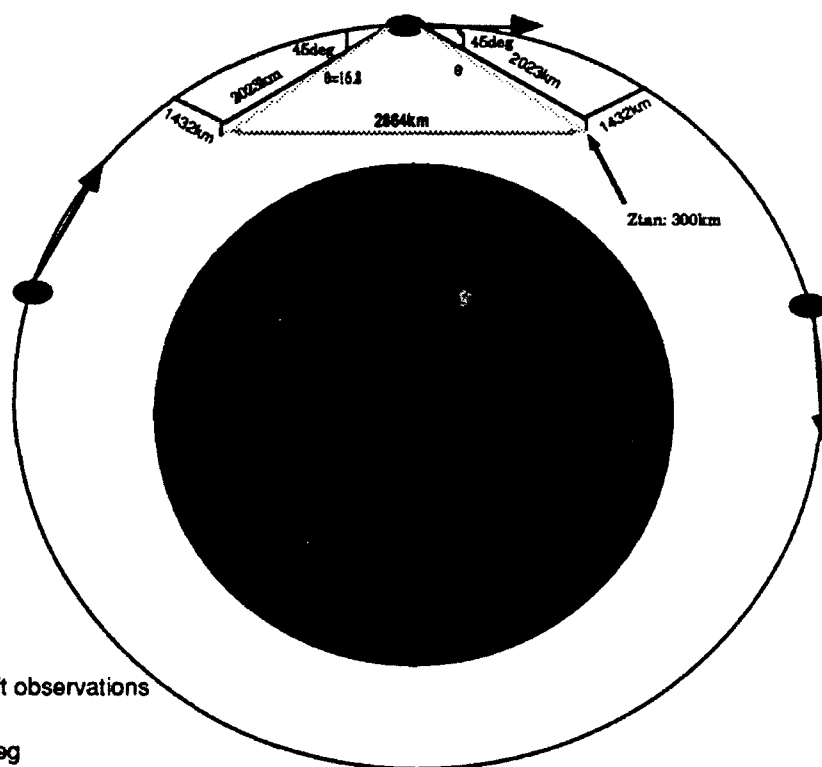
With the RPA/IDM team determining ion drifts in-track, and the FPI system looking off-track, the resulting retrieved data will be three swaths of ion drifts across the high-latitude zones. Since the elevation angle for the FPI system in this initial configuration is  $16.87^\circ$ , the tangent point is  $\sim 2023\text{km}$  from the satellite at a  $45^\circ$  angle. Resolving this triangle shows that the tangent point for the FPI observations is  $\sim 1432\text{km}$  ( $\sim 13^\circ$ ) perpendicular to the track. Hence, RPA/IDM drifts are in-track, while the FPI measurements are  $13^\circ$  off the track on either side. See Appendix E for the appropriate geometry and telemetry calculations; Appendix F discusses CONVEX software flow. Referring to Figure 6.7, one can see that when the forward looking FPI is scanning ahead at  $45^\circ$ , the FPI that is scanning backwards is sensing an area  $\sim 2864\text{ km}$  away ( $1432\text{km} \times 2$ ). To get FPI ion drift vectors, one must combine common volumes; hence, the rear-viewing FPI will sample the same volume as the forward looking FPI after the satellite travels the appropriate distance,  $\sim 5.9$  minutes with the  $16.87^\circ$  elevation angle. In Appendix E, I show how this time ranges from  $\sim 4 - 9$  minutes, depending on the elevation angle of the FPI system.

Figure 6.8 illustrates the CONVEX footprint. Assuming this satellite is at  $600\text{km}$ , its elevation angle ( $16.87^\circ$ ) is such that it is sensing the  $300\text{km}$  level and its field-of-view at  $7320\text{\AA}$  is  $\sim 2.7$  degrees (similar to DE 2) in both horizontal and vertical extent, the vertical diameter of the CONVEX footprint (shaded area at end of viewing-cone) is given by:

$$\text{diameter}(d) = \sin(2.7^\circ)(2023\text{km}) \approx 95\text{km} \quad 6.10$$

The way in which the emission is distributed within the field-of-view has important consequences on measurements since any non-uniformities can be incorrectly interpreted as drifts in the line-of-sight data analysis.

Since the 7320Å emission is a well behaved one (i.e. no lower and upper peaks, as in the 5577Å emission), the above calculation means the 252 - 348 km level will be sensed. Since the vertical length scale (~95km) of the field-of-view is smaller than the emission's (~180-550km), distortion is unimportant since all channels of the IPD will be illuminated by 7320Å photons.



Integration Time: 3-60s  
RPA/IDM Team: in-track drift observations  
Zsat: 600km  
 $\theta$  for Ztan of 300km: 16.87deg  
Orbital Period: 97.3min at Vsat of 7.5km/s  
Sensing Run of 60-90-60deg: 16min  
Common volume sampling: 5.9min

**Figure 6.7 CONVEX geometry.** The satellite is a polar orbiter at 600km. The four onboard FPIs look ahead and behind at  $\pm 45^\circ$  and  $\pm 135^\circ$  off-track. A RPA/IDM team determines *in situ* ion drifts. At this altitude, the FPI mirror elevation angle ( $\theta$ ) must be  $16.87^\circ$  in order to sample a tangent point altitude of 300km. The distance to the tangent point at this elevation angle is 2023km, which translates into 1432km ( $\sim 13^\circ$ ) normal to the satellite track at the tangent point. In this configuration, a backward-looking FPI samples the same volume a forward-looking FPI did 5.9 minutes earlier.

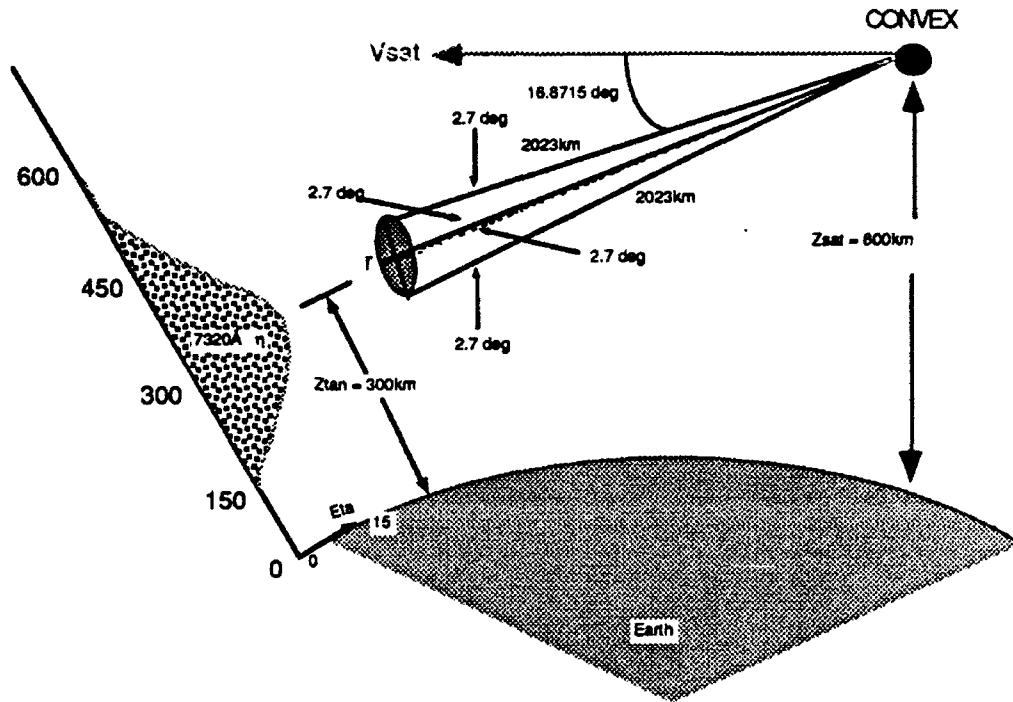


Figure 6.8 CONVEX footprint. At 600km, an FPI mirror elevation angle of  $16.87^\circ$  and a  $7320\text{\AA}$  field-of-view of  $2.7^\circ$ , the diameter of the FPI's viewing cone at a tangent point 2023km away from the satellite will be  $\sim 95\text{km}$ . In this orbital configuration, the FPI will therefore be sensing the  $7320\text{\AA}$  emission from  $\sim 252\text{--}348\text{km}$  altitude. Hence, the well-behaved (just one peak and wider in vertical extent than the FPI's field of view)  $7320\text{\AA}$  emission will be evenly distributed in the field-of-view and no distortion effects will occur. The double peaked  $5577\text{\AA}$  emission has a  $\sim 10\text{km}$  thick peak in the lower thermosphere; hence, it is narrower than the DE-2 FPI  $5577\text{\AA}$  field-of-view and distortion occurred since the outer channels were illuminated by  $5577\text{\AA}$  photons before the inner channels were (Nardi, 1991).

Figure 6.9 is an example of the relationship between the CONVEX path length, tangent point altitude and contribution function. The CONVEX simulated atmosphere is divided into 5km-thick layers. Assuming the satellite is at 600km, and its FPI system is looking down such that it is sensing the 300km region, 60 spectrograms are therefore simulated. As Figure 6.9 depicts, the  $7320\text{\AA}$  emission is peaked at  $\sim 300\text{km}$  with emission coming from  $\sim 200\text{--}500\text{km}$ . S denotes pathlength and N is the number of layers. A contribution function establishes the importance of each altitude for a given FPI view position; it is the product of the volume emission rate

and the path length of the line-of-sight through the 5km-thick layers. The contribution functions have a sharp peak at the tangent height since the pathlength peaks there; hence, the information content of CONVEX's FPI measurements is favored at the tangent height.

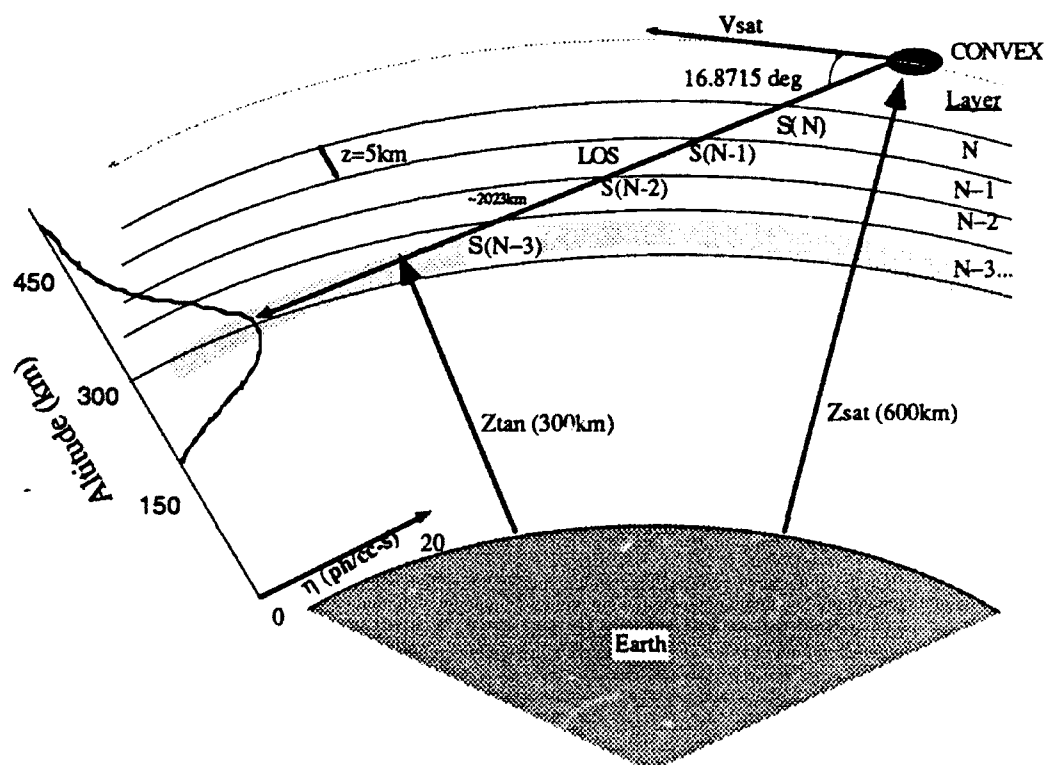


Figure 6.9 CONVEX pathlength. The dotted swath through the figure is the peak of the  $7320\text{\AA}$  emission layer. The maximum pathlength is through layer  $S(N-3)$ ; therefore, the information content of the FPI measurement is sharply favored at the tangent height ( $\sim 300\text{ km}$  in this case). In this configuration, the distance from CONVEX to the tangent point is  $2023\text{ km}$ . See text for further discussion.

The instrument sensitivity for the FPI-system on the CONVEX observing platform was the same as for the DE-2, with the exception that a Thomson 7882 CDA CCD detector was assumed, giving a sensitivity enhancement of  $\sim 12$  over the DE-2 image plane detector. The DE-2 IPD only had a quantum efficiency of  $\sim 5\%$ , meaning if  $100\ 7320\text{\AA}$  photons were

sensed by the detector, only 5 began the electron cascade through the instrument. The CCD has a quantum efficiency  $\sim 30\%$ . Since this CCD is assumed to have two rings on which the sensing can occur, the efficiency is assumed to be  $\sim 60\%$ ; hence, the factor of 12 improvement. Figure 6.10a,b illustrates this point. In the Figure 6.10a, a simulated latitudinal profile of meridional ion drifts retrieved from the DE-2 FPI ( $7320\text{\AA}$ ) Simulator is plotted. The simulated detector was the IPD. Overplotted are the "observed" drifts (from VSH). In Figure 6.10b, for the same conditions and time ( $\sim 18\text{UT}$ , quiet solar and geomagnetic conditions), is the simulated result using the CCD. As predicted, the CCD recovered simulated drifts are closer to "observed" values and the error in the simulated meridional drifts is considerably smaller.

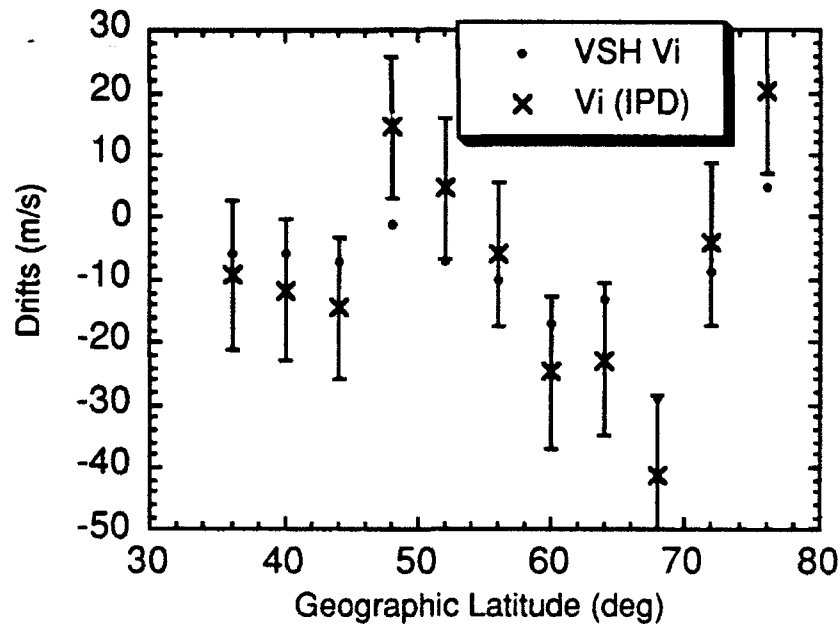


Figure 6.10a VSH ion drifts vs simulated ion drifts from the DE-2 FPI ( $7320\text{\AA}$ ) Simulator - the Simulator used an IPD in this case. Conditions for the VSH model and the Simulator were: day: 180, UT: 18, Ap: 10, F10.7: 140.



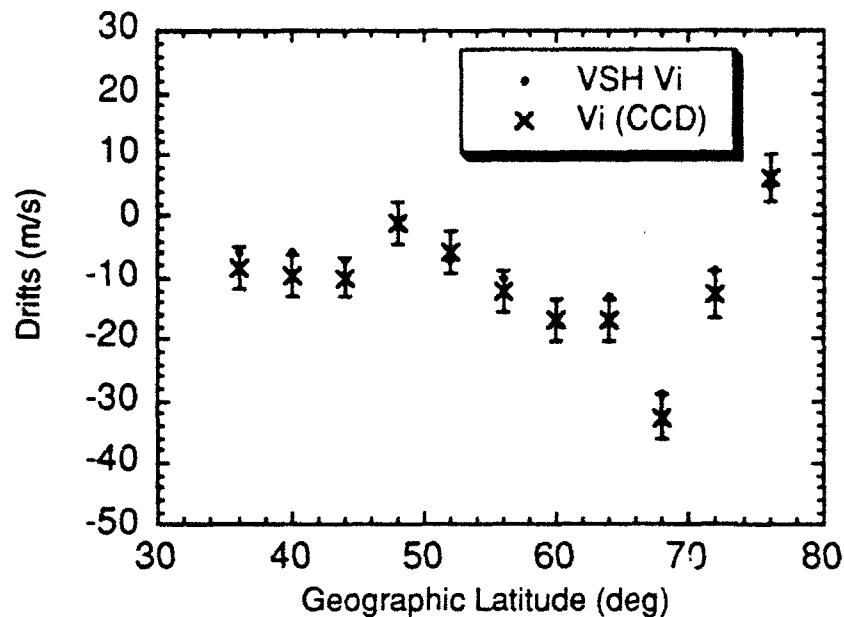


Figure 6.10b Similar to Figure 6.10a, but a CCD was used in the Simulator instead of an IPD. The addition of a CCD improves FPI sensitivity by a factor of 12.

### 6.3.2 Determination of Spectrograms and Vector Ion Drifts

In order to make the calculation as realistic as possible, the simulated spectrograms were calculated by integrating all emission contributions along the field-of-view and using the 7320Å aurora-airglow volume emission rate model, including daytime, twilight, nighttime and auroral altitude-dependent sources and sinks for the  $O^{+}(^2P)$  7320Å emission. The simulated instrumental response was modulated by the addition of Poisson noise. The horizontal ionospheric convection pattern (zero vertical drift) was based on output from VSH and was assumed to be invariant in magnetic latitude/longitude coordinates. In this mode of sensing the 300km region, the vector ion drift was derived by combining the proper off-track observations, assuming temporal invariance of the pattern over periods of ~5 minutes and using the standard DE-2 analysis software.

In addition to simulating ion drift vectors, the electric field vectors can be determined. Recall that

$$\vec{V}_d = \frac{\vec{E} \times \vec{B}}{B^2} \quad 6.11$$

Multiplying both sides of 6.11 by the magnetic field vector, one obtains

$$\vec{V}_d \times \vec{B} = \frac{\vec{E} \times \vec{B}}{B^2} \times \vec{B} = \frac{1}{B^2} (\vec{E} \times \vec{B}) \times \vec{B} \quad 6.12$$

Using vector identities and the standard assumptions that the parallel component of the electric field vector is zero and that the perpendicular component of the electric field dotted with the magnetic field is zero, one obtains

$$\begin{aligned} \vec{V}_d \times \vec{B} &= -\frac{1}{B^2} (\vec{B}) \times (\vec{E} \times \vec{B}) = -\frac{1}{B^2} (\vec{B} \cdot \vec{B}) \vec{E} - \frac{1}{B^2} (\vec{B} \cdot \vec{E}) \vec{B} \\ &= -\frac{B^2}{B^2} \vec{E} = -\vec{E} \end{aligned} \quad 6.13$$

Therefore,

$$\therefore \vec{E} = -\vec{V}_d \times \vec{B} \quad 6.14$$

Letting

$$\vec{V}_d = \vec{V}_x + \vec{V}_y, \quad \vec{B} = B\hat{z} \quad 6.15$$

then Equation 6.14 may be written as

$$\vec{E} = \begin{vmatrix} \hat{x} & \hat{y} & \hat{z} \\ V_x & V_y & 0 \\ 0 & 0 & B \end{vmatrix} = B(V_x \hat{y} - V_y \hat{x}) \quad 6.16$$

Assuming a high latitude magnetic field strength of 0.5 Gauss (Kelley, 1989), one can immediately determine the electric field vectors once the ion drift vectors have been simulated.

### 6.3.3 Simulation Results

Figure 6.11 shows the results of three simulations. The top right panel represents the convection pattern used as input to the calculation (VSH model at 15UT, quiet conditions, day 180). The top left figure depicts the recovered ion drifts after the complete simulation, including effects of spatial smearing, Poisson noise, instrument sensitivity, viewing geometry, and emission morphology. For this calculation, the satellite sensing pass began at 15UT and it was assumed that *in situ* RPA/IDM sensors provided drift measurements along the satellite track (these observations are simply the VSH outputs). The integration time period was assumed to be 30 seconds for each observation and the calculated statistical error on a single dayside measurement was  $<5$  m/sec. If one includes the two FPI swaths of recovered ion drift velocity vectors on either side of the satellite, and the RPA/IDM swath of ion drift vectors in the track, a band of  $\sim 26^\circ$  latitude has been sampled in one 16 minute pass over the high latitude region. Note that the outermost geographic latitude circle is  $40^\circ$ , and the inner most circle is  $80^\circ$ . Similarly, the plot in the middle on the right hand side represents the convection pattern used as input to the calculation (VSH model at 18UT, quiet conditions, day 180). The middle left figure depicts the recovered ion drifts after the complete simulation. In this case, the CONVEX began its sensing run at  $\sim 18$ UT. The plots on the bottom of the diagram are the input ion convection pattern at 22UT, quiet conditions, day 180 (right hand side) and the recovered ion drifts after the simulation (left hand side). In the 15

and 18 UT cases, with just the  $26^\circ$  latitudinal coverage offered by this simple method, the two-celled ion convection pattern is distinctly visible. However, in the bottom panel during the ~22UT CONVEX pass, only one cell is distinct since the second weaker cell is outside this  $26^\circ$  range; a trained eye can determine the beginnings of the second cell at about  $55^\circ$  latitude and 22UT. The solution to this problem is simple: either have the satellite sample primarily in the dawn-to-dusk plane as shown in the 18UT example or adjust the mirror angles of the FPI-system so additional locations off-track are sampled. This will be the topic of the next section.

Figure 6.12 is an example of the simulated electric field vectors that can be recovered from this study. These vectors will be everywhere perpendicular to the ion drift vectors and the magnetic field. A constant magnetic field of 0.5 Gauss was assumed for these calculations (Kelley, 1989), but on a real Small Explorer mission, the value of the magnetic field will also be measured and the calculation of the electric field vectors will still be straightforward.

#### 6.3.4 Viewing At Different Elevation Angles to Produce Multiswaths of Ion Drifts

By adjusting the look angle of the simulated satellite measurement from  $19.50^\circ$  to  $13.76^\circ$ , it is possible to simulate several sets of vector measurements at different horizontal spacing from the satellite. If the FPI elevation angle is  $19.5^\circ$ , the tangent point altitude is at ~200km and is 2327km from the satellite. Using the methods outlined in Appendix E, one sees that this swath of ion drift vectors will come ~1645km off-track ( $\sim 15^\circ$  latitude). If the FPI elevation angle were increased much more, the FPI system would look further away, providing greater latitudinal coverage, but

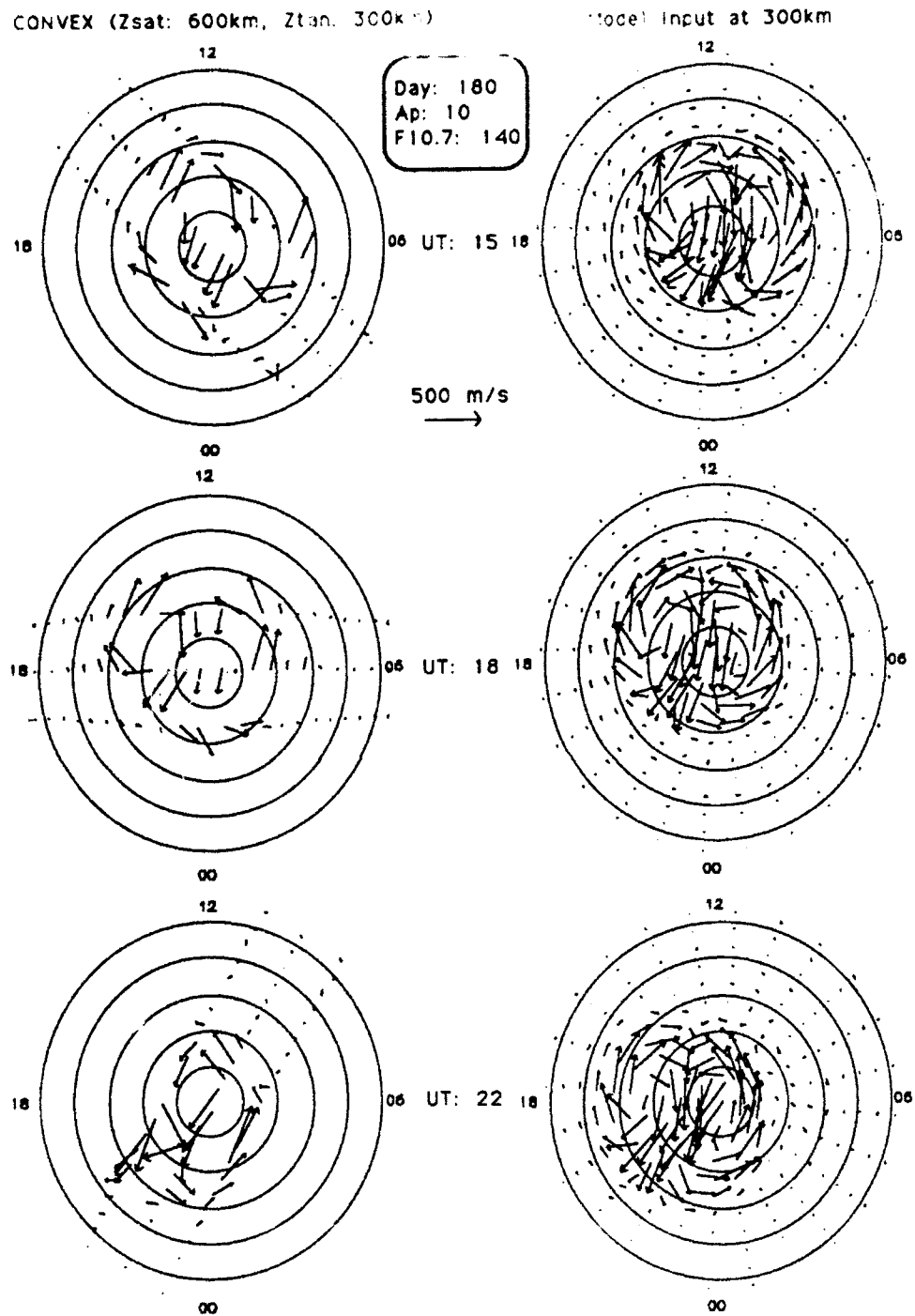


Figure 6.11 Three simulated ion drift velocity plots (left panels) vs the model that generated them (right panels). Simulated ion drifts are at tangent heights of 300km. Times on the polar dials are local solar; UT times represent the time CONVEX began its high-latitude pass. Conditions were day: 180, Ap: 10, F10.7: 140. Note that the areal coverage is  $\sim 26^\circ$  latitude, enough to determine the two-celled convection pattern in a 16 minute polar pass by CONVEX. See text for discussion.

Electric Field Vectors

Day: 180  
 Ap: 10  
 F10.7: 150  
 Zsat: 600km  
 Ztan: 300km

5 mV/m →

Latitudes: geographic  
 Dist Times: local solar

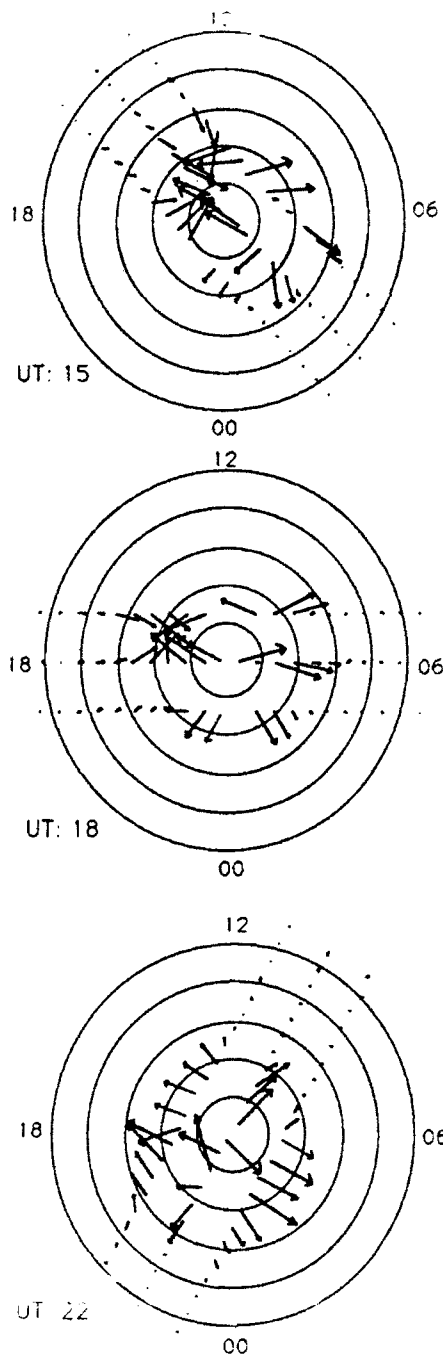


Figure 6.12 Recovered electric field vectors from the ion drift simulation.  
 Conditions are the same as Figure 6.11 - day: 180, Ap: 10, F10.7: 140.

it would begin to look into the zone of the atmosphere where this emission quickly weakens due to collisional quenching ( $<180\text{km}$ ). This elevation angle should not be exceeded for another reason: it would take  $\sim 10$  minutes for common volume sampling to occur in order to create ion drift vectors; ions drifts change very rapidly, as we saw in the DE 2 and Søndre Strømfjord analysis. Ten minutes may be assuming a temporal invariance of the ion convection pattern that is too great for acceptable resolution. As with the DE-2 FPI, the CONVEX FPI must be capable of measurement accuracies of  $\sim 5\text{m/s}$ . Accuracies for individual measurements are dependent on the respective surface brightness and chosen integration time. At an elevation angle of  $13.76^\circ$ , the tangent point altitude would be  $\sim 400\text{km}$  at an angular distance of  $1658\text{km}$  off-track (from which one can eventually show that the observation point is  $\sim 11^\circ$  off-track). This is still a zone of strong  $7320\text{\AA}$  emission. Plus, it will only take  $\sim 4.8$  minutes to combine common-volume line-of-sight measurements in order to produce ion drift vectors. In fact, I would suggest a top viewing limit of  $\sim 500\text{km}$  for the  $7320\text{\AA}$  emission; the  $7320\text{\AA}$  model developed in Chapter 3 indicates that the emission begins to tail off after this height. At a tangent height of  $\sim 500\text{km}$ , the elevation angle would be  $9.7^\circ$  and the angular distance to this tangent point would be  $\sim 1180\text{km}$ . Hence, using the methods outlined in Appendix E, this elevation angle corresponds to an off-track observing distance of  $\sim 830\text{km}$  or  $\sim 8^\circ$  latitude. Common-volume sampling for this case is  $\sim 4.5$  minutes.

Remote measurements of the ion drift using this interferometric technique were therefore calculated at several off-track tangent-point altitudes corresponding to different zenith angles for the fields of view. For

the purposes of the plot in Figure 6.13, three such sideways views to each side of the spacecraft were assumed, yielding a swath of information containing seven independent vector measurement sets at different lateral distances from the spacecraft orbital track (six FPI swaths and one RPA/IDM swath). The elevation angles used in this figure were  $19.5^\circ$  (tangent point altitude of 200km, off-track distance of  $15^\circ$ ),  $16.87^\circ$  (tangent point altitude of 300km, off-track distance of  $13^\circ$ ) and  $13.76^\circ$  (tangent point altitude of 400km, off-track distance of  $11^\circ$ ). The angular extent of the overall swath is therefore the maximum ( $\sim 30$  degrees), enabling both cells of the convection pattern to be clearly imaged. The angular extent of  $\sim 30^\circ$  is as large as one should go with this method of off-track FPI ( $7320\text{\AA}$ ) viewing.

Note that the CONVEX footprint varies as the tangent point varies. When the tangent point altitude is  $300\text{km}$ , the footprint is  $\sim 95.3\text{km}$  (see Figure 6.8). However, when tangent height is  $500\text{km}$ , the tangent point latitude and longitude (tpll) of the observation is 1177km from the spacecraft (see Appendix E). Hence, the vertical diameter of the CONVEX footprint is:

$$\text{diameter}(d) = \sin(2.7^\circ)1177\text{km} \approx 55\text{km} \quad 6.17$$

and the FPI-system is therefore viewing the  $7320\text{\AA}$  emission from  $\sim 473$ - $527\text{km}$ . When tangent height is  $200\text{km}$ , the tpll is 2327km from the spacecraft (see Appendix E), which produces a CONVEX footprint of  $\sim 100\text{km}$ . Therefore, the FPI-system in this case views the  $7320\text{\AA}$  emission from  $\sim 150$ - $250\text{km}$ . This is absolutely the lowest FPI view position CONVEX should have since quenching becomes the primary loss mechanism for the  $\text{O}^+(\text{}^2\text{P})$  ion below this altitude; plus, DE-2 FPI ( $7320\text{\AA}$ ) observations below 150km did not produce data from which drifts, brightnesses and temperatures could be recovered.



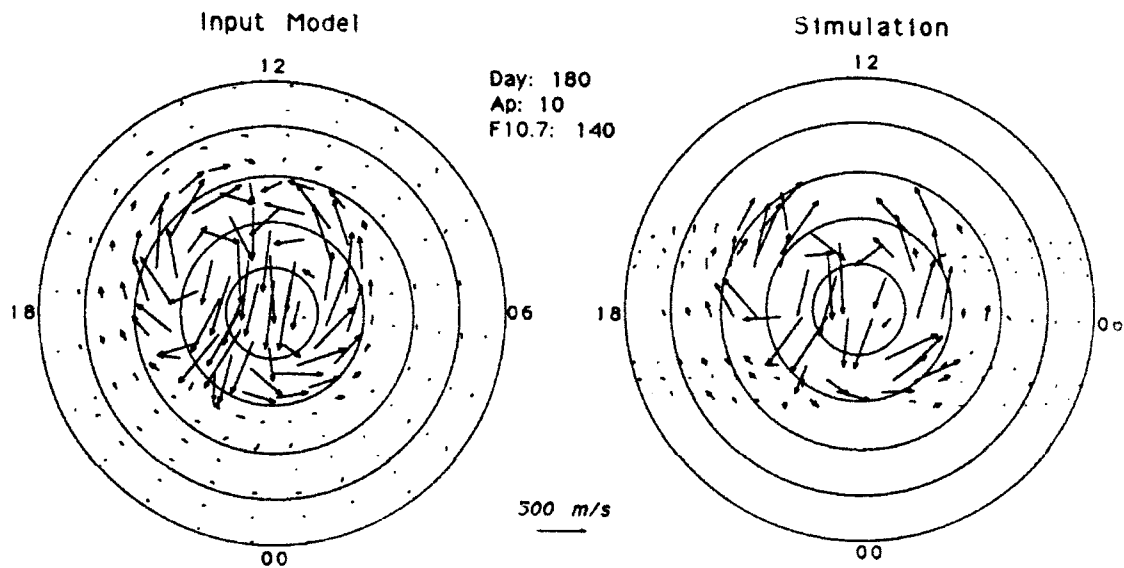


Figure 6.13 The left panel is the ion drift pattern used as input to the convection-imaging simulation. The pattern is in geographic polar coordinates, with the outer circle at  $40^\circ$  latitude. The right panel shows the recovered ion drift vectors from the simulated FPI on the polar orbiting (dawn-dusk) spacecraft. Vector measurements from an *in situ* sensor are also assumed, with these latter vectors being attached to the spacecraft orbit. The pattern provided by the simulated FPI measurements is in good agreement with the pattern used as input to the simulation, demonstrating the capability of the off-track imaging technique.

## 6.4 Conclusions

A simulated spaceborne FPI-system has been developed. The satellite is immersed in a user-defined model atmosphere consisting of ion drifts and temperatures from the VSH model (Chapter 2.4a) and 7320Å volume emission rates from the aurora-airglow model (Chapter 3); the satellite is then "flown" around the Earth at 600km in a polar orbit. The FPIs onboard this satellite have an instrument transfer function similar to that of the DE-2 FPI, with the exception that a CCD was assumed, giving a sensitivity enhancement of  $\sim 12$  over the DE-2 IPD. The satellite's velocity is  $\sim 7.5\text{km/s}$ , therefore allowing the FPI-system to observe the high-latitude portion ( $60^\circ$ - $90^\circ$ - $60^\circ$ ) of this modelled atmosphere in  $\sim 16$  minutes. With its variable look-angle, the FPI-system recovers swaths of ion drift vectors at various lateral spacings away from the satellite's velocity vector, while the (not simulated) RPA/IDM team recovers in-track ion drift vectors.

As can be seen from Figures 6.11 and 6.13, the recovered pattern agrees well with the input pattern, demonstrating that quasi-static ionospheric convection patterns can be imaged over periods of  $\sim 16$  minutes, the time taken for a polar-orbiting spacecraft to traverse the convection region. Such images could be collected twice per orbit, once in each hemisphere, with greater coverage of the summer polar region where emission rate intensities are greater. The evident good agreement between input and simulation makes this technique very attractive for the routine monitoring of high-latitude convection and electric field vectors. It is suggested that temporal sequences of such images could provide definitive information concerning convection cell numbers and geometries for differing geophysical situations. And finally, I suggest that the best

elevation angles for the FPI-system are between  $9.7^\circ$  (500km tangent point,  $8^\circ$  off-track) and  $19.5^\circ$  (200km tangent point,  $15^\circ$  off-track). Mirror angles smaller than  $9.7^\circ$  will allow FPI observations to come from an area of very weak 7320Å emission (as seen in DE-2 observations) because of decreasing atomic oxygen concentration. Mirror angles larger than  $19.5^\circ$  will produce FPI observation points that are below the 200km tangent point altitude. Since the field-of-view increases as the observation distance from the spacecraft increases, the FPI system in this case would be observing the 7320Å emission well below 150km where collisions dominate the loss process of the  $O^+(^2P)$  ion.

The DE analysis presented in Chapter 4 found dayglow summer polar 7320Å brightnesses to be ~50 - 2000R. In the daytime winter polar region, the DE-2 FPI observed 7320Å brightnesses to be ~50 - 200R. However, nightside 7320Å brightnesses could not be observed in low- and mid-latitudes since no source was present; nightside 7320Å brightnesses were only observed by the DE-2 FPI in high latitudes when the emission was sufficiently intense - this condition is satisfied at times in the polar cusp, polar cap and other high-latitude auroral regions. Hence, CONVEX may not be able to recover the entire nightside convection pattern if the nighttime auroral source is sporadic and weak, which is why the dawn-dusk plane would be the best orbit for CONVEX.

This spaceborne FPI-system opens the possibility that 7320Å-doublet emission observations can be used to routinely monitor polar thermospheric atomic oxygen concentrations (Chapter 3.4 and references therein). Complementing the suggested ground-based FPI (7320Å) emission observations and resulting atomic oxygen density retrievals discussed in Chapter 5.3, this Chapter's proposed large-scale spaceborne

retrievals of atomic oxygen densities will greatly enhance our knowledge of upper thermospheric and ionospheric structure.

## CHAPTER 7

### CONCLUSIONS AND FUTURE WORK

In this dissertation, I have presented the first-ever remotely-sensed space-based *and* ground-based determination of ionospheric energetics and dynamics using the 7320Å emission line. The DE-2 FPI (7320Å) space-based recovered ion drifts were found to compare very favorably with near-simultaneous *in situ* RPA measurements, giving confidence to this FPI remote sensing method. The FPI (7320Å) ground-based ion convection and temperature measurements at Søndre Strømfjord were compared with simultaneous ISR measurements; again, agreement was favorable, although FPI data were limited and there were difficulties comparing the optical data to the ISR data. In the DE-2 case, I had to make allowances for the temporal lag between the *in situ* and remote measurements, thereby assuming an ion drift and temperature invariance of ~ 1-3 minutes. While this is a valid assumption for the relatively sluggish neutrals, it is questionable (especially at high latitudes) for the more responsive ions. However, agreement was very favorable, verifying this technique.

At Søndre Strømfjord, the IPD made long integration times necessary. Much of the ionospheric structure was therefore difficult to observe and comparisons to the ISR were difficult. But when these two

measurement techniques were averaged into the same time bins and ordered by line-of-sight, the agreement was favorable. Ion temperatures were easier to retrieve from Søndre Strømfjord spectrograms than from DE-2 spectrograms since the 7320Å doublet components were separated by the Søndre Strømfjord FPI. The overlapping of the 7320Å doublet components by the DE-2 FPI made ion temperature recovery very difficult, even with double-Gaussian software. Future FPIs, such as the ones flown on CONVEX, should be designed to separate these 7320Å doublet components by as great a distance as possible on the detector so ion temperatures can be determined.

I have also continued the development of the 7320Å volume emission rate model by updating the known reactions affecting this emission. The model can now plot either profiles or complete global views of 7320Å emission rates; both plot types show excellent agreement with theory, observations and other models. The DE-2 FPI Simulator was extended to become the DE-2 FPI (7320Å) Simulator by modifying the optics to coincide with 7320Å measurements instead of 5577Å or 6300Å measurements. This Simulator mimics an instrument function that is similar to that of the DE-2 FPI. Using the 7320Å volume emission rate model, and drifts and temperatures from the VSH model as input to this Simulator, ion drift and temperature profiles for any geophysical or solar condition can be accurately plotted (from ~180 - 550km) for any location on the Earth at any time. As with the 7320Å volume emission rate model, this Simulator was then made "global" so the input of date, time, Ap, F10.7, latitude and longitude could produce global maps of ion drifts.

Using the Simulator and the knowledge gained from DE-2 analyses, I devised a suitably instrumented spaceborne observation platform that could

determine the high-latitude ion convection pattern in a ~16 minute pass. The 600km high polar-orbiting satellite, equipped with a system of four FPIs looking off-track at  $\pm 45^\circ$ ,  $\pm 135^\circ$  and an RPA/IDM team for in-track observations, is immersed in a user-defined model atmosphere consisting of VSH ion drifts and temperatures and 7320Å aurora-airglow model volume emission rates. The onboard FPIs have an instrument transfer function similar to that of the DE-2 FPI, with the exception that a CCD is assumed, producing a sensitivity enhancement of ~12 over the DE-2 IPD. During orbit, the spaceborne FPI system integrates all 7320Å emissions along each field of view and produces spectrograms. The spectrograms are analyzed by standard methods to produce swaths of ion drift vectors  $\sim 30^\circ$  wide over the high-latitude convection zone, enabling the cell structure of the ion convection pattern to be readily determined. Greatest coverage will occur over the summer polar regions where emission rate intensities are greatest. High-latitude nightside 7320Å emissions can be sporadic and weak, leading to patches of poor data and unrecoverable portions of the ion convection pattern. Thus, CONVEX should orbit in the dawn-dusk plane to maximize its capabilities. The primary viewing angles (sometimes referred to as mirror or look angles in the literature) of this FPI system should be between  $\sim 9-20^\circ$ , allowing the FPIs to sample tangent point altitudes from  $\sim 500 - 200\text{km}$  respectively at off-track distances of  $\sim 8-15^\circ$  respectively. The generally excellent level of agreement between the simulations and the model atmosphere leads one to believe that this spaceborne interferometric monitoring of the high latitude ion convection pattern could reap excellent results.

The detection of the 7320Å-doublet emission by ground- and space-based FPIs opens the possibility that these emissions can be used to

routinely monitor upper thermospheric atomic oxygen concentrations. Ionospheric and thermospheric structure is largely determined by atomic oxygen between ~225- 500km, where atomic oxygen is the dominant constituent. Important practical needs for the knowledge of thermospheric atomic oxygen densities are for satellite drag and surface material deterioration calculations, for studies of thermospheric and ionospheric structure, and for providing new compositional data to large, thermospheric and ionospheric empirical models. Ground-based FPI (7320Å) experiments have the capability of being modified as the experiment progresses and are much less expensive than satellite platform experiments. However, satellites obtain worldwide coverage, benefit from the Van Rhijn effect and are not affected by weather. Hence, ground- and space-based FPI (7320Å) measurements could complement each other in the retrieval of polar thermospheric atomic oxygen densities.

For future work, I suggest that the ground-based FPI at Søndre Strømfjord be upgraded with a CCD, producing a factor of ~12 enhancement over the current state of affairs. Since ion outflow, ion convection patterns and ionospheric energetics are topics of interest today, I suggest that the ground-based site also be upgraded so the filter wheel can be tele-changed by concerned scientists and even linked to the ISR; the technology to do this is currently available. Scientists would merely dial the Greenlandic phone number, enter a menu, select the 7320Å filter for the filter wheel, and get a night of observations from the comfort of their own laboratory.

Two Small Explorer missions have already been selected for flight by the Space Physics Division of NASA's Office of Space Science and Applications. These small Explorers are ~400lb spacecraft that will be



launched on Scout-class expendable launch vehicles from Vandenberg AFB, CA. I suggest the third mission be equipped with the four FPI-system and one RPA/IDM team as discussed in Chapter 6. Monitoring the high-latitude ion convection pattern from space via observations of the 7320Å-doublet emission allows one to determine this pattern in ~16 minutes and both hemispheric cells in ~60 minutes. The routine monitoring of the high-latitude ion convection pattern, especially during Bz-north conditions when our knowledge is limited, can lead to rapid advances in auroral physics and enhance our understanding of phenomena that are dependent on the electric field. It can also allow us to further investigate magnetospheric/ionospheric coupling and to retrieve polar thermospheric atomic oxygen densities. The technology for CONVEX exists, the software analyses exist and the spaceborne interferometric method was proven with the DE 2.

## **APPENDICES**

## Appendix A

### Spacecraft-Charging

*Surface* charging may be caused by plasma injections of electrons and protons during geomagnetic storms, wake charging or solar illumination (Jursa, 1985). *Interior* charging may be caused by surface charges moving inside via conduction or by deep charging by cosmic ray or high energy particle bombardment. Extremely high energy particles may cause actual sensor contamination, confusion or even physical damage via collisional effects.

Spacecraft charging is frequently defined as either *differential* or *absolute* (Higley, p.c., 1986). Absolute charging occurs when the entire spacecraft is charged to a potential that is different from the ambient potential. Differential charging exists when part of the spacecraft is charged to a potential that is different from some other spacecraft section. Absolute charging occurs relatively quickly ( $< 1s$ ) during eclipse (when the entire spacecraft is not solar illuminated). The net charge from this effect can degrade the thermal properties of the spacecraft's surface and possibly compromise instruments that measure properties of the ambient ionosphere. A net negative surface charge will repel ambient electrons thereby producing spurious particle flux measurements. Differential charging can be even more serious - this type of charging occurs in minutes and is usually caused by spacecraft surfaces constructed of different materials, the presence of non-uniformities in the spacecraft's surface, surfaces being either sunlit or shaded or directional differences in ambient particle fluxes (Jursa, 1985; Higley, p.c., 1986). Eventually, differential charging may lead to absolute charging.

As solar EUV radiation frees electrons on the vehicle's sunlit surface, a *positive* charge is created on the sunlit side. This charging mechanism acts in an opposite sense to plasma (*negative*) charging, which dominates on the dark side of the vehicle. Thus, a substantial negative charge buildup is prevented in the sunlit sector. However, in eclipse, the absence of this photoelectric effect increases the probability that plasma charging will create some sort of electrostatic discharge.

Hence, spacecraft normally accumulate negative potential on dark areas (plasma charging) and positive potential on sunlit areas (photoelectric effect). On a conducting surface, a current develops and cancels these potentials. With a non-conducting surface, charge separation can be maintained only until the voltage difference exceeds the breakdown threshold of the dielectric materials. Negative charges on the dark area of the vehicle will concentrate near the sunlit-dark border; the same happens for the positive charge in the sunlit area of the vehicle. It has been observed (Jursa, 1985; Higley, p.c., 1986) that positive charges have an effective mobility which allows them to achieve a surface distribution that is appropriate for a conductor. The result is that the sunlit-dark border may become a region of strong electric fields.

A minor form of spacecraft charging is wake charging (Higley, p.c., 1986; Jursa, 1985). The ambient thermal plasma may cause charge accumulation on a spacecraft, especially on a low altitude, high speed orbit. As the vehicle moves through the electron and proton plasmas, the temperature of the plasmas are equal, but the electrons will have a higher velocity (lower mass). The vehicle will overtake the randomly moving slow protons, causing a positive charge buildup on the forward (RAM) side.

Electrons, with a random motion faster than the spacecraft, can overtake the vehicle and cause a negative charge buildup on the wake side.

The law governing surface potential of a body immersed in a plasma is that all currents to and from the surface must balance. In equilibrium, plasma, photoelectric and all other minor types of charging must follow this law. Hence,

$$J_e + J_i + J_{se} + J_{si} + J_{photo} + J_{scat} = 0 \quad A.1$$

where  $J_e$  is the incident electron current due to external plasma electrons,  $J_i$  is the incident ion current due to external plasma ions,  $J_{se}$  is the secondary current due to electrons ejected from the surface by energetic incident electrons in  $J_e$ ,  $J_{si}$  is the secondary current due to electrons ejected from the surface by energetic incident ions in  $J_i$ ,  $J_{photo}$  is the photoelectron current due to electrons ejected from the surface by the photoelectric effect and  $J_{scat}$  is the backscattered electrons (ejecta from  $J_{se}$ ,  $J_{si}$  and  $J_{photo}$ ) that are recaptured.  $J_e$ ,  $J_{photo}$  and  $J_{se}$  dominate. All terms depend on the satellite surface potential, and for an ambient plasma environment with a certain solar illumination, that potential will adjust to a value that satisfies equation A.1. Consider a vehicle in eclipse that is immersed in an ion/electron plasma of equal temperature. Assume  $J_{se}$ ,  $J_{si}$  and  $J_{scat}$  are small. Obviously,  $J_{photo}$  is zero. Hence,  $J_i = J_e$  must be satisfied. Since the electron thermal velocity is greater than the ion thermal velocity, there is a greater probability that an electron will strike the surface than an ion. To satisfy  $J_e = J_i$ , the satellite must acquire a negative potential so the attraction for ions is *increased* and that of electrons is *decreased*. Therefore, the incident ion and electron currents are driven to equilibrium.

The retarding *potential* analyzer discussed in Chapter 2.3 and used in Chapters 4 and 6 is an electrically sensitive device. The brief introduction given here about spacecraft charging shows that the hostile environment in which the DE 2 flew (and CONVEX will fly) *may* have detrimentally affected some RPA measurements, especially in the auroral zone and low altitudes (below 275km). The various orbits of RPA data I used in Chapter 4 made logical sense and favorably compared with model and FPI results. Many researchers have used the RPA in the past and it has a proven track record. However, spacecraft charging is not a problem an FPI must deal with since it is (in DE 2's case) viewing ~ 500 - 1700 km away from the satellite. Spacecraft charging mainly affects *in situ* devices.

## APPENDIX B

### B.1 Inversion of DE-2 FPI (7320Å) LOS Parameters

Contribution functions are altitude weighting functions that establish the importance of each altitude for a given FPI view position. This function is basically the product of the path length of the line-of-sight and the volume emission rate. The contribution function will usually be sharply peaked at the tangent height since the path length peaks there. Hence, the information content is favorable at the tangent height. Unfortunately, the contribution function may have significant values at altitudes other than the tangent point where an intense emission, such as an auroral display, occurs. In this case, accurate geophysical parameters may be recovered, but spatially locating the position of these parameters will be difficult. Fortunately, most aurorae that are intense enough to alter the fringe pattern of an FPI come from altitudes less than 200km (Niciejewski, p.c., 1992; Rees, 1989) and will therefore not affect the 7320Å observations that are made from ~200-500km.

An example of this is shown in Figure B.1. Figure B.2 are simulated contribution functions for the conditions listed on the graph. As noted previously (Chapter 3), the 7320Å emission peaks at about 300km, with a spread of +/- 100 km. Note how the contribution functions for all 16 simulated DE-2 mirror positions peak in this range, suggesting that the resulting line-of-sight winds are representative of the actual "true" winds.

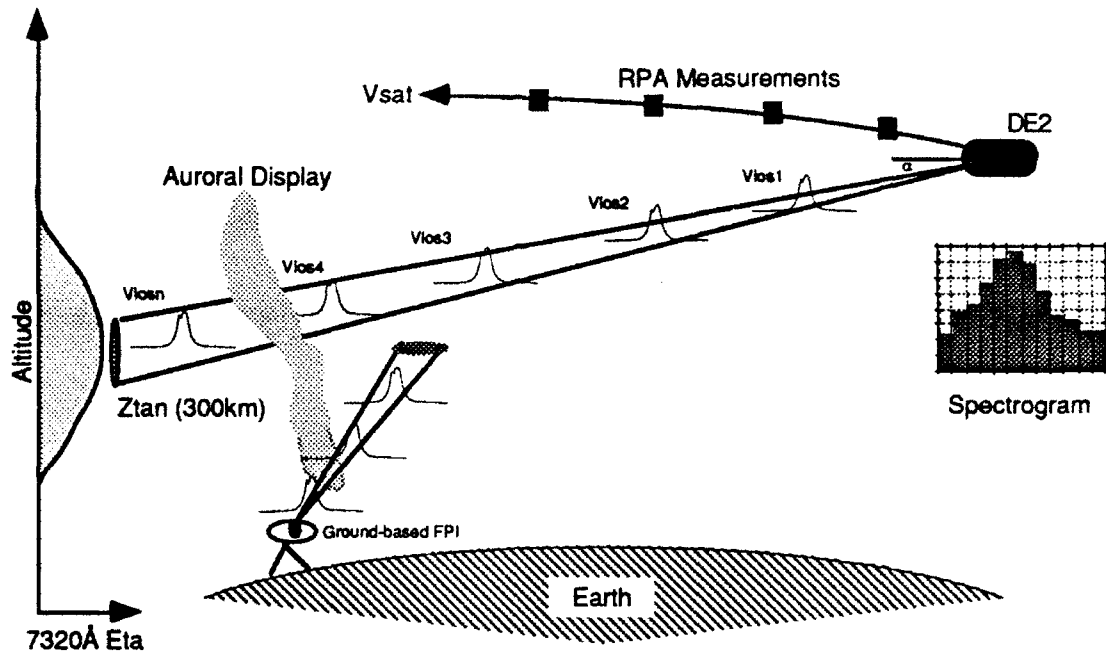


Figure B.1 DE-2 FPI senses all emissions along the line-of-sight (LOS). LOS drifts are determined by the net Doppler shift of the spectrogram which is produced from these emissions occurring along the entire LOS. The largest contribution to the emission comes from the tangent point, depicted in this case at  $\sim 300\text{km}$ . With an auroral display in the instrument's field of view, the largest contribution may be coming from  $382\text{km}$ , for example, instead of the actual  $300\text{km}$ . However, most intense aurorae occur below  $\sim 200\text{km}$  and will therefore not affect spaceborne FPI observations. The same is not true for ground-based observations, the topic of Chapter 5.



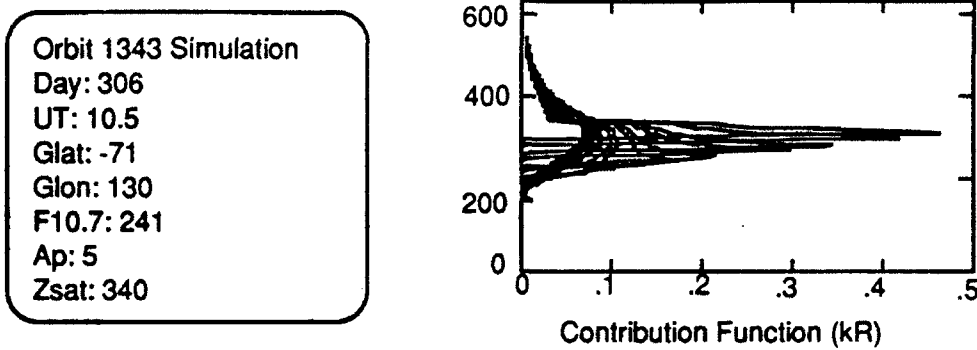


Figure B.2 Contribution functions for a model 7320Å volume emission rate profile produced for the conditions listed on the figure. The volume emission rate profile peaked at 293km and 18 ph/cc-s. Each kernel (there are 16 of them - one for each DE-2 mirror position) describes the contribution to a given measurement as a function of altitude. The maximum contribution occurs at the tangent height, denoted by the sharp peaks.

In order to obtain "true" neutral winds from DE-2 FPI (5577Å) observations, Nardi (1991) had to perform complicated inversion schemes to the data since the greenline volume emission rate has a peak at ~100km and another ~200km. A brief discussion follows.

The onion peel method of Nardi (1991) enables one to strip away brightness measurements from upper atmospheric layers in order to reveal contributions from lower layers. Brightness ( $B(z_t)$ ) at tangent height  $z_t$  is the integrated product of the volume emission rate ( $\eta$ ) profile and the brightness inversion kernel ( $K(z, z_t)$ ). This kernel may be written as

$$K(z_i, z) = \sum_{i=1}^{12} K_{A/F_i}(z_i, z) \quad \text{B.1}$$

where  $K_{A/F_i}$  are the altitude-broadened kernels for individual ring anodes (i.e. channels 1-12) for the IPD. The kernels are functions of field-of-view weighting functions from a ray-trace simulation; these ray-trace simulations corrected for distortions produced by the FPI's optics. Therefore, brightness is:

$$B(z_i) = \int_z K(z, z_i) \eta(z) dz \quad B.2$$

Using matrix notation, B.2 may be written as:

$$[B] = [K][\eta] \quad B.3$$

where  $[B]$  and  $[\eta]$  are column vectors and  $[K]$  is an  $N \times N$  matrix. To determine the volume emission rate, the onion peel (unconstrained) inversion, using single value decomposition (SVD), is used:

$$[\eta] = [K]^{-1}[B] \quad B.4$$

SVD decomposes  $[K]$  into:

$$[K] = [U][W][V]^T \quad B.5$$

where  $[U]$  is the eigenvector matrix of  $[K]$ ,  $[V]$  is the eigenvector matrix of  $K^T$  and  $[U]$  and  $[V]$  are orthogonal. Performing the inversion in this fashion allow one to consider the singularities in the kernel matrix  $[K]$  by isolating the problems in the eigenvalue matrix  $[W]$ . Since  $U$ ,  $V$  and  $W$  are either orthogonal or diagonal, they are easier to manipulate than  $W$ . Using matrix manipulations discussed in Nardi (1991), the volume emission rate is therefore:

$$[\eta] = [K]^{-1}[B] = \{[U][W_i][V]^T\}^{-1}[B] = [V] \cdot \left[ \text{diag} \left( \frac{1}{W_i} \right) \right] \cdot \{[U]^T \cdot [B]\} \quad B.6$$

The inverted volume emission rates may then be used to calculate drift inversion kernels. LOS drifts are averaged over the viewing path of the DE 2

(see Figure B.1); to get the true drifts at each altitude, the inversion must be applied.

The relationship between LOS drifts and true drifts at height  $z$  must be determined. This involves relating changes in the LOS drifts to changes in channel response of the FPI via a least squares method. The changes in the channel response of the FPI include the volume emission rate profiles just acquired. The final LOS drift equation may be written:

$$v_{\text{los}}(z_t) = \int K'(z, z_t) v(z) dz + v_{\text{los0}}(z_t) \quad \text{B.7}$$

where  $v_{\text{los}}(z_t)$  is the LOS drift at the tangent height,  $K'(z, z_t)$  is the drift inversion kernel (which includes an additive constant of 1600m/s for the 7320Å emission and 330m/s for the 5577Å emission) and  $v_{\text{los0}}(z_t)$  is the apparent drift - an artificial drift produced from gradients in the volume emission rate profile. The weighted/constrained inversion of Nardi (1991) is in equation B.8 and is weighted by a covariance matrix  $S_{v_{\text{los}}}$ :

$$v = (\gamma H + K^T S_{v_{\text{los}}}^{-1} K) (K^T S_{v_{\text{los}}}^{-1} v_{\text{los}}) \quad \text{B.8}$$

where  $v$  is the true drift,  $\gamma$  is a weighting factor,  $H$  is an  $n^{\text{th}}$ -order difference matrix (this limits the number of inflection points in the inverted drift profile; the higher the value of  $n$ , the less the constraint),  $K$  is the drift inversion kernel,  $S_{v_{\text{los}}}$  is the covariance matrix consisting of the LOS drift errors, and  $v_{\text{los}}$  are the LOS drifts. The accuracy of this method is stated as  $\pm 15\text{m/s}$  with a spatial resolution of  $\pm 10\text{km}$ .

The spectrograms shown in Chapters 2 and 4 represent convolutions of the Doppler source function (the 7320Å emission), characterized by the ambient ion drift and temperature, and the known instrument transfer

function (determined prior to flight for the DE-2 FPI). These two functions were deconvolved during the analysis procedure and the resulting *line-of-sight* drift results were *inverted* using this technique of Nardi (1991) to derive "true" drift profiles. These inverted "true" drifts were found to be nearly indistinguishable from the line-of-sight drifts in the tangent point altitude range of ~200-500km due to the peaked nature of the contribution functions (Killeen et al., 1982b; Nardi, 1991). Hence, inversions were not necessary to be performed on the 7320Å line-of-sight parameters (or 6300Å LOS parameters for similar reasons) in order to determine the "true" ones. See Figure B.3.

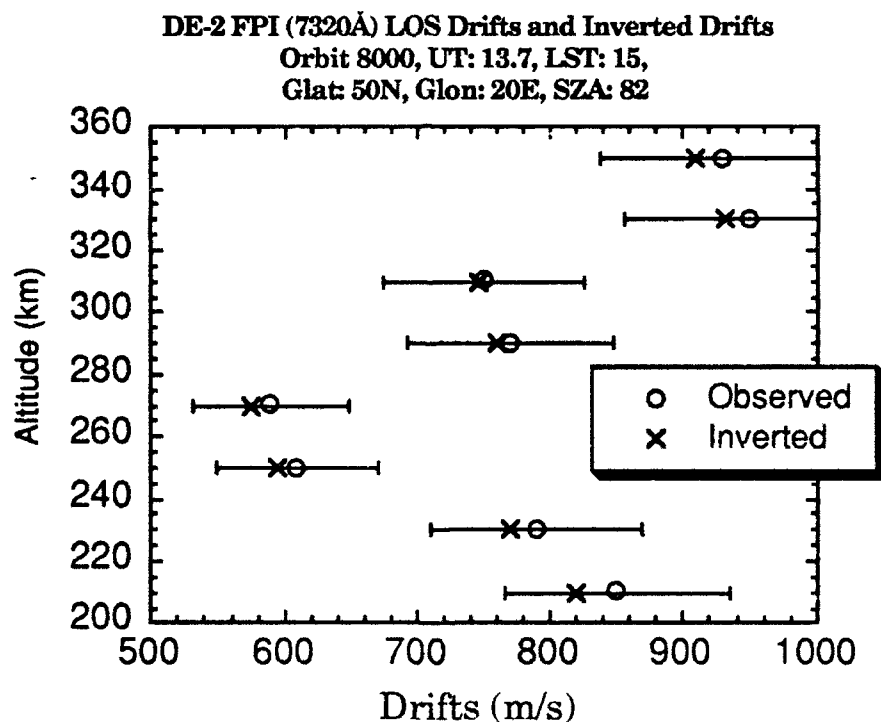


Figure B.3 Sample plot of observed "line-of-sight" drifts (with errors) and inverted "true" drifts for the conditions listed on the diagram. Because of the localized emission source and sharply peaked contribution functions, no inversion of the line-of-sight drifts is necessary. The line-of-sight winds for DE-2 FPI (6300Å) were not inverted for similar reasons. The same was not true for the DE-2 FPI (5577Å) emission.

## B.2 DE-2 FPI (7320Å) Software Flow

Over 1000 DE-2 orbits contain FPI-sensed 7320Å data; these data were placed in an image file. The raw, binary data from these image files are passed through a standard binning and fitting routine (*FPI20*) that produces counts (CNTS\*.DAT, where \* is the orbit number) and geophysical line-of-sight (LOS) parameters (drifts, temperatures and brightnesses (GU\*.DAT)). The program *SPECTRA* reads in the count data and plots spectrograms while the program *FPIBIN* reads in counts and the LOS parameters and produces a binary J\*.DAT file containing binned and averaged LOS parameters. *FPIDISP* also reads in LOS parameters and produces K\*.DAT files containing binned and averaged LOS parameters. These K\*.DAT files can be run through the IDL program *KPROCARR* to produce three-panel plots (at a certain altitude) of drifts, brightnesses and temperatures versus tangent point latitude/longitude, SZA, and UT. K\*.DAT files can also be fed into *NEWK* which produces color three-panel plots (binned in tangent-point altitude from ~ 200-500km) of drifts, brightnesses and temperatures along the satellite track.

The J\*.DAT files can be used in several ways. Firstly, the LOS brightnesses of the J\*.DAT files can be read into *INVERTF77* which produces volume emission rates. These volume emission rates are passed into *CENTROID* and *BINAVE*, which bin (in latitude or AAT) and average (~200-500km in altitude) the volume emission rates and send them to an I\*.DAT file. Once there, these DE-2 "observed" volume emission rates can be plotted by the IDL programs *ETA* (vertical profiles with volume emission rate plotted against either AAT, latitude or UT) or *3DETA* (three-

dimensional 7320Å volume emission rate profile with the emission rate on the Z-axis and altitude/latitude (or AAT or UT) on the horizontal axes. Secondly, the J\*.DAT LOS parameters can be fed into *JPROICARR* which then plots drift, temperature and brightness profiles versus latitude, AAT or UT. And thirdly, the J\*.DAT LOS parameters are fed into *CARRFPIAUTO* which bin averages the data in time (7320Å FPI data is retrieved every 0.25s; this program places them in 8 second bins in order to match the RPA integration time) and averages them in altitude (200-500km). Error-checking constraints for *CARRFPIAUTO* are listed in Table B.1. The temporary datafile created by this program is then run through *CARR\_REPAIR* which inserts this averaged FPI data into the proper spot in the DE-2 database so they can be plotted (via *KALEIDAGRAPH*) against "simultaneous" RPA data. In effect, these last two programs make a spatial and temporal correction to the FPI data and place them in the DE-2 database so FPI measurements are at the same place and time with the RPA measurements (which are made directly above the sampled volume of the FPI measurements). Figure B.4 illustrates the software flow used in Chapter 4. The software is in [DEGRP1.FPI], [DEGRP1.FPI20] or [DEGRP1.FPI.IMOIIFILES].

	Minimum	Maximum	Error
Vi (m/s)	-4500	4500	<500
Ti (K)	500	6000	<500
B (R)	50	5000	<250

Table B.1 If ion drifts, temperatures or brightnesses exceeded the values in this table, all data from that DE-2 FPI mirror scan are discarded.

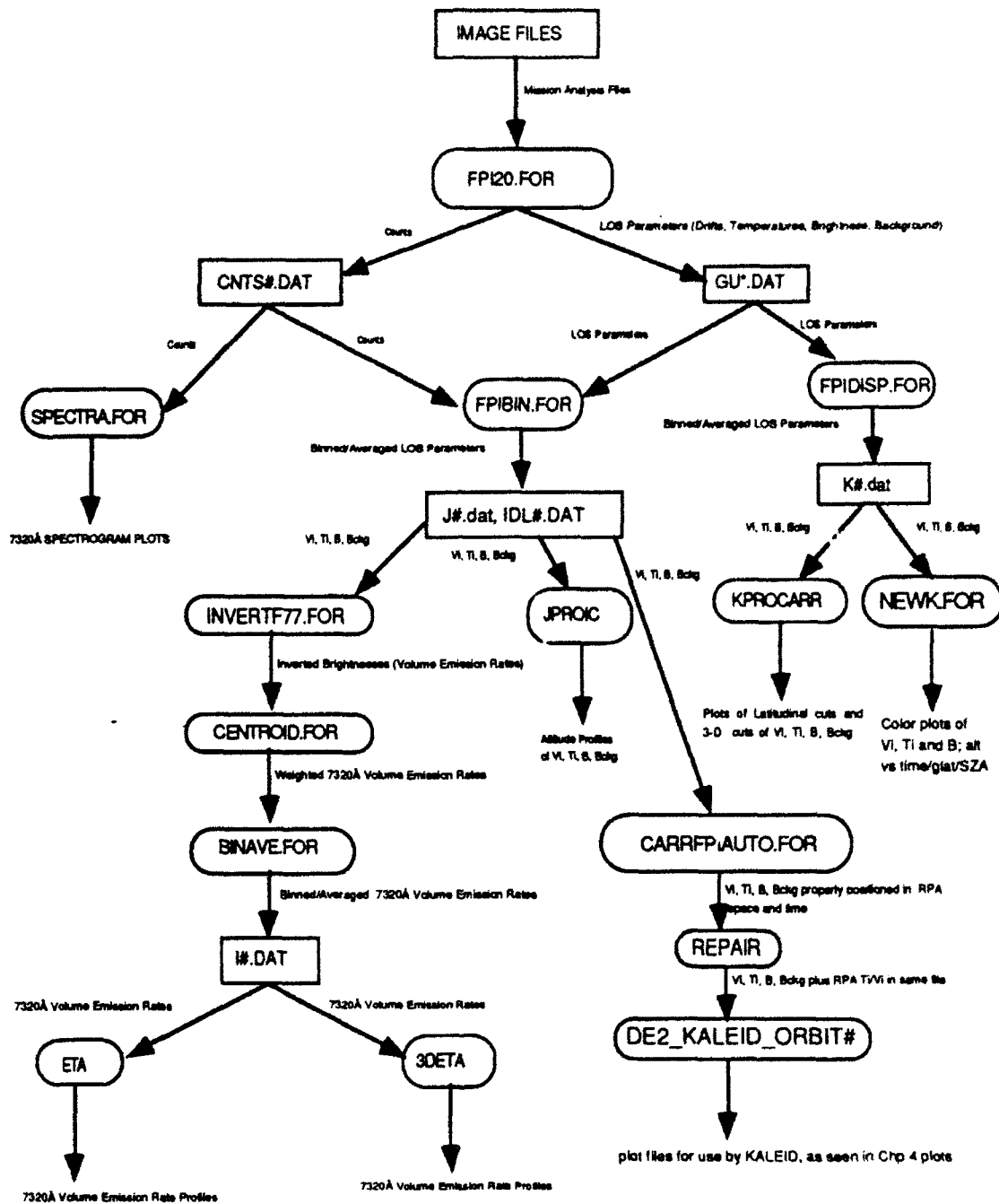


Figure B.4 The standard analysis software package for analysis of DE-2 FPI (7320Å) data.

## Appendix C

### Søndre Strømfjord Data Analysis and Flow

Figure C.1 illustrates the software used in the analysis and plotting routines of Chapter 5. Programs are in ellipses, databases and files are rectangles. Data flow is also shown. Figure C.2 is a more detailed look at the dataflow on the SPRL's VAX. On the right hand side of Figure C.2 are the programs and locations within the VAX that produce the output seen on the left of the figure. ISR data are shipped to SRI from Søndre Strømfjord, where SRI processes the data and then mails the data (on tape) to users. The tape comes in the NCAR XPORT format and is blocked. The tape is 9 track, written at 6250 BPI. All data are processed through SRI's FIT program. The FIT data from the three position antenna mode are then processed through the EPEC program to resolve the three different line-of-sight velocities at each gate into bulk plasma velocities. All of this information, along with much more, are in files on this tape which can be accessed by various codes. I wrote an extraction program called SRITAPE that grabs the data I needed from this tape and places them in the file \*SEP.DAT, where \* is the day number. This program is useable by anyone; all one needs are the desired codes and one can access  $T_i$ ,  $T_e$ ,  $V_i$  etc. for any SRI tape in this format. A list of codes and what they represent is available from SRI upon request. In this dissertation, I mainly used codes 110, 550, -550, 1240, -1240, 1250, -1250, 1260 and -1260 which represent (respectively) altitude, ion temperature, ion temperature error, ion drift in the east (positive value) or west (negative value) direction, drift error, ion drift in the north (positive value) or south (negative value) direction, ion drift error, ion



drift antiparallel to **B** (positive vertical), ion drift error. Once the desired data is extracted, one can plot it however one chooses (IDL routines, KALEIDAGRAPH). In Figure C.3, I illustrate this ISR machinery. The routines in this Appendix are all found in the GDBMS directory, or in SCRATCH.

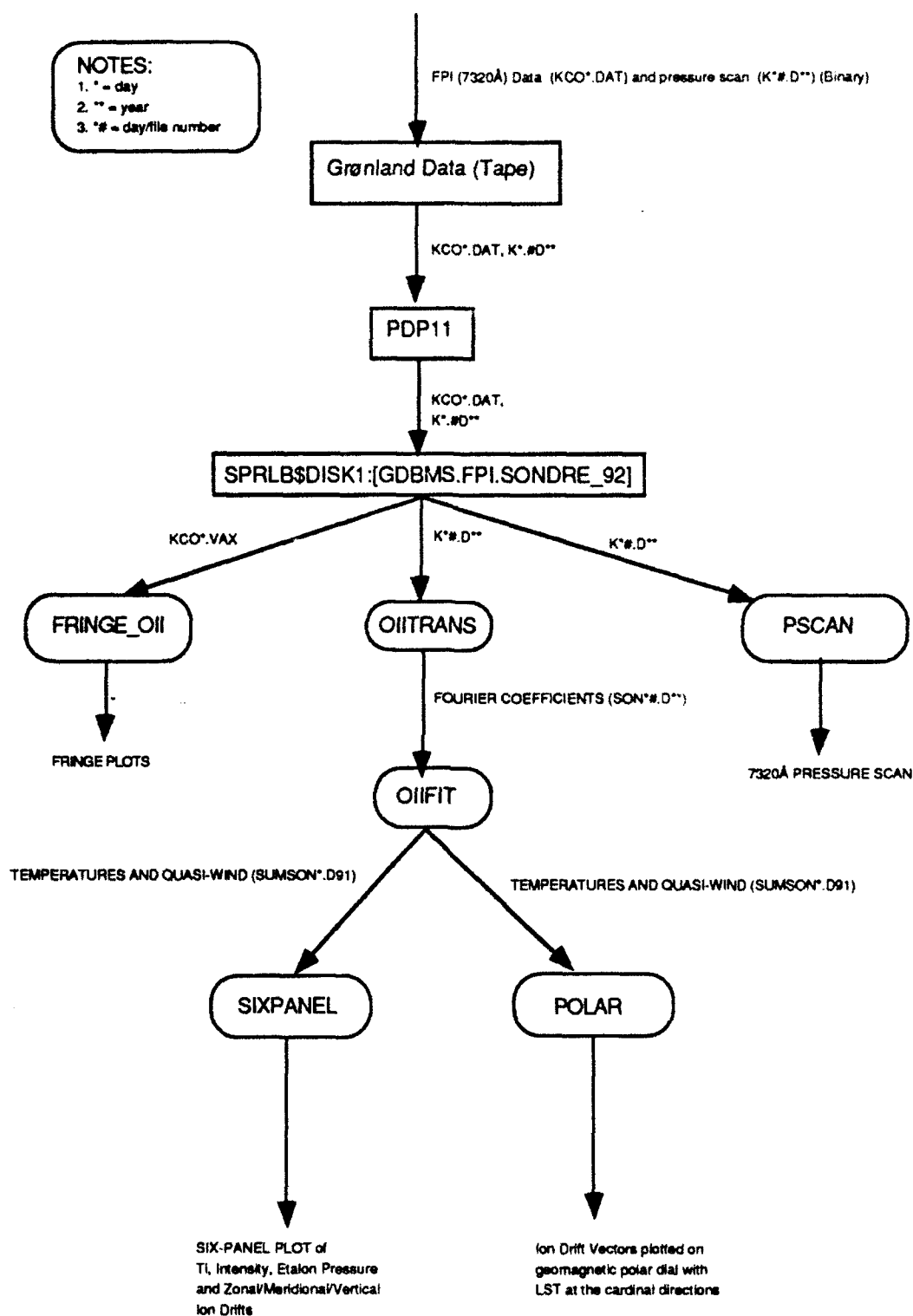


Figure C.1 FPI data from Søndre Strømfjord are placed on tape and brought back to the SPRL, where they are dumped onto the antiquated PDP11 and then downloaded to the VAX. Data are then analyzed by these programs.

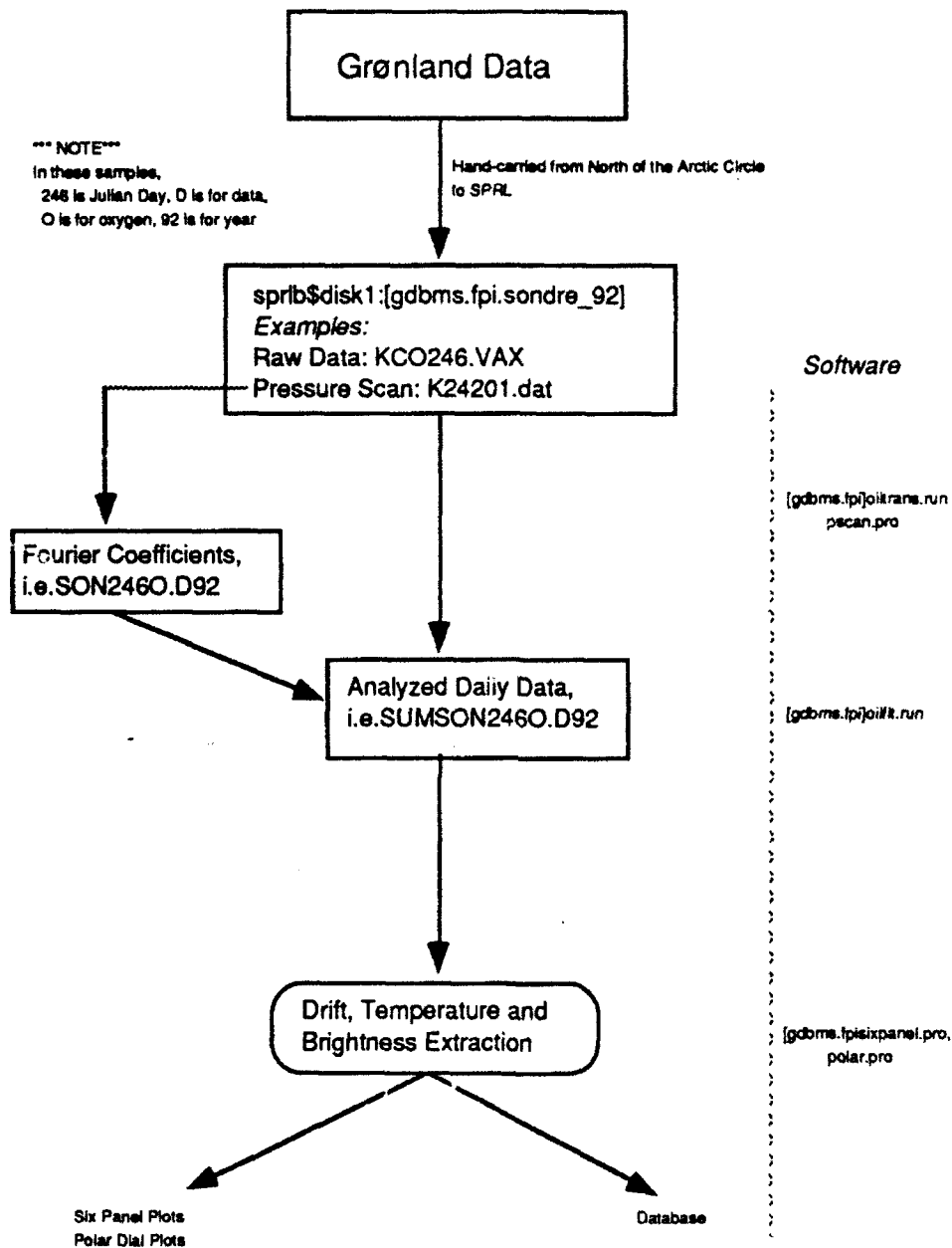


Figure C.2 Diagram of the Søndre Strømfjord FPI (7320Å) data flow used in Chapter 5.

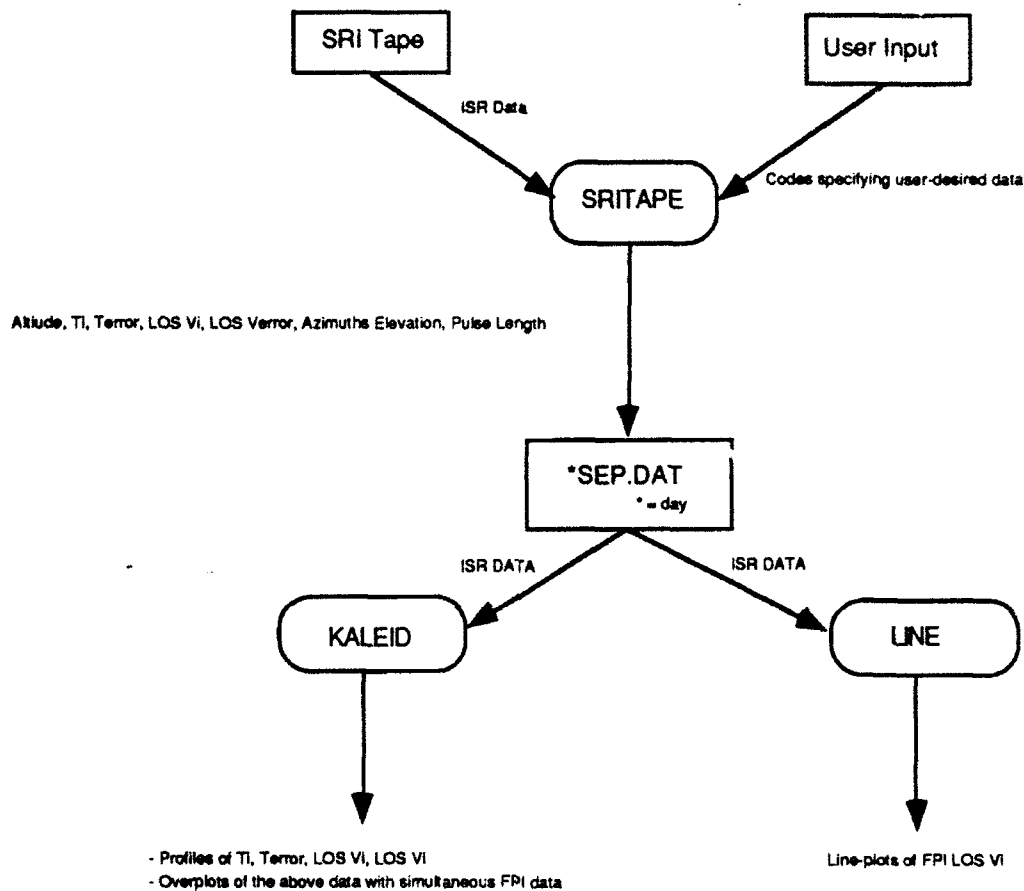


Figure C.3 Diagram of Søndre Strømfjord ISR Analysis Machinery used in Chapter 5. SRITAPE.FOR can be used for any tape in the new SRI tape-format.

## Appendix D

### DE-2 FPI (7320Å) Simulator Software Flow

To run the DE-2 FPI (7320Å) Simulator, one is queried by the software for date, UT, F10.7, F10.7A, Ap, geographic latitude and longitude, the desired FPI integration time and the height of the satellite. With these data as input, VSH and the 7320Å volume emission rate model can be called and provide their results (profiles of meridional ion drifts/temperatures and 7320Å volume emission rates, respectively) to the Simulator. These results provide the Simulator with the user-desired model profile of the atmosphere. The Simulator analyzes these profiles similar to the way in which the DE-2 FPI would have, and produces simulated meridional ion drift, temperature and brightness profiles. Figure D.1 illustrates the program and data flow. Figure D.2 is a blow-up of the DE2\_7320\_SIM ellipse from Figure D.1 and shows the inner workings of the Simulator.

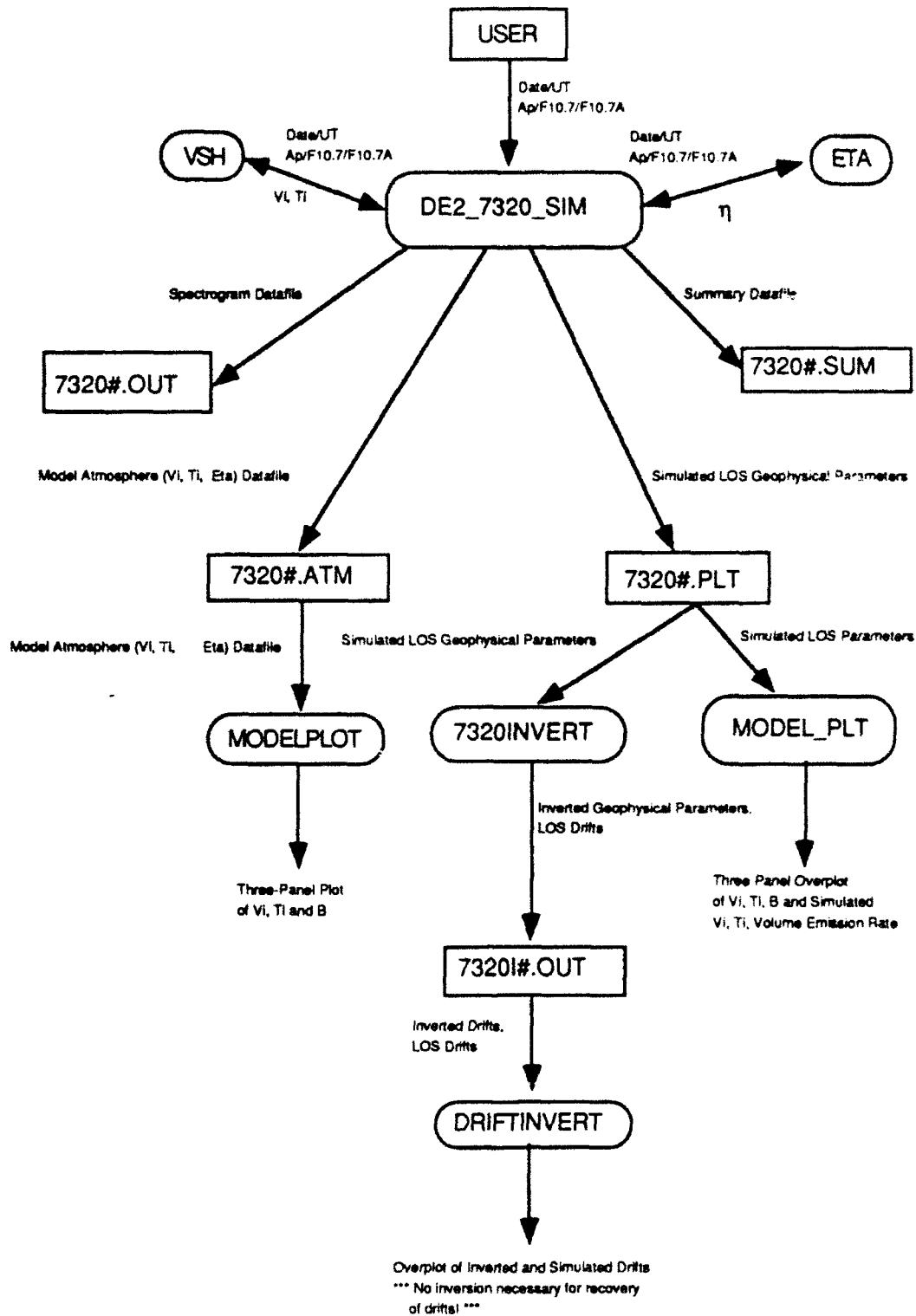


Figure D.1 DE-2 FPI (7320Å) Simulator and datafile flow.

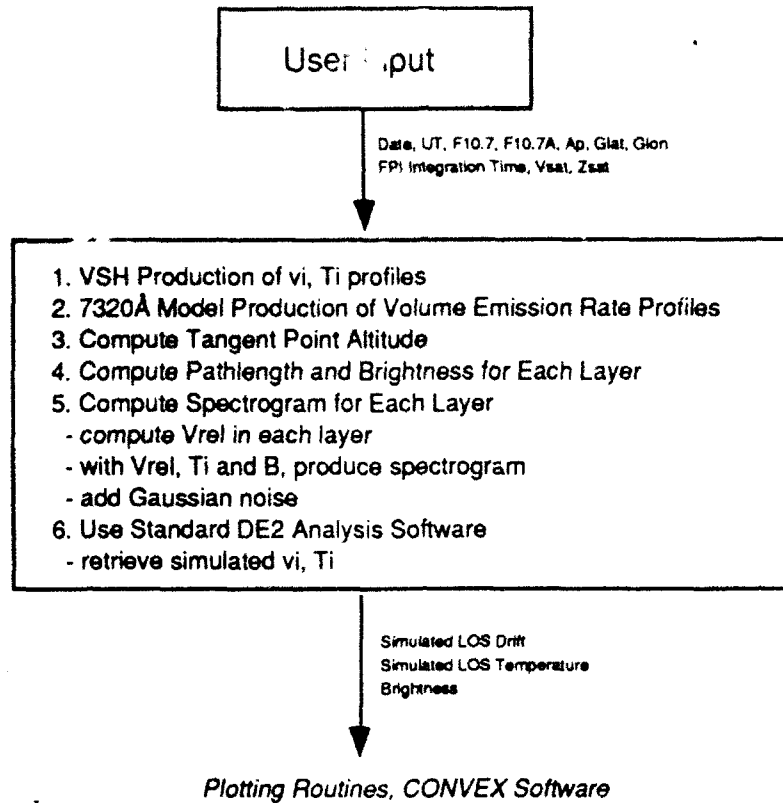


Figure D.2 Inner workings of the DE-2 FPI (7320Å) Simulator.

## Appendix E

### CONVEX Calculations

#### E.1 Tangent Point Altitude Determination

Figure E.1 illustrates how one calculates the elevation angle for a desired tangent point and satellite altitude.

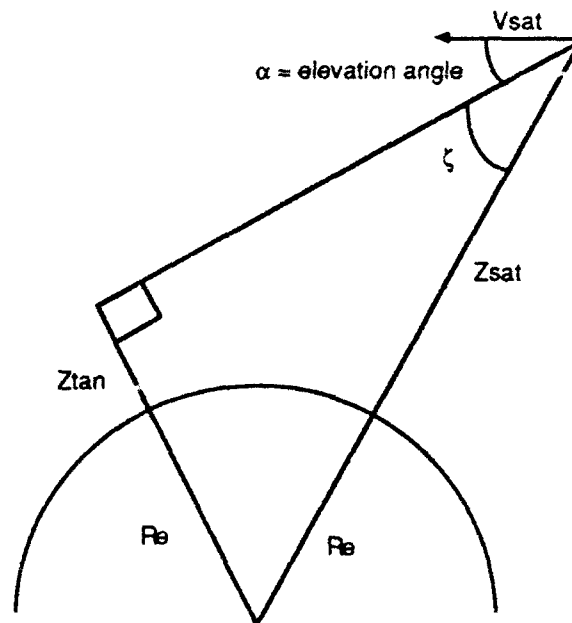


Figure E.1 Illustration of elevation angle calculation. See text for discussion.



With a satellite altitude of 600km, and a desired tangent point altitude of 300km, the angle  $\zeta$  can be defined as:

$$\sin \zeta = \left( \frac{R_e + Z_{\tan}}{R_e + Z_{\text{sat}}} \right) \quad \text{E.1}$$

where  $R_e = 6371\text{km}$ . Hence,

$$\zeta = \arcsin \left( \frac{6371\text{km} + 300\text{km}}{6371\text{km} + 600\text{km}} \right) = 73.13^\circ \quad \text{E.2}$$

Therefore, the elevation angle,  $\alpha$ , is given by:

$$\alpha = 90 - 73.13 = 16.87^\circ \quad \text{E.3}$$

Armed with this knowledge, one can then move the FPI mirror up or down, either increasing or decreasing the elevation angle. The varying elevation angle will allow the satellite's FPI to either observe further or closer to the satellite, and at different tangent point altitudes. The selection of these mirror angles must be done with care because observing too low in the atmosphere ( $<200\text{km}$ ) or too high ( $>500\text{km}$ ) will result in poor  $7320\text{\AA}$  emission data retrieval (as was noted in the DE analysis of Chapter 4). The next section of this Appendix determines the off-track distance for the  $16.87^\circ$  elevation angle, and also for the largest and smallest elevation angles possible for accurate observations of this  $7320\text{\AA}$  emission.

#### E.2 Off-track distances and the Elevation-Angle Cone

With a satellite altitude of 600km and a desired tangent point altitude of 300km, the FPI elevation angle was calculated in the previous section to

be  $16.87^\circ$ . The angular distance to the tangent point latitude/longitude is calculated by:

$$tpll = \sqrt{\{(Re + Z_{sat})^2 - (Re + Z_{tan})^2\}} = \sqrt{\{(6971\text{km})^2 - (6671\text{km})^2\}} = 2023\text{km} \quad \text{E.4}$$

where  $tpll$  is the tangent point latitude/longitude. The FPI is therefore observing a slice of ionosphere that is  $1432\text{km}$  ( $\sim 13^\circ$  latitude) normal to the satellite track. This is evident in the following figure.

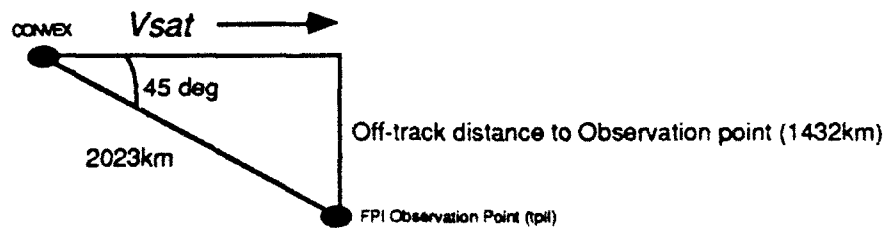


Figure E.2 In this figure, CONVEX is moving to the right and its forward-sensing FPI is looking  $45^\circ$  off-track to the tangent point latitude/longitude. This distance is  $2023\text{km}$ . The *normal* off-track distance to the FPI  $tpll$  is readily seen to be  $1432\text{km}$ .

Figure E.2 illustrates just one of the FPIs, looking in the forward ( $45^\circ$ ) direction. Now, let's assume one can "see" both FPIs on the *right* side of the satellite. From Figure E.3, it becomes clear that for the FPI sensing in the backward ( $-45^\circ$ ) direction to sample the same volume that the FPI in the forward direction senses,  $2864\text{km}$  must be travelled ( $1432\text{km} + 1432\text{km}$ ). At  $\sim 8\text{km/s}$ , CONVEX will travel this distance in  $\sim 5.9$  minutes. Hence, when I combine the simulated ion drift vectors from the forward and backward look directions, I assume ionospheric temporal invariance for those 5.9 minutes when the FPI elevation angle is  $16.87^\circ$ .

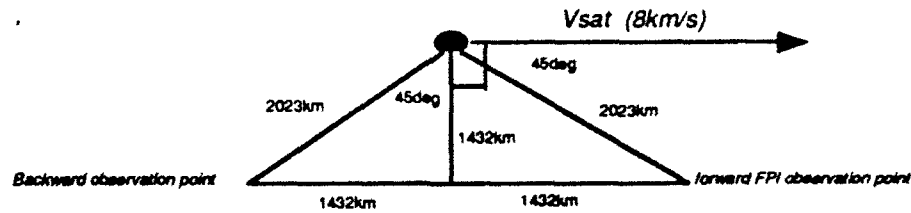


Figure E.3 In this figure, the satellite is moving to the right of the page. The forward looking FPI looks off at a  $45^\circ$  angle to the satellite track and observes at a tpll that is  $2023 \text{ km}$  away or  $1432 \text{ km}$  normal to the satellite track. The backward looking FPI does the same, only at  $-45^\circ$ . At a satellite speed of  $8 \text{ km/s}$ , it takes the backward looking FPI  $\sim 5.9$  minutes before the satellite travels the  $2864 \text{ km}$  and therefore allows it to sample the same volume the forward looking FPI did  $5.9$  minutes previously.

The lowest limit one would want to sense the  $7320\text{\AA}$  emission would be  $\sim 200 \text{ km}$ . Below this altitude, quenching begins to become important, and the  $7320\text{\AA}$  emission may be quenched before accurate observations can be made (as noted in the DE-2 analysis of Chapter 4). For a tangent point altitude of  $200 \text{ km}$ , therefore, the distance to the tangent point latitude/longitude is:

$$\text{tpll} = \sqrt{(6971 \text{ km})^2 - (6571 \text{ km}^2)} = 2327 \text{ km} \quad \text{E.5}$$

The elevation angle is given by:

$$\alpha = 90 - \arcsin \frac{6571}{6971} \approx 19.50^\circ \quad \text{E.6}$$

The normal off-track distance to the observation point is therefore:

$$\text{normal} = \sin 45^\circ * 2327 \text{ km} \approx 1650 \text{ km} \approx 15^\circ \quad \text{E.7}$$

and the time for common volume sampling is therefore:

$$\text{time} = \frac{1650 \text{ km} * 2}{8 \text{ km/s} * 60 \text{ s/min}} \approx 6.8 \text{ min} \quad \text{E.8}$$

The top limit for the 7320Å observation, according to theory and verified by the DE-2 analysis of Chapter 4, should be ~ 600km. In this case, using the same methods just outlined, t<sub>pl</sub> is ~1177km and the elevation angle is 9.7°. These values allow us to calculate an off-track distance to the observation point of ~ 830km or ~ 7.5° off-track. If the FPI elevation angle is any smaller than this value, the FPI will be scanning too high in the atmosphere to detect any of this 7320Å emission. Hence, the mirror scan positions on the CONVEX system should range between 19.5° (200km tangent point altitude, 15° off-track) to 9.7° (500km tangent point and nearly 8° off-track). Thus, the maximum angular view the four FPI system can produce a single pass is ~30° (+/- 15° off the satellite track). This is wide enough to discern the ion convection pattern at considerably better resolution and areal extent than any previous observation platform. Note that in Chapter 6, I used elevation angles of 19.5° (200km tangent point, ~15° off-track), 16.87° (300km tangent point, ~13° off-track)) and 13.76° (400km tangent point , ~11° off-track). I suggest this mirror-scan pattern to be the best since it scans the strongest part of the 7320Å emission and, with an RPA /IDM team in track, produces a swath of 30° coverage.

### E.3 Method of Common Volume Sampling to Produce Vector Ion Drifts

The method used to combine line-of-sight drifts that were measured at different times (never greater than ~ 6.9 minutes in this dissertation) by different FPIs but within the same volume was modelled after the method used by HRDI (High Resolution Doppler Imager). A brief description follows.

Refer to Figure E.4. Assume the satellite is at the bottom of the figure and moving straight up the page (North). For this illustration, assume a flat Earth. For simplicity, assume only one elevation angle ( $16.87^\circ$ ); hence, the FPI-system is sensing a set of 300km tangent points that are 1432km normal to the satellite track ( $\sim 13^\circ$  off-track). In Figure E.4, one can therefore see that when the satellite is at  $55^\circ\text{N}$  latitude, its FPIs looking in the forward direction are sensing a point that is at  $68^\circ\text{N}$  latitude and  $13^\circ$  off-track. When the satellite has travelled to the point on the graph labelled  $81^\circ$  North latitude, its FPIs looking in the backward direction sense the same volume as the forward looking FPIs did when the satellite was at  $55^\circ\text{N}$ . Using the HRDI method of line-of-sight combinations, and denoting  $S_1$  as the forward line-of-sight,  $S_2$  as the backward line-of-sight,  $u$  as the zonal ion drift component,  $v$  as the meridional component and letting  $\theta$  be the FPI azimuths ( $\pm 45^\circ$ ,  $\pm 135^\circ$ ),  $\phi$  being North ( $90^\circ$ ),  $\alpha$  the difference between these two angles, one has:

$$\tilde{S} = \tilde{V} \cdot \epsilon \quad \text{E.9}$$

where

$$S_1 = uz_1 + vm_1 \quad \text{E.10}$$

$$S_2 = uz_2 + vm_2 \quad \text{E.11}$$

Note that  $\epsilon$  is a unit vector in the view direction and the angular variables  $z$  and  $m$  are given by:

$$m_1 = \cos(\alpha - \phi) \quad \text{E.12}$$

$$m_2 = \cos(\alpha + \phi) \quad \text{E.13}$$

$$z_1 = \sin(\alpha - \phi) \quad \text{E.14}$$

$$z_2 = -\sin((\alpha + \phi)) \quad \text{E.15}$$

Solving the set of equations listed in E.1 produces

$$u = S_1 m_2 - S_2 m_1 \quad \text{E.16}$$

$$v = S_2 z_1 - S_1 z_2 \quad \text{E.17}$$

Hence, the zonal component of the ion drift velocity is a combination of the line-of-sight velocities in the forward and backward direction, plus a set of geometrical multiplication constants. Similarly, the meridional ion drift component of the velocity vector is a combination of the line-of-sight velocity observations and a set of geometrical multiplication constants. In this case (16.87° elevation angle, 300km tangent point altitude and 1432km off-track), 5.9 minutes has passed between the time the backward looking FPI at 81°N latitude sensed the same volume the forward looking FPI did when the satellite was at 55°N. On HRDI,  $m$  and  $z$  are known *a priori* and  $S$  is measured. Hence, the calculation of  $u$  and  $v$  is straightforward. Of course, spherical geometry makes this slightly more complicated and will be discussed in the next section of this Appendix.

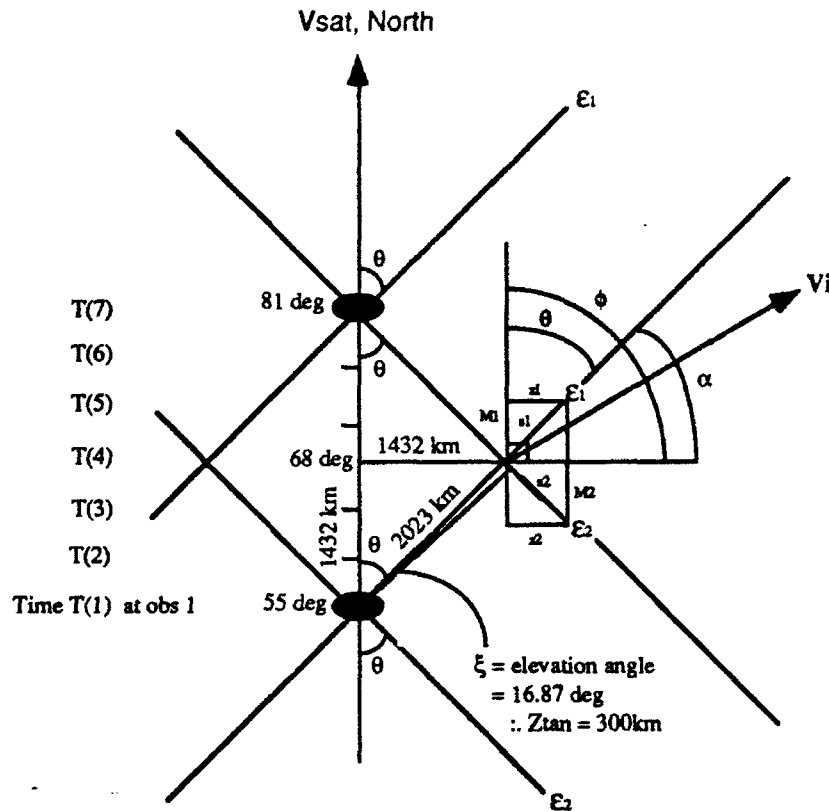


Figure E.4 Illustration of the method used to combine common-volume line-of-sight drifts to produce ion drift vectors. The vector ion drift velocity ( $V_i$ ) is the result of measurements taken by a backward looking FPI at time T(7) when the satellite is at  $81^\circ$  latitude and a forward looking FPI at T(1) when the satellite is at  $55^\circ$  latitude. See text for discussion.

#### E.4 CONVEX Telemetry Using Spherical Geometry

The calculations done previously have been accurate in the satellite's reference frame, but have not accounted for the spherical Earth. A simple transformation will convert the off-track distance and the tangent point latitude/longitude distance so one will know exactly where on Earth the FPI observation was taken. The following table illustrates a sample set of CONVEX telemetry points.

Glat (deg)	Observation Point (Glat)	Polar Distance (km)	Actual Observation (Glat/Glon)
24.5, 50.5	37.5	5775	35.9, 13.9
29.5, 55.5	42.5	5225	40.8, 15.3
34.5, 60.5	47.5	4675	45.6, 17.0
39.5, 65.5	52.5	4125	50.3, 19.1
44.5, 70.5	57.5	3575	55.0, 21.8
49.5, 75.5	62.5	3025	60.4, 25.3
54.5, 80.5	67.5	2475	64.0, 30.0
59.5, 85.5	72.5	1925	68.2, 36.6
64.5, 89.5	77.5	1375	72.0, 46.1
69.5, 84.5	82.5	825	75.0, 60.0
74.5, 79.5	87.5	275	76.8, 79.1

Table E.1 Sample CONVEX telemetry table used in Chapter 6 calculations.

In Table E.1, assume a  $16.87^\circ$  elevation angle; therefore, the FPI is sensing  $\sim 13^\circ$  (1432km) off-track. The first column represents the position of the satellite in geographical latitude. Take the first row of the first column. In this case, the satellite is either at  $24.5^\circ$  or  $50^\circ$  latitude and is looking in the forward or backward direction respectively. The second column represents the flat-Earth tangent point latitude ( $13^\circ$  away). For simplicity, assume the satellite is travelling directly up the Greenwich Meridian. Hence, if the satellite is at  $24.5^\circ$  latitude (first column, first row) and is looking forward, the tangent point latitude is  $37.5^\circ$  (column 2). Similarly, if the satellite is at  $50.5^\circ$  (first column, second row) and is looking backward, the tangent point latitude is also  $37.5^\circ$ . The third column represents the distance (d) from the observation latitude ( $37.5^\circ$  in this example) to the pole and is given by:



$$\text{distance(km)} = (90^\circ - 37.5^\circ) \times 110 \frac{\text{km}}{\text{deg}} = 5775 \text{km} \quad \text{E.18}$$

Hence, the geographic longitude of the observation point is:

$$\text{longitude} = \arctan \left\{ \frac{\text{off-track}}{\text{distance}} \right\} = \arctan \left\{ \frac{1432 \text{km}}{5775 \text{km}} \right\} = 13.9^\circ \quad \text{E.19}$$

This is the value seen as the last number in the fourth column/first row. Of course, this value can also be  $-13.9^\circ$  since there is an FPI observing on the other side of the satellite as well. The geographic latitude of the observation point is determined by the following method:

$$\text{latitude} = 90^\circ - (\text{co-glat}) \quad \text{E.20}$$

where co-glat (co-latitude) is given by:

$$\text{co-glat} = \left\{ \sin 90^\circ * \left( \frac{13^\circ}{\sin(\text{longitude})} \right) \right\} = \left\{ \frac{13^\circ}{\sin(13.9^\circ)} \right\} \approx 54.1^\circ \quad \text{E.21}$$

Hence, the geographic latitude is:

$$\therefore \text{latitude} = 90^\circ - 54.1^\circ \approx 35.9^\circ \quad \text{E.22}$$

It is this value that is the first number in the fourth column/first row. Similarly, all other numbers in Table E.1 can be determined. Thus, in the case of the forward looking FPI when the satellite is at  $24.5^\circ$  latitude,  $0^\circ$  longitude, or in the case of the backward looking FPI when the satellite is at  $50.5^\circ$  latitude,  $0^\circ$  longitude, the common volume sampling point is at  $35.9^\circ$  latitude, and  $\pm 13.9^\circ$  longitude. An illustration of this follows in Figure E.5.

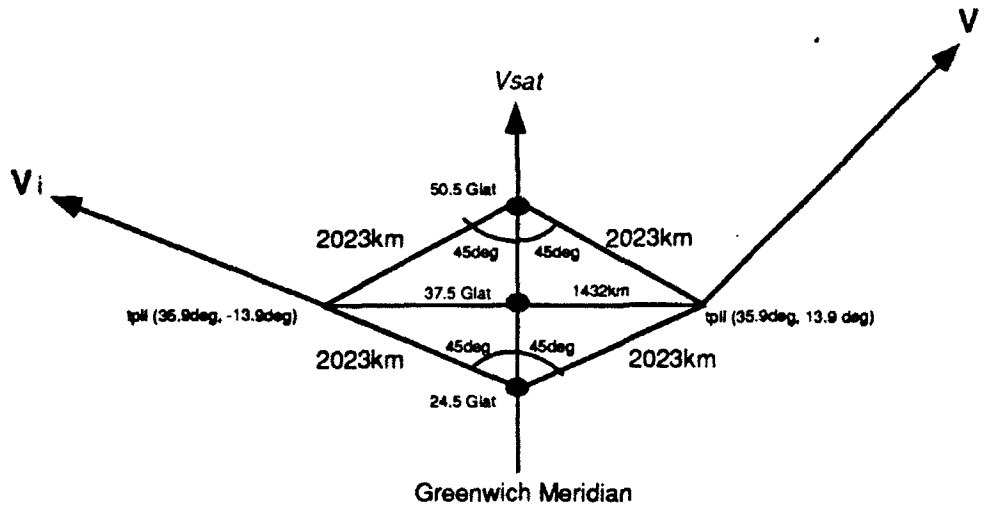


Figure E.5 Assume the CONVEX is moving directly up the Greenwich Meridian. When it is at the point labelled  $24.5^\circ$  geographic latitude, its forward looking FPIs will be sensing locations in the ionosphere that are at  $35.9^\circ$  latitude and  $\pm 13.9^\circ$  longitude. Similarly, when the CONVEX is positioned at  $50.5^\circ$  geographic latitude, the backward looking FPIs will be sensing the identical regions. Combining the line-of-sight measurements allow one to determine the ion drift velocity vector (shown as  $V_d$  in the diagram) at  $\sim 13^\circ$  ( $1432\text{km}$ ) off-track in this case.

Since the telemetry tables have been determined, I know the exact position of each CONVEX FPI measurement. I run the Simulator for the desired conditions at the known geographical position of the FPI measurement. The output (simulated) meridional and zonal drifts are combined into ion drift vectors and plotted on the polar dials as seen in Chapter 6.

## Appendix F

### CONVEX Simulation Software

Running the CONVEX simulation software is time consuming because of the many models used to prepare the plots seen in Chapter 6. MSIS, IRI, VSH, the Photoelectron Code, the Solar Flux Model, the 7320Å Volume Emission Rate Model and the DE-2 FPI Simulator are the dominant models called. Simply put, the user inputs the date, UT, geophysical conditions (Ap, F10.7 and F10.7A) and the desired telemetry table (table of tangent point latitudes and longitudes) into the CONVEX Simulation Machinery (SM). SM uses this information to call VSH and the 7320Å volume emission rate models, which in turn make their model-calls. After making calculations every 1 km along the CONVEX line-of-sight, the VSH call passes meridional and zonal ion drifts back to SM while 7320Å volume emission rates are returned to SM from the 7320Å aurora-airglow model. These values are combined and run through the CONVEX FPI (7320Å) Simulator (same as the DE-2 Simulator, but a CCD is simulated instead of the DE-2 IPD). The CONVEX Simulator then produces a CONVEXN.DAT or CONVEXS.DAT datafile (N is north and S is south) which consist of meridional and zonal ion drifts at the desired tangent point latitude and longitude. Data in the north datafile are data simulated for the right (starboard) side of the satellite, while data in the south datafile come from the port side. Once one set of LOS drifts has been simulated, SM loops back to the next point in the telemetry table. This procedure is done up to 98 times (in the case of retrieving three swaths on either side on CONVEX) and is extremely CPU-intensive. Three telemetry tables currently exist for quiet conditions (Day: 180; UT: 15, 18, or 22; Ap: 10; F10.7/A: 140). Once the

datafiles are created, two IDL routines properly format the simulated zonal and meridional drifts. MERGE merges the port and starboard datafiles into one and, assuming a high-latitude magnetic field of 0.5G (Kelly, 1989), determines the simulated electric field components from the simulated ion drift components. ADDLINE massages the MERGE datafile by simply putting it into the proper format for the final program, SWATHPS. This IDL routine combines the components into ion drift vectors (or electric field vectors if so desired) and produces the plots seen in Chapter 6. Figure F.1 illustrates the SM flow.

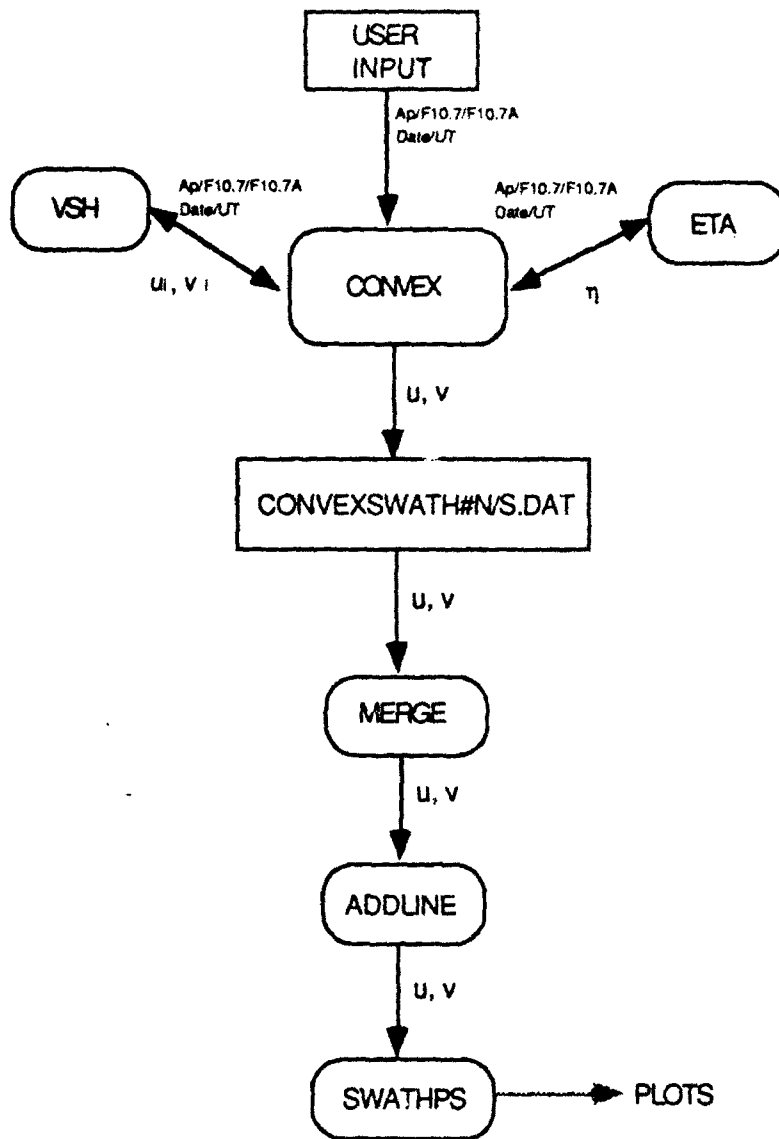


Figure F.1 CONVEX Flow. The user is queried for Ap, F10.7, F10.7A, date, UT. CONVEX flies at 600km; this value is hardwired into the code but can easily be changed. The input UT specifies which one of the three telemetry tables will be used. VSH and the 7320Å aurora-airglow model, acting as the real atmosphere, feed the CONVEX machinery the desired values of ion drifts (meridional and zonal) and volume emission rates. The CONVEX code then outputs one swath of simulated zonal and meridional ion drifts at 13° off-track. This procedure is then repeated for the swath on the opposite side of CONVEX. If one wants swaths at, for example, 11 and 15° off-track (as seen in Figure 6.15), one can change the mirror position interactively, allowing the FPI to sense at varying distances from the satellite. The programs MERGE, ADDLINE and SAWTHPS are IDL routines that simply format the data and plot them.

## REFERENCES

## REFERENCES

- Abreu, V.J., W.R. Skinner, P.B. Hays, 'Airglow Measurements of the Variation of the  $O^+(2P)$  Ionization Frequency During Solar Cycle 21', *Geophys. Res. Lettrs.*, **7**, 109, 1980.
- Abreu, V.J., J.H. Yee, P.B. Hays, 'Galactic and Zodiacal Light Surface Brightness Measurements with the Atmosphere Explorer Satellites', *Applied Optics*, **21**, 2287, 1982.
- Abreu, V.J. and W.B. Skinner, 'Inversion of Fabry-Perot CCD Images: Use in Doppler Shift Measurements', *Appl. Opt.*, **28**, 3382, 1989.
- Aller, L.H. and M.L. White, 'Forbidden lines of ionized nitrogen in the planetary nebulae', *Astrophys. J.*, **54**, 181, 1949.
- Akasofu, S.-I., 'What Causes the Aurora', *EOS, Trans., AGU*, **73**, 12 May 1992.
- Baker, D.N., G. Chin, R.F. Pfaff, 'NASA's Small Explorer Program', *Physics Today*, **44**, December 1991.
- Banks, P.M., 'Collision Frequencies and Energy Transfer: Electrons', *Planet. Space Sci.*, **14**, 1085, 1966.
- Banks, P.M., A.F. Nagy, 'Concerning the Influence of Elastic Scattering Upon Photoelectron Transport and Escape', *J. Geophys. Res.*, **75**, 1902, 1970.
- Banks, P.M., C.R. Chappell and A.F. Nagy, 'A New Model for the Interaction of Auroral Electrons with the Atmosphere: Spectral Degradation, Backscatter, Optical Emission and Ionization', *J. Geophys. Res.*, **79**, 1459, 1974.
- Basu, B., J.R. Jasperse, R.M. Robinson, R.R. Vondrak, D.S. Evans, 'Linear Transport Theory of Auroral Proton Precipitation: a Comparison with Observations', *J. Geophys. Res.*, **92**, 5920, 1987.
- Bates, D.R. and A. Dalgarno, 'Theoretical Considerations Regarding the Dayglow', *J. Atm. Terr. Phys.*, **5**, 329, 1954.
- Bates, D.R., 'Some Problems Concerning the Terrestrial Atmosphere Above the 100km Level', *Proc. Roy. Soc., Ser. A*, **253**, 451, 1959.
- Bates, D.R., 'Forbidden Oxygen and Nitrogen Lines in the Nightglow', *Planet. Space Sci.*, **26**, 897, 1978.

- Batten, S., D. Rees, D. Wade, 'Observations of Thermospheric Neutral Winds by the UCL Doppler Imaging System at Kiruna in Northern Scandinavia', **J. Atmos. Terr. Phys.**, **50**, 861, 1988.
- Bass, A.M. and D. Garvin, 'Analysis of the hydroxyl radical vibration-rotation spectrum between 3900Å and 11500Å', **J. Molec. Spectrosc.**, **9**, 114, 1962.
- Berthelier, A., M. Menvielle, 'The K-Derived Planetary Indices: Description and Availability', **Reviews of Geophysics**, **29**, 415, 1991.
- Biondi, M.A., J.W. Meriwether, B.G. Fejer, R. Woodman, 'Measurements of the Dynamics and Coupling of the Equatorial Thermosphere and the F-Region Ionosphere in Peru', **J. Atmos. Terr. Phys.**, **50**, 937, 1988.
- Bilitza, D., 'Improved Analytical Representation of Electron Temperature in the IRI', **Adv. Space Res.**, **4**(1), 93, 1984.
- Bilitza, D., 'International Reference Ionosphere: Recent Developments', **Radio Sci.**, **21**, 343, 1986.
- Bilitza, D., K. Rawer, 'New Options for IRI Electron Density in the Middle Ionosphere', **Adv. Space Res.**, **10** (11), 7, 1990.
- Bilitza, D., 'International Reference Ionosphere 1990', **NSSDC/WDC-A-R&S 90-22**, Goddard Space Flight Center, Greenbelt, MD, 1990a.
- Bilitza, D., 'Empirical Modeling of Ion Composition in the Middle and Topside Ionosphere', **Adv. Space Res.**, **10** (11), 47, 1990b.
- Bilitza, D., 'International Reference Ionosphere 1990', **COSPAR**, 1990.
- Berger, M.J., S.M. Seltzer, K. Maesa, 'Energy Deposition by Auroral Electrons in the Atmosphere', **J. Atmos. Terr. Phys.**, **32**, 1015, 1970.
- Bird, G.A., 'Aerodynamic Effects on Atmospheric Composition Measurements from Rocket Vehicles in the Thermosphere', **Planet. Space Sci.**, **Vol 36**, 921, 1988.
- Bittencourt, J. A., 'Fundamentals of Plasma Physics', **Pergamon Press**, 1986.
- Booker, H.G., 'Fitting of Multi-region Ionospheric Profiles of Electron Density by a Single Analytic Function of Height', **J. Atmos. Terr. Phys.**, **39**, 619, 1977.
- Born, M., E. Wolf, 'Principles of Optics', Sixth (Corrected) Edition, **Pergamon Press**, 1980.



- Bowen, I.S., 'The Origin of the nebulae lines and the structure of the planetary nebulae', **Astrophys. J.**, **67**, 1, 1928.
- Bowen, I.S., 'The spectrum and composition of the gaseous nebulae', **Astrophys. J.**, **81**, 1, 1935.
- Bowen, I.S., 'Wavelengths of forbidden nebulae lines', **Astrophys. J.**, **121**, 306, 1955.
- Brown, L.D., R.E. Daniell, M.W. Fox, J.A. Klobuchar, P.H. Doherty, 'Evaluation of Six Ionospheric Models as Predictors of Total Electron Content', **Radio Science**, **26**, 1007, 1991.
- Buonsanto, M., J.E. Salah, K.L. Miller, W.O. Oliver, R.G. Burnside, P.G. Richards, 'Observations of Neutral Circulation at Mid-latitudes during the Equinox Transition', **J. Geophys. Res.**, **94**, 16987, 1989.
- Burnett, T. and S.P. Roundtree, 'Differential and total cross-sections for electron-impact ionization of atomic oxygen', **Phys. Rev.**, **A20**, 1468, 1979.
- Burch, J.L., S.A. Fields, R.A. Heelis, 'Polar Cap Electron Acceleration Regions', **J. Geophys. Res.**, **84**, 5863, 1979.
- Burns, A.G., T.L. Killeen, R.G. Roble, 'Processes Responsible for the Compositional Structure of the Thermosphere', **J. Geophys. Res.**, **Vol. 94**, 3670, 1989.
- Burnside, R.G., C.A. Tepley, V.B. Wickwar, 'The O<sup>+</sup>-O Collision Cross Section-Can It Be Inferred From Aeronomical Measurements?' **Ann. Geophys.**, **5A**, 343, 1987.
- Carlson, R.W., K. Suzuki, 'Observation of O<sup>+</sup>(2P<sup>o</sup> - 2D<sup>o</sup>) $\lambda$ 7319Å in the Twilight and Night Airglow', **Nature**, **24S**, 400, 1974.
- Cannata, R.W., 'Thermal Ion Upwelling in the High-Latitude Ionosphere', **University of Michigan PhD Dissertation**, 1990.
- Carovillano, R.L., J.M. Forbes, 'Solar-Terrestrial Physics', **D. Reidel Publishing**, 1983.
- Carr, S.S., T.L. Killeen, 'Remote-Sensing Observations of F-Region Ion Drift Velocities Using Dynamics Explorer-2 Measurements of the O<sup>+</sup>(2P)  $\lambda$ 732.0 nm Emission', **Geophys. Res. Ltrs.**, **19**, 1455, 1992.
- Carr, S.S., 'On the Possible Anticorrelation of Noctilucent Clouds and Aurorae', **Masters Thesis**, The Pennsylvania State University, 1986.

- Chahine, Moustafa, 'Inverse Problems in Radiative Transfer: Determination of Atmospheric Parameters', **J. Atmos. Sci.**, **27**, 960, 1970.
- Chamberlain, J.W., 'Physics of the aurora and airglow', **Academic Press**, 1961.
- Chandrasekhar, S. 'Radiative Transfer', 393 pp, Dover Publications, New York, 1960.
- Chapman, S., 'The Electric Conductivity of the Ionosphere: A Review', **Nuovo Cimento**, **5**, Suppl., 1285, 1956.
- Cogger, L.L., G.G. Shepherd, M.M. Gogoshev, T.P. Dachev, M.G. Gerdjikova, 'Satellite Observations of OII (7320-7330Å) Emission in Aurora', **Planet. Space Sci.**, **35**, 845, 1987.
- Cogger, L.L., J.C.G. Walker, J.W. Meriwether, R.G. Burnside, 'F Region Airglow: Are the Ground-Based Observations Consistent with Recent Satellite Results?', **J. Geophys. Res.**, **85**, 3013, 1980.
- Copeland, R.A., T.G. Slinger, "Status of the OH contribution to the Surface Glow Detected from the Dynamics Explorer Satellite", **Geophys. Res. Ltrs.**, **17**, 2341, 1990.
- Crowley, G., 'Dynamics of the Earth's Thermosphere: A Review' in **Solar-Planetary Relationships, US National Report (1987-1990) to International Union of Geodesy and Geophysics**, 1143, 1991.
- Dalgarno, A., M.B. McElroy, 'Twilight Effects of Solar Ionizing Radiation', **Planet. Space Sci.**, **14**, 1321, 1966.
- Dalgarno, A and M.B. McElroy, 'Twilight Effects of Solar Ionizing Radiation', **Planet. Space Sci.**, **13**, 947, 1965.
- Deehr, C.S., G.G. Sivjee, A. Egeland, K. Henriksen, P.E. Sandholt, R. Smith, P. Sweeney, C. Duncan, J. Gilmer, 'Ground-based Observations of F Region Aurora Associated With the Magnetospheric Cusp', **J. Geophys. Res.** **85**, 2185, 1980.
- Deng, W., T.L. Killeen, A.G. Burns, R.G. Roble, 'The Flywheel Effect: Ionospheric Currents After A Geomagnetic Storm', **Geophys. Res. Ltrs.**, **in press**.
- Doering, J.P. and E. E. Gulcicek, 'Absolute Differential and Integral Electron Excitation Cross-sections for Atomic Oxygen, 7. The  $^3P-^1D$  Transitions from 4.0 to 30 eV', **J. Geophys. Res.**, **94**, 1541, 89.

- Dusenbery, P.B., G.L. Siscoe, 'Geospace Modeling Environment Program', **EOS, Trans., AGU**, 73, 3, 18 Feb 1992.
- Elgin, J.B., D.C. Cooke, M.F. Tautz, E. Murad, 'Modeling of Atmospherically Induced Gas Phase Optical Contamination from Orbiting Spacecraft', **J. Geophys. Res.**, 95, 12197, 1990a.
- Elgin, J.B., D.C. Cooke, M.F. Tautz, E. Murad, 'Correction to "Modeling of Atmospherically Induced Gas Phase Optical Contamination from Orbiting Spacecraft"', **J. Geophys. Res.**, 95, 15289, 1990b.
- Evans, J.V., 'Ionospheric Movements Measured by Incoherent Scatter Radar: a Review', **J. Atmos. Terr. Phys.**, 34, 175, 1972.
- Feldman, P.D. and P.Z. Takacs, 'Twilight Observation of the Forbidden  $O^+(^2P-^4S)$  Transition at 2470Å', **J. Geophys. Res.**, 81, 260, 1976.
- Fennelly, J.A., D.G. Torr, P.G. Richards, M.R. Torr, W.E. Sharp, 'A Method for the Retrieval of Atomic Oxygen Density and Temperature Profiles from Ground-based Measurements of the  $O^+(^2D-^2P)$  7320-Å Twilight Airglow', **J. Geophys. Res.**, 96, 1263, 1991.
- Flesch, G.D., C.Y. Ng, 'Absolute State-Selected Total Cross Sections for the  $O^+(^2D, ^2P) + N_2$  Reactions', **J. Geophys. Res.**, 96, 21407.
- Frank, L.A., J.D. Craven, 'Imaging Results from the Dynamics Explorer Mission', **Rev. Geophys.**, 26, 249, 1988.
- Fox, J.L., 'Cross Sections and Reaction Rates of Relevance to Aeronomy', in **Solar-Planetary Relationships, US National Report (1987-1990) to International Union of Geodesy and Geophysics**, 1110, 1991.
- Gentieu, E.P., P.D. Feldman, R.W. Eastes and A.B. Christensen, 'Spectroscopy of the Extreme Ultraviolet Dayglow During Active Solar Conditions', **Geophys. Res. Ltrs.**, 8, 1242, 1981.
- Gaffey, J.D., C.S. Wu, 'Distribution Function of Continuously Created Newborn and Pickup Ions in Outer Cometary Exospheres', **J. Geophys. Res.**, 94, 8685, 1989.
- Gaffey, J.D., D. Winske, C.S. Wu, 'Time Scales for Formation and Spreading of Velocity Shells of Pickup Ions in the Solar Wind', **J. Geophys. Res.**, 93, 5470, 1988.
- Hagan, M.E., D.P. Sipler, 'Combined Incoherent Scatter Radar and Fabry-Perot Interferometer Measurements of Frictional Heating Effects Over Millstone Hill During March 7-10, 1989', **Journal of Geophysical Research**, 96, 289, 1991.

- Hanson, W.B., R.A. Heelis, R.A. Power, C.R. Lippincott, D.R. Zuccaro, B.J. Holt, L.H. Harmon, S. Sanatani, 'The Retarding Potential Analyzer for Dynamics Explorer-B', **Space Sci. Instr.**, **5**, 503, 1981.
- Hardy, D.A., W.J. Burke, M.S. Gussenhoven, 'DMSP Optical and Electron Measurements in the Vicinity of Polar Cap Arcs', **J. Geophys. Res.**, **87**, 2413, 1982.
- Hargreaves, J.K., 'The Upper Atmosphere and Solar-Terrestrial Relations', **Van Nostrand Reinhold**, 1979.
- Hays, P.B., 'CLIO, A New Concept In Interferometry', **EOS Trans. AGU**, **71**, 1483, 1990.
- Hays, P.B., V. J. Abreu, S.C. Solomon and J. Yee, 'The Visible Airglow. Experiment - a Review', **Planet. Space Sci.**, **36**, 21, 1988.
- Hays, P.B., T.L. Killeen, N.W. Spencer, L.E. Wharton, R.G. Roble, B.A. Emery, T.J. Fuller-Rowell, D. Rees, L.A. Frank, J. D. Craven, 'Observations of the Dynamics of the Polar Thermosphere', **J. Geophys. Res.**, **89**, 5597, 1984.
- Hays, P.B., T.L. Killeen and B.C. Kennedy, 'The Fabry-Perot Interferometer on Dynamics Explorer', **Space Sci. Instr.**, **5**, 395, 1981.
- Hays, P.B., R.G. Roble, 'A Technique for Recovering Doppler Line Profiles from Fabry-Perot Interferometer Fringes of Very Low Intensity', **Applied Optics**, **10**, 193, 1971.
- Hecht, J.H., A.B. Christensen, D.J. Strickland, R.R. Meier, 'Deducing Composition and Incident Electron Spectra From Ground-Based Auroral Optical Measurements: Variations in Oxygen Density', **J. Geophys. Res.**, **94**, 13553, 1989.
- Hecht, J.H., D.J. Strickland, A.B. Christensen, D.C. Kayser, R.L. Walterscheid, 'Lower Thermospheric Composition Changes Derived From Optical and Radar Data Taken At Søndre Strømfjord During the Great Magnetic Storm of February, 1986', **J. Geophys. Res.**, in press, 1991.
- Hedin, A.E., 'A Revised Thermospheric Model Based on Mass Spectrometer and Incoherent Scatter Data: MSIS-83', **J. Geophys. Res.**, **88**, 188, 1983.
- Hedin, A.E., 'MSIS-86 Thermospheric Model', **J. Geophys. Res.**, **92**, 4649, 1987.

- Hedin, A.E., N.W.Spencer, T.L.Killeen, 'Empirical Global Model of Upper Atmosphere Winds Based on Atmosphere and Dynamics Explorer Satellite Data', **J. Geophys. Res.**, **93**, 9959, 1988.
- Hedin, A.E., 'Atomic Oxygen Modeling in the Upper Thermosphere', **Planet. Space Sci.**, Vol **36**, 907, 1988.
- Heelis, R. A., J. K. Lowell, and R. W. Spiro, A model of the high-latitude ionospheric convection pattern, **J. Geophys. Res.**, **87**, 6339-6345, 1982.
- Heelis, R. A., P. H. Reiff, J. D. Winningham, and W. B. Hanson, Ionospheric convection signatures observed by DE 2 during northward interplanetary magnetic field, **J. Geophys. Res.**, **91**, 5817-5830, 1986.
- Henry, R.J., P.G. Burke and A-L. Sinfailam, 'Scattering of Electrons by C, N, O, N<sup>+</sup>, O<sup>+</sup> and O<sup>++</sup>', **Phys. Rev**, **178**, 218, 1969.
- Henry, R.J., 'Photoionization Cross-section for Atoms and Ions of Argon, Nitrogen, Oxygen and Neon', **Astrophys. J.**, **161**, 1153, 1970.
- Hernandez, 'Fabry-Perot Interferometers', in **Cambridge Studies in Modern Optics**, Editors: P.L. Knight, S. D. Smith, Cambridge University Press, 1986.
- Hernandez, G., T.L. Killeen, 'Optical Measurements of Winds and Kinetic Temperatures in the Upper Atmosphere', **Adv. Space Res.**, **8**, 149, 1988.
- Hernandez, G., 'Measurement of Thermospheric Temperatures and Winds by Remote Fabry-Perot Spectrometry', **Optical Eng.**, **19**, 518, 1980.
- Herzberg, G., 'Atomic Spectra and Atomic Structure', Dover, 1944.
- Higley, S., Lectures from 'Solar Forecaster Course', AFGWC, OAFB, NE, 1986.
- Hinterregger, H.E., K. Fukui, B.R. Gilson, 'Observational, Reference and Model Data on Solar EUV, From Measurements on AE-E', **Geophys. Res. Ltrrs.**, **8**, 1147, 1981.
- Hoffman, R.A., 'Dynamics Explorer', **Space Sci. Instr.**, **5**, 503, 1981.
- Hunten, D.M. and M.B. McElroy, 'Quenching of Metastable States of Atomic and Molecular Oxygen and Nitrogen, **Rev. Geophys. Space Phys.**, **4**, 303, 1966.
- Isenberg, P.A., 'Evolution of Interstellar Pickup Ions in the Solar Wind', **J. Geophys. Res.**, **92**, 1067, 1987.

- Ismail, D., D.D. Wallis, L.L. Cogger, 'Characteristics of Polar Cap Sun-aligned Arcs', **J. Geophys. Res.**, **82**, 4741, 1977.
- Israelevich, P.L., A.K.Kuzmin, N.S.Nikolaeva, 'Observations of the Intensive OII(2P) Emission in the Polar Cap', **Planet. Space Sci.**, **38**, 1367.
- Jacchia, L.G., 'Thermospheric Temperature, Density and Composition: New Models', **Spec. Rep.**, **375**, Smithsonian Astrophys. Observ., Cambridge, MA, 1977.
- Jacchia, L.G., C.I.R.A., **Smithson. Contrib. Astrphys.**, **8**, 215, 1965.
- Johnson, R.M., 'Lower-Thermospheric Neutral Winds at High Latitude Determined From Incoherent Scatter Measurements: a Review of Techniques and Observations', **Adv. Space Res.**, **10**, 261, 1990.
- Jursa, A.S., 'Handbook of Geophysics and the Space Environment', **Air Force Geophysics Laboratory**, 1985.
- Kayser, D.C., 'Measurements of Thermospheric Meridional Wind from the S85-1 Spacecraft', **J. Geophys. Res.**, **93**, 9979, 1988.
- Kelley, M.C., 'The Earth's Ionosphere', **Academic Press, Inc.**, 1989.
- Killeen, T.L., F.G. McCormac, A.G.Burns, J.P.Thayer, R.M.Johnson, R.J.Niciejewski, 'On the Dynamics and Composition of the High-Latitude Thermosphere', **J. Atmos. Terr. Phys.**, **53**, 797, 1991
- Killeen, T.L. and R.G. Roble, 'Thermosphere Dynamics: Contributions from the First Five Years of the Dynamics Explorer Program', **Reviews of Geophysics**, **26**, 329, 1988.
- Killeen, T.L., 'Energetics and Dynamics of the Earth's Thermosphere', **Reviews of Geophysics**, **25**, 433, 1987.
- Killeen, T. L. and R. G. Roble, Thermosphere Dynamics driven by magnetospheric sources: contributions from the first five years of the Dynamics Explorer program, **Rev. Geophys. Space Phys.**, **26**, 329-367, 1988.
- Killeen, T. L., P. B. Hays, B. C. Kennedy and D. Rees, A stable and rugged etalon or the Dynamics Explorer Fabry-Perot interferometer: II Performance of the etalon, **Appl. Optics**, **21**, 3903, 1982a.
- Killeen, T. L., B. C. Kennedy, P. B. Hays, D. A. Symanow, and D. H. Ceckowski, An Image Plane Detector for the Dynamics Explorer Fabry-Perot interferometer, **Appl. Optics**, **22**, 3503, 1983.

- Killeen, T.L. and R.G. Roble, 'An Analysis of the High Latitude Thermospheric Wind Pattern Calculated by a Thermospheric General Circulation Model 1. Momentum Forcing', **J. Geophys. Res.**, **89**, 7509, 1984.
- Killeen, T.L., P.B. Hays, G.R. Carignan, R.A. Heelis, W.B. Hanson, N.W. Spencer and L.H. Brace, 'Ion-neutral Coupling in the High-latitude F Region: Evaluation of Ion Heating Terms From Dynamics Explorer 2', **J. Geophys. Res.**, **89**, 7495, 1984.
- Killeen, T.L., R.W. Smith, P.B. Hays, N.W. Spencer, L.E. Wharton and F.G. McCormac, 'Neutral Winds in the High Latitude Winter F Region: Coordinated Observations from Ground and Space', **Geophys. Res. Ltrs.**, **11**, 311, 1984.
- Killeen, T.L. and P.B. Hays, 'Doppler Line Profile Analysis for a Multichannel Fabry-Perot Interferometer', **Applied Optics**, **23**, 612, 1984.
- Killeen, T.L. and P.B. Hays, 'O(<sup>1</sup>S) From Dissociative Recombination of O<sub>2</sub><sup>+</sup>: Nonthermal Line Profile Measurements From Dynamics Explorer', **J. Geophys. Res.**, **88**, 10163, 1983.
- Killeen, T.L., P.B. Hays, N.W. Spencer, L.E. Wharton, 'Neutral Winds in the Polar Thermosphere as Measured From Dynamics Explorer', **Geophys. Res. Ltrs.**, 957, 1982.
- Killeen, T.L., R.G. Roble, N.W. Spencer, 'A Computer Model of Global Thermospheric Winds and Temperatures', **Adv. Space Res.**, **7**, 207, 1987.
- Krassovsky, V.I., 'Hydroxyl Emission in the Upper Atmosphere', **Planet. Space Sci.**, **10**, 7, 1963.
- Link, R., 'Feautrier Solution of the Electron Transport Equation', **J. Geophys. Res.**, in press, 1991.
- Link, R., S. Chakrabarti, G.R. Gladstone, J.C. McConnell, 'An Analysis of Satellite Observations of the OI EUV Dayglow', **J. Geophys. Res.**, **93**, 2693, 1988.
- Link, R., G.R. Gladstone, S. Chakrabarti, J.C. McConnell, 'A Reanalysis of Rocket Measurements of the Ultraviolet Dayglow', **J. Geophys. Res.**, **93**, 14631, 1988.
- Lui, A.T.Y., 'Magnetotail Physics', **The Johns Hopkins University Press**, 1987.

- Lummerzheim, D., M.H. Rees, H.R. Anderson, 'Angular Dependent Transport of Auroral Electrons in the Upper Atmosphere', **Planet. Space Sci.**, **37**, 109, 1989.
- Lummerzheim, D., M.H. Rees, J.D. Craven, L.A. Frank, 'Ionospheric Conductances Derived From DE1 Auroral Images', **J. Atmos. Terr. Phys.**, in press, 1991.
- Lummerzheim, D., M.H. Rees, G.J. Romick, 'The Application of Spectroscopic Studies of the Aurora to Thermospheric Neutral Composition', **Planet. Space Sci.**, **38**, 67, 1990.
- Lummerzheim, D., 'Electron Transport and Optical Emissions in the Aurora', **PhD Dissertation**, University of Alaska, 1987.
- McCormac, F.G., 'An Optical Investigation of Ion and Neutral Motions in the Polar Thermosphere', **PhD Dissertation**, Ulster Polytechnic, 1984.
- McCormac, F.G., T.L. Killeen, J.P. Thayer, 'The Influence of IMF  $B_y$  on the High-Latitude Thermospheric Circulation During Northward IMF', **J. Geophys. Res.**, **96**, 115, 1991.
- McCormac, F.G., T.L. Killeen, A.G. Burns, F.A. Marcos, R.G. Roble, "The Effect of Solar Cycle Variations on the Thermosphere", **Astrodynamics** **1991**, **76**, 2507, 1991.
- McDade, I.C., W.E. Sharp, P.G. Richards, D.G. Torr, 'On the Inversion of  $O^+(^2D-^2P)$  7320Å Twilight Airglow Observations: A Method for Recovering Both the Ionization Frequency and the Thermospheric Oxygen Atom Densities', **J. Geophys. Res.**, **96**, 259, 1991.
- McDade, I.C., E.J. Llewellyn, 'Inversion Techniques for Recovering Two-Dimensional Distributions of Auroral Emission Rates from Tomographic Rocket Photometer Measurements', in press, 1991.
- Mende, S.B., G.R. Swenson, E.J. Llewellyn, W.F. Denig, D.J.F. Kendall, T.G. Slanger, 'Measurements of Rotational Temperature in the Airglow with a Photometric Imaging Etalon Spectrometer', **J. Geophys. Res.**, **93**, 12861, 1988.
- Meng, C-I., M.J. Rycroft, L.A. Frank, 'Auroral Physics', **Cambridge University Press**, 1991.
- Meriwether, J.W., C.A. Tepley, S.A. Price, P.B. Hays and L.L. Cogger, 'Remote Ground-based Observations of Terrestrial Airglow Emissions and Thermospheric Dynamics at Calgary, Alberta, Canada', **Optical Engineering**, **22**, 128, 1983.



- Meriwether, J.W., D.G. Torr, J.C.G. Walker and A.O. Nier, 'The  $O^+(^2P)$  Emission at 7320Å at Twilight', **J. Geophys. Res.**, 83, 3311, 1978.
- Meriwether, J.W., P.B. Hays, K.D. McWatters and A.F. Nagy, 'Interferometric Measurements of the  $\lambda 7319\text{\AA}$  Doublet Emission of OII', **Planet. Space Sci.**, 22, 636, 1974.
- Minow, J.I., R.W. Smith, 'Optical Remote Sensing of the Ion Convection Pattern in the High-Latitude Ionosphere From a Polar Orbiting Satellite', **EOS Abstract, Trans. of the AGU**, 71, 1486, 1990.
- Moffett, R. J., R. Sellek, G.J. Bailey, 'The Influence of O-O<sup>+</sup> Collision Frequency on Ionospheric F-Region Behavior', **J. Atmos. Terr. Phys.**, 52, 125, 1990.
- Morrison, M.D., C.W. Bowers, P.D. Feldman, R.R. Meier, 'The EUV Dayglow at High Spectral Resolution', **J. Geophys. Res.**, 95, 4113, 1990.
- Moses, H.E., 'The Use of Vector Spherical Harmonics in Global Meteorology and Aeronomy', **J. Geophys. Res.**, Vol. 31, 1490, 1974.
- Nagy, A.F. and P.M. Banks, 'Photoelectron Fluxes in the Ionosphere', **J. Geophys. Res.**, 75, 6260, 1970.
- Nardi, B., 'An Inversion Technique to Recover Lower Thermospheric Winds From Space-Borne Remote Measurements of [OI] 5577Å, PhD Dissertation, The University of Michigan, 1991.
- Niciejewski, R.J., J.W. Meriwether, F.G. McCormac, J.H. Hecht, A.B. Christensen, G.G. Sivjee, D. J. Strickland, G. Swenson, S.B. Mende, A. Vallance Jones, R.L. Gattinger, H.C. Carlson, C. E. Valladares, 'Coordinated Satellite and Ground-Based Measurements of the Energy Characteristics of a Sun-aligned Arc Over Søndre Strømfjord', **J. Geophys. Res.**, 94, 17201, 1989.
- Noxon, J.F. and R.B. Norton, 'Changes in Thermospheric Composition Inferred from Twilight  $O^+(^2P)$  Emissions', **Planet. Space Sci.**, 27, 653, 1979.
- Omholt, A., 'The Red and Near-infrared Auroral Spectrum', **J. Atmos. Terr. Phys.**, 10, 320, 1957.
- Porter, H.S., F. Varosi, H.G. Mayr, 'Iterative Solution of the Multistream Electron Transport Equation, 1, Comparison With Laboratory Beam Injection Experiments', **J. Geophys. Res.**, 92, 5933, 1987.
- Press, W.H., B.P. Flannery, S.A. Teukolsky, W.T. Vetterling, 'Numerical Recipes', Cambridge University Press, 1989.

- Rees, D., A. Aruliah, T.J. Fuller-Rowell, V.B. Wickwar, R.J. Sica, 'Winds in the Upper Mesosphere at Mid-latitude: First Results Using a Fabry-Perot Interferometer', *Geophys. Res. Lett.*, **17**, 1259, 1990.
- Rees, M.H., D. Lummerzheim, 'Characteristics of Auroral Electron Precipitation Derived from Optical Spectroscopy', *J. Geophys. Res.*, **94**, 6799, 1989.
- Rees, M.H., D. Lummerzheim, R.G. Roble, J.D. Winningham, J.D. Craven, L.A. Frank, 'Auroral Energy Deposition Rate, Characteristic Electron Energy and Ionospheric Parameters Derived From Dynamics Explorer 1 Images', *J. Geophys. Res.*, **93**, 12841, 1988.
- Rees, M.H., V.J. Abreu and P.B. Hays, 'The Production Efficiency of  $O^+(2P)$  by Auroral Electron Impact Ionization', *J. Geophys. Res.*, **87**, 3612, 1982.
- Rees, M.H., 'Auroral Ionization and Excitation by Incident Energetic Electrons', *Planet. Space Sci.*, **11**, 1209, 1963.
- Rees, M.H., V.J. Abreu, 'Auroral Photometry from the Atmospheric Explorer Satellite', *J. Geophys. Res.*, **89**, 317, 1984.
- Rees, M.H., A.I. Stewart, W.E. Sharp, P.B. Hays, R.A. Hoffman, L.H. Brace, J.P. Doering, W.K. Peterson, 'Coordinated Rocket and Satellite Measurements of an Auroral Event, 1. Satellite Observations and Analysis', *J. Geophys. Res.*, **82**, 2250, 1977.
- Rees, D., T.J. Fuller-Rowell, 'Understanding the Transport of Atomic Oxygen within the Thermosphere, Using a Numerical Thermospheric Model', *Planet. Space Sci.*, Vol **36**, 935, 1988.
- Rees, M.H., 'Physics and Chemistry of the Upper Atmosphere', 289 pp, Cambridge University Press, 1989.
- Richards, P.G. and D.G. Torr, 'An Investigation of the Consistency of the Ionospheric Measurements of the Photoelectron Flux and Solar EUV Flux', *J. Geophys. Res.*, **89**, 5625, 1984.
- Richards, P.G. and D.G. Torr, 'Ratios of Photoelectron to EUV Ionization Rates for Aeronomic Studies', *J. Geophys. Res.*, **93**, 4060, 1988.
- Richards, P.G., D.G. Torr, 'Ratios of Photoelectron to EUV Ionization Rates for Aeronomic Studies', *J. Geophys. Res.*, **93**, 4060, 1988.
- Roble, R.G. and T.L. Killeen, 'Modeling the Global Structure of the Thermosphere: Circulation, Temperature and Density', *Astrodynamics*, **65**, 1683, 1987.

- Rodgers, C.D., 'Retrieval of Atmospheric Temperature and Composition From Remote Measurements of Thermal Radiation', **Reviews of Geophysics and Space Physics**, **14**, 609, 1976.
- Rottman, G.J., 'Rocket Measurements of the Solar Spectral Irradiance During Solar Minimum, 1972-1977', **J. Geophys. Res.**, **86**, 6697, 1981.
- Rusch, D.W., D.G. Torr, P.B. Hays and J.C.G. Walker, 'The O II (7319-7330Å) Dayglow', **J. Geophys. Res.**, **82**, 719, 1977.
- Schunk, R.W., J.C.G. Walker, 'Theoretical Ion Densities in the Lower Ionosphere', **Planet. Space Sci.**, **21**, 1875, 1973.
- Schunk, R.W., P.B. Hays, 'Photoelectrons Energy Losses to Thermal Electrons', **Planet. Space Sci.**, **19**, 113, 1971.
- Schunk, R.W., P.B. Hays and Y. Itikawa, 'Energy Losses of Low Energy Photoelectrons to Thermal Electrons', **Planet. Space Sci.**, **19**, 125, 1971.
- Seaton, M.J., 'Electron Impact Ionization of Neon, Oxygen and Nitrogen', **Phys. Rev.**, **113**, 814, 1959.
- Seaton, M.J. and D.E. Osterbrock, 'Relative OII Intensities in Gaseous Nebulae', **Astrophys. J.**, **126**, 66, 1957.
- Sharp, W.E., M.H. Rees and A.I. Stewart, 'Coordinated Rocket and Satellite Measurements of an Auroral Event' 2. The Rocket Observations and Analysis', **J. Geophys. Res.**, **84**, 1977, 1979.
- Shepherd, G.G., M.G. Gerdjikova, 'Thermospheric Atomic Oxygen Concentrations Inferred from the Auroral I(5577)/I(4278) Emission Rate Ratio', **Planet. Space Sci.**, **Vol. 36**, 893, 1988.
- Shyn, T.W., W.E. Sharp, 'Differential Excitation Cross Section of Atomic Oxygen by Electron Impact: ( $3P-1D$  Transition)', **J. Geophys. Res.**, **91**, 1691, 1986.
- Shyn, T.W., S.Y. Cho, W.E. Sharp, 'Differential Excitation Cross Section of Atomic Oxygen by Electron Impact: ( $3P-1S$  Transition)', **J. Geophys. Res.**, **91**, 13751, 1986.
- Skinner, W.R., V.J. Abreu, 'Recovery of Fabry-Perot Fringes From 1-Dimensional CCD Images', **EOS, Trans., AGU**, **71**, 1483, 1990.
- Smith, D., N.G. Adams and T.M. Miller, 'A Laboratory Study of the Reactions of  $N^+$ ,  $N_2^+$ ,  $N_3^+$ ,  $N_4^+$ ,  $O^+$ ,  $O_2^+$  and  $NO^+$  Ions with Several Molecules at 300K', **J. Chem. Phys.**, **69**, 308, 1978.

- Smith, K., R.J.W. Henry and P.G. Burke, 'Calculations on the Scattering of Electrons by Atomic Systems with Configurations  $2p^q$ ', **Physical Review**, **157**, 51, 1967.
- Smith, R.W., G.G. Sivjee, R.D. Stewart, F.G. McCormac, C. S. Deehr, 'Polar Cusp Ion Drift Studies Through High-Resolution Interferometry of  $O^+$  7320-Å Emission', **J. Geophys. Res.**, **87**, 4455, 1982.
- Smith, R.W., K.J. Winser, A.P. Van Eyken, S. Quegan, B.T. Allen, 'Observation and Theoretical Modelling of a region of downward field-aligned flow of  $O^+$  in the winter dayside polar cap', **J. Atm. Terr. Phys.**, **47**, 489, 1985.
- Sojka, J.J., R.W. Schunk, 'Problems with Deducing Ionospheric Plasma Convection Patterns', **J. Geophys. Res.**, **91**, 259, 1986.
- Solomon, S.C., 'Optical Aeronomy' in **Solar-Planetary Relationships, US National Report (1987-1990) to International Union of Geodesy and Geophysics**, 1089, 1991.
- Solomon, S.C., P.B. Hays and V.J. Abreu, 'The Auroral 6300Å Emission: Observations and Modelling', **J. Geophys. Res.**, **93**, 9867, 1988.
- Solomon, S.C., 'Tomographic Inversion of Auroral Emissions', PhD Thesis, University of Michigan, Ann Arbor, MI, 1987.
- St.-Maurice, J. -P, R.W. Schunk, 'Ion Velocity Distributions in the High Latitude Ionosphere', **Rev. Geophysics and Space Physics**, **17**, 99, 1979.
- Strickland, D.J., R.R. Meier, J.H. Hecht, A.B. Christensen, 'Deducing Composition and Incident Electron Spectra from Ground-Based Auroral Optical Measurements: Theory and Model Results', **J. Geophys. Res.**, **94**, 13527, 1989.
- Swenson, G.R., 'A Study of Sector Spectrophotometer and Auroral  $O^+(2P-2D)$  Emissions', PhD Thesis, University of Michigan Ann Arbor, 1976.
- Swift, W.R., D.G. Torr, C. Hamilton, H. Dougani, P.G. Richards, G.G. Sivjee, 'A Procedure for the Extraction of Airglow Features in the Presence of Strong Background Radiation', **J. Geophys. Res.**, **95**, 15227, 1990.
- Thayer, J.P., 'Neutral Wind Vortices in the High-Latitude Thermosphere', **University of Michigan PhD Dissertation**, 1990.

- Thomas, L.D. and R.K. Nesbet, 'Low Energy Electron Scattering by Atomic Oxygen', *Phys. Rev. A*, **14**, 1482, 1975.
- Tobiska, W.K., C.A. Barth, 'A Solar EUV Flux Model', *J. Geophys. Res.*, **95**, 8243, 1990.
- Torr, M.R., D.G. Torr and P.G. Richards, 'A Midlatitude Interhemispheric Model of the  $O^+(^2P)$  Emission at 7320Å', *Geophys. Res. Lett.*, **17**, 65, 1990a.
- Torr, M.R., D. G. Torr, P.G. Richards, S.P. Yung, 'Mid- and Low-Latitude Model of Thermospheric Emissions 1.  $O^+(^2P)$  7320Å and  $N_2(^2P)$  3371Å', *J. Geophys. Res.*, **95**, 21147, 1990b.
- Torr, M.R., D.G. Torr, 'Gas Phase Collisional Excitation of Infrared Emissions in the Vicinity of the Space Shuttle', *Geophys. Res. Lett.*, **15**, 95, 1988.
- Torr, M.R., D.G. Torr, 'Ionization Frequencies for Solar Cycle 21, Revised', *J. Geophys. Res.*, **90**, 6675, 1985.
- Torr, M.R., and D. G. Torr, 'The Role of Metastable Species in the Thermosphere', *Rev. Geophys.*, **20**, 91, 1982.
- Torr, M.R., P.G. Richards, D.G. Torr, 'A New Determination of the Ultraviolet Heating Efficiency of the Thermosphere', *J. Geophys. Res.*, **85**, 6819, 1980.
- Torr, M.R., D.G. Torr, R.A. Ong, H.E. Hinteregger, 'Solar Flux Variability in the Schumann-Runge Continuum as a Function of Solar Cycle 21', *J. Geophys. Res.*, **85**, 8063, 1980.
- Torr, M.R., D.G. Torr, R.A. Ong, H.E. Hinteregger, 'Ionization Frequencies for Major Thermospheric Constituents as a Function of Solar Cycle 21', *Geophys. Res. Lett.*, **6**, 771, 1979.
- Valladares, C.E., Su. Basu, R.J. Niciejewski, R.E. Sheehan, 'Simultaneous Radar and Satellite Observations of the Polar Cusp/Cleft at Søndre Strømfjord', in *Electromagnetic Coupling in the Polar Clefts and Caps*, Kluwer Academic Publishers, 285, 1989.
- Vallance Jones, A., 'Aurora', 301 pp, D. Reidel Publishing Co., Dordrecht-Holland, 1974.
- Vest, C.M., 'Formation of Images From Projections: Radon and Abel Transforms', *Journal of the Optical Society of America*, **64**, 1215, 1974.

- Vondrak, R.R., 'Chatanika Radar Measurements of the Electrical Properties of Auroral Arcs' in **Physics of Auroral Arc Formation**, edited by S.-I. Akasofu and J.R. Kan, pp. 185-191, 1981
- Walker, J.C.G., D.G. Torr, P. B. Hays, D. W. Rusch, K. Docken, G. Victor, M. Oppenheimer, 'Metastable  $^2P$  Oxygen Ions in the Daytime Thermosphere', **J. Geophys. Res.**, **80**, 1026, 1975.
- Walker, J.C.G. and M.H. Rees, 'Ionospheric Electron Densities and Temperatures in the Aurora', **Planet. Space Sci.**, **16**, 459, 1968.
- Wallace, L., 'An Analysis of a Spectrogram of the Aurora on 11 February 1958 in the Wavelength Range 3710-4420Å', **J. Atmos. Terr. Phys.**, **17**, 46, 1960.
- Wedde, T., T.G. Strand, 'Scattering Cross Sections for 40eV to 1keV Electrons Colliding Elastically with Nitrogen and Oxygen', **J. Phys. B7**, **7**, 1091, 1974.
- Weise, W.L., M.W. Smith, B.M. Glennon, 'Atomic Transition Probabilities', Vol.1, **Natl. Stand. Ref. Data Ser.**, US Nat. Bur. Stand., **4**, 1966.
- Wentzel, D.G., 'The Restless Sun', **Smithsonian Institution Press**, 1989.
- Whalen, B.A., J.R. Miller, I.B. McDiarmid, 'Sounding Rocket Observations of Particle Precipitation in a Polar Cap Electron Aurora', **J. Geophys. Res.**, **76**, 6847, 1971.
- Winningham, J.D., W.J. Heikkila, 'Polar Cap Auroral Electron Fluxes Observed with ISIS 1', **J. Geophys. Res.**, **79**, 949, 1974.
- Winske, D., C.S. Wu, Y.Y. Li, Z.Z. Mou, S.Y. Guo, 'Coupling of Newborn Ions to the Solar Wind by Electromagnetic Instabilities and Their Interaction with the Bow Shock', **J. Geophys. Res.**, **90**, 2713, 1985.
- Wu, C.S., D.S. Winske, J.D. Gaffey, 'Rapid Pickup of Cometary Ions Due to Strong Magnetic Turbulence', **Geophys. Res. Ltr.**, **13**, 865, 1986.
- Wu, C.S., R.E. Hartle, K.W. Ogilvie, 'Interaction of Singly Charged Interstellar Helium Ions with the Solar Wind', **J. Geophys. Res.**, **78**, 306, 1973.
- Yee, J.H., 'Non-Thermal Distribution of  $O(^1D)$  Atoms in the Night-Time Thermosphere', **Planet. Space Sci.**, Vol. **36**, 89, 1988.
- Yee, J.H. V.J. Abreu and P.B. Hays, 'The  $O II$  (7320-7330Å) Airglow: A Morphological Study', **J. Geophys. Res.**, **86**, 1564, 1981.

- Yee, J.H. and V.J. Abreu, 'Exospheric Temperatures Deduced From 7320 to 7330Å ( $O^+(^2P-^2D)$ ) Twilight Observations', *J. Geophys. Res.*, **87**, 913, 1982.
- Yee, J.H., 'A Theoretical and Experimental Study of the Atomic Oxygen Corona in the Earth's Atmosphere', **PhD Dissertation**, University of Michigan, Ann Arbor, 1980.
- Zipf, E.C., P.W. Erdman, 'Electron Impact Excitation of Atmospheric Oxygen: Revised Cross Section Values', *EOS*, **66**, 321, 1985.